



Kent Academic Repository

Lindsay, Rebecca J (2019) *Tuning Frustrated Pyrochlores*. Doctor of Philosophy (PhD) thesis, University of Kent,.

Downloaded from

<https://kar.kent.ac.uk/73058/> The University of Kent's Academic Repository KAR

The version of record is available from

This document version

UNSPECIFIED

DOI for this version

Licence for this version

UNSPECIFIED

Additional information

Versions of research works

Versions of Record

If this version is the version of record, it is the same as the published version available on the publisher's web site. Cite as the published version.

Author Accepted Manuscripts

If this document is identified as the Author Accepted Manuscript it is the version after peer review but before type setting, copy editing or publisher branding. Cite as Surname, Initial. (Year) 'Title of article'. To be published in *Title of Journal*, Volume and issue numbers [peer-reviewed accepted version]. Available at: DOI or URL (Accessed: date).

Enquiries

If you have questions about this document contact ResearchSupport@kent.ac.uk. Please include the URL of the record in KAR. If you believe that your, or a third party's rights have been compromised through this document please see our [Take Down policy](https://www.kent.ac.uk/guides/kar-the-kent-academic-repository#policies) (available from <https://www.kent.ac.uk/guides/kar-the-kent-academic-repository#policies>).

UNIVERSITY OF KENT

DOCTORAL THESIS

Tuning Frustrated Pyrochlores

Author: Rebecca J Lindsay

Supervisor: Mark A Green

*A thesis submitted in fulfilment of the requirements
for the degree of Doctor of Philosophy*

in the

Functional Materials Group
School of Physical Sciences

February 2019

Declaration of Authorship

I, Rebecca J LINDSAY, declare that this thesis titled, 'Tuning Frustrated Pyrochlores' and the work presented in it are my own. I confirm that:

- This work was done wholly or mainly while in candidature for a research degree at this University.
- Where any part of this thesis has previously been submitted for a degree or any other qualification at this University or any other institution, this has been clearly stated.
- Where I have consulted the published work of others, this is always clearly attributed.
- Where I have quoted from the work of others, the source is always given. With the exception of such quotations, this thesis is entirely my own work.
- I have acknowledged all main sources of help.
- Where the thesis is based on work done by myself jointly with others, I have made clear exactly what was done by others and what I have contributed myself.

Signed:



Date:

19th February 2019

'A Ph.D is an exhausting, emotional struggle. You are forced to confront all of your fears, insecurities and doubts you have about yourself and somehow overcome them. It's terrifying. A lot of bravery is required, which often goes unrecognised and unrewarded. Facing your own personalised set of fears (or demons, if you want to be dramatic) is where the feeling of isolation comes from - the fact that they are YOUR fears. Be brave. You know what you have to do - you know the right thing to do. Good luck.'

Unknown

UNIVERSITY OF KENT

Abstract

Faculty of Sciences
School of Physical Sciences

Doctor of Philosophy

Tuning Frustrated Pyrochlores

by Rebecca J LINDSAY

Structural studies have been conducted on a series of β -pyrochlore materials using primarily X-ray and powder neutron diffraction techniques. Mössbauer Spectroscopy and SQUID (Superconducting Quantum Interference Device) magnetometer measurements have also been performed to determine the oxidation states of Fe and the magnetic behaviour of materials, respectively. Particular attention has been paid to the fluoride family exhibiting a general formula of AM_2F_6 which exhibit both charge order and disorder on the transition metal crystallographic site. A newly developed soft chemistry synthetic route for producing a novel cubic pyrochlore, FeF_3 , with true porosity is reported which could play an instrumental role in designing a new family of β -pyrochlore materials. Finally, this work reports a possible charge ordered AM_2F_6 material exhibiting conventional spin-glass like magnetic behaviour similar to reported materials.

Acknowledgements

First of all, my greatest thanks goes to “The Boss”, Professor Mark Green, for such an enjoyable Ph.D. experience and for allowing me the opportunity to research such an interesting topic, with exceptionally talented people in such fantastic places. There is no doubt that my interest and enthusiasm in material science stems from his continual encouragement and open ended discussions. I am eternally grateful. It is at this point that I would like to thank the University of Kent’s Graduate Training Scholarship Program for funding.

I want to thank the many people who took the time to have inspiring discussions and provoke enthusiasm when motivation may have been lacking, especially, Dr. Pawel Zajdel, who I couldn’t imagine beginning my Ph.D. journey without - thank you for your knowledge and patience - I hope that I may be able to inspire someone the same way you did me. Thanks goes to both my internal and external examiners, Dr. Donna Arnold and Dr. Isaac Abrahams for all the time spent correcting my grammar and such an enjoyable discussion.

Craig Brown at ‘The National Institute of Standards and Technology’ has my greatest of thanks for allowing me to spend so much of my time at NCNR. This gave me the opportunity to meet fascinating researchers and learn a variety of skills. I will never forget having to cycle away from angry flocks of Canadian Geese whilst attempting to dodge deer most evenings after work.

I would like to extend my warmest of thanks to the wonderful people I had the opportunity to work with at the University of Kent, more specifically the Functional Materials Group and the “1st Floor Scientists”. Laura, Reeya, Chrysa, Ben and Dan - it is thanks to our discussions, supportive environment and friendship that I have made it out the other-side. I’d also like to thank Dr. Kinnear for his patience with my inability to work any form of technology when stressed despite my insistence that I know what I’m doing.

I am extremely fortunate to have had the opportunity to collaborate and work with many talented scientists from a number of Universities and central facilities. I am happy to thank Prof. Dave Harris and the Harris Group for warmly welcoming me into their work space allowing me to perform Mössbauer Spectroscopy measurements and analysis - thank you! I would also like to thank ‘The Long Group’ at the University of California, Berkeley for performing Gas Absorption measurements, which proved to be an integral part of this work. I would like to acknowledge Dr. Dave Pickup, Prof. Alan Chadwick and Dr. Silvia Ramos for analysis and useful discussions regarding XAFS data and Jake Minns for his help with single crystal diffraction refinements. I would like to thank all of

the instrument scientists at central facilities for their hard work and assistance, ensuring my experiments were successful making this Ph.D. thesis possible.

I want to thank my friends for all their support and motivational speeches despite not having any clue what it is that I actually do - if anything you are all just total distractions and maybe without you lot I would have finished this sooner!! I never imagined that I would be playing in a sports team called Geometrically Frustrated Magnets and travelling around the country educating the Ultimate Frisbee community on the meaning of long range order thanks to you guys.

I like to thank my family for their encouragement, friendship and life-long support (moral, financial or otherwise!) - had it not been for you I wouldn't have had the confidence to push myself into doing a Ph.D. Also Nada and Dejan, who have quickly become my family, thank you for everything.

Finally, I would like to thank Dr. Vid Čalovski, my best friend and happiness. You've build my confidence, made me laugh and feel supported throughout this journey. You've taught me so many thing, from how to be a better person to every spam fact a person could possibly need. I am forever grateful to have you in my life.

Contents

Declaration of Authorship	i
Abstract	iii
Acknowledgements	iv
Contents	vi
List of Figures	x
List of Tables	xx
Abbreviations	xxii
Symbols	xxiv
1 Structure and Properties	1
1.1 Fluoride Materials	1
1.1.1 Synthesis	1
1.1.2 Crystal Structure of Fluoride Materials	2
Open Framework Fluoride Materials	2
Layered Fluoride Materials	3
Chain Fluoride Materials	5
1.1.3 Physical Characteristics of Fluorides	6
Ferroelectric Behaviour	6
Multiferroic Behaviour	6
Spin Glass Behaviour	7
1.2 Designing new Materials	8
1.2.1 The Pyrochlore Structure	8
1.2.2 Defect Pyrochlore	10
1.3 Overview of Thesis	11
2 Theory and Experimental	12
2.1 Introduction	12
2.2 Synthesis	12

2.2.1	Hydrothermal Synthesis	12
	Experimental Details	13
2.3	Powder X-ray Diffraction (PXD)	14
2.3.1	Diffraction Theory	14
2.3.2	PXRD Instrumentation	18
2.3.3	The Rietveld Method	19
2.4	Powder Neutron Diffraction (PND)	20
2.4.1	Constant Wavelength PND	25
	High-Resolution Powder Diffractometer - BT1	25
2.4.2	Time of Flight (TOF) PND	26
	Wide - angle In a Single Histogram - WISH	27
2.5	Theory of Magnetic Interactions	28
2.5.1	Magnetic Moment	28
2.5.2	Magnetism in Bulk Materials	29
2.5.3	Mechanisms for Magnetic Exchange Interactions	32
	Direct Exchange	33
	Superexchange	33
	Magnetic Exchange in Metallic Systems	34
	Double Exchange	34
2.5.4	Geometric Magnetic Frustration	35
2.6	Correlation of Structure and Properties	37
2.7	Structure of Solids	37
2.7.1	Group Chemistry	37
2.7.2	Magnetic Structure	39
2.8	Measurement of Structural and Magnetic Properties	40
2.8.1	DC Susceptibility Measurements	40
2.8.2	Mössbauer Spectroscopy	41
2.8.3	X-ray Absorption Spectroscopy	42
2.8.4	X-ray Fluorescence (XRF)	43
3	A new topotactic de-intercalation synthesis method, producing the first truly porous, single phase, magnetically frustrated pyrochlore FeF_3.	44
3.1	Introduction	44
3.2	Experimental	48
3.2.1	Reagents	48
3.2.2	Synthesis	49
	Synthesis of RbFe_2F_6	49
	RbFe_2F_6 characterisation	49
	Synthesis of pyr- FeF_3	53
3.2.3	Structural Properties	54
	Crystal Structure	54
	Oxidation State of Iron	56
	Porosity	57
3.2.4	Magnetic Properties	59
	Magnetometry	59
	Powder Neutron Diffraction	62

3.3	The synthetic route	71
3.3.1	Structural Properties	71
	Sample 1	71
	Sample 2	77
	Sample 3	78
	Sample 4	82
3.3.2	Iron Oxidation State	84
	Mössbauer Spectroscopy	84
	XAFS	87
3.3.3	Magnetic Evolution	89
3.3.4	Sample 1	89
3.3.5	Sample 2	91
3.3.6	Sample 3	91
3.3.7	Sample 4	94
3.4	Applications	96
3.4.1	Battery Cycling	96
3.5	Conclusion	100
4	Synthesis, Structure and Characterisation of CsFe₂F₆	102
4.1	Introduction	102
4.2	Experimental	103
	4.2.1 Reagents	103
	4.2.2 Synthesis	103
4.3	Results and discussion	103
	4.3.1 Synthesis	103
	4.3.2 Structural Properties	104
	4.3.3 Neutron Diffraction Data	109
	4.3.4 Mössbauer Spectroscopy	115
	4.3.5 Magnetic Properties	115
4.4	Conclusion	119
5	Mixed Transition Metal Pyrochlore Fluorides	120
5.1	Introduction	120
5.2	Experimental	121
	5.2.1 Reagents	121
	5.2.2 Synthesis	121
5.3	Results and Discussion	122
	5.3.1 RbFeCrF ₆	122
	Crystallographic Structure	122
	Mössbauer Spectroscopy	125
	Magnetic Properties	126
	5.3.2 Cubic Mixed Metal Fluorides	129
5.4	Conclusion	136
6	Conclusions	137

A Supplementary Information	139
B Supplementary Information	146
C Supplementary Information	153
Bibliography	157

List of Figures

1.1	Examples of three dimensional framework fluorides: (a) Perovskite NaNiF_3 , ²² (b) Bronze $\text{K}_{0.6}\text{FeF}_3$, ²³ (c) Weberite $\text{Na}_2\text{Fe}_2\text{F}_7$, ²⁴ and (d) Pyrochlore RbFe_2F_6 , ¹³ where grey represents the metal octahedra and yellow the A site cation.	3
1.2	Layered fluoride examples: Single layer, (a) NH_4FeF_4 , ²⁵ (b) BaZnF_4 , ¹⁹ (c) K_2NiF_4 ²⁶ and (d) $\text{Na}_5\text{Al}_3\text{F}_{14}$. ²⁷ Double layer, (e) $\text{K}_3\text{Zn}_2\text{F}_7$ ²⁸ and (f) $\text{Cs}_4\text{CoCr}_4\text{F}_{18}$, ²⁹ where grey represents the metal octahedra and yellow the A site cation.	4
1.3	Examples of chain fluoride materials: Single chain structures, (a) BaMnF_5 ³⁰ and (b) $\text{BaMnF}_5\text{H}_2\text{O}$. ³¹ Double chain structures (c) CsCrF_4 ³² and (d) $\text{NaBaFe}_2\text{F}_9$, ³³ where the metal octahedra are shown in grey, purple, blue and orange respectively, the A site cation is shown in yellow and green and H_2O is shown in red.	5
1.4	The CaF_2 fluorite structure, ⁵⁵ showing Ca ions in blue and F ions in grey.	9
1.5	A comparison between a typical pyrochlore, (a), with the general formula $A_2B_2X_6X'$ and a defect (or β) pyrochlore, (b) with the general formula AB_2X_6 , where the B site metal octahedra are represented in green, the A site cation in grey and the X/X' site anion in yellow. ⁵⁹	10
2.1	Schematic diagram of stainless steal hydrothermal autoclave with Teflon liner.	13
2.2	Diffraction of X-rays incident upon parallel planes of atoms separated by a distance, d_{hkl} . The angle between the incident and scattered X-rays is 2θ . ⁷³	15
2.3	Diffraction of X-rays from isotropic powder sample resulting in <i>diffraction cones</i> that are at an angle of 2θ from the incident beam. ⁷³	15
2.4	Diffraction pattern of NaCl as taken from the National Chemical Database Service showing Miller indices for each Bragg reflection. A Cu $K\alpha_1$ radiation source was used with $\lambda = 1.54056\text{\AA}$	16
2.5	Neutrons and X-rays interact with a material differently. X-ray (blue) interact with the electron cloud but do not penetrate the material very deeply. Neutrons (red) interact with the atomic nuclei and penetrate the material deeper than X-rays. Neutrons also interact via a dipole-dipole interaction between the magnetic moment of an unpaired electron and the magnetic moment of the neutron. ⁸⁰	21
2.6	High resolution powder neutron diffractometer schematic BT1, at the NIST Center for Neutron Research, showing the location of monochromators, sample space and detectors. ⁸³	26
2.7	Paramagnetism and Diamagnetism in an applied field	29

2.8	Common magnetic states	31
2.9	Curie law and Curie-Weiss law	32
2.10	180° and 90° geometry which can affect the long-range magnetic ordering through superexchange.	34
2.11	Geometric Frustration	36
2.12	The four types of antiferromagnetic interactions	40
3.1	RbFe ₂ F ₆ three-dimensional crystal structure obtained from single crystal diffraction where pink, dark blue and light blue represent Rb, Fe ²⁺ F ₆ polyhedra and Fe ³⁺ F ₆ polyhedra respectively. Kagome-planes are the result of the octahedral connectivity in both planes.	45
3.2	The magnetic structure of the RbFe ₂ F ₆ at 1.6 K obtained from BT1 powder diffraction data. The Fe ⁺² ions, yellow, aligning along the a-axis forming antiferromagnetic chains along the b-axis and the Fe ⁺³ ions, green, aligning along the b-axis forming antiferromagnetic chains down the a-axis. The theoretical spin only value is 7.7 μ _B (Fe ⁺² = 4.9 μ _B , Fe ⁺³ = 5.9 μ _B), which is considerably higher than the observed value of 3.99(5) μ _B . ¹³	46
3.3	The crystallographic structure of FeF ₃ phases, (a)R-FeF ₃ , ¹⁰⁴ (b) HTB-FeF ₃ ¹⁰⁵ and pyr-FeF ₃ ¹⁰⁶ (c) along the [011] and (d) [0-11] direction, showing the three dimensional interconnecting tunnel network without H ₂ O or (NH ₃) _x , where green shows the Fe-F octahedral, grey shows the fluorine ions and red as H ₂ O.	48
3.4	Fitted powder neutron diffraction data collected on the BT1 diffractometer of RbFe ₂ F ₆ at 300 K, with lattice parameters $a = 7.022(3)$ Å, $b = 7.447(3)$ Å and $c = 10.177(5)$ Å and $\alpha = \beta = \gamma = 90^\circ$ consistent with the previously published structure. ¹³	50
3.5	Mössbauer absorption spectra of RbFe ₂ F ₆ at 250 K, (3.5a), showing the fit to Fe ³⁺ which gives an isomer shift of $\delta = 0.494(2)$ mm/s and a quadrupole splitting of $\Delta E_Q = 0.699(4)$ mm/s. Fe ²⁺ gives an isomer shift of $\delta = 1.322(2)$ mm/s and a quadrupole splitting of $\Delta E_Q = 2.673(3)$ mm/s. At 80 K, (3.5b), the fit to Fe ³⁺ gives an isomer shift of $\delta = 0.558(2)$ mm/s and a quadrupole splitting of $\Delta E_Q = 0.694(4)$ mm/s and Fe ²⁺ gives an isomer shift of $\delta = 1.418(2)$ mm/s and a quadrupole splitting of $\Delta E_Q = 2.762(4)$ mm/s. Both temperatures give no indication of magnetic splitting displaying the octahedral coordination of Fe ³⁺ and Fe ²⁺	51
3.6	The magnetic susceptibility for a powder sample of RbFe ₂ F ₆ with an anomaly at 18 K indicating the antiferromagnetic transition as well as a small feature in the data at 3 K which has not yet been reported. The inset displays the analysis of the paramagnetic region between 300 K to 200 K giving $\theta_{CW} = -135$ K.	52
3.7	X-ray diffraction data collected at 300 K (red), Rietveld refined model (black) and the difference (blue) plot for powder sample of pyr-FeF ₃ . The data were collected using the methods described in Section 2.3.2. The fit parameters are $\chi^2 = 2.24$, $R_p = 6.28\%$ and $R_{wp} = 8.02\%$	54
3.8	The crystallographic structure of pyr-FeF ₃ displaying no chemical distortion within the cationic lattice and all iron ions nominally of a 3 ⁺ oxidation state.	55

- 3.9 Mössbauer absorption spectrum for pyr-FeF₃ taken at 80 K. The red line corresponds to Fe³⁺, confirming that all Fe are normally 3⁺ free from Fe²⁺. The fit gives an isomer shift of $\delta = 0.570(3)$ mm/s and a quadrupole splitting of $\Delta E_Q = 0.265(5)$ mm/s. 56
- 3.10 Dihydrogen adsorption isotherms collected at 77 K (blue) and 87 K (yellow). The lines represent the best fit to the adsorption data using a dual-site Langmuir-Freundlich equation. Dinitrogen adsorption at 77 K (green) is also plotted. 58
- 3.11 Isothermic heats of adsorption calculated as a function of dihydrogen loading in pyr-FeF₃ using the Clausius-Clapeyron equation and adsorption isotherms collected at 77 K and 87 K. 58
- 3.12 The magnetic susceptibility for a powder sample of pyr-FeF₃. The inset, the inverse susceptibility as a function of temperature, shows the fit of the paramagnetic region between 300 K and 200 K. From the fit the effective magnetic moment is calculated as $\mu_{eff} = 4.99(3) \mu_B$, and the Curie-Weiss constant is $\theta_{CW} = -699.14(7)$ K. 60
- 3.13 The field cooled and zero field cooled inverse magnetic susceptibility for a powder sample of pyr-FeF₃ between 200 K and 2 K measured in 100 Oe. The dashed line at 18 K indicates the temperature at which a cusp is observed in the susceptibility indicating a phase transition occurring at this temperature. 61
- 3.14 The 6-fold coordination environment of Fe in the pyr-FeF₃ structure. 62
- 3.15 The Rietveld refined BT1 NPD data of pyr-FeF₃ collected at 300 K. Data points and calculated fit are displayed in the upper curve and the difference between the observed and calculated pattern is displayed in the lower curve. Sets of vertical tick marks represent the expected positions of nuclear reflections for pyr-FeF₃. 63
- 3.16 Temperature evolution of the magnetic scattering of pyr-FeF₃ (diffraction patterns have been offset along the y-axis for clarity) collected on the BT1 Neutron Powder Diffractometer. The blue dotted lines at $33.0867 2\theta(220)$ and $52.0566 2\theta(331)$ represent nuclear diffraction peaks which have magnetic contributions as temperature decreases. The red dotted line at $53.52 2\theta(420)$ highlights the single magnetic only reflection. 64
- 3.17 Fitted diffraction data for pyr-FeF₃ using powder neutron diffraction collected on the BT1 diffractometer at (a) 25 K and (b) 6 K. Data points and calculated fit are displayed in the upper curve and the difference between the observed and calculated pattern is displayed in the lower curve. Sets of vertical tick marks (from top to bottom) represent the expected positions of nuclear reflections for pyr-FeF₃ and the expected magnetic reflections for pyr-FeF₃ respectively. Where there is only one set of vertical tick marks, this represents the nuclear diffraction pattern without magnetic contribution. The fit parameters are $\chi^2 = 0.969$, $R_p = 7.98\%$ and $R_{wp} = 10.4\%$ and $\chi^2 = 0.837$, $R_p = 7.95\%$ and $R_{wp} = 10.4\%$ for 25 K and 6 K respectively. The agreement factors for the nuclear and magnetic phases shown in (b) are $R_{nuc} = 1.67\%$ and $R_{mag} = 5.24\%$ 65

3.18	The magnetic structure of ptr-FeF ₃ at 6 K determined from Rietveld refinement performed on neutron scattering data collected on the BT1 diffractometer. The magnetic structure can be described as two interpenetrating networks of tetrahedra with four iron spins aligned towards the center of the tetrahedron in all-in or all-out configurations.	66
3.19	Pyr-FeF ₃ diffuse scattering as a function of temperature where 'x' marks the low angle diffuse scattering.	67
3.20	Temperature evolution of ordered moment in pyr-FeF ₃ . It is only possible to fit the order parameter in the temperature region of 11 K - 17 K as the curve deviates above and below this region. The critical exponent obtained was found to be 0.326(8), which is close to the value for a 2D Ising model (0.31).	67
3.21	The fitted area of the 420 magnetic only reflection as a function of temperature.	68
3.22	Fitted diffraction data for pyr-FeF ₃ using powder neutron diffraction collected on the BT1 diffractometer at (a) 25 K and pyr-FeF ₃ ·0.05(4)D ₂ at (b) 25 K. Data points and calculated fit are displayed in the upper curve and the difference between the observed and calculated pattern is displayed in the lower curve. Sets of vertical tick marks (from top to bottom) represent the expected positions of nuclear reflections for pyr-FeF ₃ and pyr-FeF ₃ ·0.05(4)D ₂	69
3.23	Fitted diffraction data pyr-FeF ₃ using powder neutron diffraction collected on the BT1 diffractometer at (a) 5 K and pyr-FeF ₃ ·0.04(5)D ₂ at (b) 5 K. Data points and calculated fit are displayed in the upper curve and the difference between the observed and calculated pattern is displayed in the lower curve. Sets of vertical tick marks (from top to bottom) represent the expected positions of nuclear reflections for pyr-FeF ₃ and pyr-FeF ₃ ·0.04(5)D ₂ . The lower set of tick marks represent the expected magnetic reflections.	70
3.24	Fitted diffraction profile for Sample 1 Wish NPD data collected at 300 K. Data points and calculated fit are displayed in the upper curve and the difference between the observed and calculated pattern is displayed in the lower curve. Sets of vertical tick marks (from top to bottom) represent the expected positions of nuclear reflections for Sample 1 _{orth} and the expected nuclear reflections for Sample 1 _{cub} , respectively. The inset shows the presence of three unrefined peaks, both peaks (highlighted in pink) at 4.86 Å and 6.46 Å are suspected to be from the magnetite structure, Fe ₃ O ₄ . The peak at 5.18 Å (highlighted in green) is suspected to be an iron oxide impurity.	72
3.25	Zero Field Cooled and Field Cooled SQUID magnetometry data of Sample 1 in a field of 100 Oe. The Verwey transition is displayed as a 'bump' at 120 K.	73
3.26	The magnetic evolution of the impurity peak for Sample 1 at 5.18 Å.	74
3.27	Sample 1 _{orth} along the ac, (a), and bc, (b), plane and Sample 1 _{cub} , (c), both of which are present in the samples.	74
3.28	The 10-fold coordination environment of Rb (3.28a) and the 6-fold coordination environment of Fe ²⁺ (3.28b), shown in blue, and Fe ³⁺ (3.28c), shown in red, obtained from rietveld refinement of Sample 1 _{orth}	75

3.29	Fitted Wish NPD data collected at 20 K for Sample 2. Data points and calculated fit are displayed in the upper curve and the difference between the observed and calculated pattern is displayed in the lower curve. Sets of vertical tick marks (from top to bottom) represent the expected positions of nuclear reflections for Sample 2 _{orth} and the expected nuclear reflections for Sample 2 _{cub} respectively. Three unrefined peaks are present, similar to Sample 1, where both peaks at 4.86 Å and 6.46 Å are suspected to be from the magnetite structure, Fe ₃ O ₄ . The peak at 5.18 Å is suspected to be an iron oxide impurity.	77
3.30	Fitted diffraction profile for Sample 3a, Rb _{0.236(8)} FeF ₃ and Sample 3b, Rb _{0.18} FeF ₃ , X-ray diffraction data collected at 300 K respectively. Data points and calculated fit are displayed in the upper curve and the difference between the observed and calculated pattern is displayed in the lower curve. The set of vertical tick marks represent the expected positions of nuclear reflections for Rb _{0.236(8)} FeF ₃ and Rb _{0.18} FeF ₃ . There is no evidence of impurity peaks.	79
3.31	Fitted diffraction profiles for Sample 3b _{cub} Wish NPD data collected at 300 K from bank 2. Data points and calculated fit are displayed in the upper curve and the difference between the observed and calculated pattern is displayed in the lower curve. Sets of vertical tick marks represent the expected positions of nuclear reflections for Rb _{0.18} FeF ₃	80
3.32	Sample 3b _{cub} lattice parameter as a function of temperature, decreasing until approximately 25 K where a plateau is seen.	81
3.33	Fitted diffraction profile for Sample 4 _{cub} Wish NPD data collected at 20 K (highest temperature measured) from bank 2. Data points and calculated fit are displayed in the upper curve and the difference between the observed and calculated pattern is displayed in the lower curve. Sets of vertical tick marks represent the expected positions of nuclear reflections for Rb _{0.11} FeF ₃	82
3.34	The lattice parameter as a function of temperature for Sample 4 _{cub}	83
3.35	Rietveld refined x-ray diffraction pattern for (a) Sample 5 _{cub} , Rb _{0.197(5)} FeF ₃ , (b) Sample 6 _{cub} , Rb _{0.166(5)} FeF ₃ and (c) Sample 7 _{cub} , Rb _{0.14(6)} FeF ₃	85
3.36	Mössbauer absorption spectra for three samples, Sample 5 _{cub} , Rb _{0.197(5)} FeF ₃ , Sample 6 _{cub} , Rb _{0.166(5)} FeF ₃ and Sample 7 _{cub} , Rb _{0.14(6)} FeF ₃ respectively. All spectra were collected at 80 K. Both Sample 5 _{cub} and Sample 6 _{cub} have Fe ²⁺ present whilst Sample 7 _{cub} has all Fe ions fully oxidised to Fe ³⁺ indicating that all Fe will be fully oxidised at a Rb occupancy between 0.16 and 0.01.	86
3.37	Fe K-edge x-ray absorption near edge structure (XANES) spectra for FeF ₃ , Sample 5 _{cub} (Rb _{0.197(5)} FeF ₃), Sample 6 _{cub} (Rb _{0.166(5)} FeF ₃), Sample 7 _{cub} (Rb _{0.14(6)} FeF ₃) and RbFe ₂ F ₆	88

- 3.38 Refined structural and magnetic data for Sample 1 using powder neutron diffraction collected on the WISH diffractometer, bank 2, at 1.6 K. Data points and calculated fit are displayed in the upper curve and the difference between the observed and calculated pattern is displayed in the lower curve. Sets of vertical tick marks (from top to bottom) represent the expected positions of nuclear reflections for Sample 1_{cub} phase, the expected magnetic reflections for Sample 1_{cub}, the expected positions of nuclear reflections for Sample 1_{orth} phase and the expected magnetic reflections for Sample 1_{orth}. The fit parameters for Sample 1_{cub} are $\chi^2 = 40.5$, Bragg R-factor = 5.47% and Rf-factor = 2.47% with the magnetic R-factor = 7.06%. The fit parameters for Sample 1_{orth} are $\chi^2 = 40.5$, Bragg R-factor = 5.77% and Rf-factor = 5.01% with the magnetic R-factor = 19.6%. 89
- 3.39 The refined moment on the Fe ion in Sample 1_{cub}. It is only possible to fit the order parameter between 13 K and 8 K as the curve deviates above and below these temperatures. The critical exponent obtained was found to be 0.33(2) which is close to the expected value of a 3D Ising model (0.326).¹¹¹ 90
- 3.40 The refined values of both Fe moments in Sample 1_{orth}, where the order parameter has been fitted between temperatures of 15 K and 10 K, for Fe⁺², and 17 K and 10 K, for Fe⁺³, giving critical exponents of 0.33(4) and 0.33(6), respectively. 91
- 3.41 Fitted diffraction profile for Sample 2 using powder neutron diffraction collected on the WISH diffractometer at (a) 20 K and (b) 1.6 K. Data points and calculated fit are displayed in the upper curve and the difference between the observed and calculated pattern is displayed in the lower curve. Sets of vertical tick marks (from top to bottom) represent the expected positions of nuclear reflections for Sample 2_{cub}, the expected magnetic reflections for Sample 2_{cub}, the expected position of nuclear reflections for Sample 2_{orth} and the magnetic reflections for Sample 2_{orth} respectively. Where there is only one set of vertical tick marks, this represents the nuclear diffraction pattern without magnetic contribution. . . 92
- 3.42 A comparison of diffraction patterns collected at a range of temperatures of Sample 3b_{cub} with no magnetic ordering. 93
- 3.43 The refined magnetic moments of the cubic phase as a function of overall Rb occupancy, for Samples 1 - 4 including pyr-FeF₃. 94
- 3.44 The refined magnetic moments of the orthorhombic RbFe₂F₆ phase as a function of Rb occupancy, exhibiting similar disorder to that of the cubic phase with a reduction of magnetic moment on both Fe ions. 95
- 3.45 Charge capacity, in milliamperere per hour per gram, of pyr-FeF₃ as a function of voltage. 97
- 3.46 The charge and discharge of pyr-FeF₃ for each cycle. 98
- 4.1 Comparison of experimental and calculated powder X-ray diffraction patterns for CsFe₂F₆. 104
- 4.2 X-ray diffraction data collected at 300 K (red), calculated profile (black) and the difference (blue) plot for powder sample of CsFe₂F₆. The data were collected using the methods described in Section 2.3.2. The fit parameters are $\chi^2 = 1.10$, $R_p = 8.29\%$ and $R_{wp} = 10.6\%$ 105

- 4.3 CsFe₂F₆ structure, with Fe⁺² shown in blue, Fe⁺³ shown in yellow and Cs in red along the, 4.3a, ac-plane displaying the Fe⁺² ions connected along the c-axis and, 4.3b, Fe⁺³ ions connected along the b-axis with a Cs cation within the pores of the structure. 107
- 4.4 The 10-fold coordination environment of Cs (4.4a) and the 6-fold coordination environment of Fe²⁺ (4.4b), shown in blue, and Fe³⁺ (4.4c), shown in yellow. 108
- 4.5 Refined model of CsFe₂F₆ using powder neutron diffraction collected on the BT1 diffractometer at 30 K. Data points (red) and calculated fit (black) are displayed in the upper curve and the difference (blue) between the observed and calculated pattern is displayed in the lower curve. Sets of vertical tick marks (orange) represent the expected positions of nuclear reflections for CsFe₂F₆. The fit parameters are $\chi^2 = 2.25$, $R_p = 9.36\%$ and $R_{wp} = 11.36\%$ 109
- 4.6 Lattice parameters, a (4.6a), b (4.6b), c (4.6c) and volume (4.6d) of CsFe₂F₆ as a function of temperature (K) obtained from Rietveld refinement of powder neutron diffraction data from the BT1 diffractometer. There is a consistent decrease in lattice parameter in each lattice as well as the volume of the unit cell, however, a negative thermal expansion is observed after approximately 50 K, more considerably with the b lattice. Error bars present are smaller than point size. 111
- 4.7 BT1 neutron diffraction data collected at 5 K and 25 K both displaying diffuse scattering (highlighted by a red box) around the (111) peak. Data collected above 25 K is of insufficient quality to determine the temperature at which this diffuse scattering is no longer present. 112
- 4.8 Fitted powder neutron diffraction data for CsFe₂F₆ using powder neutron diffraction collected on the BT1 diffractometer at 5 K. Data (red) points and calculated fit (black) are displayed in the upper curve and the difference (blue) between the observed and calculated pattern is displayed in the lower curve. Sets of vertical tick marks (orange), from top to bottom, represent the expected positions of nuclear reflections for CsFe₂F₆ and the expected magnetic reflections for CsFe₂F₆ respectively. 113
- 4.9 The magnetic structure of CsFe₂F₆ with an overall effective magnetic moment of 4.11(6) μ_B . The first Fe site, (0.76, 0.25, 0.74), in yellow, has a magnetic moment of 1.57(2) μ_B confined along the b-axis and can be described as forming antiferromagnetic chains along the a-axis. These antiferromagnetic chains are perpendicular to the moments of the second Fe at (0.5, 0.5, 0.5), in green. The second Fe has a magnetic moment of 3.76(2) μ_B sitting along the a-axis forming antiferromagnetic chains parallel to the b-axis. This magnetic structure is in good agreement with the magnetic structure of RbFe₂F₆ discussed in the previous Chapter. . . 114

- 4.10 Mössbauer absorption spectra of CsFe₂F₆ displaying the individual Fe fits and the sum of quadrupole doublets with different intensity and splitting . The fit to Fe³⁺ gives an isomer shift of $\delta = 0.538(5)$ mm/s and a quadrupole splitting of $\Delta E_Q = 0.716(9)$ mm/s and Fe²⁺ gives an isomer shift of $\delta = 1.439(6)$ mm/s and a quadrupole splitting of $\Delta E_Q = 2.835(11)$ mm/s, both with no magnetic splitting displaying the octahedral coordination of Fe³⁺ and Fe²⁺. With reference to the peak area, the ratio between Fe²⁺ and Fe³⁺ sites are similar being within 3 standard deviations, however, it is suggested that Fe³⁺ is more dominant within the system. 116
- 4.11 Temperature dependence of the inverse magnetic susceptibility with the inset showing a close up of the low temperature region where a phase transition takes place at 22 K. 117
- 4.12 The magnetic susceptibility for a powder sample of CsFe₂F₆. The inverse susceptibility as a function of temperature is displayed throughout the paramagnetic region and the fit of this region between 300 K and 200 K is shown. From the fit the effective magnetic moment is calculated as $\mu_{eff} = 8.71 \mu_B$, and the Curie-Weiss constant is $\theta_{CW} = -304(2)$ K. The inset shows the linear magnetisation vs. field at 1.8 K. 118
- 5.1 Previously reported structure of RbFeCrF₆, where Rb = pink and the disordered Fe/Cr octahedra are in yellow, crystallising in the *Fd-3m* space group with lattice parameter $a = 10.274 \text{ \AA}$.¹³⁸ 121
- 5.2 RbFeCrF₆ three-dimensional crystal structure obtained from single crystal diffraction where pink, dark blue and yellow represent Rb, Cr³⁺F₆ polyhedra and Fe²⁺F₆ polyhedra respectively. Kagome planes are the result of the octahedral connectivity in both planes. 123
- 5.3 Mössbauer absorption spectra of RbFeCrF₆ at 80 K displaying the individual Fe fits. The values for the isomer shift and quadrupole splitting of each Fe present is given in the Figure. The ratio between Fe²⁺ and Fe³⁺ is 9:1 respectively. No magnetic splitting is observed. 125
- 5.4 Temperature variation of ZFC and FC dc magnetic susceptibility in a temperature range 1.8 K - 300 K with an applied external field of 1 kOe. Inset shows the clear bifurcation between ZFC and FC curves typical of spin glass character. 126
- 5.5 Inverse susceptibility versus temperature of RbFeCrF₆ in a temperature range of 1.8 K - 300 K and an applied magnetic field of 1 kOe. The Curie-Weiss fit (line) with the Curie-Weiss temperature $\theta_{CW} = -100$ K and an effective moment of $0.018 \mu_B$. The inset shows a close up of the low temperature deviation from paramagnetic behaviour. 127
- 5.6 The hysteresis, magnetization (*M*) vs. applied field (*H*), loop at 2 K, 20 K and 200 K for RbFeCrF₆. The inset shows the low field measurements for 2 K suggesting a coercive field $H_c \approx 250$ Oe. 128

- 5.7 Fitted diffraction profiles for (a) CsCoCrF₆ and (b) RbCoCrF₆ using powder X-ray diffraction collected at 296 K. Data points and calculated fit are displayed in the upper curve and the difference between the observed and calculated pattern is displayed in the lower curve. Sets of vertical tick marks represent the expected positions of nuclear reflections for each material. The fit parameters are $\chi^2 = 2.23$, $R_p = 6.55\%$ and $R_{wp} = 8.67\%$ and $\chi^2 = 2.47$, $R_p = 4.11\%$ and $R_{wp} = 5.89\%$ for CsCoCrF₆ and RbCoCrF₆ respectively. 130
- 5.8 Fitted diffraction profiles for (a) CsNiCrF₆ and (b) RbNiCrF₆ using powder X-ray diffraction collected at 296 K. Data points and calculated fit are displayed in the upper curve and the difference between the observed and calculated pattern is displayed in the lower curve. Sets of vertical tick marks represent the expected positions of nuclear reflections for each material. The fit parameters are $\chi^2 = 2.42$, $R_p = 9.43\%$ and $R_{wp} = 12.3\%$ and $\chi^2 = 2.73$, $R_p = 7.38\%$ and $R_{wp} = 9.71\%$ for CsNiCrF₆ and RbNiCrF₆ respectively. 131
- 5.9 An example of the typical cubic $Fd-3m$ space group crystal structure that ACoCrF₆ and ANiCrF₆ (where A = Cs, Rb) adopt. The corner sharing MF₆ octahedra are shown in blue and the A cation in pink. 132
- 5.10 Temperature variation of ZFC and FC dc magnetic susceptibility of CsCoCrF₆ in a temperature range 1.8 K - 300 K with an applied external field of 100 Oe. The inset shows the inverse susceptibility versus temperature in a range of 1.8 K - 20 K. The Curie-Weiss fit (line) has been extrapolated from a higher temperature region (200 K - 300 K) not shown, with the Curie-Weiss temperature $\theta_{CW} = -62$ K. 133
- 5.11 Inverse susceptibility versus temperature of CsNiCrF₆ in a temperature range of 1.8 K - 300 K and an applied magnetic field of 100 Oe. The Curie-Weiss fit (line) with the Curie-Weiss temperature $\theta_{CW} = -41$ K. . 134
- 5.12 Fitted diffraction profile for CsNiCrF₆ using powder neutron diffraction collected on the BT1 diffractometer at 5 K. Data points (red) and calculated fit (black) are displayed in the upper curve and the difference (blue) between the observed and calculated pattern is displayed in the lower curve. Sets of vertical tick marks (orange) represent the expected positions of nuclear reflections for CsNiCrF₆. The fit parameters are $\chi^2 = 3.19$, $R_p = 4.15\%$ and $R_{wp} = 5.39\%$ 135
- A.1 Refined model of CsFe₂F₆ using powder neutron diffraction collected on the BT1 diffractometer at 10 K. 140
- A.2 Refined model of CsFe₂F₆ using powder neutron diffraction collected on the BT1 diffractometer at 14 K. 140
- A.3 Refined model of CsFe₂F₆ using powder neutron diffraction collected on the BT1 diffractometer at 16 K. 141
- A.4 Refined model of CsFe₂F₆ using powder neutron diffraction collected on the BT1 diffractometer at 18 K. 141
- A.5 Refined model of CsFe₂F₆ using powder neutron diffraction collected on the BT1 diffractometer at 20 K. 142
- A.6 Refined model of CsFe₂F₆ using powder neutron diffraction collected on the BT1 diffractometer at 20.5 K. 142

A.7	Refined model of CsFe ₂ F ₆ using powder neutron diffraction collected on the BT1 diffractometer at 21 K.	143
A.8	Refined model of CsFe ₂ F ₆ using powder neutron diffraction collected on the BT1 diffractometer at 21.5 K.	143
A.9	Refined model of CsFe ₂ F ₆ using powder neutron diffraction collected on the BT1 diffractometer at 22 K.	144
A.10	Refined model of CsFe ₂ F ₆ using powder neutron diffraction collected on the BT1 diffractometer at 23 K.	144
A.11	Refined model of CsFe ₂ F ₆ using powder neutron diffraction collected on the BT1 diffractometer at 25 K.	145
B.1	Refined model of pyr-FeF ₃ using powder neutron diffraction collected on the BT1 diffractometer at 6 K.	146
B.2	Refined model of pyr-FeF ₃ using powder neutron diffraction collected on the BT1 diffractometer at 8 K.	147
B.3	Refined model of pyr-FeF ₃ using powder neutron diffraction collected on the BT1 diffractometer at 10 K.	147
B.4	Refined model of pyr-FeF ₃ using powder neutron diffraction collected on the BT1 diffractometer at 12 K.	148
B.5	Refined model of pyr-FeF ₃ using powder neutron diffraction collected on the BT1 diffractometer at 13 K.	148
B.6	Refined model of pyr-FeF ₃ using powder neutron diffraction collected on the BT1 diffractometer at 14 K.	149
B.7	Refined model of pyr-FeF ₃ using powder neutron diffraction collected on the BT1 diffractometer at 15 K.	149
B.8	Refined model of pyr-FeF ₃ using powder neutron diffraction collected on the BT1 diffractometer at 16 K.	150
B.9	Refined model of pyr-FeF ₃ using powder neutron diffraction collected on the BT1 diffractometer at 17 K.	150
B.10	Refined model of pyr-FeF ₃ using powder neutron diffraction collected on the BT1 diffractometer at 5 K.	151
B.11	Refined model of pyr-FeF ₃ using powder neutron diffraction collected on the BT1 diffractometer at 100 K.	152
B.12	Refined model of pyr-FeF ₃ using powder neutron diffraction collected on the BT1 diffractometer at 300 K.	152
C.1	Page 1 of checkcif.file for single crystal refinement of RbFeCrF ₆	153
C.2	Page 2 of checkcif.file for single crystal refinement of RbFeCrF ₆	154
C.3	Page 3 of checkcif.file for single crystal refinement of RbFeCrF ₆	155
C.4	Page 4 of checkcif.file for single crystal refinement of RbFeCrF ₆	156

List of Tables

1.1	Atomic parameter coordinates for a pyrochlore cell	9
2.1	Monochromator information for BT1, NIST, USA.	25
2.2	The Seven Crystal Systems	38
3.1	The crystallographic parameters of FeF_3 phases, R- FeF_3 , ¹⁰⁴ HTB- FeF_3 ¹⁴ and $Fd-3m$. ¹⁰⁶ ^a The cell is given in its rhombohedral setting. ^b In the referenced paper, the space group is given as $P6/mmm$, there is no report of structural data and the data of the hydrated form from which it is derived is given alternatively. ^c No reports of truly porous pyr- FeF_3 have been produced, the data here are that of Pyr- $(\text{NH}_3)_x\text{FeF}_3$	47
3.2	Crystallographic data for pyr- FeF_3 obtained through Rietveld refinement of powder X-ray diffraction.	55
3.3	Synthesis parameters of intermediate samples between RbFe_2F_6 and pyr- FeF_3	71
3.4	Rietveld refinement results of WISH NP Diffractometer for samples 1 - 4 at the highest temperature recorded. Sample 1 and 2 consist of two phases in different ratios, an orthorhombic RbFe_2F_6 phase and a cubic $\text{Rb}_{1-x}\text{FeF}_3$ phase. Whilst Samples 3 and 4 only consist of the cubic $\text{Rb}_{1-x}\text{FeF}_3$ with differing Rb occupancies.	72
3.5	Bond distances form Sample 1 _{orth}	76
3.6	The crystallographic and occupancy refined values for Sample 3a displaying two Rb crystallographic sites.	78
3.7	Synthesis parameters of intermediate samples between RbFe_2F_6 and pyr- FeF_3	84
3.8	The K-edge values for pyr- FeF_3 , Sample 5 _{cub} , Sample 6 _{cub} , Sample 7 _{cub} and RbFe_2F_6	87
3.9	The effective magnetic moments of each phase for each Sample analysed including pyr- FeF_3 and RbFe_2F_6	95
3.10	The Li^+ discharge/charge values in mAh g^{-1} for pyr- FeF_3	98
4.1	Crystallographic data for CsFe_2F_6 obtained through rietveld refinement of powder X-ray diffraction.	106
4.2	The refined positions from rietveld refinement of powder X-ray diffraction data of CsFe_2F_6 at 300 K, with lattice parameters $a = 7.2443(1) \text{ \AA}$, $b = 7.415(9) \text{ \AA}$ and $c = 10.4238(1) \text{ \AA}$ with $\alpha = \beta = \gamma = 90^\circ$	106
4.3	Bond distances of CsFe_2F_6	107

4.4	The refined positions from Rietveld refinement of powder neutron diffraction data collected on the BT1 diffractometer of CsFe_2F_6 at 5 K, with lattice parameters $a = 7.211(8) \text{ \AA}$, $b = 7.425(8) \text{ \AA}$ and $c = 10.41(1) \text{ \AA}$ with $\alpha = \beta = \gamma = 90^\circ$	112
4.5	Mössbauer parameters for iron fluoride materials similar to that of CsFe_2F_6 reported in this work.	115
5.1	Crystallographic data for RbFeCrF_6 obtained through rietveld refinement of single crystal X-ray diffraction.	123
5.2	Atomic coordinates for RbFeCrF_6	124
5.3	Relevant bond distances of RbFeCrF_6	124
5.4	Crystallographic data for CsCoCrF_6 and RbCoCrF_6 obtained through rietveld refinement of Powder X-ray diffraction.	129
5.5	Crystallographic data for CsNiCrF_6 and RbNiCrF_6 obtained through rietveld refinement of Powder X-ray diffraction.	132

Abbreviations

FM	FerroMagnetic
AFM	AntiFerroMagnetic
PPMS	Physical Property Measurment System
MPMS	Magnetic Property Measurment System
SQUID	Superconducting QUantum Interference Device
PXRD	Powder X-Ray Diffraction
SXRD	Single crystal X-Ray Diffraction
SEM	Scanning Electron Microscope
XANES	X-ray Absorption Near Edge Spectroscopy
T	Temperature [K], Tesla
T_C	Curie Temperature
T_N	Néel Temperature
T_f	Freezing Temperature
AC	Alternating Current
DC	Direct Current
FC	Field Cooled
ZFC	Zero Field Cooled

'Is iomaí slí muc a mharú seachas a thachtadh le h-im.'

Symbols

χ	Susceptibility
θ	Curie-Weiss Temperature
μ_B	Bohr Magneton

Dedicated to Grampsie...

Chapter 1

Structure and Properties

This chapter gives a brief overview into some currently known fluoride materials, giving insight into the breath of crystallographic structures and physical properties they can exhibit. The structures and physical characteristics presented in this chapter are not necessarily the main focus of this work; however, more detail is given on the pyrochlore and related structures due to the relevance of this thesis.

1.1 Fluoride Materials

Transition metal compounds have become an increasingly popular field of study due to the range of physical properties they exhibit, including electronic and magnetic, such as ferromagnetism, ferroelectric, ferroelectric and multiferroic.¹⁻¹² However, the vast majority of studies have been focused on oxides rather than non-oxides due to the relative difficulty in synthesis. Fluorides possess strongly correlated electrons, exhibiting similarly interesting physical properties to oxides, regardless, they are still poorly understood in comparison. New synthesis techniques have recently been investigated¹³ which has been instrumental in the development and progression of this field. This chapter reviews the synthesis, general crystal structures and properties of fluoride materials.

1.1.1 Synthesis

Oxides are a more dominant area of study with respect to fluorides, as fluorides have low thermal stability and a high tendency to hydrolyse to oxides during synthesis.¹⁴ To prevent this, solid state synthesis of fluorides typically use HF, F₂ and CF₄ for fluorination.¹⁵⁻¹⁷ These gases are extremely toxic and require specific and elaborate health and safety procedures to be able to handle them safely. It has been shown that

fluorides can be synthesised hydrothermally, which is described in Section 2.2.1, using HF,^{14,18} although this still poses possible risks. An alternative route has been designed where pure crystalline BaMF₄, M = Mg, Mn, Co, Ni and Zn, has been synthesised using CF₃COOH aqueous solution to generate in situ aqueous HF under hydrothermal conditions.¹⁹ The metal fluoride will react with the aqueous CF₃COOH forming metal trifluoroacetate salts and HF_(aq) which then react with one another to produce BaMF₄. This technique has recently been applied to synthesis RbFe₂F₆ and has proven to be a useful synthesis technique for the generation of mixed metal fluorides.¹³

1.1.2 Crystal Structure of Fluoride Materials

In comparison to oxides, fluoride materials have a narrower range of structures due to the low polarizability of fluoride ions and the ionic nature of fluoride bonds. In addition, structural distortions are less prevalent than oxides.^{14,20,21} Metal fluoride materials have a tendency to form an octahedral coordination environment with isolated, corner-sharing, face-sharing or edge-sharing octahedra being observed. Structures with direct linking of octahedra in one, two or three dimensions will be emphasised with the purpose of displaying the vast array of structures fluorides can exhibit and give a brief overview of the crystal structures fluorides can adopt. Framework fluorides are of particular interest to this work, and several structure types are presented below; chain and layered fluorides are also mentioned in short. P. Hagemuller has produced a detailed review of inorganic solid fluorides.¹⁴

Open Framework Fluoride Materials

Perovskites (AMF₃),²² hexagonal and tungsten bronze (A_xMF₃),²³ weberites (A₂M⁺²M⁺³F₇)²⁴ and pyrochlores (AM⁺²M⁺³F₆)¹³ are four structures which are observed in framework fluorides,²⁰ shown in Figure 1.1. Physical properties are dominated by the structure of the material. This is seen especially with pyrochlore-related fluorides where various elements can sit on differing crystallographic sites in each lattice. This is particularly dominant in the pyrochlore-related family of AM⁺²M⁺³F₆, which this thesis is focused on. This series of structures have been reported with disorder and order between the metal cations, with A = K, Rb, Cs, NH₄; M⁺² = Mg, Mn, Fe, Co, Ni, Cu; M⁺³ = Al, Ga, V, Cr, Fe. With a fixed trivalent Fe ion this structure is known with either one of two symmetries at room temperature, cubic Fd-3m, when M⁺² = Mn, Ni, or Co, or orthorhombic Pnma, when M⁺² = Ag or Fe, due to the relationship between the di- and trivalent metal atoms.¹ Some examples of framework fluorides are shown in Figure 1.1, including the perovskite NaNiF₃,²² tetragonal bronze K_{0.6}FeF₃,²³ weberite

$\text{Na}_2\text{Fe}_2\text{F}_7$ ²⁴ and distorted pyrochlore RbFe_2F_6 ,¹³ demonstrating the array of framework fluoride structures know.

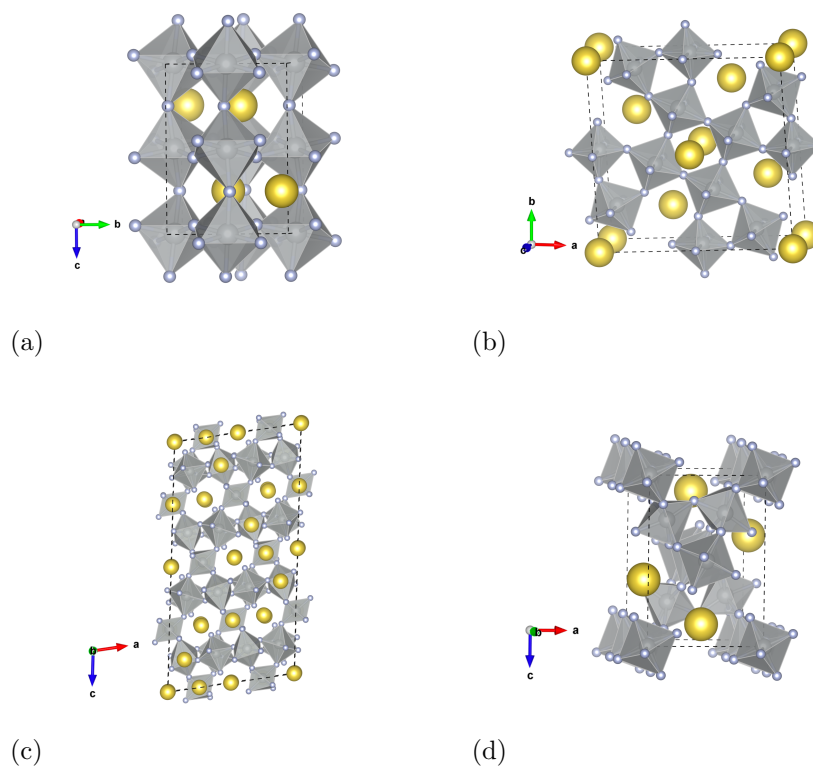


FIGURE 1.1: Examples of three dimensional framework fluorides: (a) Perovskite NaNiF_3 ,²² (b) Bronze $\text{K}_{0.6}\text{FeF}_3$,²³ (c) Weberite $\text{Na}_2\text{Fe}_2\text{F}_7$,²⁴ and (d) Pyrochlore RbFe_2F_6 ,¹³ where grey represents the metal octahedra and yellow the A site cation.

Layered Fluoride Materials

When only four of the six corners of the octahedra are shared, this results in a $(\text{MF}_4)^{-n}$ composition normally exhibiting a layer-type network. Single, double and triple layered materials have all been reported.²⁰ Differences in the layer structure arise from the connectivity of the corner shared octahedra and can be achieved in many different ways, and this is the main factor that leads to the range of layered structures observed. Additionally, there is a series of possible stacking of these layers, dictated by the larger cation coordination residing between them.¹⁴ Some examples of layered fluoride structures are shown in Figure 1.2 including single layer NH_4FeF_4 ,²⁵ BaZnF_4 ,¹⁹ K_2NiF_4 ²⁶ and $\text{Na}_5\text{Al}_3\text{F}_{14}$ ²⁷ as well as double layer, $\text{K}_3\text{Zn}_2\text{F}_7$ ²⁸ and $\text{Cs}_4\text{CoCr}_4\text{F}_{18}$.²⁹

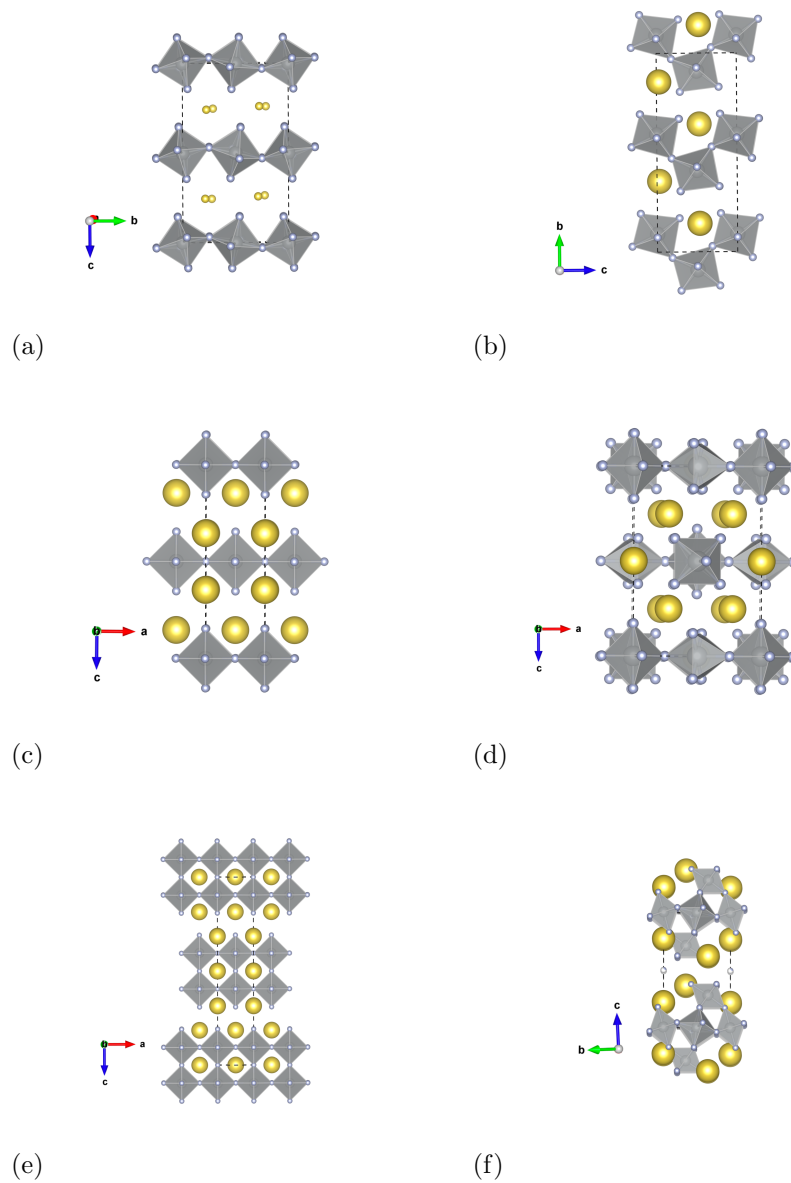


FIGURE 1.2: Layered fluoride examples: Single layer, (a) NH_4FeF_4 ,²⁵ (b) BaZnF_4 ,¹⁹ (c) K_2NiF_4 ²⁶ and (d) $\text{Na}_5\text{Al}_3\text{F}_{14}$.²⁷ Double layer, (e) $\text{K}_3\text{Zn}_2\text{F}_7$ ²⁸ and (f) $\text{Cs}_4\text{CoCr}_4\text{F}_{18}$,²⁹ where grey represents the metal octahedra and yellow the A site cation.

Chain Fluoride Materials

A large family of fluorides displaying 1D crystallographic features possesses the general formula A_xMF_5 . These are generally characterised by isolated MF_5 chains of octahedra sharing two vertices.¹⁴ Single, double and triple chain structures have been reported with solely corner sharing octahedra. Examples of chain fluoride structures are shown in Figure 1.3 including single chain structures, $BaMnF_5$ ³⁰ and $BaMnF_5H_2O$ ³¹ as well as double chain structures $CsCrF_4$ ³² and $NaBaFe_2F_9$.³³

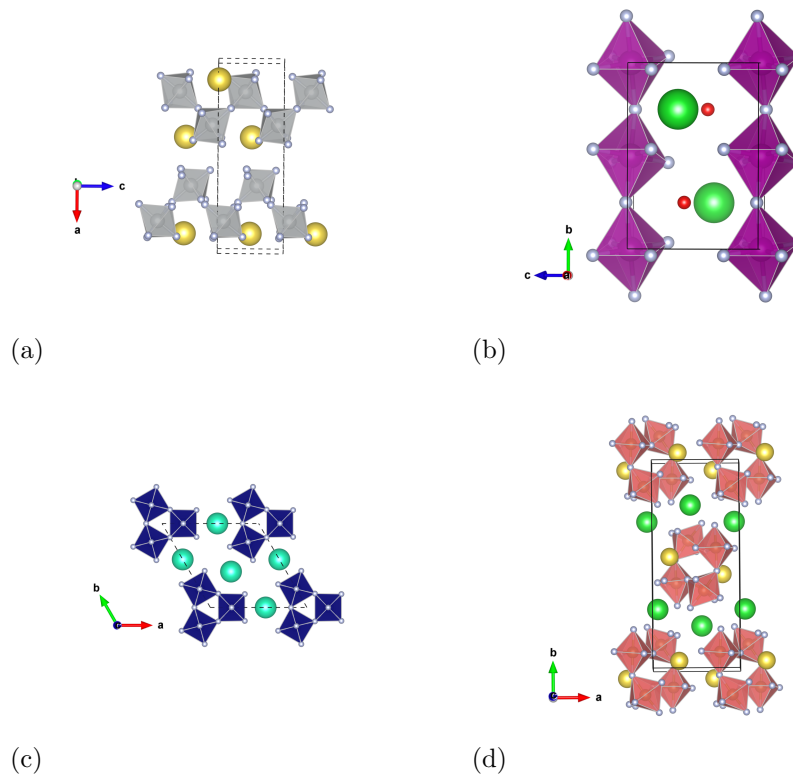


FIGURE 1.3: Examples of chain fluoride materials: Single chain structures, (a) $BaMnF_5$ ³⁰ and (b) $BaMnF_5H_2O$.³¹ Double chain structures (c) $CsCrF_4$ ³² and (d) $NaBaFe_2F_9$,³³ where the metal octahedra are shown in grey, purple, blue and orange respectively, the A site cation is shown in yellow and green and H_2O is shown in red.

1.1.3 Physical Characteristics of Fluorides

There are several factors allowing fluorides to have distinct physical properties; high reactivity, strong electronegativity, low-polarizability and size. With a more detailed approach of fluorine ions, it is the π -donor character and the absence of any π -acceptor character which determines its low crystalline field, high-spin, character. It is this absence that is key to the unique magnetic and optical behaviour of transition metal fluorides.¹⁴ A description of magnetic properties can be found in Section 2.5. Discussed below are some of the physical properties that fluorides can exhibit giving context to the diversity of fluorides, however, these are not necessarily the focus of this thesis. Geometric frustration is a common physical property of fluorides, which is discussed in Section 2.5.3.

Ferroelectric Behaviour

All ferroelectric materials are pyroelectric, however, not all pyroelectric materials are ferroelectric, therefore, ferroelectrics can be described as a pyroelectric which exhibits spontaneous polarization reversible by an external electric field.³⁴ All ferroelectric materials must be polar so that there is a permanent dipole moment. For a pyroelectric material to be considered ferroelectric, it must crystallise in one of ten symmetry classes (1, 2, 3, 4, 6, m, mm2, 3m, 4mm, or 6mm). A ferroelectric hysteresis loop is observed when measuring the changes of polarization within a material as a function of voltage change. Another feature found in ferroelectrics is the phase transition at the Curie temperature from non-centrosymmetric to centrosymmetric structures. Examples of ferroelectric fluorides are BaMF_4 , $(\text{NH}_4)_2\text{BeF}_4$ and $\text{K}_3\text{Fe}_5\text{F}_{15}$.³⁵

Multiferroic Behaviour

Multiferroic materials are inherently those that possess at least two ferroic properties; ferromagnetism (or anti-ferromagnetism, ferrimagnetism), ferroelectricity (or anti-ferroelectricity), and ferroelasticity. They are of fundamental interest to understand electronic behavior coupling magnetic interactions and electric dipolar order. Examples of fluorides with multiferroic behaviour are the $\text{K}_3\text{Fe}_5\text{F}_{15}$, an orthorhombic material with distorted tetragonal tungsten bronze-type structure,³⁶ and $\text{Pb}_5\text{Cr}_3\text{F}_{19}$, crystallising in the tetragonal $I4cm$ space group,³⁷ families.³⁸

Spin Glass Behaviour

When spin glass materials are cooled, using SQUID magnetometry, to 2 K in the absence of an applied magnetic field, they will undergo spin glass freezing. When an external magnetic field is applied the spins remain frozen, and the field itself is not high enough to allow for spin fluctuation. As these materials are heated, the spins ‘defrost’ and begin to align with the applied field and hence magnetisation increases and a maximum appears at $T_{(f)}$. The continual heating causes randomization with spin fluctuation resulting in paramagnet behaviour. On FC the spins align with the applied field which reasons higher magnetization and on heating magnetization decreases joining the ZFC curve. This type of behaviour is observed typically in mixed metal pyrochlore fluorides such as $\text{Pb}_2\text{Mn}_2\text{FeF}_9$ ³⁹ and CsMnFeF_6 .⁴⁰

1.2 Designing new Materials

There are many naturally occurring minerals with known structures. These structures can be used as a starting point to identify materials which have interesting properties such as the pyrochlore structure. Many complex metal oxides adopt the naturally occurring mineral pyrochlore $(\text{Ca, Na})_2\text{Nb}_2\text{O}_6\text{F}$, which was first described by Gaertner in 1930.⁴¹ The mineral can be found at several sites throughout the world providing the main source of mined niobium, normally in the form of small octahedral crystals suspended in other mineral deposits. A vast amount of other compounds with the general formula $\text{A}_2\text{B}_2\text{O}_7$ (where A and B are transition metals) have been discovered since.^{42–44} The ability to support a large range of atoms on different crystallographic sites leads to a wider range of properties being observed, these include metal-insulator transitions,⁴⁵ magnetic frustration,⁴⁶ magnetoresistance,⁴⁷ superconductivity,⁴⁸ ferroelectrics,⁴⁹ ionic conductivity⁵⁰ and catalysis.⁵¹ For example, the pyrochlore-related structure, AM_2F_6 (where A = alkali metal or NH_4 and M is typically a transition metal, normally of two separate oxidation states, better written as $\text{AM}^{2+}\text{M}^{3+}\text{F}_6$) has a reduced orthorhombic cell of the conventional β - pyrochlore lattice. This can exhibit a three-dimensional crystal structure consisting of corner-shared MF_6 octahedra separated by A^+ cations. It is possible to manipulate this structure and design different compounds by the substitution of any of the ions, providing a charge balance is maintained, and the new ion has an appropriate size. The A^+ cation cannot be too large to fit between the corner-shared octahedra, while not being too small to form strong interactions with the framework.

1.2.1 The Pyrochlore Structure

The normal pyrochlore structure consisted of four crystallographic non-equivalent atoms, two potentially different cations, A and B, and two different anions, X and X'. The general formula of a pyrochlore structure is $\text{A}_2\text{B}_2\text{X}_6\text{X}'$ which tends to crystallise in the $Fd-3m$ cubic space group arranged in interconnecting AX_8 and BX_6 polyhedra.⁵² Despite there being four origin choices, throughout this work the origin will be fixed on the B site. The four atoms locations are described as follows: 16d (A), 16c (B), 48f (X), and 8b (X').^{52–54} The lattice contains eight atoms per unit cell with a normal lattice parameter of $\approx 10\text{\AA}$. Table 1.1 displays the atomic parameter coordinates for a cubic pyrochlore cell with the origin at the B site.

Visually, there are many ways to describe the pyrochlore structure. With reference to symmetry, it is comparable to the fluorite structure. The fluorite structure of CaF_2 is displayed in Figure 1.4 where each Ca^{2+} is in an 8-fold coordination. Within the pyrochlore structure, both cations are in an ordered arrangement with one-eighth of

Atom	Site	Site Symmetry	Coordinate
<i>A</i>	$16d$	$\bar{3}m(D_{3d})$	$\frac{1}{2}, \frac{1}{2}, \frac{1}{2}$
<i>B</i>	$16c$	$\bar{3}m(D_{3d})$	$0, 0, 0$
(<i>X</i>)	$48f$	$mm(C_{2v})$	$x, \frac{1}{2}, \frac{1}{2}$
<i>X'</i>	$8B$	$\bar{4}3m(T_d)$	$\frac{3}{8}, \frac{3}{8}, \frac{3}{8}$

TABLE 1.1: Atomic parameter coordinates for a pyrochlore cell ($Fd\bar{3}m$) with origin at $16c$, *B* site. ($x = 0.3125, \frac{5}{6}$, for a regular octahedra)^{52–54}

the anions being removed. The anion vacancies are directly coordinated only to the B-site cation and the remaining anions surrounding the B cation shift along the edges of the coordination cube to form a trigonal antiprism. The A-site cations keeps the 8-fold coordination environment, however, the displacement of the anions surrounding the B-site cation causes the formation of a puckered ring around the A-site cation leaving one-eighth of the anions on a fixed position.

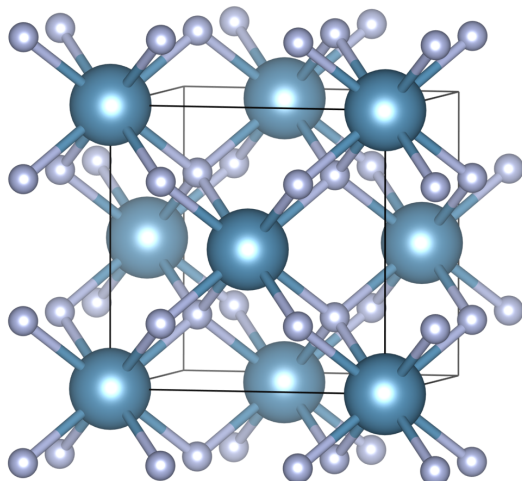


FIGURE 1.4: The CaF_2 fluorite structure,⁵⁵ showing Ca ions in blue and F ions in grey.

Alternatively, the pyrochlore structure can be described as two sets of inter-penetrating networks. One resulting from the corner sharing of four BX_6 octahedra where four sets of octahedra form a tetrahedral cluster. These clusters form channels through which the $\text{A}_2\text{X}'$ networks penetrate. The A-X interaction tends to be ignored because the bond distance is marginally longer than that of the A-X' bond distance. Regarding the $\text{A}_2\text{X}'$, the A cation is in linear coordination, while the X' is in the center of the A_4 tetrahedron, identical to the network displayed in the anticyrstobalite Cu_2O .⁵⁶ This way of describing the pyrochlore structure displays the independence of both networks. The BX_6 is structurally stable with the A cations maintaining charge balance.

1.2.2 Defect Pyrochlore

When all or a proportion of the X' anions are missing, a defect pyrochlore is formed taking the general formula AB_2X_6 or $A_2B_2X_{7-y}$ respectively, leaving the BX_6 networks intact. Examples of compounds having the AB_2X_6 pyrochlore structure are KOs_2O_6 , $PbSnO_3$,⁵⁷ $RbFe_2F_6$ ¹³ and $CsFe_2F_6$.⁵⁸ For these compounds, the closely coordinated X' anions are all missing leaving the A-site cation surrounded by a puckered ring of 6 X anions.

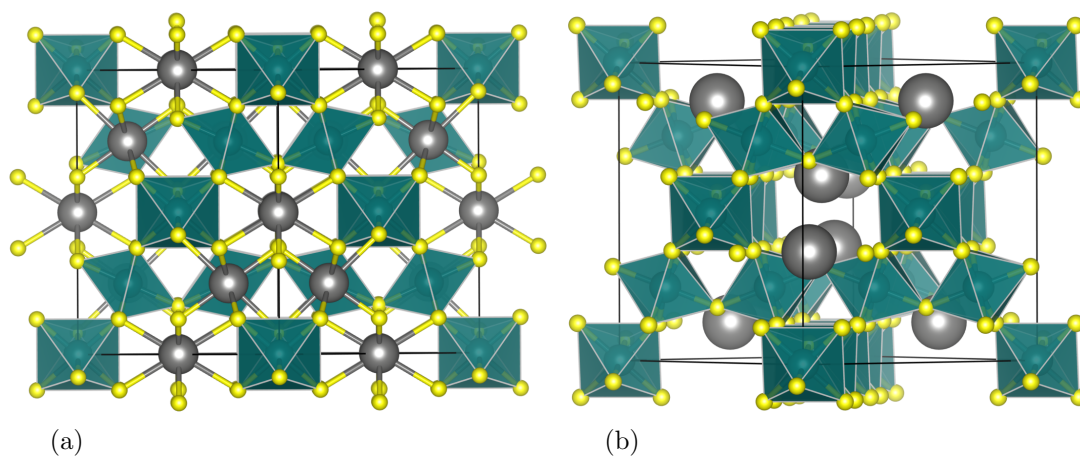


FIGURE 1.5: A comparison between a typical pyrochlore, (a), with the general formula $A_2B_2X_6X'$ and a defect (or β) pyrochlore, (b) with the general formula AB_2X_6 , where the B site metal octahedra are represented in green, the A site cation in grey and the X/X' site anion in yellow.⁵⁹

1.3 Overview of Thesis

It is essential to understand pyrochlore type fluorides due to their ability to display a vast array of exotic properties. This work aims to provide a novel soft chemistry synthesis route to investigate a new family of porous fluorides, with the general formula MF_3 , whilst attempting to fully understand some of the magnetic behaviours exhibited in the defect pyrochlores $\text{AM}^{2+}\text{M}^{3+}\text{F}_6$ which are suspected to exhibit magnetic frustration. Exploratory synthetic techniques were performed to synthesise mixed valence transition metal fluorides with the understanding that geometric frustration may be exhibited. Hydrothermal methods using CF_3COOH aqueous solution and new topotactic deintercalation with Br_2 produced new and cleaner methods to synthesise pyrochlore fluorides which have been characterised. Powder X-ray diffraction has been implemented to determine phase purity and crystal structure. Mössbauer absorption spectroscopy was used to determine the oxidation state of the transition metals and the ratio of Fe^{2+} and Fe^{3+} where applicable. SQUID magnetometry was used to determine fundamental magnetic properties with powder neutron diffraction being implemented to determine the magnetic arrangement and ordering temperatures.

Chapter 2 describes all experimental techniques and theory implemented.

Chapter 3 introduces FeF_3 , a cubic pyrochlore. Significant attention has been paid to the synthetic method. Synthesis, structure, characterisation and magnetic properties are discussed.

Chapter 4 introduces CsFe_2F_6 , a defect pyrochlore mixed metal fluoride with charge ordering. Synthesis, structure and magnetic properties are discussed.

Chapter 5 introduces RbFeCrF_6 , a new charge ordered, mixed-metal, spin glass, defect-pyrochlore. Synthesis, structure and magnetic properties are discussed.

Chapter 2

Theory and Experimental

2.1 Introduction

This chapter gives an overview and introduction to general theories and experimental techniques used in the structure and physical property characterisation of materials discussed in this thesis. Specific mechanisms for synthesis of individual materials will be described in the experimental section of the relevant chapter.

2.2 Synthesis

2.2.1 Hydrothermal Synthesis

This solvothermal technique normally involves the synthesis (usually crystallisation) of inorganic materials by heating in a solution above the boiling point of the solvent. This is done in a sealed container under self-generated pressure. In this instance the solvent is water, hence, hydrothermal.

The first report of hydrothermal synthesis in a laboratory setting was in 1845 when Schafhäütl witnessed the formation of quartz micro-crystals in a high-pressure steam cooker.⁶⁰ Three years later, Robert Bunsen, synthesised single crystals of BaCO_3 and SrCO_3 in thick-walled glass tubes. The method of hydrothermal synthesis in sealed glass ampoules became increasingly common, and for the next seventy years, many types of materials were synthesised, producing many compounds from oxides to silicates. It was not until 1913 that a closed reaction vessel, designed by Morey, was introduced that is broadly the design of the autoclaves used today.⁶¹ After the Second World War, there was a substantial demand for zeolites and large-sized quartz crystals, which prompted

commercial interest in hydrothermal synthesis.⁶² Since, this hydrothermal technique has been fine-tuned into a versatile approach for the crystallisation of inorganic materials directly from solution.⁶³ The method is advantageous to that of traditional solid-state synthesis, which is the most conventional preparative method for multinary oxides.^{64–66} It is widely regarded to produce high-quality samples, often as single crystals. With reference to industry, an array of metal oxides have been produced using hydrothermal synthesis on an industrial scale. This highlights the scalability of this method which is precisely controlled and can continuously produce nano-particulate materials.^{67,68}

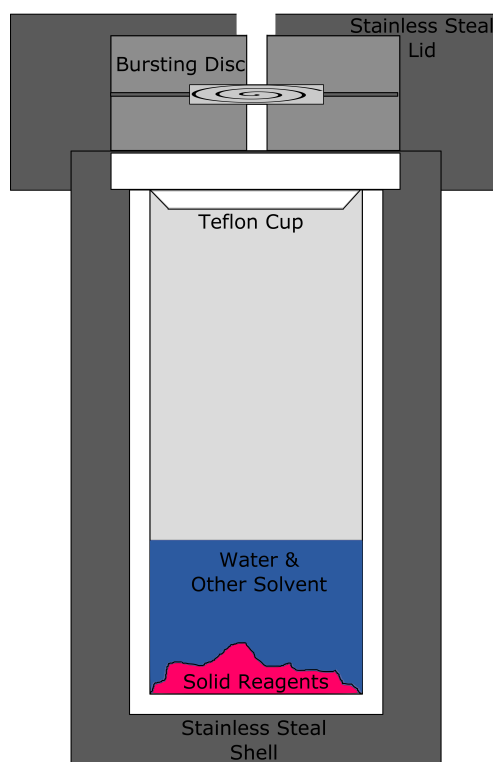


FIGURE 2.1: Schematic diagram of stainless steel hydrothermal autoclave with Teflon liner.

Experimental Details

Throughout this thesis, hydrothermal synthesis was carried out using Parr Instrument Company general purpose acid digestion vessels. These are Teflon[®]-lined stainless steel autoclaves possessing an internal volume of 45 mL. Depending on the reaction, a usual ratio of 3:5 of acid to water was used with the solution never exceeding 50% of maximum capacity. The sealed autoclaves were heated in an oven to 230 °C for 12 - 72 hours and then cooled to room temperature either naturally or at a controlled ramp rate. The polycrystalline powders were then removed from solution through gravity filtration, washed several times with deionised water and dried at 70 °C in air for characterisation.

2.3 Powder X-ray Diffraction (PXD)

X-ray diffraction has become the most widely used technique for characterising crystalline materials. This section contains a description of the theoretical basis for the process of diffraction.

“By crystal we mean any solid having an essentially discrete diffraction diagram, and by a periodic crystal we mean any crystal in which three-dimensional lattice periodicity can be considered to be absent.”⁶⁹

2.3.1 Diffraction Theory

The interaction of a monochromatic beam with a crystalline sample can result in three basic processes: absorption, refraction and scattering (in the case of a crystal, scattering is known as diffracting). Von Laue, in 1912, realised that crystals could act as diffraction gratings for radiation of an appropriate wavelength.⁷⁰ This was later shown by Friedrich and Knipping.⁷¹ An incident beam can be diffracted providing that the wavelength of the beam is of the same magnitude as the distance between neighbouring atoms within the crystal lattice. Father and son, William Henry Bragg and William Lawrence Bragg, showed this to be the case with X-rays in 1914.⁷²

Bragg’s theory of diffraction considers crystals to be made up of parallel planes of atoms from which the incident radiation is reflected, the perpendicular distance between the plane is known as the d -spacing. It is constructive interference of the scattered X-rays that leads to this diffraction, illustrated in Figure 2.2. X-rays are electromagnetic radiation with a wavelength of approximately 1Å (*e.g.* 0.71073 Å for MoK α and 1.5418 Å for CuK α), since this is similar to the distance between atoms in a crystal then they can be scattered by crystalline materials to give structural information. When X-rays interact with electrons, scattering can produce a diffraction pattern unique to that crystalline material.

When entering the crystal, the incident waves are in phase; however, some waves penetrate deeper than others. Constructive interference and therefore diffraction only happens when the scattered waves are in phase. This will only occur if the additional distance travelled by the deeper penetrating wave is equal to an integer number of wavelength, $n\lambda$. This can be calculated using Equation 2.1 and Figure 2.2 for context.

$$n\lambda = AB + BC \quad (2.1)$$

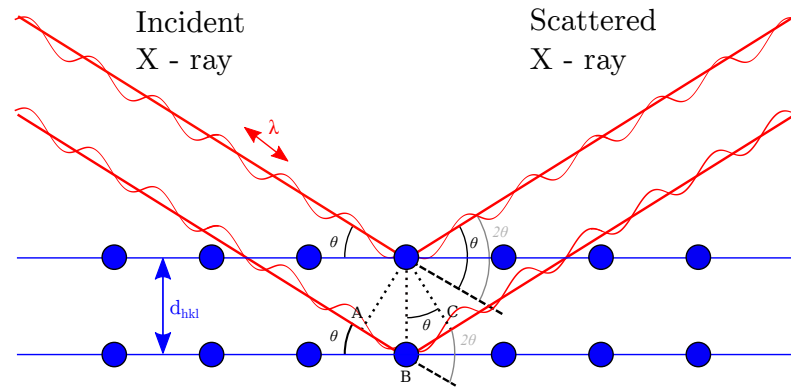


FIGURE 2.2: Diffraction of X-rays incident upon parallel planes of atoms separated by a distance, d_{hkl} . The angle between the incident and scattered X-rays is 2θ .⁷³

Since the angle of incidence is known and the perpendicular distance between the plane is given by d_{hkl} then Equation 2.1 can be expressed as Equation 2.2, where the relationship shown is known as the Bragg Law, showing that constructive interference will occur for different incident angles, θ , for different plane separations, d_{hkl} .

$$AB + BC = 2d \sin \theta = n\lambda \quad (2.2)$$

An ideal ground powder consists of a large number of crystallites all with random orientations. There are enough crystallites in every direction to fulfil the Bragg equation when in the line of the monochromatic beam and this occurs for all lattice spacings. This gives rise to diffraction from each set of lattice planes which produces a ‘cone’ of diffraction illustrated in Figure 2.3.

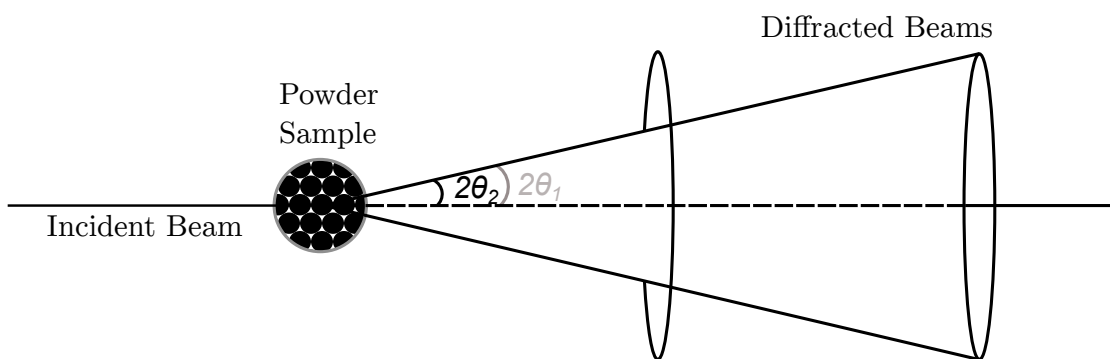


FIGURE 2.3: Diffraction of X-rays from isotropic powder sample resulting in *diffraction cones* that are at an angle of 2θ from the incident beam.⁷³

For structural information to be extracted from fixed wavelength radiation, data are collected as a series of diffracted intensities as a function of their position, 2θ . When angles satisfy the Bragg equation, sharp peaks appear producing a diffraction pattern, each corresponding to a separate lattice plane.

d -spacing can be determined from the Bragg equation for individual reflections since both the position in 2θ and the wavelength of the monochromatic beam are known. The cell dimensions can be determined using indexing. Since the Miller indices are related to the particular crystal planes within the unit cell the peak position can be indexed to particular set of Miller indices, seen in Figure 2.4.

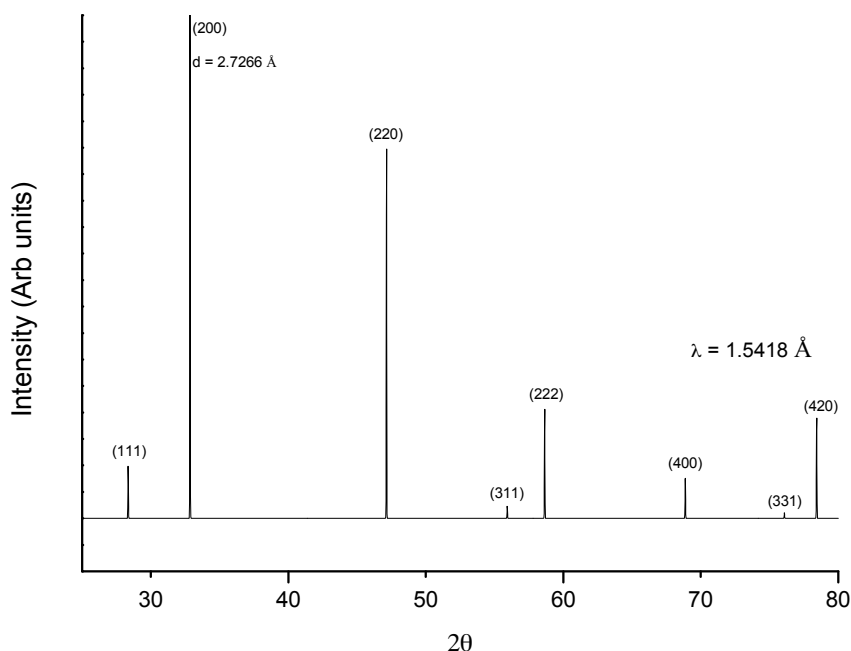


FIGURE 2.4: Diffraction pattern of NaCl as taken from the National Chemical Database Service showing Miller indices for each Bragg reflection. A Cu $K\alpha_1$ radiation source was used with $\lambda = 1.54056\text{\AA}$.

Miller indices are labelled as h , k and l and are represented by integer numbers. Each of these is associated with the reciprocal of the fractional value of where the lattice plane intersects each axis of the unit cell (x , y and z respectively).

$$d_{hkl} = \frac{a}{\sqrt{h^2 + k^2 + l^2}} \quad (2.3)$$

The relationship between d -spacing and the lattice parameter, a , for cubic symmetry is displayed in Equation 2.3. This can be combined with the Bragg equation and rearranged to Equation 2.4.

$$\sin^2\theta = \frac{\lambda^2}{4a^2}(h^2 + k^2 + l^2) \quad (2.4)$$

The position and number of reflections in a diffraction pattern are used to determine the crystal class, lattice type, size of the unit cell and overall crystal symmetry. Generally, the lower the symmetry of the crystal the more reflections there are in a powder sample. Systematic absences dictate the specific space group present. This is when reflections are technically allowed within the crystal system but their intensity is zero due to cancelling. An example of this is in a face-centred cubic cell; the (200) plane diffracts X-rays which are precisely out of phase with the X-rays diffracted by the (100) crystal plane. This results in the (100) crystal plane having no intensity or a zero structure factor. When every plane in a face-centred cubic system is considered, the Miller indices must be all odd or all even for the reflection to be observed.

Atom types and positions within the unit cell determine the intensities or structure factor of the reflections.

X-rays are scattered by the electron cloud surrounding the nucleus of the atom. When the electric field of the incident beam hits the atom the electron begins to oscillate about its position. This then results in a new scattered wave being emitted with the exact wavelength of the incident wave. The scattering process is known as *coherent* scattering. Each element will have its own scattering factor, f_j , since all elements have a different number of electrons, Z , which is shown in Equation 2.5.

$$f_j = \frac{\text{the amplitude of the wave scattered by the atom, } j}{\text{the amplitude of the wave scattered by a single electron}} \quad (2.5)$$

The size of the electron cloud and the incident X-ray have similar wavelengths. The intensities of reflections will decrease rapidly as 2θ increases due to there being more scattered waves out of phase. The electron cloud is not an ideal point scatterer and waves that are scattered at different points will be out of phase. At $2\theta = 0$, $Z = f_j$, however, this decreases with increasing 2θ .

Multiple atoms are contained within the unit cell of a crystal, each of these atoms has its own f_j which varies with θ and affects the amplitude of the diffracted wave. Each separate atom will have a particular contribution to the intensity of a reflection. This is dependent on the hkl plane it resides on as well as its position in the unit cell. The structure factor (F_{hkl}), is the sum of all scattering factors of each atom in the unit cell. This is shown in Equation 2.6 where, x_j , y_j and z_j are the atomic coordinates of the j th atom and h , k and l are the Miller indices of the reflection.

$$F_{hkl} = \sum_j f_j e^{2\pi i(hx_j + ky_j + lz_j)} \quad (2.6)$$

The intensity (I_{hkl}) of a particular hkl reflection is directly proportional to the square of F_{hkl} , Equation 2.7, where the k is a scaling constant, containing terms such as adsorption, reflection, multiplicity, temperature factors and polarisation factor, L is the Lorentz factor.

$$I_{hkl} = kL^2|F_{hkl}|^2 \quad (2.7)$$

The electron density of an atom is the Fourier transform of the unit cells overall structure factor. With this in consideration, the structure factor, electron density distribution and Fourier map can be gained from measuring the observed intensities, hence, the positions of each atom in the unit cell.

2.3.2 PXRD Instrumentation

Powder X-ray diffraction was conducted with primarily in-house lab-based diffractometers. X-rays are generated by the acceleration of electrons from a tungsten filament (cathode) towards a target (anode) using high voltage. Electrons with energy high enough will eject core electrons from the target's atomic orbitals causing electrons in higher energy orbitals to decay, emitting X-ray radiation. Cu and Mo are the most common examples of targets used giving K_α wavelengths of 1.5148 Å and 0.7107 Å respectively. The K_α X-ray wavelength is selected using a monochromator or filter. In typical PXRD performed during this work, the sample is irradiated from a moving source, and a moving detector measures the intensities of the diffracted X-rays. The measurements are carried out in the Bragg-Brentano geometry as a flat plane sample. X-ray diffraction patterns are collected from the elastic scattering of the X-rays by electrons within the sample. Elements with a higher number of electrons will scatter X-rays more increasing the intensity of observed peaks, the opposite effect is seen with lighter elements. These techniques can be used to characterise liquids, gases or amorphous materials but do not have the characteristic Bragg reflections.

PXRD data were collected using a PANalytical Empyrean instrument utilising Cu- K_α radiation at 300 K. Samples were ground using a pestle and mortar to increase the amount of crystals randomly orientated. The powder was then scattered evenly onto a silica plate using petroleum jelly as an adhesive. Diffraction patterns were collected using a step size of 0.02 2θ over a 5 - 120 2θ range and a step time of 0.8 seconds.

2.3.3 The Rietveld Method

A fundamental problem associated with powder diffraction is the random orientation of crystallites in the diffraction beam which causes the superposition of the three crystallographic axes onto the same axis (d -spacing, or 2θ) of the diffraction pattern. This results as the distance between the Miller planes is often similar causing overlapping peaks. This peak overlap prevents accurate measurement of the observed intensities and complete examination of structure factors of individual reflections. Hugo Rietveld proposed a solution, based on linear least squares for overlapping reflections in a powder pattern in the 1960s.⁷⁴ In the Rietveld method, an initial structural model is refined to obtain the best possible fit between the observed and calculated diffraction profiles. This process requires the accurate description of the peak shape by a mathematical function, S_i , composed of the observed and calculated intensities for each individual point, i , in the profile.

$$S_i = \sum_i w_i |y_i - y_{ic}|^2 \quad (2.8)$$

This is shown in Equation 2.8, where y_i is the observed intensities for the i th point and y_{ic} is the calculated intensity at the i th point, w_i is the weighting of the observed. w_i can be defined by Equation 2.9.

$$w_i = \frac{1}{y_i} \quad (2.9)$$

Observed intensity is not directly related to any particular Bragg reflection, to achieve an accurate profile, a relatively good starting model is required. Typically an isostructural material, with known structure, is used to provide this starting model. When a suitable model is not available, there are many techniques used to obtain a starting model.

$$y_{ic} = s \sum_{hkl} m_{hkl} L_{hkl} |F_{hkl}|^2 A_i G(2\theta_i - 2\theta_{hkl}) P_{hkl} T + y_{ib} \quad (2.10)$$

The observed intensity, y_i is comprised from many (d_{hkl}) reflections and the calculated intensity y_{ic} is dependent on $|F_{hkl}|^2$ values obtained from the model, calculated using Equation 2.10 where, s is the scale factor, L_{hkl} is the Lorentz-polarisation factor for the reflection (hkl), m_{hkl} is the multiplicity factor, A_i is the symmetry parameter, $G(\theta)$ is the reflection profile function, $2\theta_{hkl}$ is the calculated position of the Bragg peak, corrected for the zero point shift, P_{hkl} is the preferred orientation function, T is the absorption correction and y_{ib} is the background intensity at the i th step.

The reflection profile is a function of both the sample and the instrument and varies as a function of 2θ . Most commonly the function is a combination of Lorentzian and Gaussian components, which is known as the pseudo-Voigt approximation. The refinements of both X-ray and neutron diffraction data presented in this thesis were performed using the FullProf Suite.⁷⁵

It is possible to monitor the progress of the refinement by both graphical visualisation of the observed and calculated diffraction patterns and statistical quantities which are calculated during the refinement process. The agreement between the observed and calculated diffraction patterns is measured by the goodness-of-fit factors. There are several statistical quantities, all of which give different statistical weightings on the quality of fit, however, the ones used are expressed in Equations 2.11 - 2.13.

The weighted profile, R_{wp} , shown in Equation 2.11 compares how well the structural model under refinement accounts for relatively small and large Bragg peaks across the diffraction profile. The weighting factor is given by w_i .

$$R_{wp} = \left\{ \frac{\sum_i w_i [y_i - y_{ic}]^2}{\sum_i w_i [y_i]^2} \right\}^{\frac{1}{2}} \quad (2.11)$$

The expected R-factor, R_{exp} , accounts for the statistical quality of the data and the number of variables used in the refinement, Equation 2.12.

$$R_{exp} = \left[(N - P) + C / \sum_i w_i y_i^2 \right]^{\frac{1}{2}} \quad (2.12)$$

where N, P and C are the number of profile, refined parameters and constraints, respectively. During the refinement, the goodness-of-fit factor, χ^2 , is used to compare the quality of the data, Equation 2.13.

$$\chi^2 = R_{wp} / R_{exp} \quad (2.13)$$

When an accurate calculated fit for the observed diffraction data is achieved, the value of χ^2 will be close to one.

2.4 Powder Neutron Diffraction (PND)

In 1932 the neutron was discovered by James Chadwick⁷⁶ and as early as 1936^{77,78} it was shown that thermal neutrons have a similar wavelength to inter-atomic distances

in condensed matter can undergo diffraction, and this valuable tool has been rapidly developed.⁷⁹ The neutron, with a neutral charge, is scattered by the nucleus of the atom rather than the electron cloud, unlike X-rays, giving neutrons a much higher penetrating capacity, see Figure 2.5. The neutron scattering power, or cross-section, varies randomly across the periodic table and even between different isotopes of the same element, it does not have a relationship to the atomic number, which scales as Z^2 for X-rays, allowing neutrons to be sensitive to different isotopes of a material. This means neutrons have many advantages over X-rays, the first of which is that neutrons scatter more strongly from *lighter* elements such as hydrogen and oxygen. This can be particularly useful when heavier elements are involved, which otherwise dominate the PXRD pattern. The second advantage is that due to the erratic variation of cross-sections across the periodic table, elements that are hard to distinguish between using PXRD can be differentiated, such as iron and nickel. Additionally, neutrons are a natural technique for studying magnetism, as the neutron has a spin and will interact with the ordered magnetic moments present in a material.

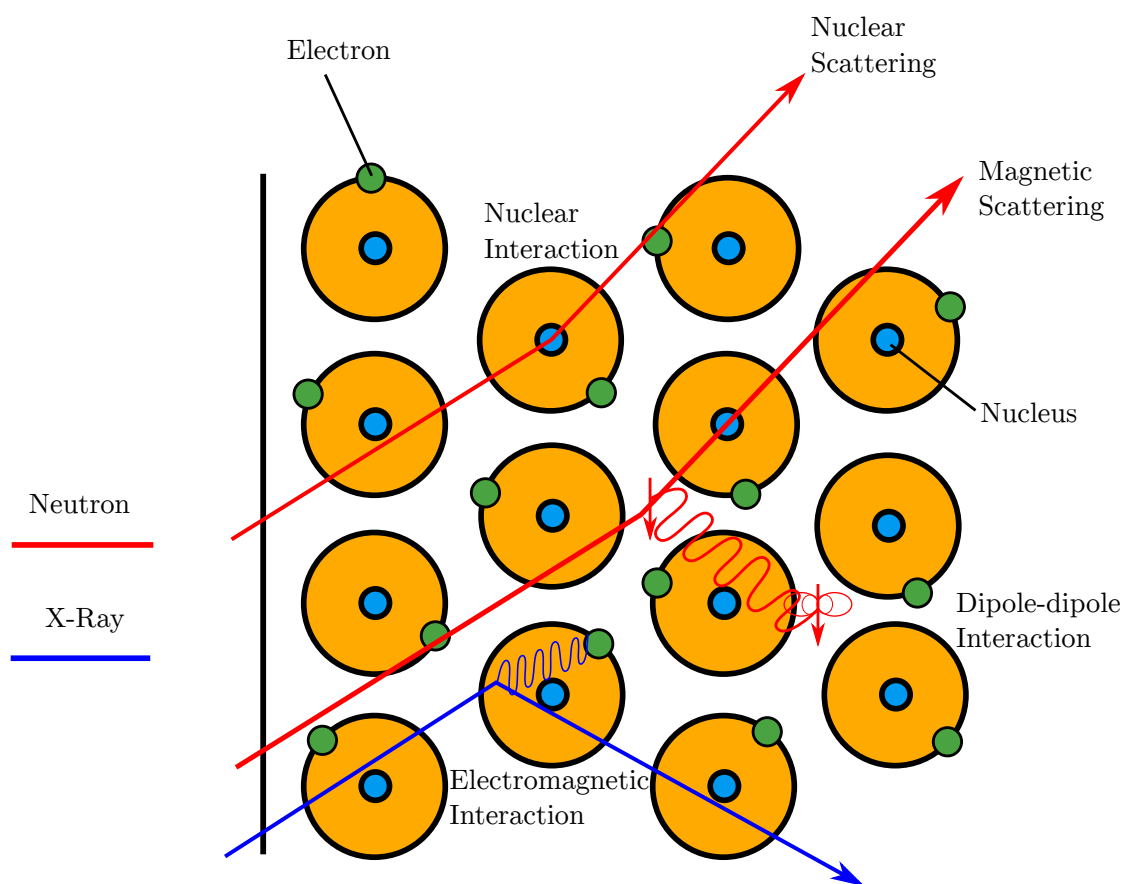


FIGURE 2.5: Neutrons and X-rays interact with a material differently. X-ray (blue) interact with the electron cloud but do not penetrate the material very deeply. Neutrons (red) interact with the atomic nuclei and penetrate the material deeper than X-rays. Neutrons also interact via a dipole-dipole interaction between the magnetic moment of an unpaired electron and the magnetic moment of the neutron.⁸⁰

Another advantage of neutrons over X-rays is that neutrons do not have a form factor. The form factor of X-rays originate from the size of the electron cloud around the nucleus. Since the nucleus is effectively a point scatterer relative to the neutron wavelength, the scattering length, b , does not depend on the scattering angle. What this means is that the range of useful data in reciprocal space obtained by a neutron diffraction experiment is increased compared to that of an PXRD experiment.

In order for neutrons to successfully diffract, like X-rays, the wavelength of the beam must be of the same order of magnitude as the inter-atomic distances in the unit cell. It is shown in Equation 2.14 that using the de Broglie relationship the wavelength (λ) of the incoming neutron beam can be changed by varying the speed (v) of the beam, where h is Plank's constant, and m_n is the mass of the neutron.

$$\lambda = \frac{h}{m_n v} \quad (2.14)$$

Moderation is the term used to describe the process of controlling the speed or energy of neutrons. A neutron moderator is a medium which reduces the velocity of fast neutrons, turning them into thermal neutrons capable of sustaining a nuclear chain reaction. Commonly used moderators include deuterium (as heavy water), hydrogen (as ordinary or light water) and graphite, but mostly regular water, methane or liquid hydrogen. Beryllium has also been used in some experimental types, and hydrocarbons have been suggested as another possibility. A good neutron moderator is a material with elements that scatter neutrons greatly, but not absorb. In this process, energy is transferred between the nucleus and the neutron. More energy is transferred per collision with elements with high scattering cross sections. After a sufficient amount of impacts, the velocity of the neutrons will be comparable to the temperature of the moderator. If this temperature is room temperature these are called thermal neutrons and have a wavelength suitable for performing diffraction experiments. Low energy neutrons, such as those passed through liquid hydrogen are called cold neutrons and find application in small angle scattering and inelastic experiments. Equation 2.15 displays this when considering the kinetic energy and shows that thermal neutrons which are produced at 300 K have a speed of 2200 ms^{-1} corresponding to a wavelength of approximately 1.8 \AA . This wavelength is similar to the bond distance in a large array of crystalline materials.⁸¹

$$\frac{1}{2} m_n v^2 = k_B T \quad (2.15)$$

The change in momentum is used to understand the scattering of a neutron by a sample.⁸² The diffraction vector or momentum vector, \mathbf{Q} , is used to express the change in momentum, shown in Equation 2.16 where k_i is the incident vector wavelength and k_f is the diffracted vector wavelength.

$$\mathbf{Q} = k_i - k_f \quad (2.16)$$

When there is no momentum change due to no energy transfer (elastic scattering), \mathbf{Q} is related to the wavelength and scattering angle shown in Equation 2.17.

$$|\mathbf{Q}| = Q = \frac{4\pi \sin\theta}{\lambda} \quad (2.17)$$

The quantity being measured during a neutron diffraction experiment is the cross-section, σ , where the total scattering cross-section is the number of neutrons scattered in all directions per second per unit of incident neutron flux, defined in Equation 2.18.

$$\sigma_{tot} = \frac{\text{Total number of neutrons scattered per second}}{N\Phi} \quad (2.18)$$

The number of neutrons scattered per second into a solid angle $d\Omega$ per unit incident flux per solid angle $d\Omega$ is known as the differential cross section, shown in Equation 2.19, which is the quantity measured in a diffraction experiment, where Φ is the flux of incident neutrons, and N is the number of atom in the sample.

$$\frac{d\sigma}{d\Omega} = \frac{\text{No. of neutrons scattered into a solid angle } d\Omega \text{ at angle } 2\theta, \Phi}{N\Phi d\Omega} \quad (2.19)$$

The strength of the scattering from the nucleus of a particular element is described by the scattering length, b , which is independent of wavelength. The quantity is usually determined experimentally and recorded in look-up tables. The relationship between scattering length and the coherent scattering cross-section is given in Equation 2.20. In the same way that the intensity of scattered X-rays are proportional to the square of the form factor, coherent scattering cross-section is proportional to the square of the scattering amplitude.

$$\sigma_{coh} = \frac{\text{Scattering flux}}{\text{Incident flux}} = 4\pi b^2 \quad (2.20)$$

The coherent scattering length of the incident neutron, b is unchanged by the scattering angle and the wavelength. The target nucleus is responsible for the magnitude of b . Values for b can be positive or negative (and sometimes imaginary numbers are used to denote neutron absorption) indicating that the incident and scattered waves are 180° out of phase or that both the incident and scattered waves are in phase respectively. In a neutron powder diffraction experiment, the recorded pattern will consist of two components, the Bragg peaks associated with the coherent scattering and the incoherent background.

The production of neutrons can be split into two main categories: a spallation source and a fission reactor source. Spallation sources generally generate pulses of neutrons analysed through time of flight (TOF) techniques, an example of a spallation source is ISIS at the Rutherford Appleton Laboratories (RAL) in Didcot, Harwell Oxford, UK. At ISIS the production of neutrons begins with the formation of hydride ions. The hydride ions are then linearly accelerated and all electrons are stripped off to form protons. Protons are accelerated to above the threshold energy for spallation in a synchrotron (800 MeV) and then hit a tungsten target, creating an intranuclear cascade, producing neutrons. The neutrons produced by the spallation process have a range of different energies (*i.e.* are polychromic) and are moderated by 300 K water, 105 K liquid methane or 25 K liquid hydrogen before use on the beamline. Constant wavelength diffraction is performed using a fission reactor source, the National Institute of Standards and Technology (NIST) in Gaithersburg, MD, USA is an example of a neutron source that employs a fission reactor source. All neutron experiments shown in this thesis were performed at either RAL or NIST.

2.4.1 Constant Wavelength PND

It is common to perform neutron diffraction experiments using constant wavelength beams from steady-state fission reactor sources. Typically, the thermal neutrons are directed from the nuclear reactor through a collimator towards a large single crystal monochromator, which directs single wavelength radiation onto the sample. The sample will then scatter the radiation and be picked up by the detectors.

High-Resolution Powder Diffractometer - BT1

Powder neutron diffraction data for some phases described in this thesis were collected using the BT1 Diffractometer at the NIST Center for Neutron Research (NCNR) Gaithersburg, Maryland, USA. Experiments performed on the BT1 diffractometer are at a constant wavelength with the reactor producing a flux of 4×10^4 neutrons/cm²s¹ using uranium fuel cells. Neutrons are detected using 32 ³He detectors placed at 5° intervals allowing data to be collected over a range of 0 to 165 degrees in 2θ . Finite detector slits lead to shifting, broadening and asymmetry of the Bragg peaks. The low angle detectors are partially masked to minimise these distortions. There is a choice of three different monochromators, Ge(311), Cu(311) and Ge(733) and three different incident Soller collimators, allowing for a tailored experiment. A schematic is shown in Figure 2.6, from left to right, the monochromators are positioned Ge(311), Cu(311) and Ge(733) with respective take off angles of 75°, 90° and 120°. The properties of the different monochromators are listed in Table 2.1.⁸³

Monochromator Information					
Monochromator	in-pile Collimation	Monochr. 2θ	Relative Bragg Intensities	Flux (ns ⁻¹ cm ⁻²)	Wavelength (Å)
Ge(311)	60'	75°	5.78	1,160,000	2.079
Ge(311)	15'	75°	2.86	570,000	2.079
Ge(311)	7'	75°	1.44	290,000	2.079
Cu(311)	60'	90°	1.84	870,000	1.540
Cu(311)	15'	90°	1.00	440,000	1.540
Cu(311)	7'	90°	0.54	230,000	1.540
Ge(733)	60'	120°	0.31	330,000	1.197
Ge(733)	15'	120°	0.20	200,000	1.197
Ge(733)	7'	120°	0.11	120,000	1.197

TABLE 2.1: Monochromator information for BT1, NIST, USA.

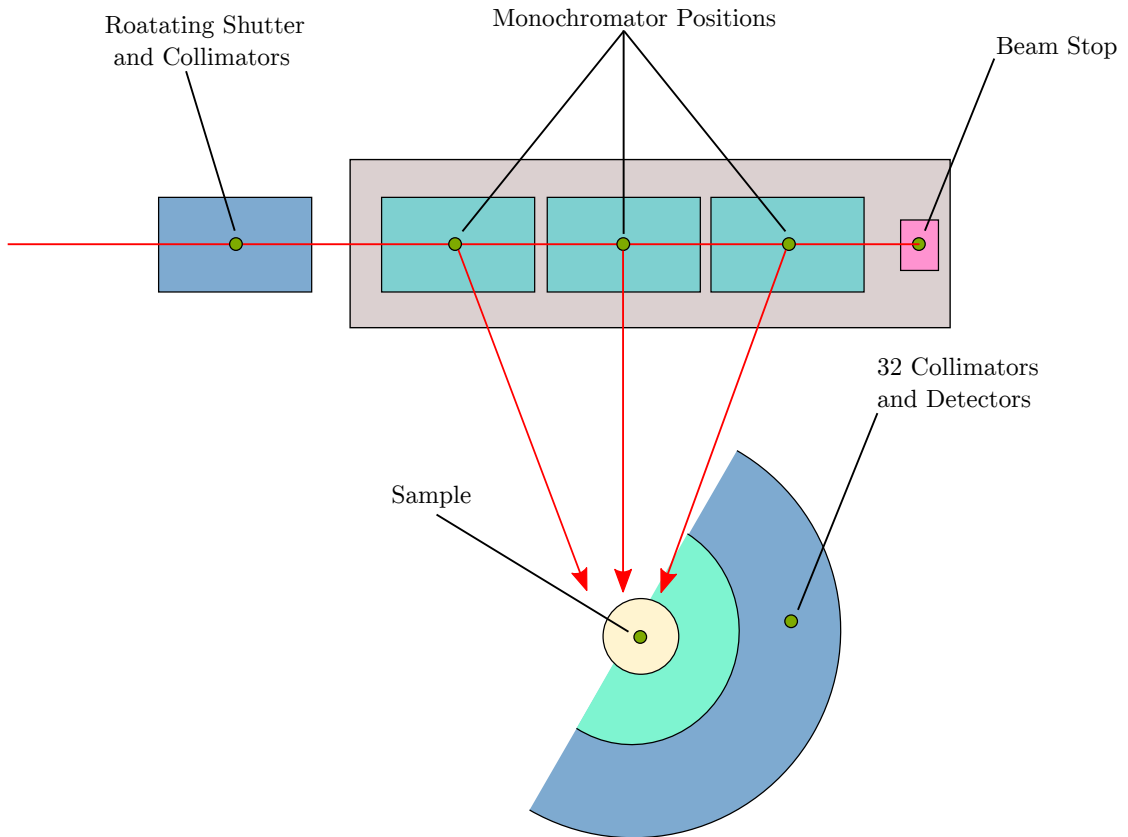


FIGURE 2.6: High resolution powder neutron diffractometer schematic BT1, at the NIST Center for Neutron Research, showing the location of monochromators, sample space and detectors.⁸³

2.4.2 Time of Flight (TOF) PND

Due to the production method of neutrons in a spallation source, explained in Section 2.4, neutrons possess a range of wavelengths. This means that for TOF neutron sources, Bragg's Law is solved by knowing the distribution of wavelengths of the neutrons before and after scattering. Normally the detectors of the TOF instrument do not move and are at fixed 2θ . The wavelengths of the neutrons are calculated using the time taken for the neutrons to travel from the moderator to the sample and finally to the detector. It is typical that a neutron with a shorter wavelength has a higher energy and will travel from the moderator to the detector in a shorter period of time than that of a neutron with a longer wavelength. Since the scattering angle and the distance are known, the relationship between the wavelength and TOF is given in Equation 2.21, where h is Plank's constant, m is the mass of the neutron, L is the path length of the diffractometer and t is the TOF.

$$\lambda = \frac{ht}{mL} \quad (2.21)$$

Combining Bragg's Law, TOF is proportional to d -spacing by:

$$t = 505.56 L \sin \theta d \quad (2.22)$$

and using Equation 2.17, neutron count can be plotted as a function of Q .

TOF experiments ultimately utilise the vast majority of neutron flux, making the total number of neutron detected significantly higher than that of a reactor based experiment whilst also allowing an entire diffraction pattern to be obtained from a single fixed angle detector. Although, typically a number of banks of detectors are used at different angles and distances to cover greater range of Q .

Wide - angle In a Single Histogram - WISH

WISH at the ISIS pulsed neutron source is a long-wavelength diffractometer primarily designed for powdered diffraction analysis at long d -spacing in magnetic and large unit cell systems. WISH is a high resolution, high-flux beamline which receives neutrons from a solid methane moderator at incident wavelengths between $1.5 \rightarrow 15 \text{ \AA}$ ($Q \sim 0.06 \rightarrow 4.5 \text{ \AA}^{-1}$). This neutron energy range combined with the large Q -range covered by each detector bank gives WISH a high flux of detected neutrons whilst maintaining the intrinsically low background of a pulse neutron source. This makes it ideal for observing magnetic Bragg peaks for simultaneous magnetic and nuclear structural refinement.⁸⁴

2.5 Theory of Magnetic Interactions

2.5.1 Magnetic Moment

The property of magnetism can have three origins:

- Intrinsic angular momentum (Spin)
- Orbital angular momentum about the nucleus
- Change in the dipole moment due to an applied field

The moment observed in a material stems from the motion of individual electrons in the material. Of particular interest are those electrons that are unpaired, as these give the largest signal. As it applies to materials with localized electrons, the magnetic moment, μ , for a particular atom is associated with the total angular momentum, \mathbf{J} . For an atom with a lone electron, \mathbf{J} is given by Equation 2.23, where \mathbf{L} is the quantum number that describes the orbital angular momentum and \mathbf{S} is the quantum number associated with intrinsic spin on the electron.

$$\mathbf{J} = \mathbf{L} + \mathbf{S} \quad (2.23)$$

The relationship between μ and \mathbf{J} is described by Equation 2.24 when a material exhibits a linear magnetic response to an applied magnetic field.

$$\mu = g_J \mu_B \sqrt{\mathbf{J}(\mathbf{J} + 1)} \quad (2.24)$$

Here, μ_B is the Bohr magneton, where $\mu_B = e\hbar/2m_e$, and g_J is the Landé g-factor, which is expressed in term of quantum numbers \mathbf{J} , \mathbf{L} and \mathbf{S} as follows:

$$g_J = \frac{3}{2} + \frac{\mathbf{S}(\mathbf{S} + 1) - \mathbf{L}(\mathbf{L} + 1)}{2\mathbf{J}(\mathbf{J} + 1)} \quad (2.25)$$

The first-row transition elements have little orbital contribution and the effective magnetic moment (μ_{eff}) is described more approximately by the following:

$$\mu_{\text{eff}} = 2\sqrt{\mathbf{S}(\mathbf{S} + 1)} \quad (2.26)$$

Each unpaired electron has a spin of $\mathbf{S} = \frac{1}{2}$ which is used to determine an overall net spin. For example, Fe^{2+} has four unpaired electrons giving rise to a net spin only contribution, $\mathbf{S} = \frac{4}{2}$ or 2. By understanding the localised electrons on individual atoms we can now discuss types of magnetism that arise in bulk materials.

2.5.2 Magnetism in Bulk Materials

The observed magnetic behaviour of a material is an important part of material characterisation and typically performed with the application of a magnetic field. Magnetic fields are produced when charges are in motion. Within a material that is magnetic, the electrons that are spinning and orbiting the nucleus of an atom generate a magnetic field. Lenz's Law states that when a material is placed within a magnetic field, \mathbf{H} , the field within the material, \mathbf{B} , differs from \mathbf{H} by the induced field, $4\pi M$, given by Equation 2.27, which is proportional to the intensity of magnetization, \mathbf{M} . Magnetization is the contribution from the interaction of the sample with the applied magnetic field.

$$\mathbf{B} = \mathbf{H} + 4\pi M \quad (2.27)$$

A material's response to an applied magnetic field is referred to as magnetic susceptibility, χ , this being the ratio of the magnetisation to the field:

$$\chi = \frac{\mathbf{M}}{\mathbf{H}} \quad (2.28)$$

The magnetisation of materials which are diamagnetic is negative due to the repulsion caused by the magnetic fields, whereas paramagnetic materials display a positive magnetisation due to the attraction to magnetic fields. This is displayed in Figure 2.7.

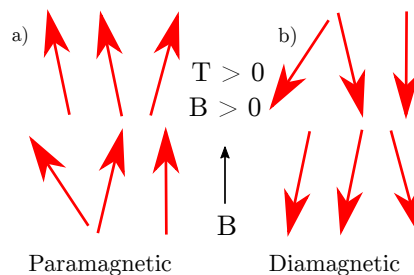


FIGURE 2.7: Paramagnetic a) and diamagnetic b) materials at non-zero temperature within a small applied magnetic field. Both magnetic states need an applied field to produce finite magnetisation.⁸⁵

Several magnetic effects are possible:

- **Diamagnetism** is present in all materials as it arises from the motion of paired electrons in their orbitals, however, it is classed as the weakest magnetic behaviour because paired electrons do not have a net spin, hence, there is no effective magnetic moment. Paired electrons do display a very small repulsion to a magnetic field which results in a negative susceptibility which is very weak and normally not taken into account. There is an exception of superconducting materials which are perfect diamagnets and show extremely strong diamagnetic effects.
- **Paramagnetism** is present in materials with unpaired electrons as atoms with unpaired electrons have a magnetic moment. In paramagnets there is no strong interaction of the moments between one another and these moments randomly orientate and continually fluctuate because of thermal energy. The susceptibility will increase as temperature decreases as there is less thermal energy to disrupt the orientation of the various spins. The spins also begin to align more with an external magnetic field, meaning it is possible for materials with other magnetic behaviours, shown in Figure 2.7, to exhibit paramagnetic behaviours at temperatures where the thermal energy is much greater than the interaction strength between atoms.
- **Ferromagnetism (FM)** occurs when all spins align parallel with one another resulting in a large positive net magnetic moment which is proportional to the number of unpaired electrons. When the atoms are cooled to the Curie Temperature (T_c) the magnetic susceptibility will jump. This is because there is insufficient thermal energy to disrupt the spin interaction and the spins rapidly align with the applied magnetic field and each other to create a net magnetization.
- **Antiferromagnetism (AFM)** occurs when spins align anti-parallel to one another. This anti-parallel arrangement cancels out individual spins resulting in no net magnetization. Below the antiferromagnetic transition temperature, otherwise known as the Néel Temperature (T_N), the magnetic susceptibility is considerably lower than that of a paramagnetic system. This is because the AFM interactions make it more favourable for spins to align against each other rather than the magnetic field. A sudden and precipitous drop in susceptibility is indicative of an AFM interaction which happens at T_N when there is insufficient thermal energy to disrupt the spin interactions.
- **Other types of magnetic ordering** which cause an increase in magnetic susceptibility are also possible. *Ferromagnetism with two different ions* and *ferrimagnetism* occurs when spins align parallel and anti-parallel, respectively, to one another, however, the individual spins have varying strengths causing there to

be an overall net magnetization. Both magnetic properties have been described differently in the literature, sometimes being referred to as ferrimagnetic and antiferromagnetic, respectively. *Canted-antiferromagnetism* is when the spins align with an AFM interaction but all spins are slightly tilted. This prevents the cancellation of spins and allows for an overall net magnetic moment.

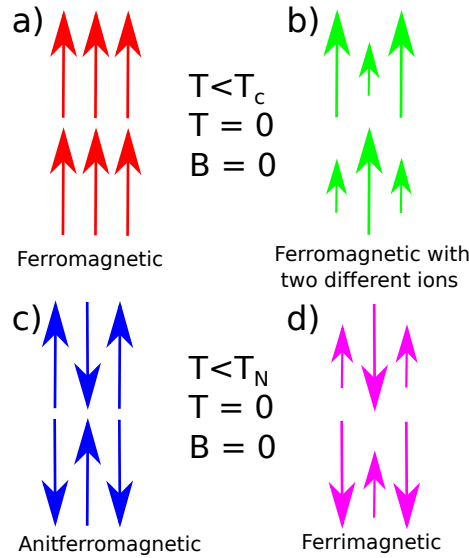


FIGURE 2.8: Possible magnetic states: Ferromagnetic a) Ferromagnetic with two different ions b) Antiferromagnetic c) and Ferrimagnetic d) which can all be a spontaneous magnetic state without an applied magnetic field.⁸⁵

Magnetic susceptibility, χ , is inversely proportional to temperature, \mathbf{T} , and this is described by the Curie Law (where \mathbf{C} is the Curie constant):

$$\chi = \frac{\mathbf{C}}{\mathbf{T}} \quad (2.29)$$

The Curie constant is proportional to the experimental effective magnetic moment. This is shown by:

$$C = \frac{N_A \mu_B^2 p_{\text{eff}}^2}{3k_B} \quad (2.30)$$

Where N_A is Avogadro's number and k_B is the Boltzmann constant. When this equation is rearranged it can be used to give an approximation of the effective magnetic moment (p_{eff}) in units of μ_B as given:

$$p_{\text{eff}} = \sqrt{8C} \mu_B \quad (2.31)$$

The Curie Law can be modified to give the Curie-Weiss Law, where θ is the Weiss temperature, which takes into account the interactions between magnetic moments:

$$\chi = \frac{C}{T - \theta} \quad (2.32)$$

In small fields where \mathbf{M} vs \mathbf{H} is linear, the Curie-Weiss Law can be rearranged and expressed in a $y = mx + b$ format. This is conducive to parametrizing experimental data, however, this is only valid within high temperature regions significantly above ordering temperatures (if present). In a non-interacting paramagnet which obeys the Curie Law, plots of $1/\chi$ against T in the high-temperature region are linear and equivalent to Curie-Weiss law with $\theta = 0$. If magnetic ordering occurs there will be a deviation from this at the ordering temperature. This can be used to calculate magnetic moments and obtain the Weiss temperature, θ , the sign of which indicates whether the material is interacting in a ferromagnetic ($\theta > 0$) or antiferromagnetic ($\theta < 0$) fashion as shown in Figure 2.9.

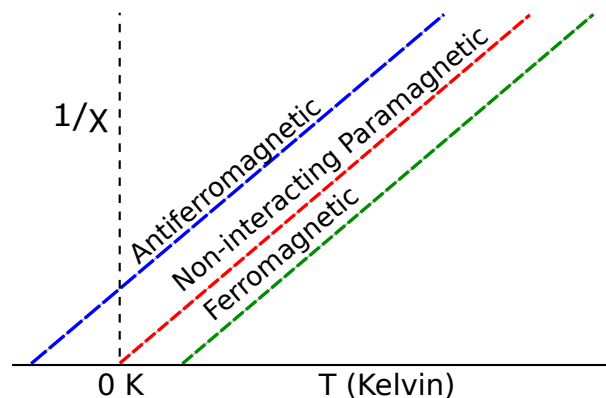


FIGURE 2.9: Plot of inverse susceptibility against temperature showing the Curie law for paramagnetic materials and the Curie-Weiss law for ferromagnetic and antiferromagnetic materials.

2.5.3 Mechanisms for Magnetic Exchange Interactions

The origin of magnetic coupling is the Pauli exclusion principle; electrons of parallel spin have a tendency to stay away from each other. Therefore, a pair of electrons of like spins will be lower in energy than a pair with opposite spins. The energy difference between these two states is the interaction exchange energy, or exchange coupling. The different types of magnetic interactions which can be important in allowing the magnetic moments in a solid to communicate with one another and potentially produce long-range order will be discussed in this section.

Direct Exchange

Direct exchange requires overlap of the orbitals containing the unpaired electrons, hence it requires a short metal-metal distance with no intervening anion. It gives a strong but short range coupling which decreases rapidly as the ions are separated. When the atoms are very close together the Coulomb interaction is minimal when the electrons spend most of their time in between the nuclei. Since the electrons are then required to be at the same place in space at the same time, Pauli's exclusion principle requires that they possess opposite spins. Electrons spend most of their time in between neighbouring atoms when the inter atomic distance is small. If it occurs between two singly occupied orbitals, the Pauli exclusion principle requires it to be antiferromagnetic. If the atoms are far apart the electrons spend their time away from each other in order to minimize the electron-electron repulsion. This gives rise to parallel alignment or positive exchange (ferromagnetism).

Superexchange

To explain the way that most magnetic materials order, the interaction between magnetic ions through an intermediate non-magnetic ion needs to be addressed. Superexchange describes the interaction between moments on ions too far apart to be strongly influenced by direct exchange but coupled over a relatively long distance through a non-magnetic ion. This happens when direct exchange is not possible and is the dominant form of exchange in real systems. The most recognised example is that of two transition metal ions separated by an oxygen atom. The type of ordering that results from superexchange is dependent on the geometry of the ions and the electronic configuration of the metal ions. Figure 2.10 shows two typical geometries and many forms of magnetic superexchange interactions exist as a result of electronic configurations of the metals. When considering a geometry of 180° an antiferromagnetic superexchange will occur if both metal ions have unpaired electrons in the e_g orbitals which directly overlap with the $2p$ orbitals on the oxygen. If one metal ion has unpaired electrons in the e_g orbital whilst the other metal ion has no electrons in the e_g orbital, the partially filled t_{2g} orbital will contribute to the superexchange interaction typically giving an overall ferromagnetic interaction. When considering a 90° geometry, more typical in edge-sharing octahedra, the superexchange occurs through two oxygen $2p$ orbitals resulting in an overall ferromagnetic interaction, however, this type of exchange is weaker than 180° antiferromagnetic superexchange. This is because the interaction is taking place through two oxygen orbitals rather than one, and hence the closer the geometry is to 180° , the stronger the interaction.

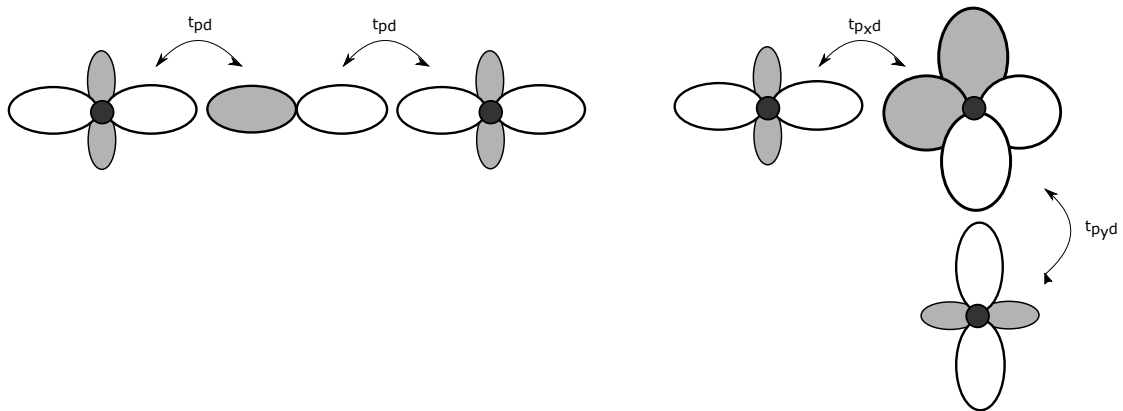


FIGURE 2.10: 180° and 90° geometry which can affect the long-range magnetic ordering through superexchange.

Magnetic Exchange in Metallic Systems

There are several magnetic interactions that can occur in a metallic system. A magnetic impurity in a metallic system causes an oscillation in the susceptibility of the surrounding conduction electrons, described by the RKKY mechanism, named after Ruderman, Kittel, Kasuya and Yosida. This oscillation leads to an indirect exchange between neighbouring impurity spins, over long ranges; the sign of the exchange interaction is dependant on the distance.⁸⁶ If the magnetic impurity ions are so dilute that they cannot be coupled by this mechanism, then it is possible to observe the Kondo effect. In this case, the coupling occurs between the localised impurity ion and the conduction electrons, below the Kondo temperature, the conduction electrons form a cloud of oppositely polarised spins. This results in a loss of the magnetic moment, and paramagnetic behaviour.

Double Exchange

Double exchange arises from electron delocalisation allowing spin coupling. The term was originally introduced by Zener to explain the magneto-conductive properties of mixed-valence solids, namely Mn doped Perovskites. Zener proposed the translocation of an electron from one Mn to another through an intervening O^{2-} .⁸⁷ Since the oxygen p orbital is doubly occupied, the translocation of the electron has to occur in two steps: the movement of an electron from the oxygen to the Mn^{4+} and then the filling of the vacant oxygen orbital by an electron from Mn^{3+} , hence the term double exchange. At the end of these steps, an electron has been moved between the neighbouring metal ions retaining spin. The metallic conduction, via hopping of e_g electrons, can only occur if the electrons of the t_{2g} orbitals for both ions are ferromagnetically aligned.

2.5.4 Geometric Magnetic Frustration

Geometric frustration is a broad phenomenon that results from an intrinsic incompatibility between some fundamental interactions and the underlying lattice geometry based on triangles and tetrahedra.⁸⁸ One of the most interesting features of the pyrochlore structure is its natural inclination to exhibit frustration effects for a wide range of interactions. Competing interactions means that there is no unique ground state and frustration is the term given to systems with such degenerate ground states. The most common example is geometrically frustrated magnetic interactions which stem from a triangular arrangement of spins which are antiferromagnetically coupled, shown in Figure 2.11. In this 2D model the antiferromagnetic interactions cannot be satisfied on all three sites when the spin direction is up at one vertex and down at another, this leads to the spin on the third vertex not being able to align, up or down, without an energetically unfavourable interaction between one of the other spins.

The effect of frustration may lead to materials which never enter a long-range ordered state. Frustrated systems which have a high degree of correlation, but still retain fluctuations at the lowest temperatures are known as Spin-liquids.⁸⁹ 3D spin-liquids where Ising spins sit on the apexes of corner-sharing tetrahedra, otherwise known as the pyrochlore lattice, are referred to as spin-ice materials which have proven to be of particular interest due to the discovery of ‘magnetic monopoles’, a semi-infinite string of spins with a magnetic charge.⁸⁹

One way of parameterizing the extent of magnetic frustration in a material is to look at the frustration index, $f = \theta/T^*$, where θ is the Weiss temperature and T^* is the magnetic order transition temperature.⁹⁰ A frustration index of 1 would be the expected behaviour of an unfrustrated material and a frustration index of 10 would indicate that the material is extremely frustrated. Generally speaking, as the frustration index increases the likelihood of exotic low-temperature magnetic states increase. It is not impossible to have materials with a frustration index of 100 or above, an example of which is spin liquids where no ordering is observed down to the lowest of temperatures.

The way in which magnetic interactions between atomic sites in the crystal lattice effects geometric frustration, and being able to understand the way that these interactions are mediated it is essential to fully understand frustration. Some long range ordering may seem insignificant at first; however, magnetically frustrated systems are at a tipping point where small energy changes can cause a transition. Practically, the superexchange that dictates the interactions is significantly more complex.⁹¹

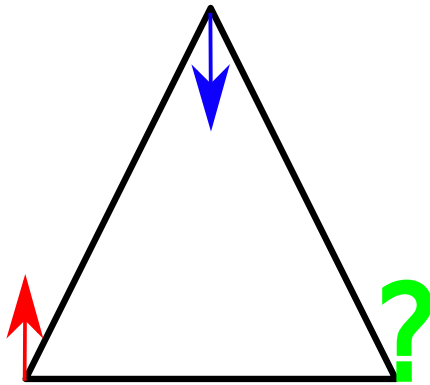


FIGURE 2.11: Antiferromagnetic nearest neighbour interactions on a 2D triangular lattice. It is not possible to orientate all spins in a way that all interactions between spins are antiferromagnetically satisfied.

2.6 Correlation of Structure and Properties

The underlying crystal structure of materials is critical in determining their ultimate properties. For instance, pencil 'lead' works due to the weak van der Waals bonding between the layers in graphite which allows the material to shear off and transfer to the page with little friction. Similarly, optical, electronic and magnetic properties are all controlled by the symmetry or the crystal structure.

All crystalline materials (excluding quasicrystals) have a unit cell which can be described by one of the 14 Bravais lattices, each of which have minimum symmetry requirements, the relationship between the lattice parameters and angles are explained in Table 2.2. This is discussed further in Section 2.7.

2.7 Structure of Solids

Crystalline solids have regular ordered arrays of components held together by uniform intermolecular forces, whereas the components of amorphous solids are not arranged in regular arrays.

2.7.1 Group Chemistry

Crystals are built from regular arrangements of atoms in three dimensions, these arrangements can be described by a repeating unit known as a unit cell, which is associated with a motif or array of atoms. This unit cell is the smallest repeating unit which describes the symmetry of the whole crystal structure. The vectors defining the sides of the unit cell are known as the lattice parameters, and it is the relationship that these lattice parameters have to one another and to that of the interaxial angles, which defines the crystal system and is determined from the symmetry elements present. The seven crystal systems are described in Table 2.2, where there are seven independent geometries that can be possible in three dimensions. Six of these systems are closely related and are either cubic or can be derived by distorting a cube in various ways.

These crystal systems can then be either primitive (P), face-centred (F), body-centred (I) or side-centred (A, B or C), giving the 14 Bravais lattices, each with essential symmetry operations displayed in Table 2.2. The International Tables of Crystallography describe a variety of symmetry operations which can be associated with each of these lattices.

The Seven Crystal Systems			
Crystal System	Parameters	Interaxial Angles	Essential Symmetry
Triclinic	$a \neq b \neq c$	$\alpha \neq \beta \neq \gamma$	None
Monoclinic	$a \neq b \neq c$	$\alpha = \gamma = 90^\circ \neq \beta$	One twofold axis or mirror plane
Orthorhombic	$a \neq b \neq c$	$\alpha = \beta = \gamma$	Three twofold axis or mirror planes
Trigonal	$a = b = c$	$\alpha = \beta = \gamma \neq 90^\circ$	One threefold axis
Hexagonal	$a = b \neq c$	$\alpha = \beta = 90^\circ, \gamma = 120^\circ$	One sixfold axis
Tetragonal	$a = b \neq c$	$\alpha = \beta = \gamma$	One fourfold axis
Cubic	$a = b = c$	$\alpha = \beta = \gamma = 90^\circ$	Four threefold axis

TABLE 2.2: The structures of all crystals can be classified according to the symmetry of the unit cells. There are in total 7 groups, collectively called Crystal Systems: Triclinic, Monoclinic, Orthorhombic, Tetragonal, Trigonal (Rhombohedral being a sub-group of Trigonal), Hexagonal, and Cubic. The symmetry of each group is described by the relationship between the lattice sides a , b , and c and angles α , β and γ .

Translation and point symmetry of atoms, otherwise known as space groups, are used to describe the overall symmetry of a crystal structure. There are four point symmetry operations:

- Rotations: The number of rotations is denoted by a number between 1 and 6
- Mirror planes: A mirror plane is denoted by the letter m
- Centre symmetry: Centrosymmetric structures have inversion symmetry, denoted by $\bar{1}$
- Rotoinversion: This is a combination between a rotation and inversion operation, such that $\bar{3}$ would represent a 3-fold rotation plus inversion

These operations often present in combination, for example, a 2-fold rotation axis normal to a mirror plane is denoted by $2/m$. The combination of the 32 possible point groups and the 14 Bravais lattices gives rise to 61 of the possible 230 space groups. The remaining 169 space groups are given by the addition of translational symmetry in the form of screw axes and glide planes. Screw axes are the combination of a rotation and translation operations which are denoted by n_m , where n is the order of rotations and m is the translation as a fraction of the lattice vector $1/m$. Glide planes are a combination of a reflection in a given plane and a translation parallel to it. This is denoted by a , b , c , n or d dependent of the translation direction. Overall the grouping of the space group and Wyckoff positions of the atoms within the cell will entirely describe the crystal structure of a material.

A structure whose periodicity does not match the periodicity of the crystal lattice is known as incommensurate. This is usually associated with a phase transition, and may

only be present across a small temperature range. A system whose incommensurability is a finite fraction of the crystal lattice is known as modulated and involves a periodic distortion. This distortion will give rise to satellite reflections which could also be described by a unit cell of lower symmetry, or superstructure, compared to the original unit cell is the parent structure. Such commensurate and incommensurate structural modulations are often associated with Jahn-Teller lattice distortions, charge and orbital ordering, and have been intensely studied in the context of the combination of ferroelectricity and antiferromagnetism in the manganites.

2.7.2 Magnetic Structure

The arrangement of spin in a crystal lattice can be described by defining the magnetic structure. Similar to the crystal structure, a magnetic space group provides the symmetry operations defined to generate atoms at all symmetry-equivalent positions in the magnetic unit cell. In comparison to the crystallographic space groups, there are 1651 magnetic space groups, the excess is due to the need for a time reversal operator. The magnitude and direction of the spin on each magnetic atom must be specified. The magnetic structure is a static approximation of the configuration of magnetic moments in the lattice since magnetism is a dynamic process involving spin waves. Magnetism may also be described using group theory.

The key parameter when defining the magnetic structure is the propagation vector which describes the relationship between the magnetic unit cell and the unit cell of the crystal structure. In a commensurate magnetic structure, the crystallographic and magnetic unit cells are the same or integral multiples. A typical propagation vector is $(0,0,0)$. The magnetic unit cell is often bigger than that of the crystallographic unit cell such as in the case of a single antiferromagnetic spin per crystallographic unit cell, where the magnetic unit cell will be doubled. The propagation vector will have no integer relationship to the lattice parameter in any direction when the magnetic unit cell is completely incommensurate. This implies a spin density wave propagating through the lattice in the direction of the incommensuration, and at least one of the terms in the propagation vector will be a non-integer.

The magnetic structure describes the arrangement of spins on a lattice. This can be important because, for instance with an antiferromagnet, there many possible arrangements of spins. A basic antiferromagnetic ordered cubic structure can be described in four different ways: type A, type C, type E and type G shown in Figure 2.12.

There are several models to describe magnetic interactions, the use of which depends on the dimensionality of the magnetic order. Magnetic dimensionality is separate from

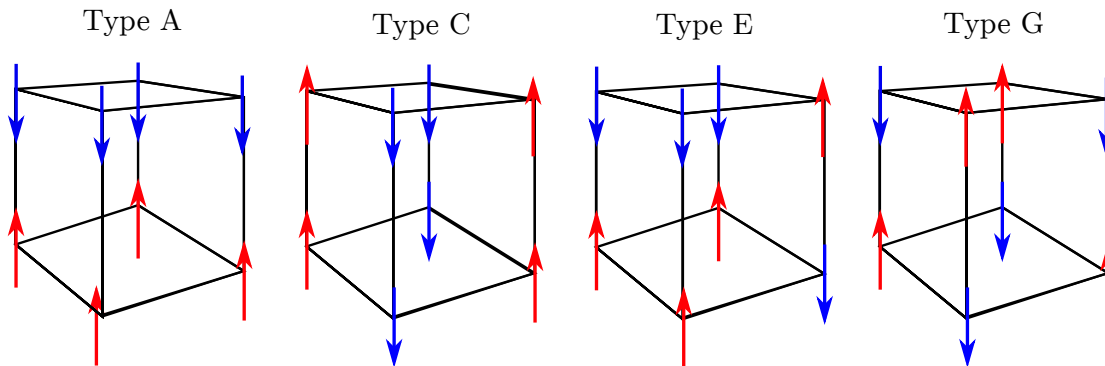


FIGURE 2.12: The four types of antiferromagnetic interactions that can occur on a simple cubic lattice; A-type has planes that are ferromagnetic with antiferromagnetic coupling, C-type has antiferromagnetic interactions in two planes and ferromagnetism in the third, E-type has a “zig-zag” antiferromagnetic interaction between the lattices and G-type corresponds to antiferromagnetic interactions in all three directions.

that of the crystallography dimensionality. This may be 1, 2 or 3D dependent on atom positions. The dimensionality of the magnetic structure describes how the spins are correlated within the lattice. For magnetic correlations that are 3D, the nearest-neighbour Heisenberg model is used, shown in Equation 2.33, where J is the nearest-neighbour exchange integral and the spins S_i and S_j are 3D vectors. The dimensionality of the lattice for the 3D Heisenberg model can be 1, 2 or 3D.

$$H = - \sum_{ij} J_{ij} S_i \cdot S_j \quad (2.33)$$

2.8 Measurement of Structural and Magnetic Properties

In addition to PXRD and PND, magnetic and structural properties of materials were measured using a variety of in-house techniques which are described below.

2.8.1 DC Susceptibility Measurements

Superconducting Quantum Interference Device or SQUID dc-susceptibility measurements were performed using a Quantum Design Magnetic Property Measurement System (MPMS). The magnetometer consists of a second-order gradiometer (counter-wound pick-up coils) connected to two parallel Josephson junctions in a superconducting ring. The sample of known weight is placed in a gelatin capsule and the capsule was then loaded into the sample holder. The sample holder is packed with other empty capsules to prevent movement and provide an average background. All capsules are kept in place with the aid of non-magnetic kapton tape. The sample is moved through the gradiometer

so that the current is introduced in the coils by electromagnetic induction. The SQUID then functions as an extremely sensitive current to voltage converter, outputting the change in magnetic flux measured by the pickup coils as a dipole voltage response. When calibrated to a sample of known mass and magnetic susceptibility, this response can be used to calculate the magnetic moment of the sample in electromagnetic units (emu). Measurements of 5×10^{-8} emu can be detected with SQUID, allowing it to be used for very small or subtle changes in susceptibility.

A superconducting magnet is incorporated into the MPMS system allowing measurements to be made in an applied magnetic field ($\mu_0 H$) of up to 7 T, with a field uniformity of 0.01 % over 4 cm. Magnetisation measurements can be done as both a function of temperature and applied magnetic field over a temperature range of 1.8 – 400 K. Higher temperatures of up to 800 K can be reached using a furnace insert, however samples need to be mounted in an aluminium holder to withstand the high temperatures. This increases the distortion of the dipole signal and therefore the background noise of the measurement. High temperature measurements were not performed during this work.

DC magnetic susceptibility measurements were typically carried out in a temperature range of 2 – 300 K, with a step size of 2 K below 50 K, and 5 K above. Normally, all samples had Zero Field Cooled, ZFC, and Field Cooled, FC, magnetic susceptibility measurements taken in a field of 100 Oe, where necessary the same measurements were repeated in a field of 1000 Oe. In some cases hysteresis measurements were performed to investigate the application of a magnetic field range at a given temperature on the magnetisation. Specifics of each experiment will be given with each hysteresis loop presented.

2.8.2 Mössbauer Spectroscopy

Mössbauer Spectroscopy is a technique used to provide information regarding the chemical, structural, magnetic and time-dependent properties of materials. In 1957, Rudolf Mössbauer discovered recoil-free emission and absorption of γ -radiation by nuclei which is now referred to as the ‘Mössbauer effect’. Even though the Mössbauer effect has been observed in many isotopes, only few are useful for practical application with ^{57}Fe being the most commonly studied which has both a very low energy γ -ray and a long-lived excited state. Nuclei in an atom normally go through energy level transitions based on the emission and absorption of γ -radiation. Within a free atom, the nucleus will recoil due to the conservation of momentum. This results with the emitted γ -ray being a lower

energy to that of the nuclear transition energy. The same principle is applied to absorption where the absorbing nucleus recoils, meaning that the energy of the resonantly absorbed photon must be greater than the energy of the transition.

The chemical isomer shift, δ , arises when the nuclei in the absorber and the source are in different environments. The energy gap between their ground and excited states is different, shifting the absorbed γ -ray energy from zero velocity by a value of δ . This stems from the electric monopole interaction between the nuclear and electronic charges. This is affected by changes in electron density at the nucleus, and hence, can be used to investigate the different ions of the same element as well as covalency effects. A typical example of this in ^{57}Fe Mössbauer spectroscopy, is the difference in Fe^{2+} and Fe^{3+} ions, where Fe^{2+} has a more positive isomer shift than Fe^{3+} . This is because Fe^{2+} has more d-electrons which provide greater screening of the nucleus from the outer s-electrons.

If a nucleus has a nuclear spin quantum number, $I > \frac{1}{2}$, quadrupole splitting, Δ , will be seen as it will have a non-spherical charge distribution and a nuclear quadrupole moment. If an asymmetric electric field is present, from asymmetric arrangement of electrons, the nuclear quadrupole moment will interact with it causing the nuclear energy level to split. This results in splitting of the absorption lines in the Mössbauer spectrum by an amount, Δ , and gives information about bonding and local structure. In the example of ^{57}Fe Mössbauer spectroscopy a two line spectrum is seen as the excited state splits into two sub-states, giving rise to two possible transitions. High spin Fe^{2+} has a larger quadrupole splitting than high spin Fe^{3+} , as Fe^{2+} has an asymmetric d^6 configuration whereas Fe^{3+} has a symmetric d^5 configuration.

A magnetic hyperfine splitting is observed when nuclei with spin $I > 0$ interact with magnetic fields via a magnetic dipole interaction, however, this was not observed in any of the materials in this thesis. All the Mössbauer spectroscopy data in this thesis was collected and interpreted by Assistant Professor T. David Harris and Jordan DeGayner at Northwestern University.

2.8.3 X-ray Absorption Spectroscopy

X-ray absorption Fine Structure (XAFS) can be divided into two main categories, XANES (X-ray Absorption Near Edge Structure) and EXAFS (Extended X-ray Absorption Fine Structure) which can determine the local atomic coordination and chemical/oxidation state of transition metals.⁹² Typically, X-ray absorption spectra are obtained from ≈ 200 eV below the absorption edge to ≈ 1000 eV above. The XANES is the region ranging from the absorption edge to ≈ 40 eV above the edge which is associated with the coordination geometry and oxidation states. The EXAFS region is the region

after XANES which gives information about local structure. XANES experiments were carried out on the B18 general purposes XAS beamline on Diamond Light Source located at the Diamond Synchrotron in Oxfordshire. Analysis of XANES was performed by Dr. Dave Pickup at the University of Kent.

2.8.4 X-ray Fluorescence (XRF)

The Panalytical Epsilon 3^{XL} is an energy dispersive X-ray fluorescence spectrometer which makes use of the same elemental phenomena as EDX, however, high-energy X-rays are used as the excitation source rather than electrons. When the X-ray beam with an energy higher than the binding energy of the electrons, interacts with a sample, electrons from the inner orbitals are displaced. When this displacement occurs, a vacancy is left behind which can be filled by higher orbital electrons which will have a higher binding energy and therefore lose energy as a result. The energy loss is equivalent to the energy difference between the two electron shells, which is determined by the distance between them, which is unique to each element. This energy loss can be used to identify the element from which it emanates. XRF was used for quick preliminary elemental analysis on a range of powder samples throughout this work.

Chapter 3

A new topotactic de-intercalation synthesis method, producing the first truly porous, single phase, magnetically frustrated pyrochlore FeF_3 .

3.1 Introduction

In order to further our understanding of magnetic frustration, it is essential to design new materials with different interactions and bondings that could lead to new properties. Pyrochlore oxides have been prominent in this, notably, with the discovery of “spin ice” materials,⁹³ whereas fluorides have been investigated less due to the difficulty in controlling stoichiometry. A new low temperature synthetic route has been designed for pyrochlore fluorides which has potential to expand this field of study.¹⁹ Recently, RbFe_2F_6 has been reported as a mixed-metal, magnetically frustrated, charge-ordered, defect pyrochlore. The structure refines to a $Pnma$ space group, with lattice parameters $a = 7.0177(6) \text{ \AA}$, $b = 7.4499(6) \text{ \AA}$ and $c = 10.1765(8) \text{ \AA}$, which exhibits a 3D structure comprising of Rb cations located between corner-sharing FeF_6 octahedra.¹³ The charge ordering can be understood as distinct Fe^{2+} and Fe^{3+} , therefore, the material is better described as $\text{RbFe}^{2+}\text{Fe}^{3+}\text{F}_6$. This structure is composed of two separate FeF_6 sublattices. The Fe^{3+}F_6 chains are connected through Fe^{2+}F_6 octahedra along the c-axis where the Fe^{2+}F_6 octahedral share corners along the b-axis. The Fe^{2+}F_6 octahedra share corners along the a-axis connected through Fe^{3+}F_6 octahedra along the c-axis.

The structure of RbFe_2F_6 is shown in Figure 3.1 displaying the FeF_6 sub-lattices and the Kagome-planes which result from the octahedral connectivity in both planes.¹³

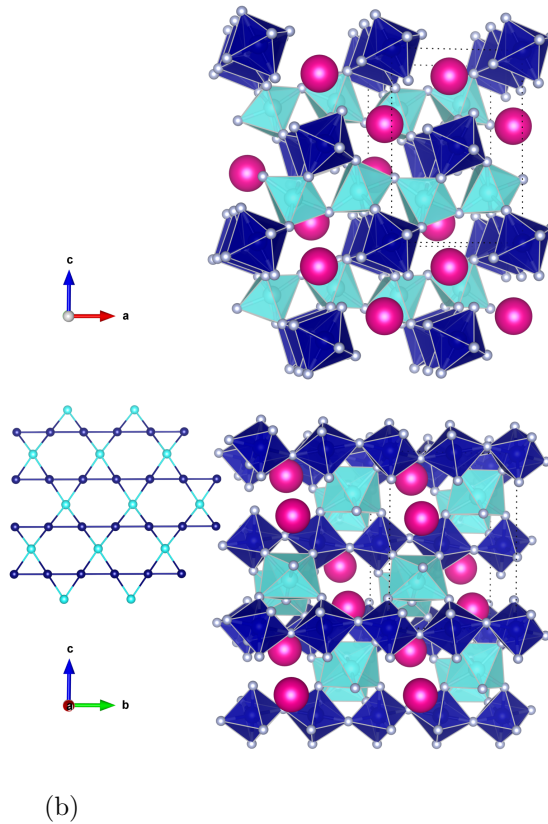


FIGURE 3.1: RbFe_2F_6 three-dimensional crystal structure obtained from single crystal diffraction where pink, dark blue and light blue represent Rb, Fe^{2+}F_6 polyhedra and Fe^{3+}F_6 polyhedra respectively. Kagome-planes are the result of the octahedral connectivity in both planes.

Unlike typical defect pyrochlores, RbFe_2F_6 does not show any signs of site disorder or partial occupancy, which tend to hinder these materials from being model magnetic systems. Both M sites are driven by charge rather than different elemental distribution with energetics being favoured rather than kinetics during the synthesis process. The magnetic structure of RbFe_2F_6 can be described as having a propagation vector of $\mathbf{k}=0$ with the Fe^{+2} ions aligning along the a-axis forming antiferromagnetic chains along the b-axis and the Fe^{+3} ions aligning along the b-axis forming antiferromagnetic chains down the a-axis. This is shown in Figure 3.2 where the magnetic moments on Fe^{+2} and Fe^{+3} are $4.9 \mu_B$ and $5.9 \mu_B$, respectively. The larger magnetic magnitude of Fe^{+3} is consistent with the oxidation state. The theoretical spin only value of RbFe_2F_6 is $7.7 \mu_B$, considerably higher than that of published data, $3.99(5) \mu_B$ which is consistent with diffuse scattering observed at 4 K resulting from magnetic frustration, suggesting that not all the moments display long range order.¹³

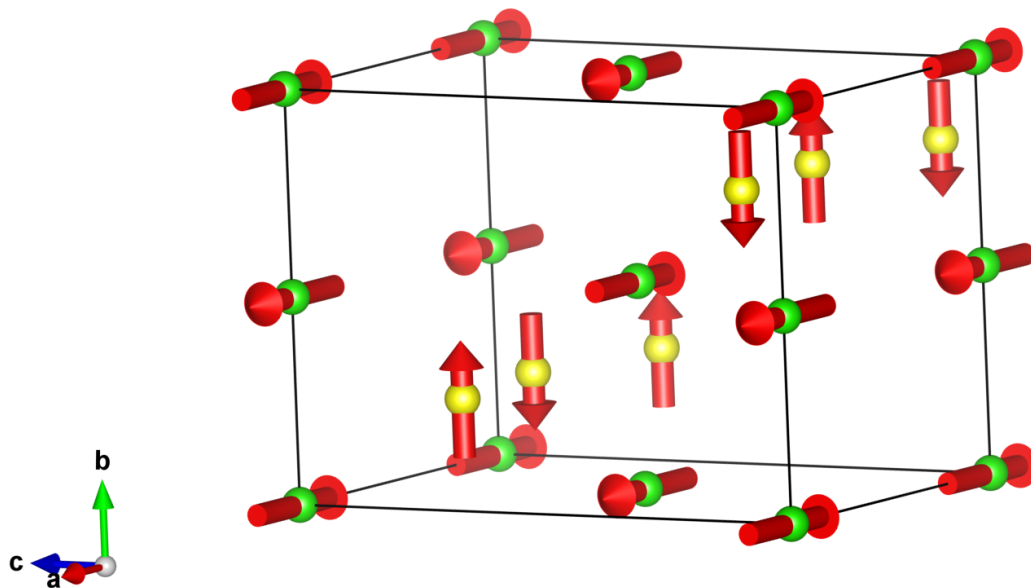


FIGURE 3.2: The magnetic structure of the RbFe_2F_6 at 1.6 K obtained from BT1 powder diffraction data. The Fe^{+2} ions, yellow, aligning along the a-axis forming antiferromagnetic chains along the b-axis and the Fe^{+3} ions, green, aligning along the b-axis forming antiferromagnetic chains down the a-axis. The theoretical spin only value is $7.7 \mu_{\text{B}}$ ($\text{Fe}^{+2} = 4.9 \mu_{\text{B}}$, $\text{Fe}^{+3} = 5.9 \mu_{\text{B}}$), which is considerably higher than the observed value of $3.99(5) \mu_{\text{B}}$.¹³

Defect pyrochlores, normally crystallising in the $Fd-3m$ space group, are closely related to the more common pyrochlore structure ($\text{A}_2\text{B}_2\text{X}_6\text{X}'$) through two ordered vacancies, as described in Section 1.2.1. One of the A-site cations becomes vacant as well as the anion, X' . The removal of the anion reduces the 8-fold coordination of the A-site cation leaving an open cage site. The isotropic thermal factor of Rb, being five times higher than the lighter Fe and twice that of F which is over four times lighter, which is a result of the rattling effect present for Rb within RbFe_2F_6 . The A-site cation rattling effect of defect pyrochlores have been documented heavily and is caused by the large mismatch between the ionic radii of the cation and the available space.^{48,94,95} Studies of the family of AOs_2O_6 materials, where $\text{A} = \text{Cs}$, Rb and K , revealed the features of rattling and showed that rattling induces or enhances the superconductivity of β -pyrochlore oxides.⁹⁶⁻⁹⁹ This rattling effect gives RbFe_2F_6 the potential to act as a starting material for the synthesis of a new truly porous pyrochlore iron fluoride with the ability to remove the large rattling cation.

There are three known forms of iron(III) fluoride, rhombohedral (R-FeF_3), hexagonal tungsten bronze-type (HTB-FeF_6) and pyrochlore-type (pyr-FeF_3). Traditionally, iron(III) fluoride is synthesised by reacting anhydrous FeCl_3 with anhydrous HF in a gas-solid apparatus until HCl formation stops, shown in Equation 3.1.¹⁰⁰

Parameter	R-FeF ₃ ^a	HTB-FeF ₃	Pyr-FeF ₃
Space Group	<i>R-3c</i>	<i>Cmcm</i> ^b	<i>Fd-3m</i> ^c
<i>a</i> (Å)	5.362(1)	7.423(3)	10.325(2)
<i>b</i> (Å)	5.362(1)	12.730(4)	10.325(2)
<i>c</i> (Å)	5.362(1)	7.526(3)	10.325(2)
α , °	57.94(2)	90	90
β , °	57.94(2)	90	90
γ , °	57.94(2)	90	90
<i>V</i> (Å ³)	103.86	711.17	1100.7
<i>Z</i>	2	12	16
Pore ϕ , (Å)	-	3.1	1-2.5

TABLE 3.1: The crystallographic parameters of FeF₃ phases, R-FeF₃,¹⁰⁴ HTB-FeF₃¹⁴ and *Fd-3m*.¹⁰⁶ ^a The cell is given in its rhombohedral setting. ^b In the referenced paper, the space group is given as *P6/mmm*, there is no report of structural data and the data of the hydrated form from which it is derived is given alternatively. ^c No reports of truly porous pyr-FeF₃ have been produced, the data here are that of Pyr-(NH₃)_xFeF₃.



This method produces amorphous FeF₃ which is heated to 600 °C to induce crystallisation in the rhombohedral space group, *R-3c*.^{101,102} R-FeF₃ is isostructural with a distorted ReO₃-type structure, also being described as an A-site deficient perovskite consisting of corner-shared FeF₆ octahedra in all three directions. R-FeF₃ is otherwise referred to as α -FeF₃. HTB-FeF₃·0.33H₂O is synthesised by reacting amorphous FeF₃ and H₂O at 360 °C hydrothermally. HTB-FeF₃·0.33H₂O consists of large channels along the *c*-axis in which trapped water molecules reside.¹⁰³ Above 120 °C, HTB-FeF₃·0.33H₂O can be dehydrated, without any structural changes, to give anhydrous HTB-FeF₃. The third form of iron(III) fluoride, pyr-(NH₃)_xFeF₃, where 0.025 < *x* < 0.40, can be synthesised through topotactic oxidation of mixed valence fluoride, NH₄Fe₂F₆ an ordered pyrochlore structure, in a boiling solution of Br₂ in acetonitrile at 81 °C. Pyr-(NH₃)_xFeF₃ consists of corner sharing FeF₆ octahedra creating three dimensional interconnecting channels in which NH₃ reside. It is important to note that structural phase transitions from the pyrochlore form of FeF₃ to HTB-FeF₃ and then to R-FeF₃ occurs on annealing at 280 °C and 380 °C, respectively. The crystallographic parameters of FeF₃ phases are outlined in Table 3.1 and displayed in Figure 3.3.^{100,104–106}

More recently a hydrated pyrochlore-type iron(III) fluoride, FeF₃·0.5H₂O, has been reported, formed by means of non-aqueous chemical synthesis. Fe(NO₃)₃·9H₂O powder is added to BmimBF₄, 1-butyl-3-methylimidazolium tetrafluoroborate, and C₁₀minBF₄, 1-decyl-3-methylimidazolium tetrafluoroborate where BF₄⁻ anions hydrolyze to form BF₃·H₂O and F⁻. The solvated Fe⁺³ reacts with F⁻ ion to form precipitated iron(III) fluoride, and on vacuum drying at 50 °C for 6 hours, yellow precipitates of FeF₃·0.5H₂O

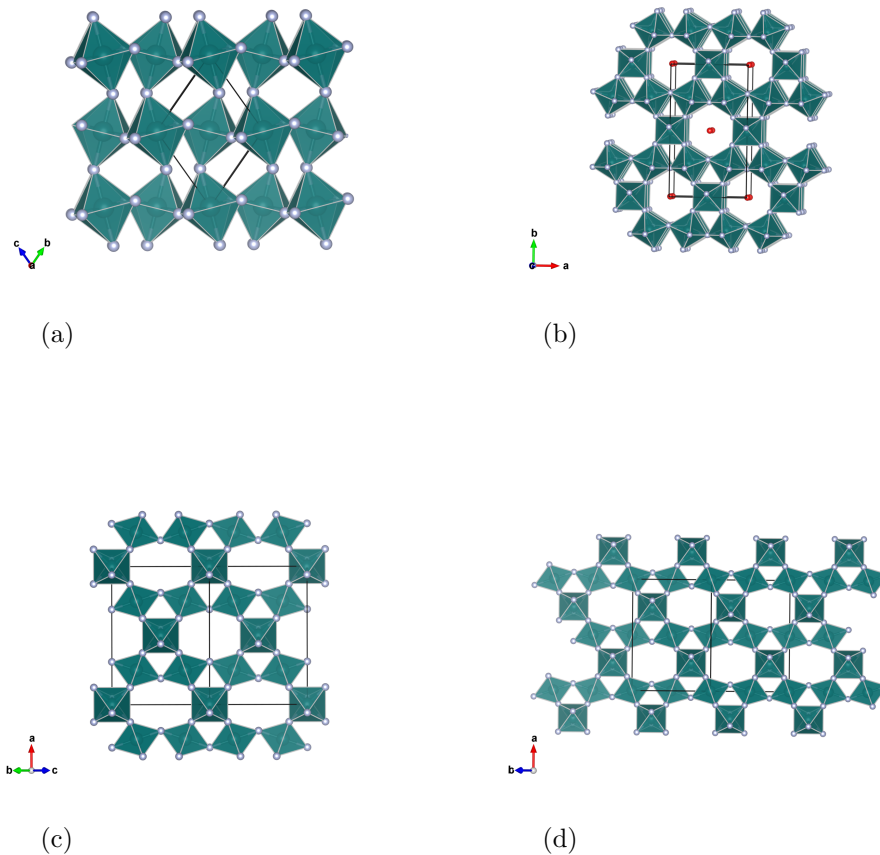


FIGURE 3.3: The crystallographic structure of FeF_3 phases, (a) R-FeF_3 ,¹⁰⁴ (b) HTB-FeF_3 ,¹⁰⁵ and pyr-FeF_3 ,¹⁰⁶ (c) along the $[011]$ and (d) $[0-11]$ direction, showing the three dimensional interconnecting tunnel network without H_2O or $(\text{NH}_3)_x$, where green shows the Fe-F octahedral, grey shows the fluorine ions and red as H_2O .

were formed.^{107,108} With reference to pyr-FeF_3 , there have been no reports of a *truly porous* single phase structure. Using RbFe_2F_6 as a starting material, topotactic deintercalation of the A-site Rb cation and oxidation of the Fe^{+2} could lead to the first reports of *truly porous* pyr-FeF_3 .

3.2 Experimental

3.2.1 Reagents

The reagents used to synthesis RbFe_2F_6 were RbF (Alfa Aesar, 99%), FeF_3 anhydrous (Alfa Aesar, 97% min), FeF_2 anhydrous (Alfa Aesar, 99%) and CF_3COOH (Alfa Aesar,

99%) without any further modification of purification. Br₂ (Alfa Aesar, 99.5%) and CH₃CN (Alfa Aesar, 99%) were used for further reactions.

3.2.2 Synthesis

Synthesis of RbFe₂F₆

RbFe₂F₆ was prepared hydrothermally following the synthesis methods previously published in the literature.^{13,19} Using Parr Instrument Company general purpose acid digestion vessels with an internal volume of 45 ml, 0.238 g (2.28×10^{-3} mol) of RbF, 0.2141 g (2.28×10^{-3} mol) of FeF₂ and 0.2573 g (2.28×10^{-3} mol) of FeF₃ were added to 3 ml (3.90×10^{-2} mol) of CF₃COOH, and 5 ml of H₂O in the autoclave. The autoclave was sealed, gradually heated to 230 °C and held for 24 h before being cooled to room temperature at a rate of 0.1 °C/min. The mother liquid was decanted and the remaining solid washed with H₂O using gravity filtration. The sample was then dried for \approx 12 h at 70 °C before analysis.

RbFe₂F₆ characterisation

Before reacting RbFe₂F₆ further, standard in-house characterisation techniques were implemented to ensure sample purity. The Rietveld refined PXRD pattern of RbFe₂F₆ is displayed in Figure 3.4, where the material crystallises in the *Pnma* space group with lattice parameters $a = 7.022(3)$ Å, $b = 7.447(3)$ Å and $c = 10.177(5)$ Å and $\alpha = \beta = \gamma = 90^\circ$ consistent with the previously published structure¹³ at room temperature.

Mössbauer spectroscopy was used to determine the amount of Fe⁺² and Fe⁺³ ions in RbFe₂F₆ formed. Figure 3.5 shows the Mössbauer absorption spectrum at 250 K and 80 K, displaying the individual Fe fits and the sum of quadrupole doublets with different intensity and splitting. At 250 K the fit to Fe³⁺ gives an isomer shift of $\delta = 0.494(2)$ mm/s and a quadrupole splitting of $\Delta E_Q = 0.699(4)$ mm/s and Fe²⁺ gives an isomer shift of $\delta = 1.322(2)$ mm/s and a quadrupole splitting of $\Delta E_Q = 2.673(3)$ mm/s. At 80 K the fit to Fe³⁺ gives an isomer shift of $\delta = 0.558(2)$ mm/s and a quadrupole splitting of $\Delta E_Q = 0.694(4)$ mm/s and Fe²⁺ gives an isomer shift of $\delta = 1.418(2)$ mm/s and a quadrupole splitting of $\Delta E_Q = 2.762(4)$ mm/s both with no magnetic splitting displaying the octahedral coordination of Fe³⁺ and Fe²⁺. From the peak area, the ratio between Fe²⁺ and Fe³⁺ sites are very similar, 53.1(9) % and 46.9(6) % although it is possible that there are small amount of disorder between the two sites.

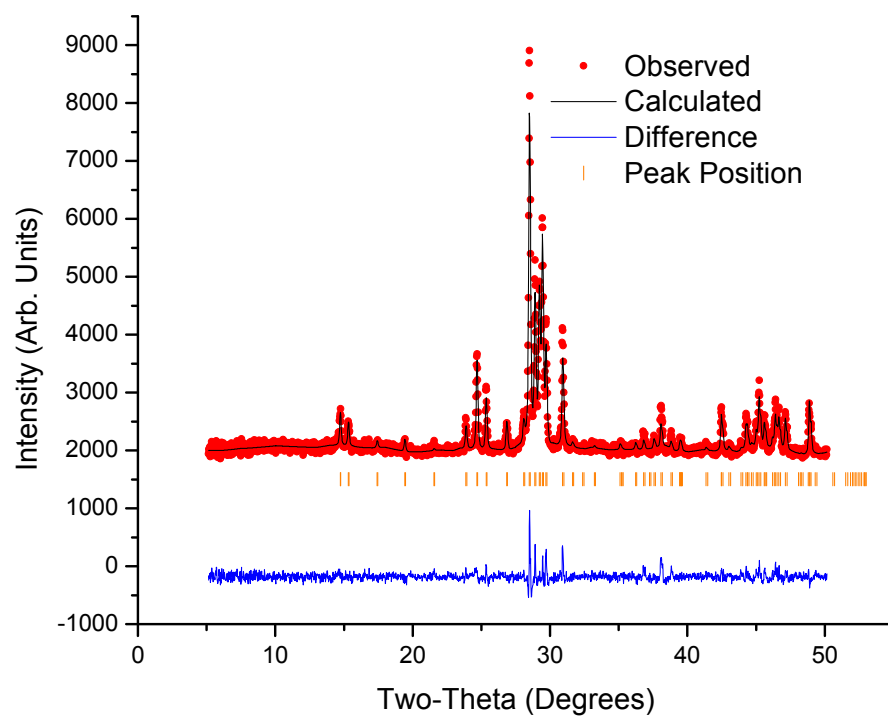
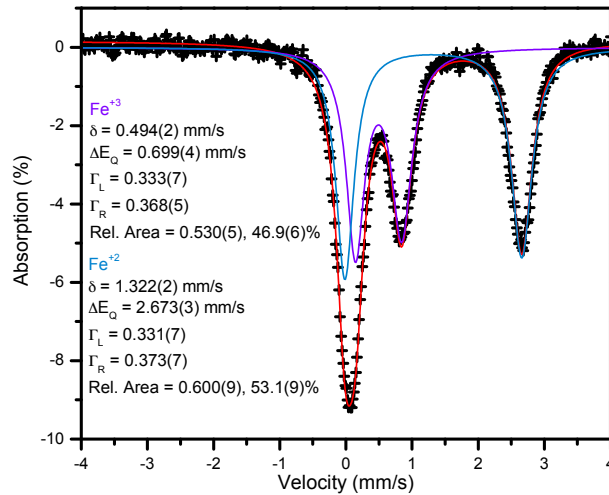
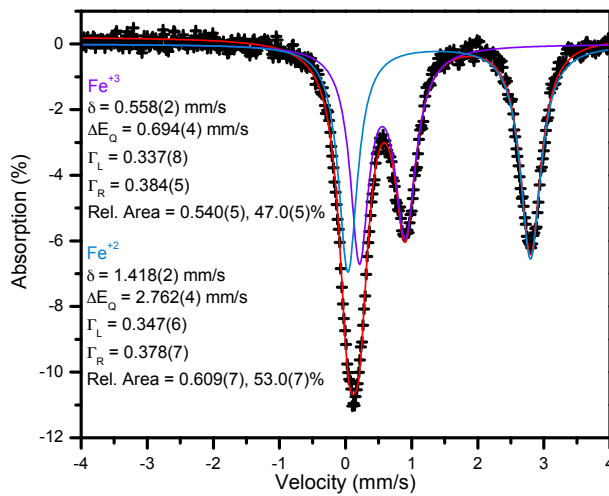


FIGURE 3.4: Fitted powder neutron diffraction data collected on the BT1 diffractometer of RbFe_2F_6 at 300 K, with lattice parameters $a = 7.022(3) \text{ \AA}$, $b = 7.447(3) \text{ \AA}$ and $c = 10.177(5) \text{ \AA}$ and $\alpha = \beta = \gamma = 90^\circ$ consistent with the previously published structure.¹³



(a)



(b)

FIGURE 3.5: Mössbauer absorption spectra of RbFe_2F_6 at 250 K, (3.5a), showing the fit to Fe^{3+} which gives an isomer shift of $\delta = 0.494(2)\text{mm/s}$ and a quadrupole splitting of $\Delta E_Q = 0.699(4)\text{mm/s}$. Fe^{2+} gives an isomer shift of $\delta = 1.322(2)\text{mm/s}$ and a quadrupole splitting of $\Delta E_Q = 2.673(3)\text{mm/s}$. At 80 K, (3.5b), the fit to Fe^{3+} gives an isomer shift of $\delta = 0.558(2)\text{mm/s}$ and a quadrupole splitting of $\Delta E_Q = 0.694(4)\text{mm/s}$ and Fe^{2+} gives an isomer shift of $\delta = 1.418(2)\text{mm/s}$ and a quadrupole splitting of $\Delta E_Q = 2.762(4)\text{mm/s}$. Both temperatures give no indication of magnetic splitting displaying the octahedral coordination of Fe^{3+} and Fe^{2+} .

The magnetic susceptibility of a powder sample of RbFe_2F_6 was measured from 300 K down to 2 K. Both zero field cooled and field cooled magnetic susceptibility were measured at 100 Oe for 94.17 mg of powdered RbFe_2F_6 using a SQUID magnetometer. Figure 3.6 shows a close up of the low temperature region where a clear divergence from high temperature paramagnetic behaviour is seen at 18 K indicating the antiferromagnetic transition, furthermore, the zero-field cooled and field cooled susceptibility curves separate below 18 K, showing a hysteresis behaviour consistent with published literature.¹³ Additionally, a small feature is seen at 3 K which has not yet been reported or observed. This could be explained by a magnetic transition due to strong distortion of the Fe^{2+}F_6 octahedra from a Jahn-Teller effect, whilst the Fe^{3+}F_6 octahedra remain only slightly distorted. Heat capacity measurements should be done to confirm the presence of this anomaly, and to better understand this feature and how it is related to the magnetic structure, a detailed temperature dependence study using powder neutron diffraction should be done. The inset in Figure 3.6 shows the inverse susceptibility as a function of temperature and the paramagnetic behaviour between 300 K to 200 K has been extrapolated to calculate a $\theta_{CW} = -135$ K consistent with an antiferromagnetic magnetic transition.

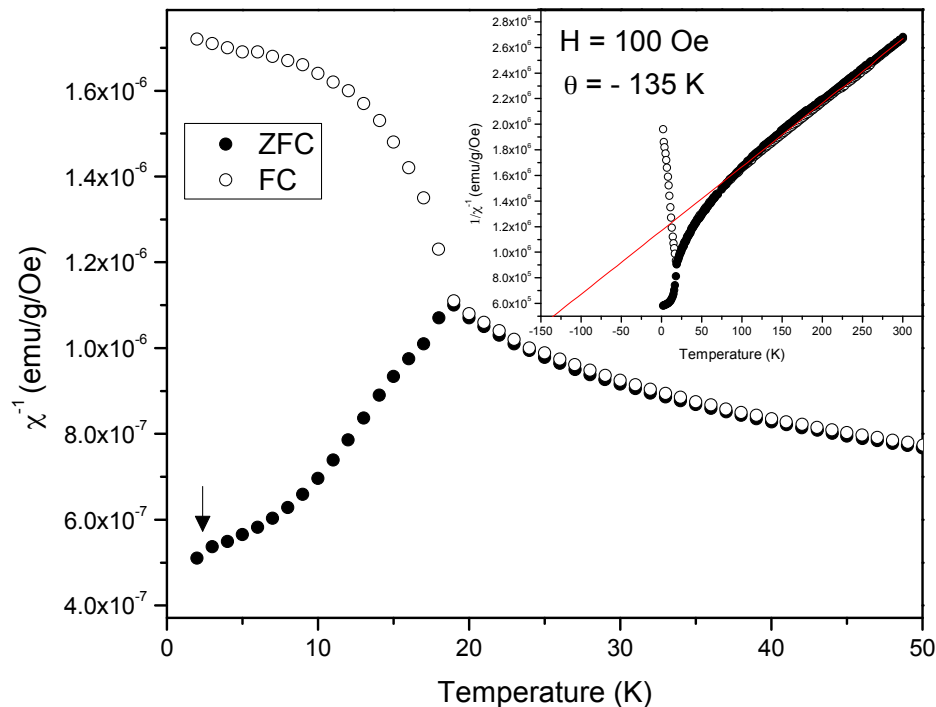


FIGURE 3.6: The magnetic susceptibility for a powder sample of RbFe_2F_6 with an anomaly at 18 K indicating the antiferromagnetic transition as well as a small feature in the data at 3 K which has not yet been reported. The inset displays the analysis of the paramagnetic region between 300 K to 200 K giving $\theta_{CW} = -135$ K.

Synthesis of pyr-FeF₃

Previous reports of the pyr-FeF₃ structure type have been shown to indicate NH₃ or H₂O within the three-dimensional tunnels of the structure. The synthesis method for pyr-(NH₃)_xFeF₃, (NH₃)_xFeF₃, $x = \approx 0.25$, involved the de-intercalation of ammonium and oxidation of Fe²⁺ using a boiling solution of bromine in acetonitrile. It is worth noting that it is difficult to prevent the simultaneous formation of the HTB-FeF₃ phase without altering the starting composition, this may be due to the non-stoichiometric character of this phase whose homogeneity range varies from (NH₃)_{0.46}FeF₃ to (NH₃)_{0.56}FeF₃.¹⁰⁶ The pyrochlore form of previously reported FeF₃ structures with trapped water or molecules decompose during heating making it impossible to produce pure pyr-FeF₃ once molecules or water are intercalated.^{100,102}

Post analysis of RbFe₂F₆, ≈ 500 mg of product was added to 100 cm³ of CH₃CN and on stirring, 8.3 cm³ of Br₂ was added. The solution was left to stir for 66 h, washed with CH₃OH and dried in two stages; 80 °C for ≈ 12 h and 200 °C for 2 h, both in a vacuum after decanting the solvent. This newly developed synthesis technique for stabilising pyr-FeF₃ uses bromine at ambient temperature to de-intercalate Rb from RbFe₂F₆, transforming the purple orthorhombic structure to a pale green cubic phase free from Br⁻, Fe²⁺ or occupation of the A site. The excess of bromine favours the dissolution of rubidium bromide in acetonitrile, most likely in the form of RbBr, whilst only oxidising the Fe²⁺. After gravitational filtration with CH₃OH, impurities may be present on the surface structure of pyr-FeF₃, these can be eliminated by vacuum drying at 80 °C for ≈ 12 h and 200 °C for 2 h. The latter stage of drying ensure that all H₂O has been evacuated from the sample surface, giving a purely porous, single phase pyr-FeF₃ structure. It is worth noting that, from Infrared spectroscopy, there is no H₂O present in the large cavities as seen with FeF₃·0.5H₂O. The attempted removal of H₂O or molecules from the cavities of FeF₃ has previously resulted in structural decomposition from pyrochlore to hexagonal tungsten bronze.^{100,102}

3.2.3 Structural Properties

Crystal Structure

Pyr-FeF₃ was characterised using the Panalytical Empyrean X-ray diffractometer, described in Section 2.3.2. Rietveld refinement shows that there is a space group change from pyrochlore-like *Pnma* RbFe₂F₆ to *Fd-3m* pyr-FeF₃ after Br reaction. An example data set of pyr-FeF₃ including the fit from the refinement model and the difference plot is shown in Figure 3.7. Pyr-FeF₃ has lattice parameter $a = 10.304(5)$ Å with $\alpha = \beta = \gamma = 90$. The final refinement of pyr-FeF₃ confirmed 100 % purity free from Fe²⁺, Rb⁺ and Br⁻. The fit parameters are $\chi^2 = 2.24$, $R_p = 6.28\%$ and $R_{wp} = 8.02\%$. Table 3.2 shows the crystallographic parameters for pyr-FeF₃ obtained from the Rietveld refinement of powder X-ray diffraction data and Figure 3.8 visualises the crystallographic structure. It is important to note that the crystallinity of pyr-FeF₃ is extremely high. The chemical procedure was shown not to destroy the Fe-F framework. This is likely to be due to the extended reaction under ambient conditions rather than previous, Br₂, reflux methods.

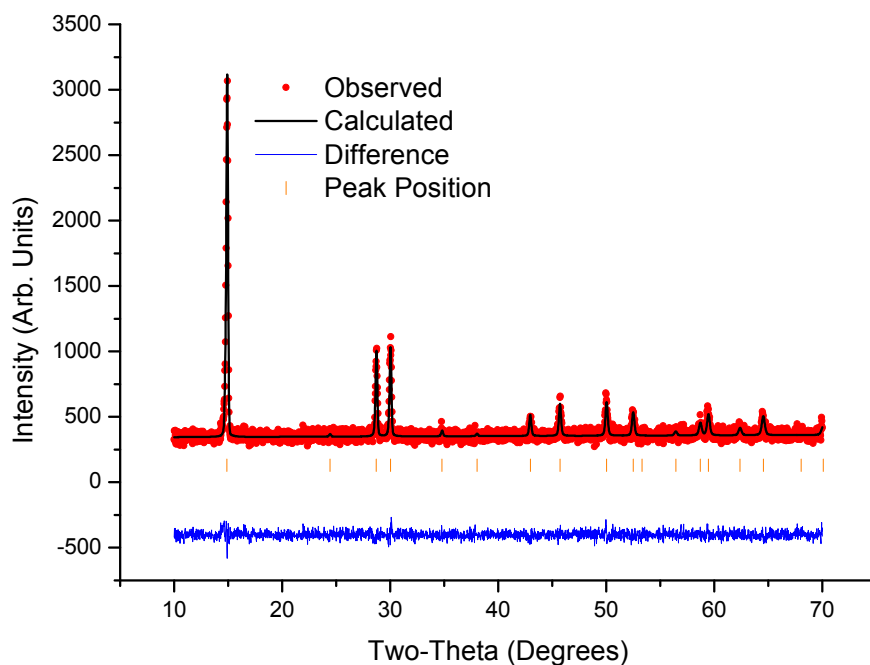


FIGURE 3.7: X-ray diffraction data collected at 300 K (red), Rietveld refined model (black) and the difference (blue) plot for powder sample of pyr-FeF₃. The data were collected using the methods described in Section 2.3.2. The fit parameters are $\chi^2 = 2.24$, $R_p = 6.28\%$ and $R_{wp} = 8.02\%$.

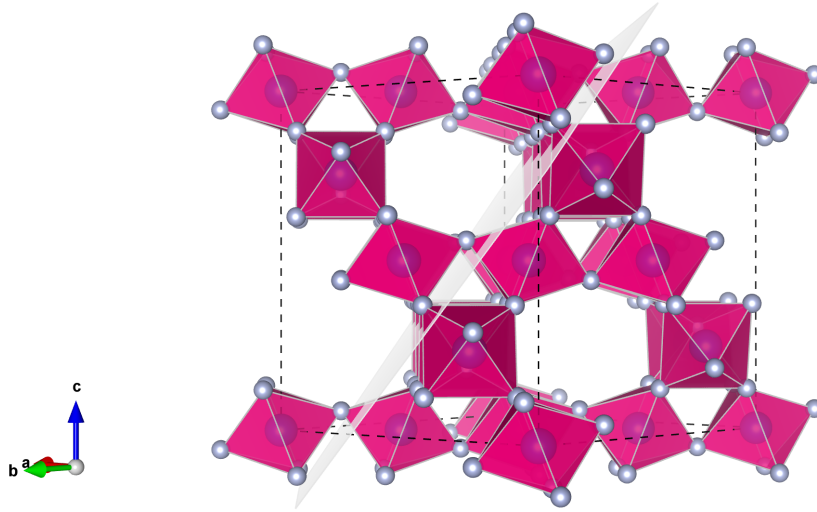


FIGURE 3.8: The crystallographic structure of pyr-FeF₃ displaying no chemical distortion within the cationic lattice and all iron ions nominally of a 3⁺ oxidation state.

Parameter	FeF ₃
Formula Weight, fw	112.84 g mol ⁻¹
Temperature (K)	298
λ (Å)	1.54059
Crystal Structure	Cubic
Space Group	<i>Fd-3m</i> (No.227)
a (Å)	10.304(5)
b (Å)	10.304(5)
c (Å)	10.304(5)
V (Å ³)	1098.257 (0.031)
Z	8
ρ_{calc} (g/cm ³)	2.730
2θ max.	99.99
GOF	1.3

TABLE 3.2: Crystallographic data for pyr-FeF₃ obtained through Rietveld refinement of powder X-ray diffraction.

Oxidation State of Iron

Mössbauer Spectroscopy was used to determine the oxidation state of Fe and to ensure all Fe atoms are in a 3^+ oxidation state. The Mössbauer absorption spectrum at 80 K and fit of Fe^{3+} is shown in Figure 3.9. The absorption spectrum exhibits a singlet free from Fe^{2+} . The fit to the singlet gives an isomer shift of $\delta = 0.570(3)\text{mm/s}$ and a quadrupole splitting of $\Delta E_Q = 0.265(5)\text{mm/s}$ with no magnetic splitting showing the octahedral environment of the Fe^{3+} ions. This confirms the full oxidation of the Fe^{+2} ions during the Br reaction, within the resolution of the experiment. A previous study reports that pyr- FeF_3 , obtained from previously described soft chemistry techniques, contains a small Fe^{+2} component.¹⁰⁹ HTB- FeF_3 can be characterised as a major impurity, splitting at 130 K.¹¹⁰ Fe^{+2} begins to split magnetically between a temperature range of 130 K and 77 K which is likely to indicate that Fe^{+2} is in the rutile FeF_2 form. In any case, there is no observed splitting in Figure 3.9 indicating that no HTB- FeF_3 or FeF_2 impurities exist.

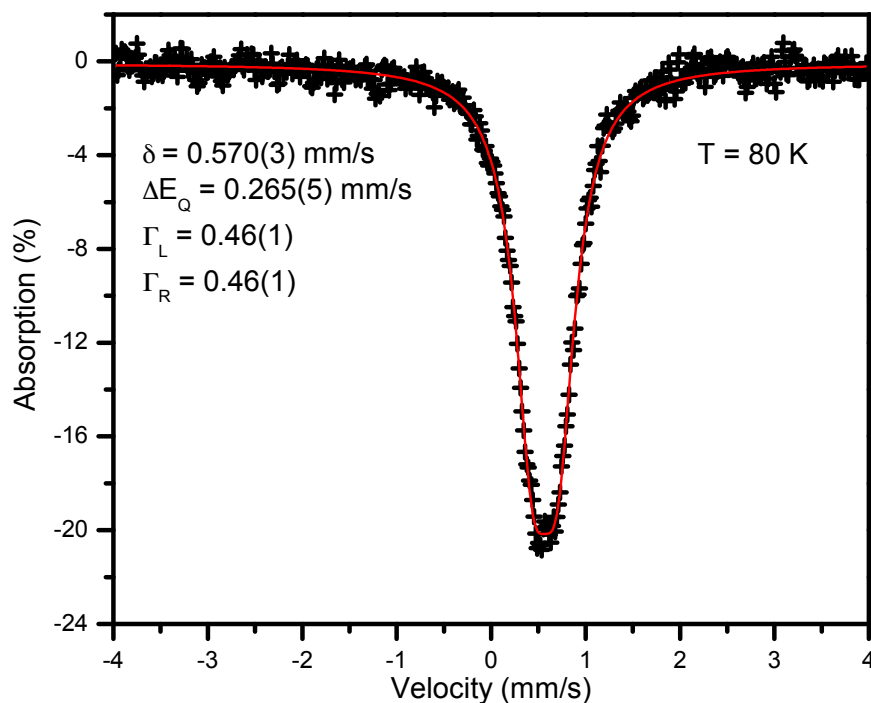


FIGURE 3.9: Mössbauer absorption spectrum for pyr- FeF_3 taken at 80 K. The red line corresponds to Fe^{3+} , confirming that all Fe are normally 3^+ free from Fe^{2+} . The fit gives an isomer shift of $\delta = 0.570(3)\text{mm/s}$ and a quadrupole splitting of $\Delta E_Q = 0.265(5)\text{mm/s}$.

Porosity

Gas adsorption isotherms were collected using a Micromeritics 3Flex Surface Characterization Analyzer or ASAP 2420 between 0 and 1 bar by the volumetric method. These measurements and fits were performed by the ‘The Long Group’ at UC Berkeley. Pyr-FeF₃ was transferred to a pre-weighed analysis tube in a dry dinitrogen filled glovebox. The tube was then sealed and evacuated at 150 °C for 48 h achieving an outgas rate of less than 1 μ bar/min. The sample tube mass was again assayed and the sample mass was calculated (\approx 250 mg). The sample tube was then attached to an analysis port and evacuated. Prior to each adsorption measurement, warm and cold free spaces were determined using He as a probe gas. H₂ isotherms were collected at 77 K and 87 K by submerging the sample tube in N₂ and Ar filled isothermal baths respectively. An N₂ adsorption isotherm was collected at 77 K and a CO₂ adsorption isotherm was collected at 23 °C using an isothermal water bath. Oil free vacuum pumps and pressure regulators were used for all measurements. Dihydrogen isotherms collected at 77 K and 87 K were independently fitted to a dual-site Langmuir-Freundlich equation. While the 87 K isotherm could be reasonably reproduced using a single site expression, the shape of the 77 K isotherm could not be adequately described with a simpler model. Fits were optimized using nonlinear least squares analysis in python using predefined functions in the Scipy and Numpy open source libraries. The fit results are shown in Figure 3.10. Isothermic heats of H₂ adsorption were then calculated using the Clausius-Clapeyron equation at equivalent loadings shown in Figure 3.11. Gas adsorption measurements confirm the truly porous nature of pyr-FeF₃ which has previously not been reported. This constitutes a new form of microporous material that is likely to have sensitive magnetic properties compared to FeF₃ with intercalated ions or molecules.

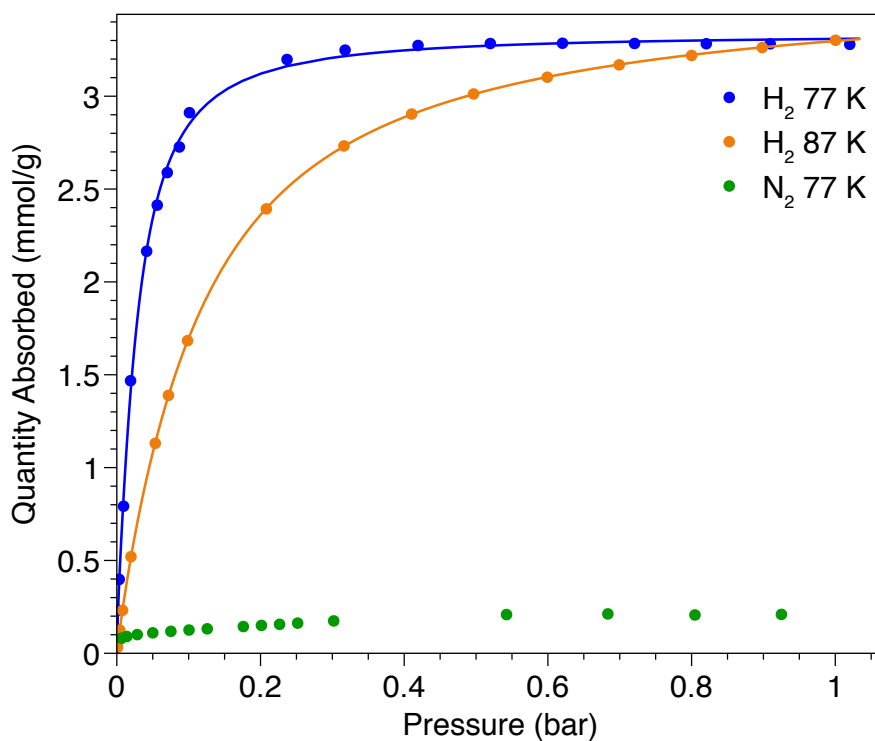


FIGURE 3.10: Dihydrogen adsorption isotherms collected at 77 K (blue) and 87 K (yellow). The lines represent the best fit to the adsorption data using a dual-site Langmuir-Freundlich equation. Dinitrogen adsorption at 77 K (green) is also plotted.

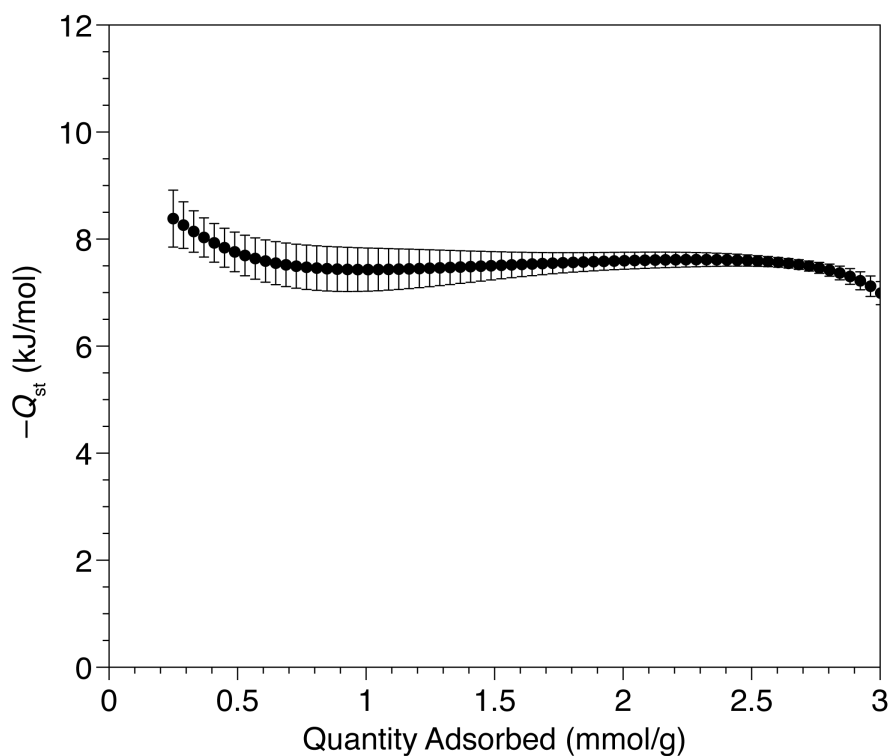


FIGURE 3.11: Isothermic heats of adsorption calculated as a function of dihydrogen loading in pyr-FeF₃ using the Clausius-Clapeyron equation and adsorption isotherms collected at 77 K and 87 K.

3.2.4 Magnetic Properties

Previous studies of iron(III) fluorides show HTB-FeF₃ has very strong antiferromagnetic interactions ($T_N = 97(2)$ K, $\theta = -600$ K). The magnetic structure at 4.2 K is described as three antiferromagnetic sub-lattices at 120 deg, between two layers the coupling of Fe³⁺ spins are strictly antiferromagnetic. When compared with the α -rhombohedral form of FeF₃, HTB-FeF₃ is evidently frustrated. R-FeF₃ is an antiferromagnet of the G -type with moments lying in the (111) plane and a T_N four times in magnitude compared to HTB-FeF₃. The lowering of T_N is related to frustrating effects which appear when the topology of the cationic sub-network of Fe³⁺ exhibits odd cycles. In R-FeF₃ there are 12 squares and in HTB-FeF₃ 2 triangles and 8 squares. Pyr-FeF₃ is expected to order antiferromagnetically below 20(2) K, considerably lower than that of previously reported iron(III) fluorides due to there being only six triangles. Here the first magnetometry and neutron diffraction study of truly porous pyr-FeF₃ is discussed.

Magnetometry

The magnetic susceptibility of a powder sample of pyr-FeF₃ was measured from 300 K down to 2 K. Both zero field cooled and field cooled magnetic susceptibility were measured at 100 Oe for 15.77 mg sample of powdered pyr-FeF₃ using a SQUID magnetometer. The data for this are shown in Figure 3.12. The paramagnetic behaviour between 300 K and 200 K, used for calculating the effective magnetic moment and the Curie-Weiss constant, is shown in the inset of Figure 3.12 where the data are fitted with a least-squares regression line. The Curie-Weiss constant has been calculated as $\theta_{CW} = -699.14(7)$ K and the calculated effective magnetic moment is $\mu_{eff} = 4.99(3) \mu_B$ compared to the Hund's rules prediction for a Fe³⁺ ion at 4.89(8) μ_B . This may be due to a small impurity which was not detectable from XRD or NPD.

The inverse magnetic susceptibility for pyr-FeF₃ ranging from 200 K to 2 K is shown in Figure 3.13. The dashed line at 18 K shows a divergence from the paramagnetic trend indicating a phase transition at this temperature. The frustration index of pyr-FeF₃ was calculated to be 38.84(1), suggesting an extremely frustrated material. It can also be noted that there is the presence of an anomaly at ≈ 70 K which may be the onset of short-range correlations.

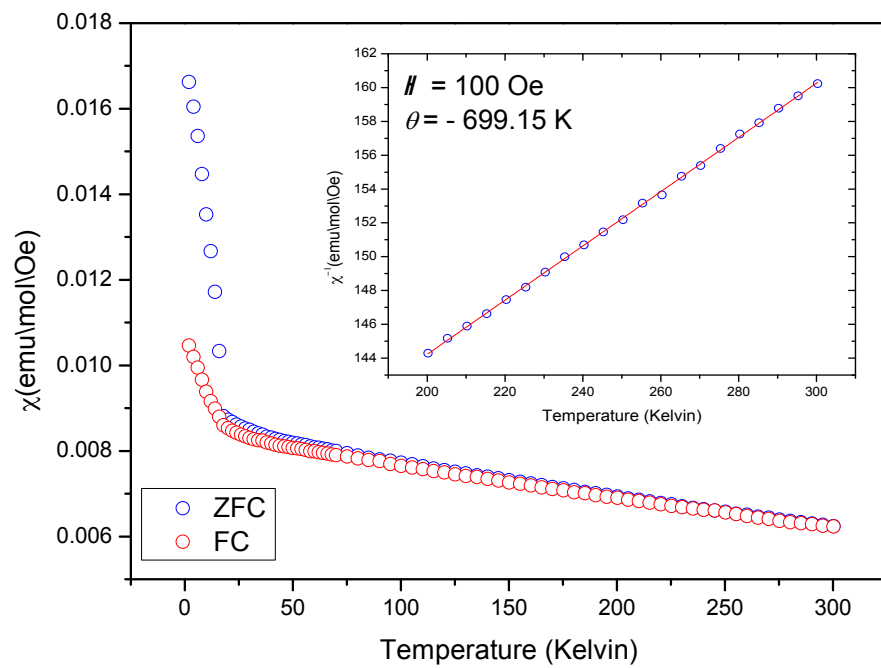


FIGURE 3.12: The magnetic susceptibility for a powder sample of pyr-FeF₃. The inset, the inverse susceptibility as a function of temperature, shows the fit of the paramagnetic region between 300 K and 200 K. From the fit the effective magnetic moment is calculated as $\mu_{eff} = 4.99(3) \mu_B$, and the Curie-Weiss constant is $\theta_{CW} = -699.14(7)$ K.

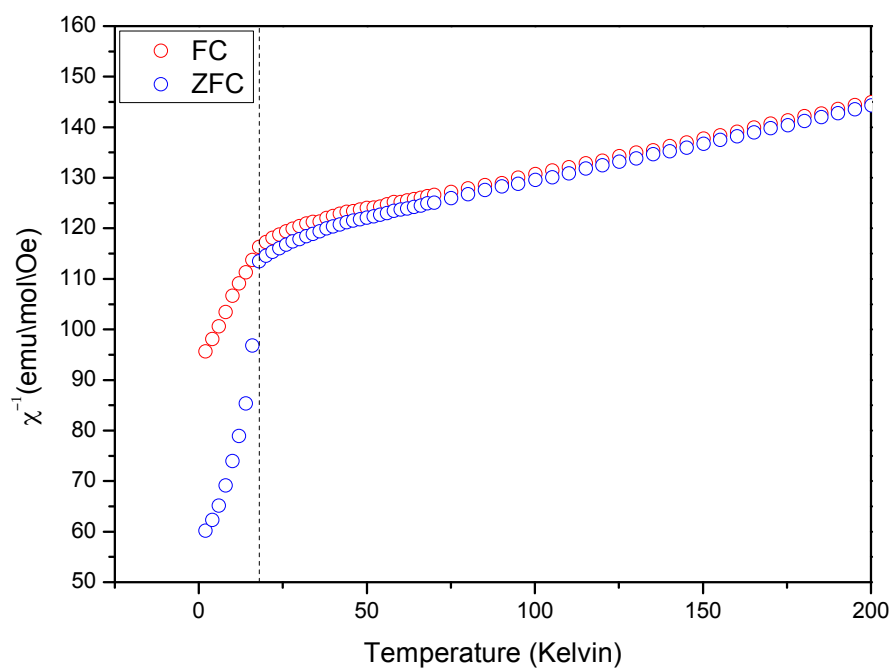


FIGURE 3.13: The field cooled and zero field cooled inverse magnetic susceptibility for a powder sample of pyr-FeF₃ between 200 K and 2 K measured in 100 Oe. The dashed line at 18 K indicates the temperature at which a cusp is observed in the susceptibility indicating a phase transition occurring at this temperature.

Powder Neutron Diffraction

The BT1 instrument, described in Section 2.4.1, was used to collect neutron diffraction data from a powdered sample of pyr-FeF₃ over a range of temperatures. Approximately 0.3 g of pyr-FeF₃ was loaded into a vanadium can and mounted onto a closed cycle refrigerator (CCR) reaching temperatures between 3 K - 325 K. A variety of monochromators were used, each will be specified for individual experiments. The specifications for each can be found in Table 2.1. Pyr-FeF₃ crystallises in the $Fd-3m$ space group, Fe³⁺ and F⁻ are positioned on the 16c and 48f sites respectively, with the 8b site left unoccupied. The structure can be described as consisting of corner-sharing FeF₆ octahedra with interconnecting three-dimensional tunnels. The iron is in a six-fold coordination environment with Fe-F bond distances of 1.914(4) Å. There are two Fe-F distances, 2.768(8) Å and 2.644(17) Å, significantly larger than the Fe³⁺-F bond distances in RbFe₂F₆ which range from 1.9098(14) Å to 1.9488(6) Å. The six-fold coordination of Fe in pyr-FeF₃ can be seen in Figure 3.14.

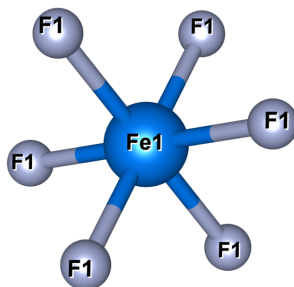


FIGURE 3.14: The 6-fold coordination environment of Fe in the pyr-FeF₃ structure.

To begin nuclear refinement, Rb was positioned on the 8b site refining close to zero, to ensure that all Rb had been removed. The occupancy was then fixed at zero as the refinement would crash with a chemical occupancy = 0 and no improvement to the fit was seen. The fluorine free parameter, (x, 1/8, 1/8), refined to 0.310(2) remaining the same within error throughout the temperature range. The three-dimensional crystal structure of pyr-FeF₃ is shown in Figure 3.8 displaying the corner sharing Fe⁺³F₆ octahedra with large windows.

The FULLPROF software⁷⁵ suite was used to refine the nuclear and magnetic structure of pyr-FeF₃ using the BT-1 neutron diffraction data, in collaboration with Pawel Zajdel (University of Silesia in Katowice). The Rietveld refinement process is previously described in Section 2.3.3. To begin the refinement the first step is to index the pattern,

initially the input parameters were of the pyr-FeF₃ space group ($Fd\bar{3}m$) and the unit cell dimensions which were known previously from the x-ray diffraction refinement at room temperature. For the powder sample of pyr-FeF₃, the nuclear structure and the background were then refined using the neutron data collected at room temperature in the paramagnetic state, Figure 3.15. Once the nuclear structure and the background are known these are normally kept fixed whilst refining the magnetic structure.

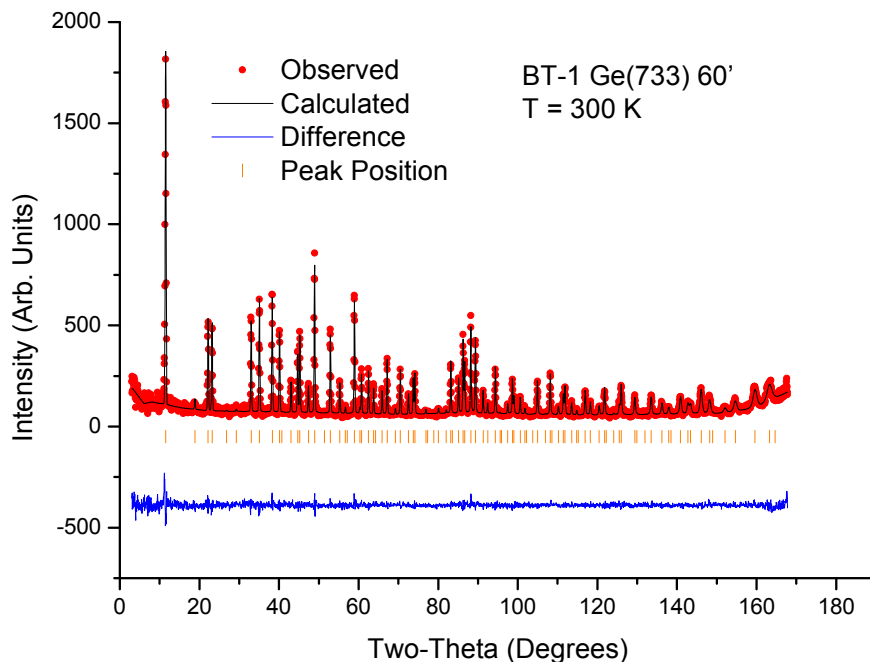


FIGURE 3.15: The Rietveld refined BT1 NPD data of pyr-FeF₃ collected at 300 K. Data points and calculated fit are displayed in the upper curve and the difference between the observed and calculated pattern is displayed in the lower curve. Sets of vertical tick marks represent the expected positions of nuclear reflections for pyr-FeF₃.

Figure 3.16 shows the magnetic evolution of pyr-FeF₃ for ten temperatures between 5 K and 25 K. No structural phase transitions are observed during low temperature neutron diffraction analysis, however, two nuclear diffraction peaks display magnetic contribution. These appear at $33.09\ 2\theta(220)$ and $52.06\ 2\theta(331)$ and increase in intensity as temperature decreases, in addition there is a single magnetic only contribution at $53.52\ 2\theta(-401)$.

To begin the magnetic refinement, the propagation vector and the symmetry of the magnetic cell must be known. For pyr-FeF₃, all the magnetic reflections can be indexed with the propagation vector $\mathbf{k} = (0,0,0)$ and one irreducible representation, Γ_3 . Representational analysis was used to find the symmetry of the magnetic cell using the software BasIreps in the FULLPROF software suite. Throughout the refinement of the magnetic

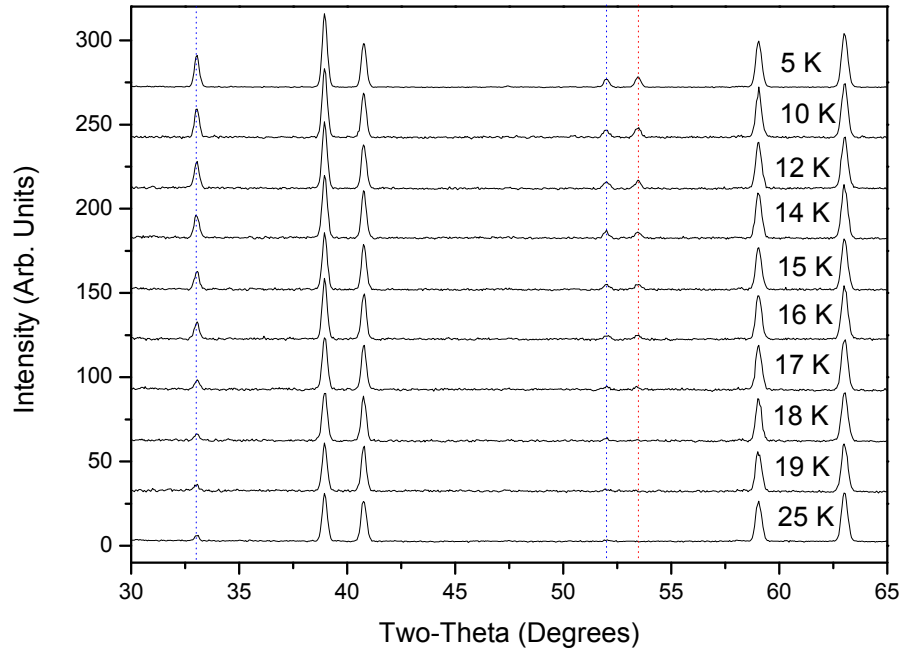
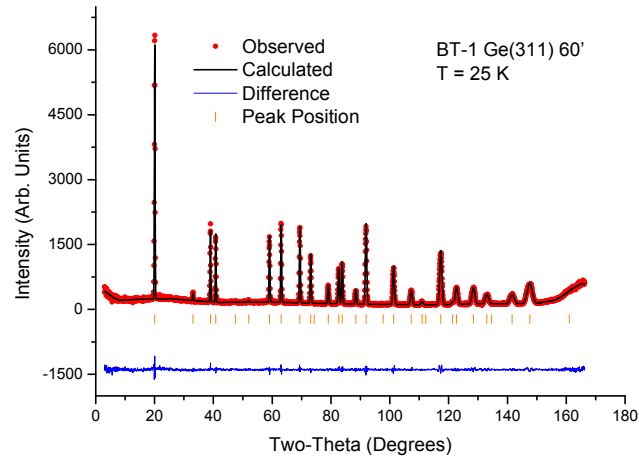


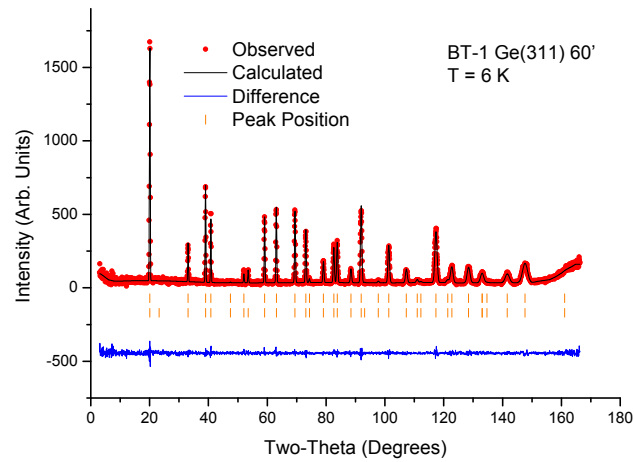
FIGURE 3.16: Temperature evolution of the magnetic scattering of pyr-FeF₃ (diffraction patterns have been offset along the y-axis for clarity) collected on the BT1 Neutron Powder Diffractometer. The blue dotted lines at 33.0867 2θ(220) and 52.0566 2θ(331) represent nuclear diffraction peaks which have magnetic contributions as temperature decreases. The red dotted line at 53.52 2θ(420) highlights the single magnetic only reflection.

unit cell, all possible combinations of symmetry operators provided by BasIreps were trialled, however, only one gave a sensible result fitting the experimental data well. The Rietveld refinement procedure can then be employed to solve details of the magnetic unit cell from the magnitude to the direction of spin of the magnetic moments that give best fit to the experimental data. The full model for the nuclear and magnetic structure of pyr-FeF₃ consists of many refined parameters that contribute to the overall goodness of fit. These include the background, scale factor, atomic positions, unit cell dimensions or lattice parameters, isotropic temperature corrections and the magnetic moment parameters.

Figure 3.17 shows the observed and calculated diffraction pattern for 25 K and 6 K, where there is no magnetic contribution at 25 K. The fit parameters are $\chi^2 = 0.969$, $R_p = 7.98\%$ and $R_{wp} = 10.4\%$ and $\chi^2 = 0.837$, $R_p = 7.95\%$ and $R_{wp} = 10.4\%$ for 25 K and 6 K respectively. The agreement factors for the nuclear and magnetic phases shown in Figure 3.17(b) are $R_{nuc} = 1.67\%$ and $R_{mag} = 5.24\%$.



(a)



(b)

FIGURE 3.17: Fitted diffraction data for pyr- FeF_3 using powder neutron diffraction collected on the BT1 diffractometer at (a) 25 K and (b) 6 K. Data points and calculated fit are displayed in the upper curve and the difference between the observed and calculated pattern is displayed in the lower curve. Sets of vertical tick marks (from top to bottom) represent the expected positions of nuclear reflections for pyr- FeF_3 and the expected magnetic reflections for pyr- FeF_3 respectively. Where there is only one set of vertical tick marks, this represents the nuclear diffraction pattern without magnetic contribution. The fit parameters are $\chi^2 = 0.969$, $R_p = 7.98\%$ and $R_{wp} = 10.4\%$ and $\chi^2 = 0.837$, $R_p = 7.95\%$ and $R_{wp} = 10.4\%$ for 25 K and 6 K respectively. The agreement factors for the nuclear and magnetic phases shown in (b) are $R_{nuc} = 1.67\%$ and $R_{mag} = 5.24\%$.

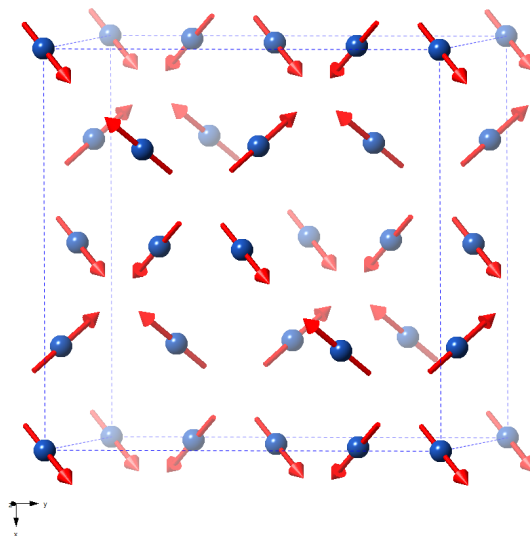


FIGURE 3.18: The magnetic structure of ptr-FeF₃ at 6 K determined from Rietveld refinement performed on neutron scattering data collected on the BT1 diffractometer. The magnetic structure can be described as two inter-penetrating networks of tetrahedra with four iron spins aligned towards the center of the tetrahedron in all-in or all-out configurations.

The proposed magnetic structure of pyr-FeF₃ that appears below 16 K is shown in Figure 3.18. The magnetic structure can be described as two inter-penetrating networks of tetrahedra with four iron spins aligned towards the center of the tetrahedron in all-in or all-out configurations. The magnitude of the ordered magnetic moment, $3.32(5) \mu_B$, is lower than expected for the free Fe³⁺ ion in a high-spin configuration ($5 \mu_B$). This is consistent with the remnant diffuse scattering observed around the (111) peak, displayed in Figure 3.19, as a result of magnetic frustration. This suggests that not all moments become long range ordered.

A series of variable temperature scans were performed to above the temperature of long range ordering in order to obtain the order parameter. The diffraction patterns were analysed using the same model and the refined values of the Fe moments are presented in Figure 3.20. It is only possible to fit the order parameter in the temperature region of 11 K - 17 K as the curve deviates above and below this region. The critical exponent obtained was found to be $0.326(8)$, which is close to the value for a 3D Ising model (0.326). For comparison an area plot of the 420 magnetic only reflection was fit, this is displayed in Figure 3.21.

In addition, powder neutron diffraction experiments were performed at 25 K and 5 K with and without D₂ absorption. Pyr-FeF₃ was measured at both temperatures before being held for 4 h in an atmosphere of D₂ to prove porosity further. Initially all four diffraction patterns were refined without D₂, the magnetic structure described above was added to the diffraction pattern at 5 K. D₂ was added on the 8b position which improved the

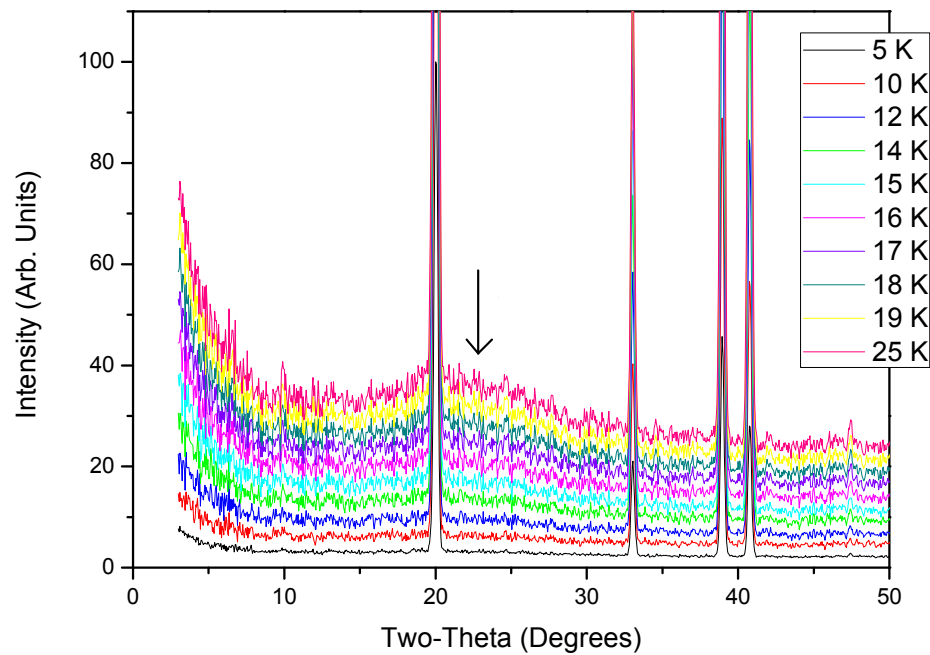


FIGURE 3.19: Pyr-FeF₃ diffuse scattering as a function of temperature where ‘x’ marks the low angle diffuse scattering.

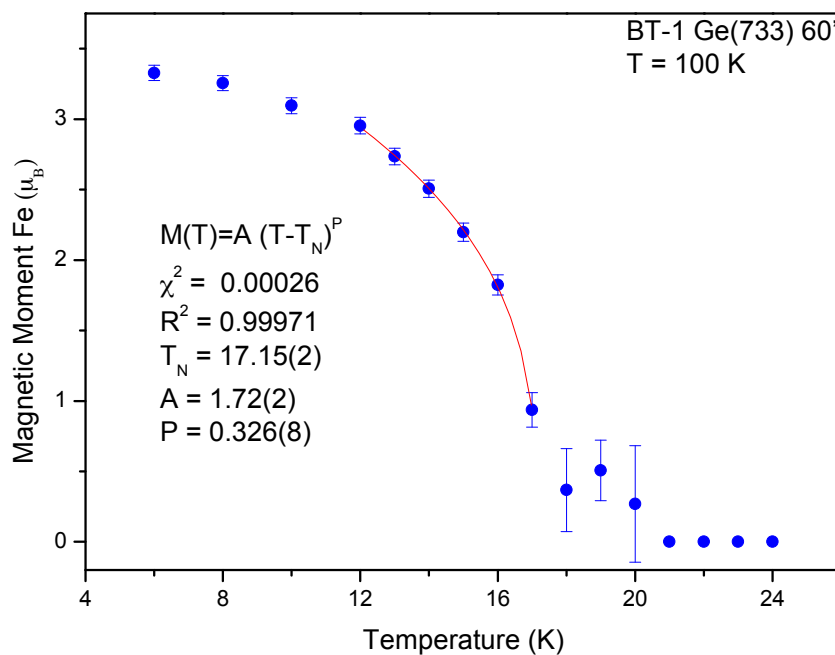


FIGURE 3.20: Temperature evolution of ordered moment in pyr-FeF₃. It is only possible to fit the order parameter in the temperature region of 11 K - 17 K as the curve deviates above and below this region. The critical exponent obtained was found to be 0.326(8), which is close to the value for a 2D Ising model (0.31).

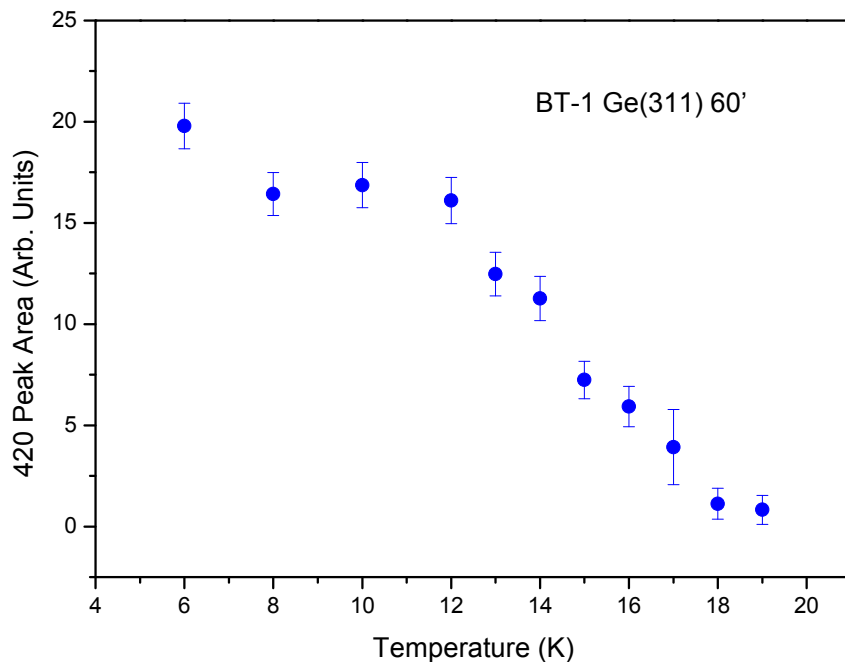
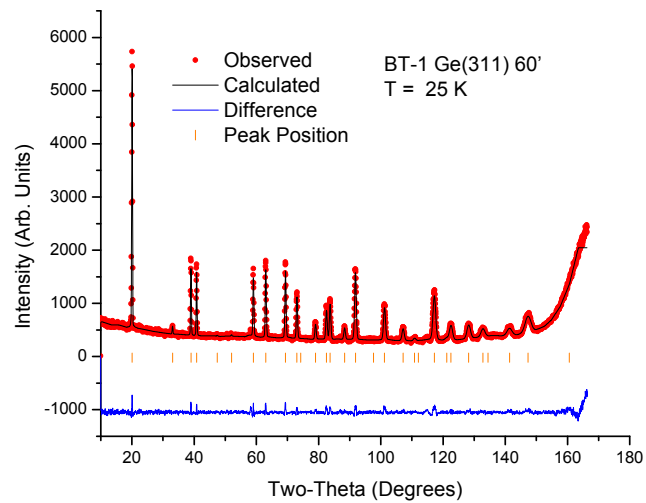
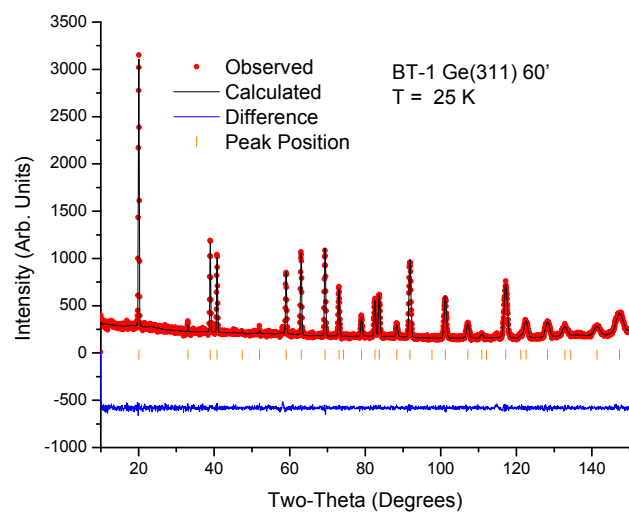


FIGURE 3.21: The fitted area of the 420 magnetic only reflection as a function of temperature.

goodness of fit. Lattice parameters for pyr-FeF₃ at 25 K and 5 K refined to 10.333(1) Å and 10.327(1) Å respectively with no difference after D₂ absorption (10.3337(9) Å and 10.328(1) Å). The magnetic moment of pyr-FeF₃ and pyr-FeF₃·XD₂ at 5 K remained consistent at 2.3(6) μ_B and 2.6(5) μ_B. D₂ occupancy refined to 0.05(4) and 0.04(4) with B_{iso} of 6(1) and 6(2) at 25 K and 5 K respectively, however, both of these values are within error and further studies would need to be conducted to confirm the presents of D₂. The large thermal parameters support the large rattling effect of the three dimensional tunnels and the true porosity of pyr-FeF₃. In comparison to the gas absorption measurements mentioned previously, the absorption of D₂ is significantly reduced, this can be explained by the low kinetic energy of the absorption. The rate of absorption is low meaning that pyr-FeF₃ needs to be in an atmosphere of D₂ for a significant time period. Gas absorption measurements were taken after being held for 48 h in comparison to 4 h for neutron diffraction measurements. The the fitted diffraction data for pyr-FeF₃ and pyr-FeF₃·XD₂ at 25 K and 5 K are shown in Figure 3.22 and Figure 3.23, respectively.

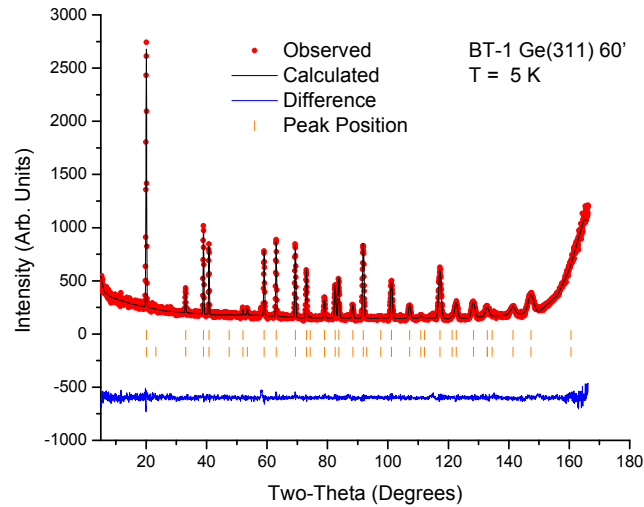


(a)

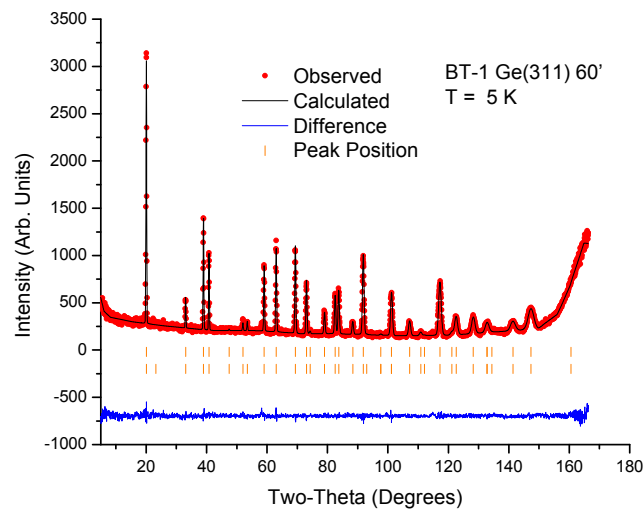


(b)

FIGURE 3.22: Fitted diffraction data for pyr-FeF₃ using powder neutron diffraction collected on the BT1 diffractometer at (a) 25 K and pyr-FeF₃·0.05(4)D₂ at (b) 25 K. Data points and calculated fit are displayed in the upper curve and the difference between the observed and calculated pattern is displayed in the lower curve. Sets of vertical tick marks (from top to bottom) represent the expected positions of nuclear reflections for pyr-FeF₃ and pyr-FeF₃·0.05(4)D₂.



(a)



(b)

FIGURE 3.23: Fitted diffraction data pyr-FeF₃ using powder neutron diffraction collected on the BT1 diffractometer at (a) 5 K and pyr-FeF₃·0.04(5)D₂ at (b) 5 K. Data points and calculated fit are displayed in the upper curve and the difference between the observed and calculated pattern is displayed in the lower curve. Sets of vertical tick marks (from top to bottom) represent the expected positions of nuclear reflections for pyr-FeF₃ and pyr-FeF₃·0.04(4)D₂. The lower set of tick marks represent the expected magnetic reflections.

3.3 The synthetic route

To understand the route taken during synthesis of pyr-FeF₃ several samples were synthesised using the method described in Section 3.2.2 varying the Rb occupancy with Br₂ concentration and reaction times. Table 3.3 displays the variable parameters during each initial syntheses.

Sample	RbFe ₂ F ₆	Br	Time Stirred
1	≈1 g	0.09 cm ³	88 h
2	≈1 g	0.9 cm ³	80 h
3	≈0.5 g	2.1 cm ³	40 h
4	≈0.5 g	4.1 cm ³	44 h

TABLE 3.3: Synthesis parameters of intermediate samples between RbFe₂F₆ and pyr-FeF₃.

3.3.1 Structural Properties

Each material was characterised using the WISH Neutron Powder Diffractometer, described in Section 2.4.2. Table 3.4 shows the results from NPD Rietveld refinements at the highest temperature measured. Initially, the nuclear structure was refined using the starting point of RbFe₂F₆ taken from the ICSD,¹³ the pyr-FeF₃ structure was then added with a rubidium atom positioned on the 8b site. During the refinement the occupancy of this rubidium site was varied, however, over a series of temperatures, the value differed dramatically. As a result the rubidium occupancy was fixed for all refinements in correlation with other parameters. Varying the occupancy of the rubidium from the ideal model of the orthorhombic phase from 1.0 gave a refined value of 0.99(1) with no improvement to the goodness of fit factors, this is consistent with previous studies on RbFe₂F₆¹³ and this parameter was fixed in all subsequent refinements. Sample 1 and 2 consist of an orthorhombic and cubic phase, where Samples 3 and 4 consist only of the cubic phase.

Sample 1

Sample 1 consists of two phases, Sample 1_{orth}, an orthorhombic RbFe₂F₆ phase (50.3(5) %) and Sample 1_{cub}, a pyr-FeF₃ phase (49.7(7) %). Figure 3.24 shows the fitted WISH neutron diffraction pattern at 300 K from detector bank 2. The experimental data collected are shown in red and the refined fit in black. The two sets of tick marks, top and bottom, correspond to Sample 1_{orth} and Sample 1_{cub}, respectively. The fit parameters of the Rietveld refinement for Sample 1_{orth} are $R_p = 6.22\%$ and $R_{wp} = 6.08\%$, for bank 2.

Sample	1	2	3	4
Temperature (K)	300	20	300	20
RbFe ₂ F ₆ Phase (%)	49.7(7)	12.1(8)	-	-
Lattice a (Å)	7.03(3)	6.9(1)	-	-
Lattice b (Å)	7.45(3)	7.4(1)	-	-
Lattice c (Å)	10.18(5)	10.1(1)	-	-
Rb _{1-x} FeF ₃ Phase (%)	50.3(5)	87.9(1)	100	100
Lattice a (Å)	10.39(1)	10.37(1)	10.37(1)	10.33(2)
Rb Occupancy	0.27	0.23	0.18	0.11
Average Rb Occupancy	0.63(2)	0.32(3)	0.18	0.11

TABLE 3.4: Rietveld refinement results of WISH NP Diffractometer for samples 1 - 4 at the highest temperature recorded. Sample 1 and 2 consist of two phases in different ratios, an orthorhombic RbFe₂F₆ phase and a cubic Rb_{1-x}FeF₃ phase. Whilst Samples 3 and 4 only consist of the cubic Rb_{1-x}FeF₃ with differing Rb occupancies.

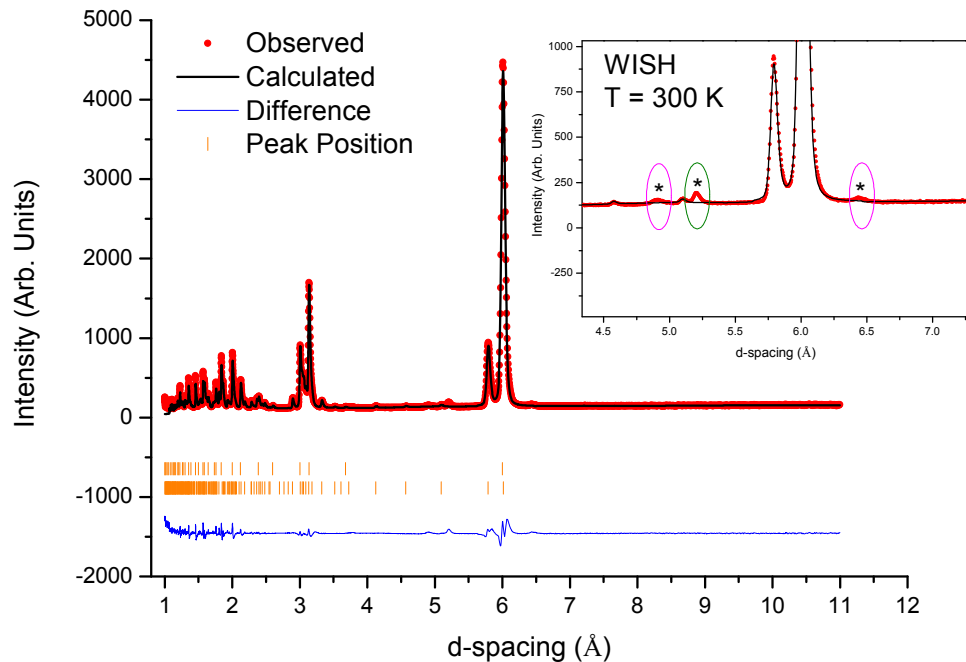


FIGURE 3.24: Fitted diffraction profile for Sample 1 Wish NPD data collected at 300 K. Data points and calculated fit are displayed in the upper curve and the difference between the observed and calculated pattern is displayed in the lower curve. Sets of vertical tick marks (from top to bottom) represent the expected positions of nuclear reflections for Sample 1_{orth} and the expected nuclear reflections for Sample 1_{cub}, respectively. The inset shows the presence of three unrefined peaks, both peaks (highlighted in pink) at 4.86 Å and 6.46 Å are suspected to be from the magnetite structure, Fe₃O₄. The peak at 5.18 Å (highlighted in green) is suspected to be an iron oxide impurity.

The inset in Figure 3.24 shows the presence of three unrefined peaks, both peaks (highlighted in pink) at 4.86 Å and 6.46 Å correspond to the magnetite structure, Fe₃O₄ which is present as a small impurity. This is observed in Figure ??; magnetite is a mixed valence ferrite which forms an inverse spinel structure with Fe²⁺ and Fe³⁺ ions randomly arranged at the octahedral sites and all tetrahedral sites being occupied by ferrous ions. Fe₃O₄ is a ferrimagnet with a Curie temperature of 858 K where the moments inside the A and B sublattice are ferromagnetically aligned and the two sublattices are antiferromagnetic with respect to one another, giving an overall moment of 4.1 μ_B. At 120 K, Fe₃O₄ undergoes a transition better known as the Verwey transition. This transition can be seen in the SQUID magnetometry measurements, taken of Sample 1, displayed in Figure 3.25 where there is a feature in the data at ≈ 120 K, consistent with the Verwey transition associated with Fe₃O₄.

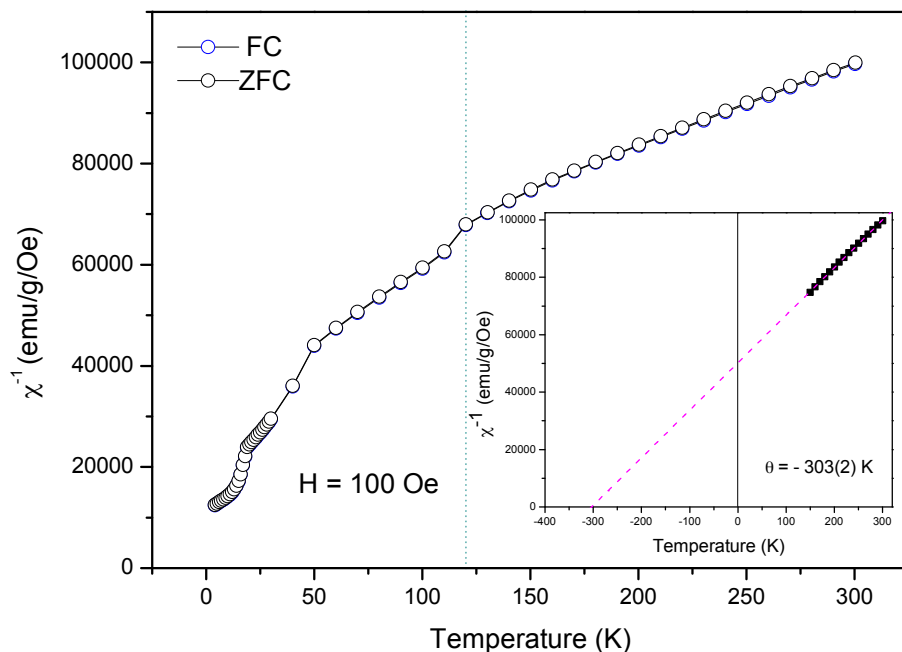


FIGURE 3.25: Zero Field Cooled and Field Cooled SQUID magnetometry data of Sample 1 in a field of 100 Oe. The Verwey transition is displayed as a 'bump' at 120 K.

The peak at 5.18 Å (highlighted in green), inset Figure 3.24, is suspected to be an iron oxide impurity. This nuclear peak has visible magnetic contributions from temperatures below 15 K shown in Figure 3.26.

Table 3.4 shows the refined structural properties of Sample 1. Sample 1_{orth} makes up 50.3(5)% of the overall material. The Rb occupancy relating to Sample 1_{cub} refined to 0.2(1). Figure 3.27 shows Sample 1_{orth} structure along the ac, (a), and bc, (b), plane and Sample 1_{cub}, (c), both of which contribute to Sample 1.

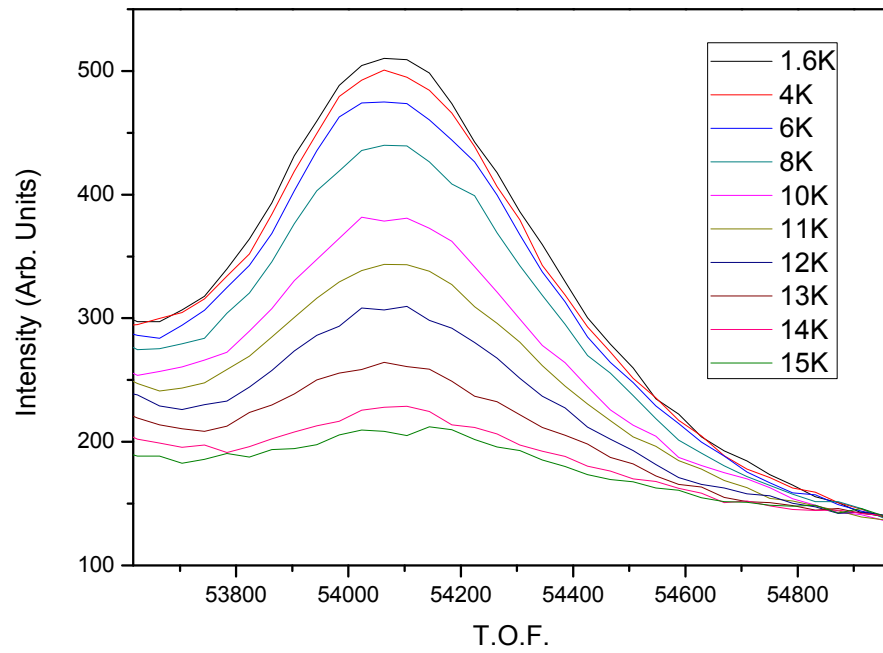


FIGURE 3.26: The magnetic evolution of the impurity peak for Sample 1 at 5.18 Å.

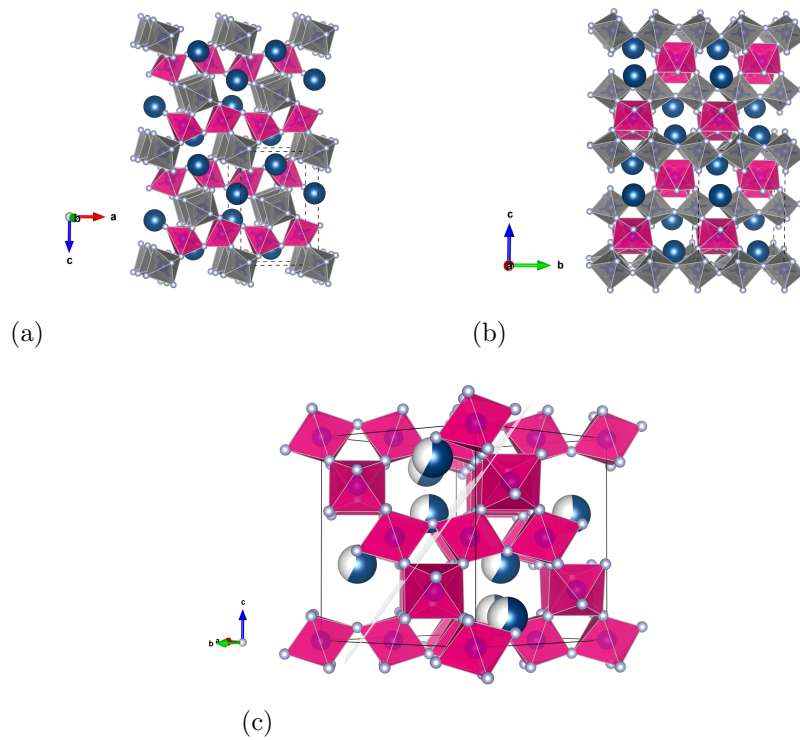


FIGURE 3.27: Sample 1_{orth} along the ac, (a), and bc, (b), plane and Sample 1_{cub}, (c), both of which are present in the samples.

From the refinement of Sample 1_{orth}, the structure is consistent with the sample previously described in the literature and discussed earlier.¹³ Figure 3.28 shows the 10-fold coordination environment of Rb and the 6-fold coordination environment of both Fe atoms. Table 3.5 highlights the bond distances in Sample 1_{orth}, where the Fe²⁺-F bond distances are in the range of 1.957(10) Å-2.115(9) Å and the Fe³⁺-F bond distances range between 1.900(7) Å-1.932(6) Å, both in a 6-fold coordination environment. The Rb cation is in a 10-fold coordination environment with Rb-F bond distances ranging from 2.965(11) Å-3.242(9) Å. These bond distances are consistent with the reported structure of RbFe₂F₆.¹³

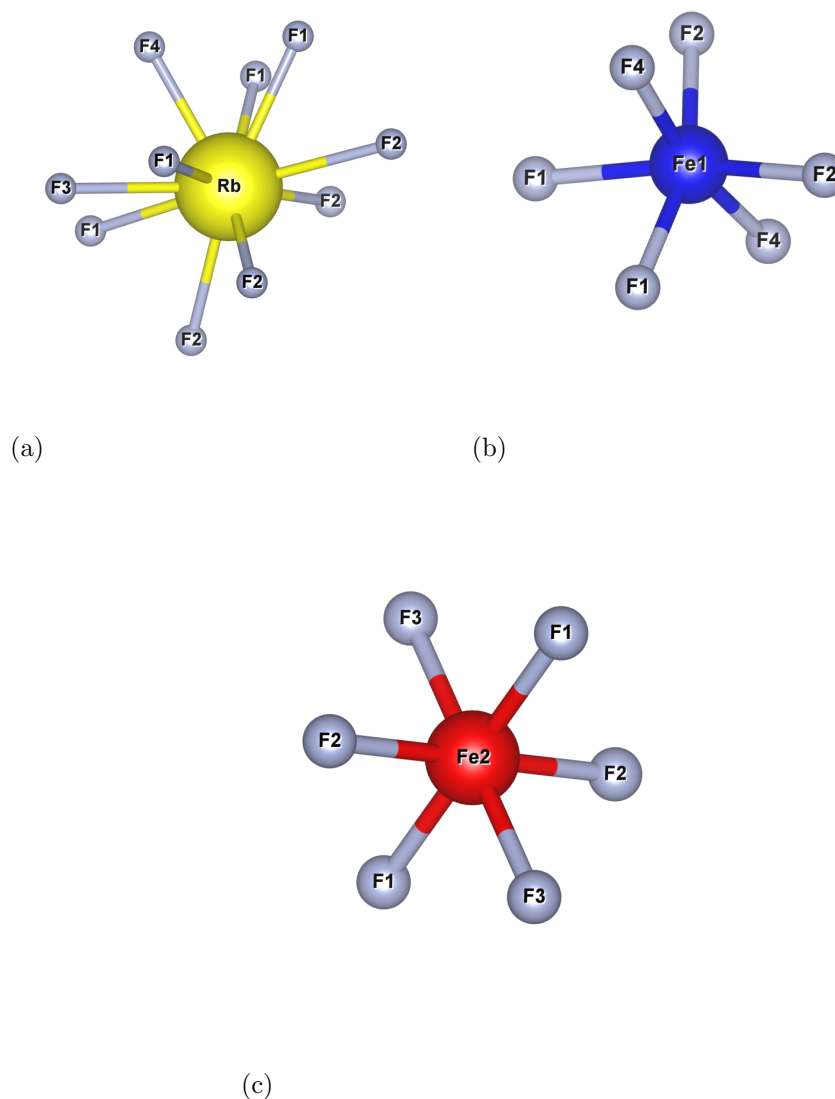


FIGURE 3.28: The 10-fold coordination environment of Rb (3.28a) and the 6-fold coordination environment of Fe²⁺ (3.28b), shown in blue, and Fe³⁺ (3.28c), shown in red, obtained from rietveld refinement of Sample 1_{orth}.

Bond	Distance Å	Bond	Distance Å
Rb - F(1)	$3.079(8) \times 2$	Fe(1) - F(1)	$2.090(9) \times 2$
Rb - F(1)	$3.058(9) \times 2$	Fe(1) - F(2)	$2.115(9) \times 2$
Rb - F(2)	$3.242(9) \times 2$	Fe(1) - F(4)	1.967(10)
Rb - F(2)	$3.102(9) \times 2$	Fe(1) - F(4)	1.957(10)
Rb - F(3)	3.232(12)	Fe(2) - F(1)	$1.932(6) \times 2$
Rb - F(4)	2.965(11)	Fe(2) - F(2)	$1.900(7) \times 2$
		Fe(2) - F(3)	$1.959(3) \times 2$
		Fe(1) - Fe(2)	$3.684(5) \times 2$
		Fe(1) - Fe(2)	$3.582(6) \times 2$
		Fe(1) - Fe(1)	$3.5329(12) \times 2$
		Fe(2) - Fe(2)	$3.72630(16) \times 2$

TABLE 3.5: Bond distances form Sample 1_{orth}.

Sample 2

Sample 2 has very a similar structure to that of Sample 1, however, the ratio of orthorhombic to cubic phase differs. The orthorhombic phase, Sample 2_{orth}, contributes to 12.1(8) % whereas the cubic phase, Sample 2_{cub}, is more dominant at 87.9(1) %. It is worth noting the structure of Sample 2_{cub} as Rb_{0.23(6)}FeF₃ and the Sample 2_{orth} remains at RbFe₂F₆, indicating that once Rb starts to be removed from the original *Pnma* orthorhombic phase a structural phase transition is made to pyr-*Fd-3m* cubic phase. This would suggest that RbFe₂F₆ is only stable with a full Rb occupancy, similar to Sample 1. The same three impurity peaks are also present in Sample 2 as seen in Sample 1. Figure 3.29 shows the fitted diffraction data for Sample 2 from powder neutron diffraction data collected on the WISH diffractometer, bank 2, at 20 K, (highest temperature analysed) displaying only nuclear reflections. Similar to Sample 1 the peaks at 4.86 Å and 6.46 Å are suspected to be from the magnetite structure, Fe₃O₄ and the peak at 5.18 Å is suspected to be an iron oxide impurity.

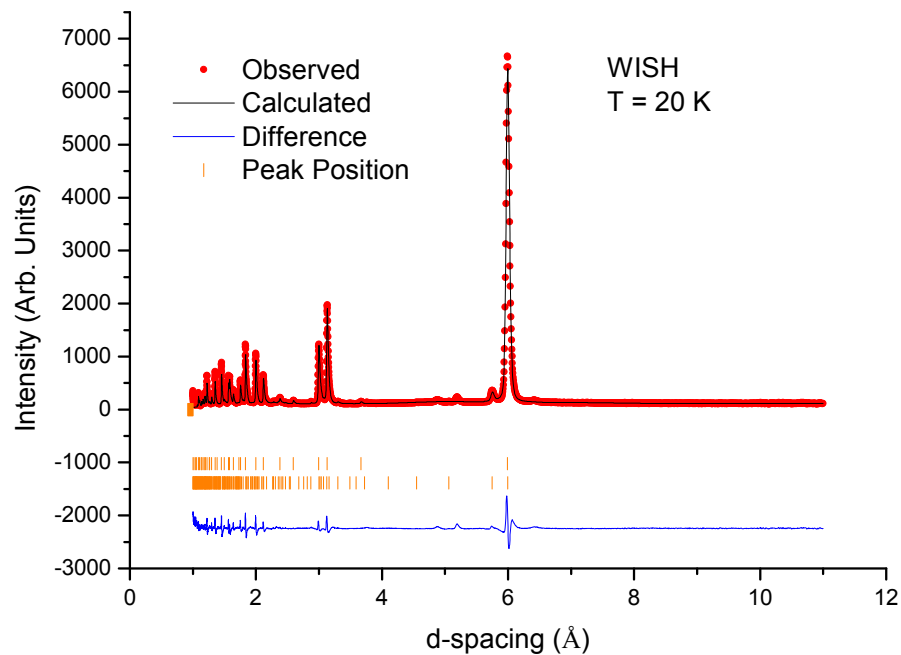


FIGURE 3.29: Fitted WISH NPD data collected at 20 K for Sample 2. Data points and calculated fit are displayed in the upper curve and the difference between the observed and calculated pattern is displayed in the lower curve. Sets of vertical tick marks (from top to bottom) represent the expected positions of nuclear reflections for Sample 2_{orth} and the expected nuclear reflections for Sample 2_{cub} respectively. Three unrefined peaks are present, similar to Sample 1, where both peaks at 4.86 Å and 6.46 Å are suspected to be from the magnetite structure, Fe₃O₄. The peak at 5.18 Å is suspected to be an iron oxide impurity.

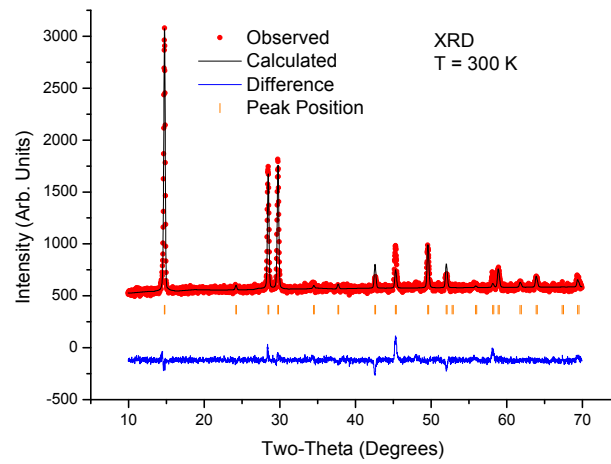
Sample 3

After gravitational filtration, Sample 3 produced two distinct products, one a dark brown colour, Sample 3a, and the other a light pale green colour, Sample 3b. These products were separated from one another by hand and analysed individually. Figure 3.30 shows the fitted X-ray diffraction data collected for both products. The refinement was initially started by adding the RbFe_2F_6 phase with the scale refining to zero, indicating that the orthorhombic RbFe_2F_6 phase was not present. A refinement was performed using only the cubic pyrochlore phase. Sample 3a refined to $\text{Rb}_{0.236(8)}\text{FeF}_3$ with lattice parameter $a = 10.39(2)$ Å and $\alpha = \beta = \gamma$, however, the Rb cation has two distinct crystallographic sites, Table 3.6 illustrates these data. These are the 16d and 48f sites, and due to this Sample 3b was focused on. For Sample 3b, when Rb occupancy was refined it was unstable and an occupancy of 0.18 was set throughout each refinement, giving an overall formula of $\text{Rb}_{0.18}\text{FeF}_3$ and lattice parameter $a = 10.40(2)$ Å.

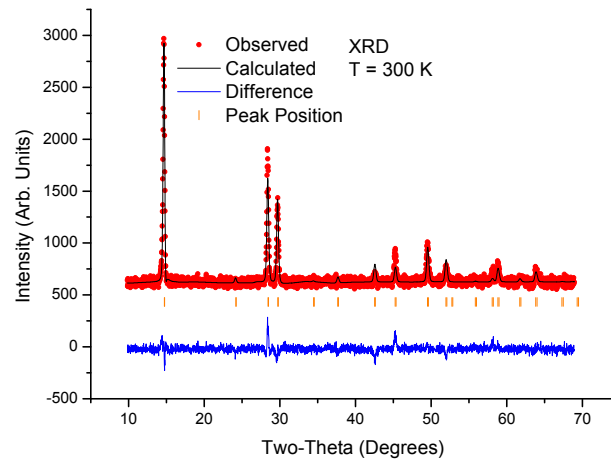
Atom	x	y	z	Occupancy
F	0.322(8)	0.125	0.125	3
Fe	0	0	0	1
Rb(1)	0	0.625	0.125	0.18(4)
Rb(2)	0	0.75	0.25	0.05(2)

TABLE 3.6: The crystallographic and occupancy refined values for Sample 3a displaying two Rb crystallographic sites.

$\text{Rb}_{0.18}\text{FeF}_3$, now referred to as Sample $3b_{cub}$, was chosen for comparative analysis on WISH due to the single Rb crystallographic position. Figure 3.31 displays the fitted data for Sample $3b_{cub}$ from powder neutron diffraction data collected on the WISH diffractometer, bank 2, at 300 K, displaying only nuclear reflections. The lattice parameter at 300 K refined to $a = 10.371(1)$ Å with $\alpha = \beta = \gamma$ and Figure 3.32 displays the lattice parameter as a function of temperature. It is worth noting that impurity peaks observed in Sample 1 and Sample 2 are still present.



(a)



(b)

FIGURE 3.30: Fitted diffraction profile for Sample 3a, $\text{Rb}_{0.236(8)}\text{FeF}_3$ and Sample 3b, $\text{Rb}_{0.18}\text{FeF}_3$, X-ray diffraction data collected at 300 K respectively. Data points and calculated fit are displayed in the upper curve and the difference between the observed and calculated pattern is displayed in the lower curve. The set of vertical tick marks represent the expected positions of nuclear reflections for $\text{Rb}_{0.236(8)}\text{FeF}_3$ and $\text{Rb}_{0.18}\text{FeF}_3$. There is no evidence of impurity peaks.

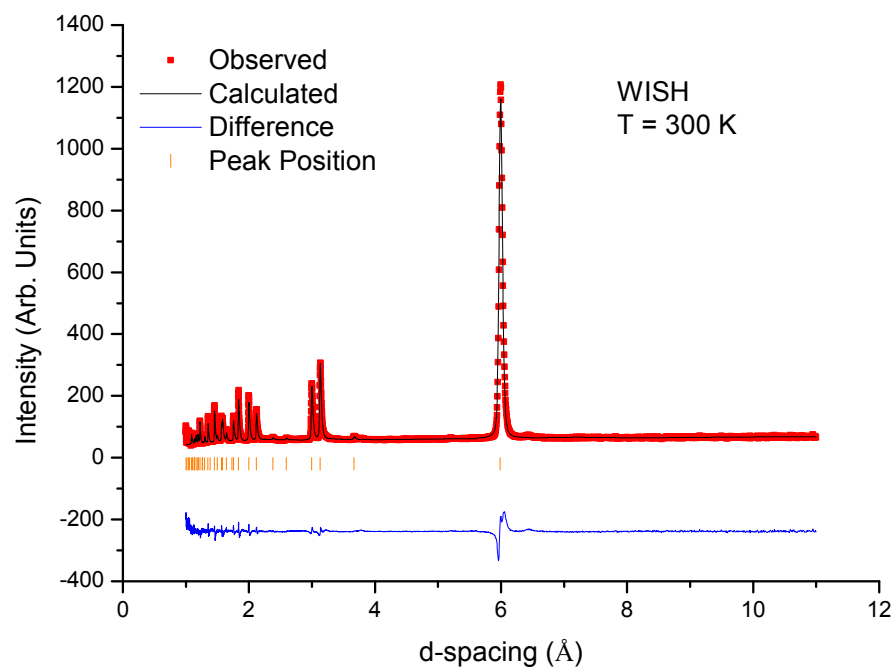


FIGURE 3.31: Fitted diffraction profiles for Sample $3b_{cub}$ Wish NPD data collected at 300 K from bank 2. Data points and calculated fit are displayed in the upper curve and the difference between the observed and calculated pattern is displayed in the lower curve. Sets of vertical tick marks represent the expected positions of nuclear reflections for $Rb_{0.18}FeF_3$.

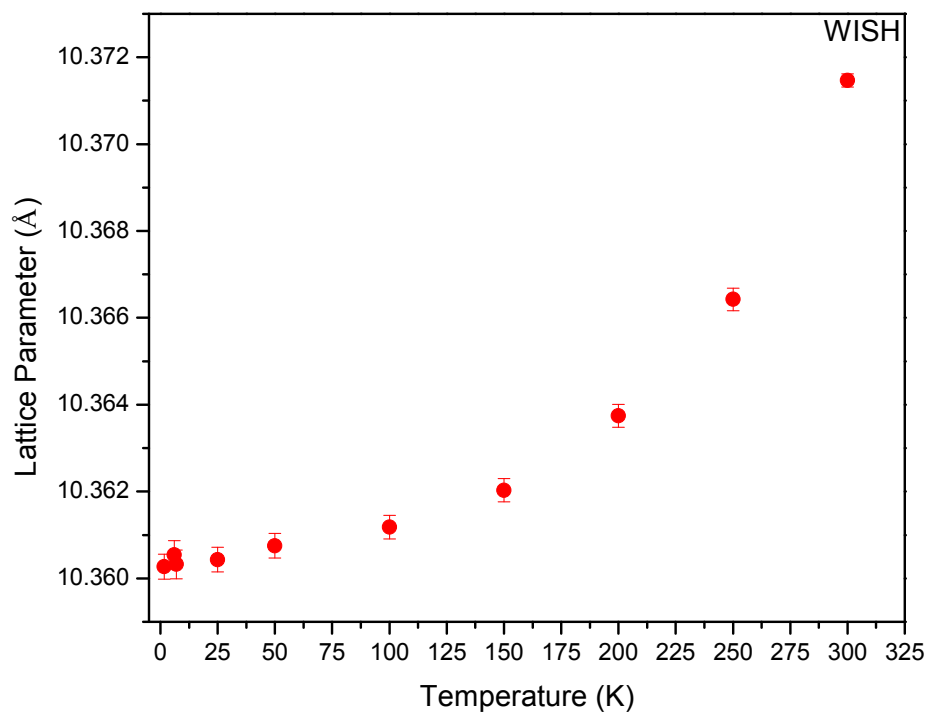


FIGURE 3.32: Sample 3b_{cub} lattice parameter as a function of temperature, decreasing until approximately 25 K where a plateau is seen.

Sample 4

The nuclear structure of Sample 4 was refined initially with RbFe_2F_6 , however, as expected this phase was not present, a refinement was done only with pyr- FeF_3 phase. Similarly to Sample 1, 2, and 3, when the Rb occupancy was varied a difference was seen over the temperature range analysed and was then fixed at 0.11 giving the overall structure as $\text{Rb}_{0.11}\text{FeF}_3$ for Sample 4_{cub}. This study would suggest that pyr- FeF_3 phase has a Rb saturation of ≈ 0.27 , however, due to the complicated synthesis procedure, obtaining an exact saturation value was not achieved. Impurity peaks are also observed in Sample 4_{cub}, however, the magnetic reflection at 5.18 \AA , previously discussed with reference to Figure 3.24, is no longer present indicating that the only impurity phase present is that of Fe_3O_4 . Figure 3.33 displays the fitted diffraction data for Sample 4_{cub} at 20 K (highest temperature measured) with a lattice parameter of $a = 10.333(2) \text{ \AA}$ and $\alpha = \beta = \gamma$. Figure 3.34 shows the lattice parameter variation as a function of temperature.

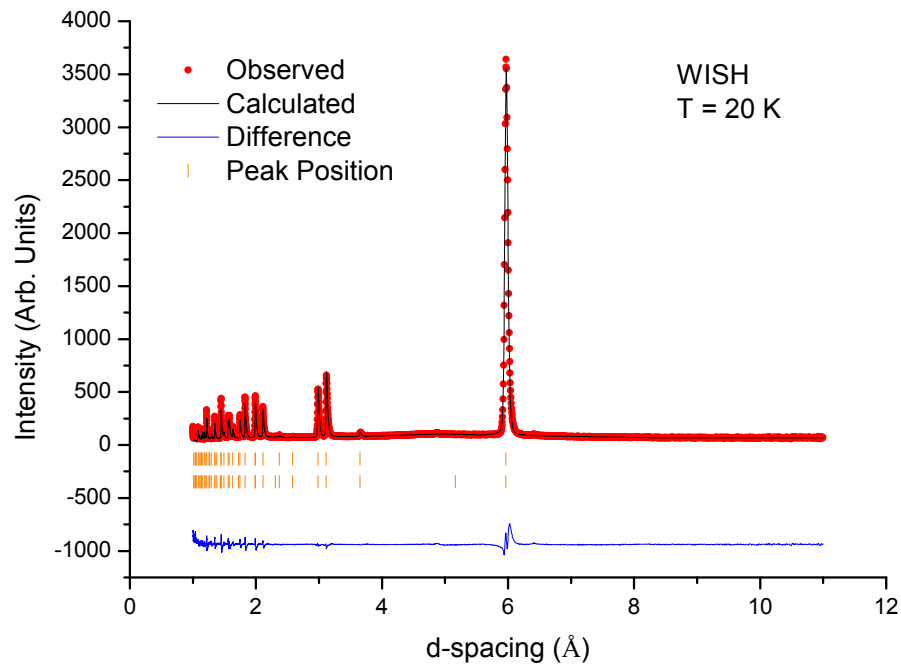
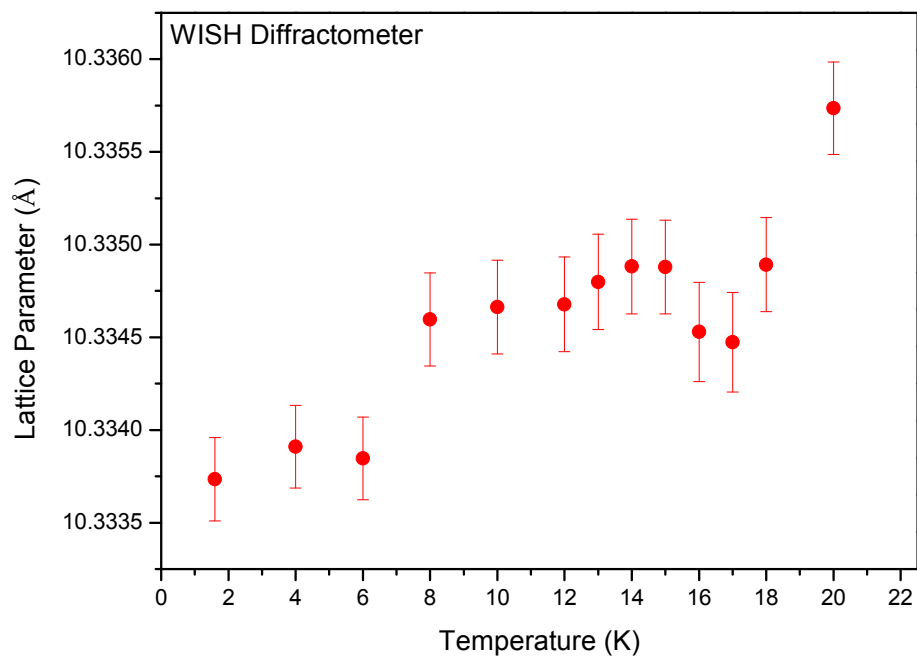


FIGURE 3.33: Fitted diffraction profile for Sample 4_{cub} Wish NPD data collected at 20 K (highest temperature measured) from bank 2. Data points and calculated fit are displayed in the upper curve and the difference between the observed and calculated pattern is displayed in the lower curve. Sets of vertical tick marks represent the expected positions of nuclear reflections for $\text{Rb}_{0.11}\text{FeF}_3$.

FIGURE 3.34: The lattice parameter as a function of temperature for Sample 4_{cub}.

3.3.2 Iron Oxidation State

Three samples were synthesised to determine the oxidation state of Fe at different points when only the single cubic phase was present. These samples were synthesised using the procedure specified in Section 3.3 varying the rubidium concentration: Sample 5_{cub}, Rb_{0.197(5)}FeF₃, Sample 6_{cub}, Rb_{0.166(5)}FeF₃ and Sample 7_{cub}, Rb_{0.14(6)}FeF₃. Table 3.7 displays the synthesis parameters for each sample.

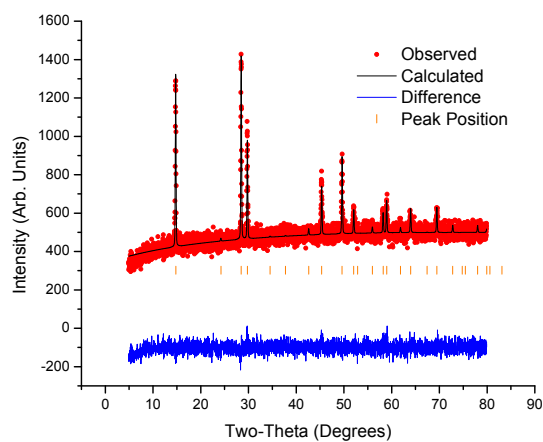
Sample	RbFe ₂ F ₆	Br	Time Stirred
5	≈1 g	1.9 cm ³	26 h
6	≈1 g	2.6 cm ³	18 h
7	≈1 g	3.4 cm ³	43 h

TABLE 3.7: Synthesis parameters of intermediate samples between RbFe₂F₆ and pyr-FeF₃.

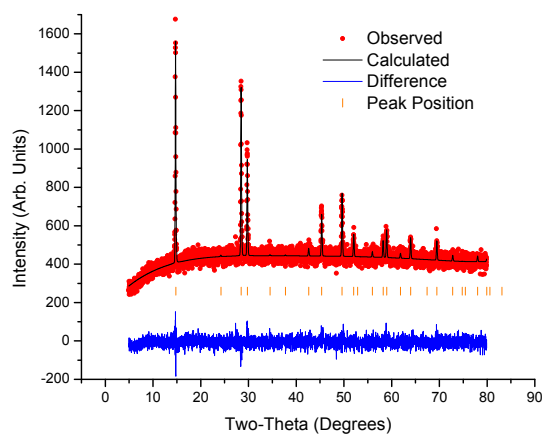
Each sample was characterised using x-ray diffraction, the Rietveld refined diffraction patterns are shown in Figure 3.35 and each have been fitted to a *Fd-3m* space group with lattice parameters 10.38(1) Å, 10.33(1) Å and 10.32(1) Å respectively.

Mössbauer Spectroscopy

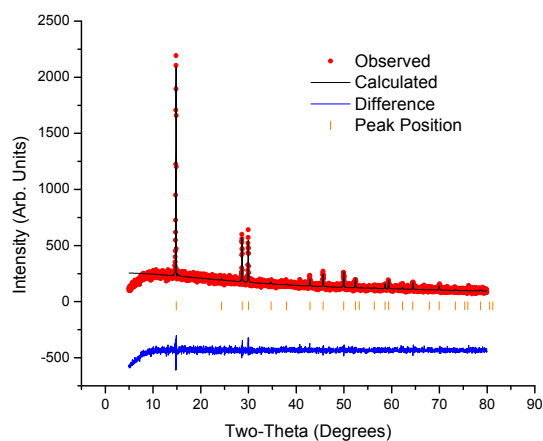
Mössbauer spectroscopy was used to determine the oxidation state of Fe in all three samples. Figure 3.36 displays the Mössbauer absorption spectra for Sample 5_{cub}, Sample 6_{cub} and Sample 7_{cub} collected at 80 K. The Mössbauer absorption spectrum of Sample 5_{cub} has a fit to Fe³⁺ giving an isomer shift of $\delta = 0.572(3)$ mm/s and a quadrupole splitting of $\Delta E_Q = 0.547(5)$ mm/s and Fe²⁺ gives an isomer shift of $\delta = 1.467(6)$ mm/s and a quadrupole splitting of $\Delta E_Q = 2.853(13)$ mm/s. Sample 6_{cub} has a fit to Fe³⁺ giving an isomer shift of $\delta = 0.559(4)$ mm/s and a quadrupole splitting of $\Delta E_Q = 0.516(6)$ mm/s and Fe²⁺ gives an isomer shift of $\delta = 1.472(7)$ mm/s and a quadrupole splitting of $\Delta E_Q = 2.782(12)$ mm/s and Sample 7_{cub} has a fit to Fe³⁺ giving an isomer shift of $\delta = 0.565(2)$ mm/s and a quadrupole splitting of $\Delta E_Q = 0.260(4)$ mm/s with no Fe²⁺ present. Referencing the peak area, the ratio between Fe²⁺ and Fe³⁺ sites are similar for Sample 5_{cub} and Sample 6_{cub}, 79(1) % and 83(1) % for Fe³⁺ and 21(1) % and 17(1) % for Fe²⁺ respectively. The increase in Fe³⁺ occupancy is expected as the reaction has been tailored to oxidise more Fe²⁺. Sample 7_{cub} is fully oxidised from Fe²⁺ to Fe³⁺, suggesting that between a Rb occupancy of approximately 0.16 and 0.01 all Fe ions are normally ³⁺. This is not directly comparable to the proposed composition by XRD experiments due to the low signal to noise ratio.



(a)



(b)



(c)

FIGURE 3.35: Rietveld refined x-ray diffraction pattern for (a) Sample 5_{cub}, Rb_{0.197(5)}FeF₃, (b) Sample 6_{cub}, Rb_{0.166(5)}FeF₃ and (c) Sample 7_{cub}, Rb_{0.14(6)}FeF₃.

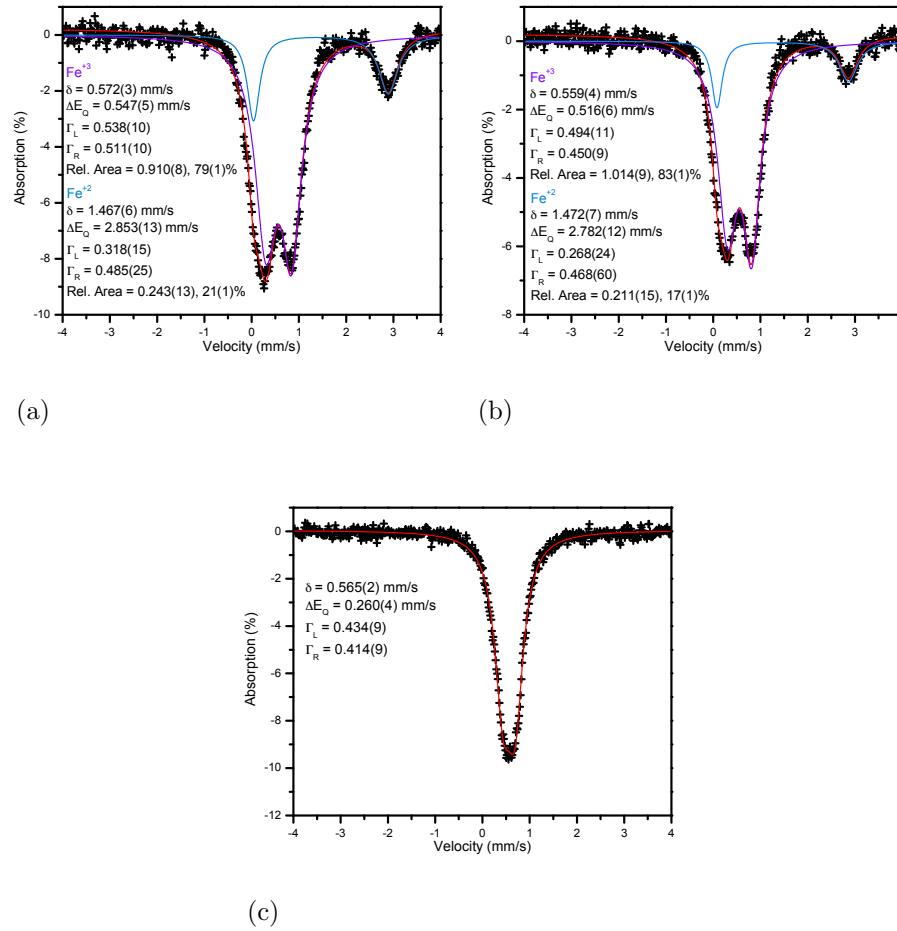


FIGURE 3.36: Mössbauer absorption spectra for three samples, Sample 5_{cub}, Rb_{0.197(5)}FeF₃, Sample 6_{cub}, Rb_{0.166(5)}FeF₃ and Sample 7_{cub}, Rb_{0.14(6)}FeF₃ respectively. All spectra were collected at 80 K. Both Sample 5_{cub} and Sample 6_{cub} have Fe²⁺ present whilst Sample 7_{cub} has all Fe ions fully oxidised to Fe³⁺ indicating that all Fe will be fully oxidised at a Rb occupancy between 0.16 and 0.01.

XAFS

XAFS measurements were carried out on pyr-FeF₃, Sample 5_{cub}, Sample 6_{cub}, Sample 7_{cub} and RbFe₂F₆ to fully understand the oxidation state change of Fe²⁺/Fe³⁺ to Fe³⁺ as a function of Rb occupancy in the phase transition of RbFe₂F₆ to FeF₃. Figure 3.37 displays the Fe K-edge x-ray absorption near edge structure (XANES) spectra for all samples analysed where Fe²⁺ is progressively oxidised to Fe³⁺. Table 3.8 displays the K-edge values at half height for each sample measured showing the gradual increase in energy as Rb occupancy is deintercalated. This indicated that as Rb occupancy decreases, so does the amount of Fe²⁺. This is consistent with Mössbauer absorption spectra previously discussed. These data were collected with Dr. Silvia Ramos and Professor Alan Chadwick and analysed by Dr. Dave Pickup at the University of Kent.

Sample	K-Edge (eV)
RbFe ₂ F ₆	7124.49
Sample 5 _{cub}	7127.09
Sample 6 _{cub}	7127.59
Sample 7 _{cub}	7128.75
FeF ₃	7128.75

TABLE 3.8: The K-edge values for pyr-FeF₃, Sample 5_{cub}, Sample 6_{cub}, Sample 7_{cub} and RbFe₂F₆.

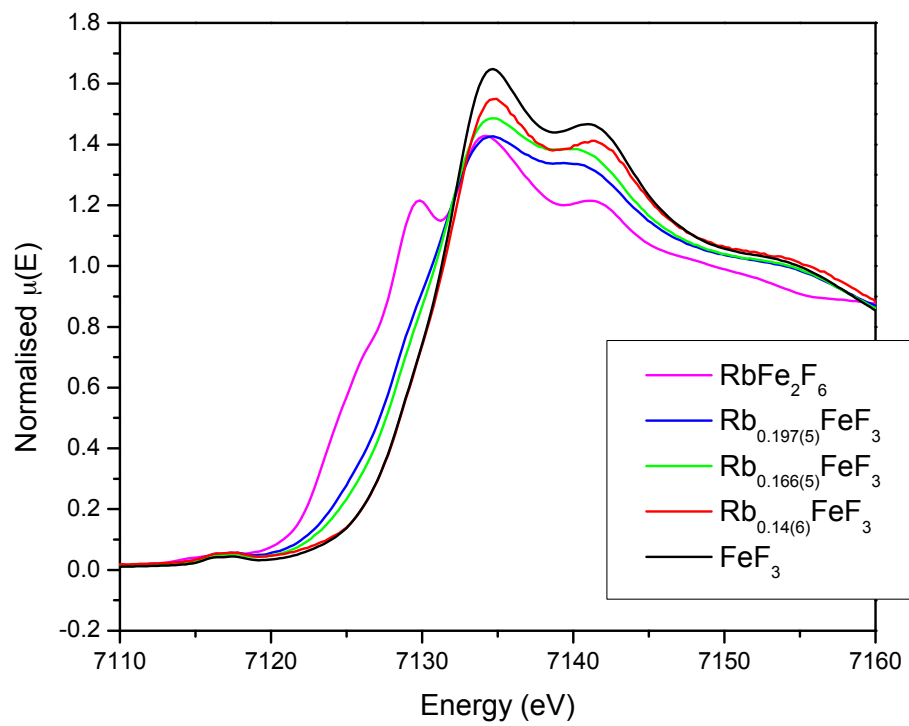


FIGURE 3.37: Fe K-edge x-ray absorption near edge structure (XANES) spectra for FeF_3 , Sample 5_{cub} ($\text{Rb}_{0.197(5)}\text{FeF}_3$), Sample 6_{cub} ($\text{Rb}_{0.166(5)}\text{FeF}_3$), Sample 7_{cub} ($\text{Rb}_{0.14(6)}\text{FeF}_3$) and RbFe_2F_6 .

3.3.3 Magnetic Evolution

3.3.4 Sample 1

The WISH Neutron powder diffractometer was used to characterise the magnetic properties of Sample 1. A series of temperature scans were taken between temperatures of 300 K to 1.6 K focusing mainly on the temperature region below 24 K where long range magnetic ordering is expected. Once the nuclear refinement of the material was characterised for each temperature this was set during the magnetic refinement. The refined diffraction pattern at 1.6 K is shown in Figure 3.38.

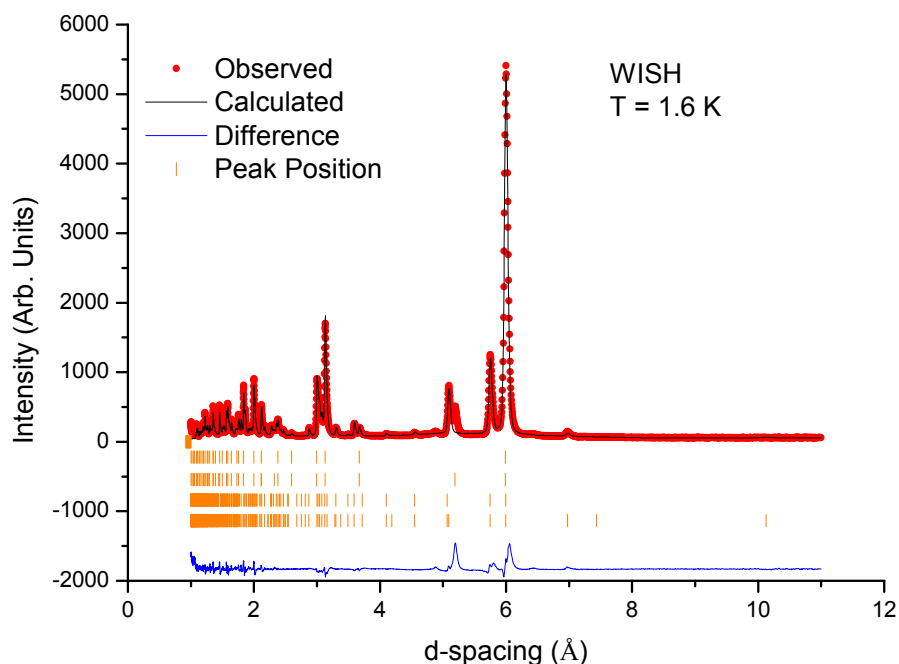


FIGURE 3.38: Refined structural and magnetic data for Sample 1 using powder neutron diffraction collected on the WISH diffractometer, bank 2, at 1.6 K. Data points and calculated fit are displayed in the upper curve and the difference between the observed and calculated pattern is displayed in the lower curve. Sets of vertical tick marks (from top to bottom) represent the expected positions of nuclear reflections for Sample 1_{cub} phase, the expected magnetic reflections for Sample 1_{cub} , the expected positions of nuclear reflections for Sample 1_{orth} phase and the expected magnetic reflections for Sample 1_{orth} . The fit parameters for Sample 1_{cub} are $\chi^2 = 40.5$, Bragg R-factor = 5.47% and Rf-factor = 2.47% with the magnetic R-factor = 7.06%. The fit parameters for Sample 1_{orth} are $\chi^2 = 40.5$, Bragg R-factor = 5.77% and Rf-factor = 5.01% with the magnetic R-factor = 19.6%.

Each structural phase exhibits long range magnetic ordering. Sample 1_{cub} structural phase exhibits the same magnetic ordering as that of pure pyr- FeF_3 , with two interpenetrating networks of tetrahedra with four iron spins aligned towards the center of

the tetrahedron in all-in/all-out configuration, however the T_C is significantly lower than previous samples mentioned earlier, $T_C = 14.2$ K. This can possibly be explained by the high levels of disorder experienced within the system. Figure 3.39 displays the refined moment on the Fe ion. It is only possible to fit the order parameter between 13 K and 8 K as the curve deviates above and below these temperatures. The critical exponent obtained was found to be 0.33(2) which is close to the expected value of a 3D Ising model (0.326).¹¹¹ Sample 1_{orth} also displays the same long range magnetic ordering at low temperatures as observed in pure RbFe₂F₆. Figure 3.40 shows the refined values of both Fe moments, where the order parameter has been fitted between temperatures of 15 K and 10 K, for Fe⁺², and 17 K and 10 K, for Fe⁺³, giving critical exponents of 0.33(4) and 0.33(6), respectively.

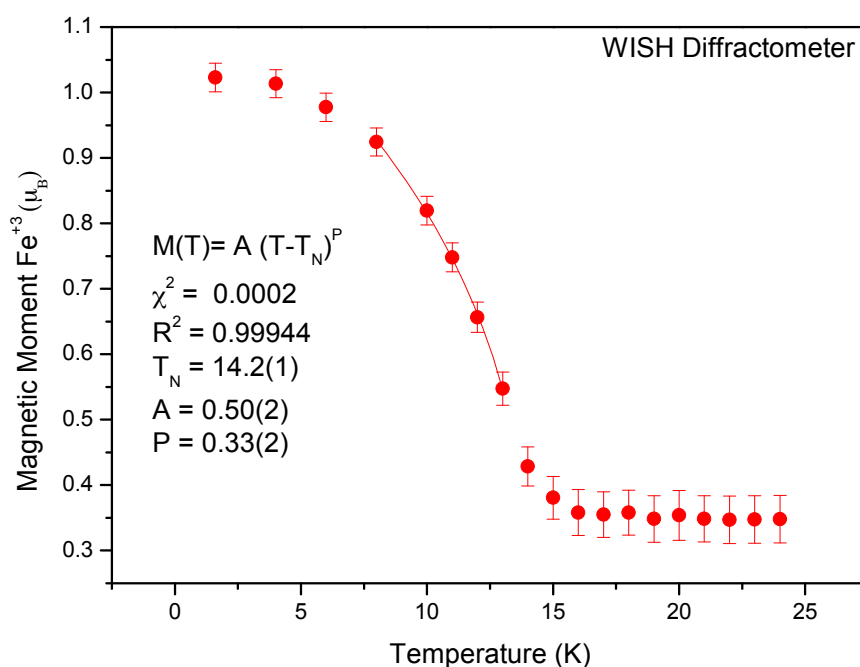


FIGURE 3.39: The refined moment on the Fe ion in Sample 1_{cub}. It is only possible to fit the order parameter between 13 K and 8 K as the curve deviates above and below these temperatures. The critical exponent obtained was found to be 0.33(2) which is close to the expected value of a 3D Ising model (0.326).¹¹¹

The refined magnetic structure of Sample 1_{orth} at 1.6 K is shown in Figure 3.2. The magnetic structure has a propagation vector of $k = 0$ with the Fe⁺² ions aligning along the a - axis forming antiferromagnetic chains along the b - axis and the Fe⁺³ ions aligning along the b - axis forming antiferromagnetic chains down the a - axis. This is consistent with the already published RbFe₂F₆ magnetic structure.¹³ The theoretical spin only value is $7.7 \mu_B$ (Fe⁺² = $4.9 \mu_B$, Fe⁺³ = $5.9 \mu_B$), which is considerably higher

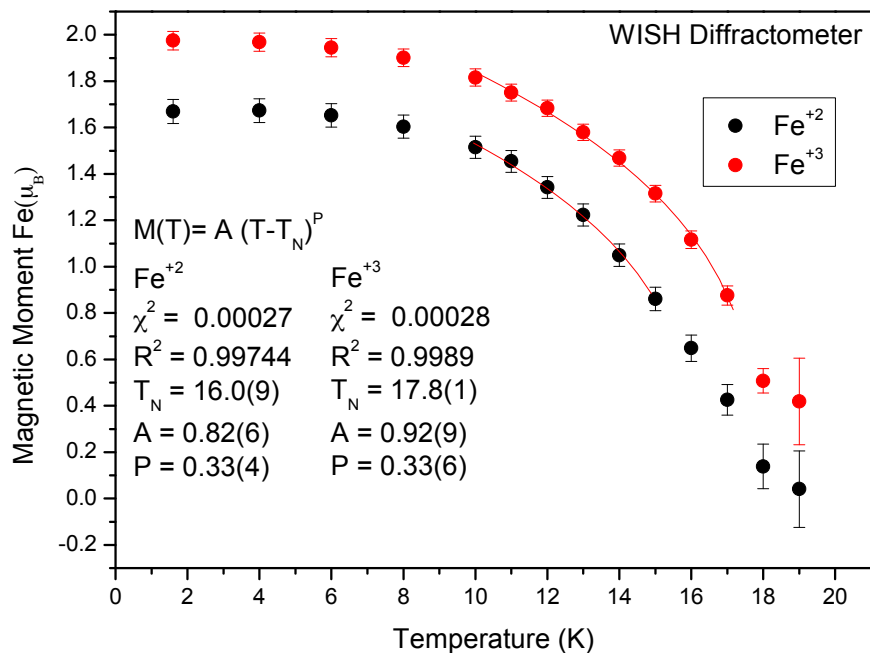


FIGURE 3.40: The refined values of both Fe moments in Sample 1_{orth}, where the order parameter has been fitted between temperatures of 15 K and 10 K, for Fe⁺², and 17 K and 10 K, for Fe⁺³, giving critical exponents of 0.33(4) and 0.33(6), respectively.

than observed, 2.58(2) μ_B . This is attributed to short range correlations as a result of magnetic frustration.

3.3.5 Sample 2

The WISH powder neutron diffractometer was used to analyse Sample 2 at temperatures of 20 K and 1.6 K, above and below the onset of long range magnetic ordering. The fitted diffraction profiles of both can be seen in Figure 3.41. Table 3.9 shows the comparison of refined values for both temperatures. Two magnetic phases are present for both structural phases, similar to that of Sample 1.

3.3.6 Sample 3

As aforementioned in Section 3.3.1, Sample 3a was not selected for PND studies due to two Rb sites present and limited PND instrument time. Sample 3b_{cub} has only the cubic pyrochlore phase present. Analysis was carried out between temperatures of 300 K and 1.6 K, however, there was no long range magnetic ordering present at lower temperatures. The same magnetic refinement method for pyr-FeF₃ was employed here,

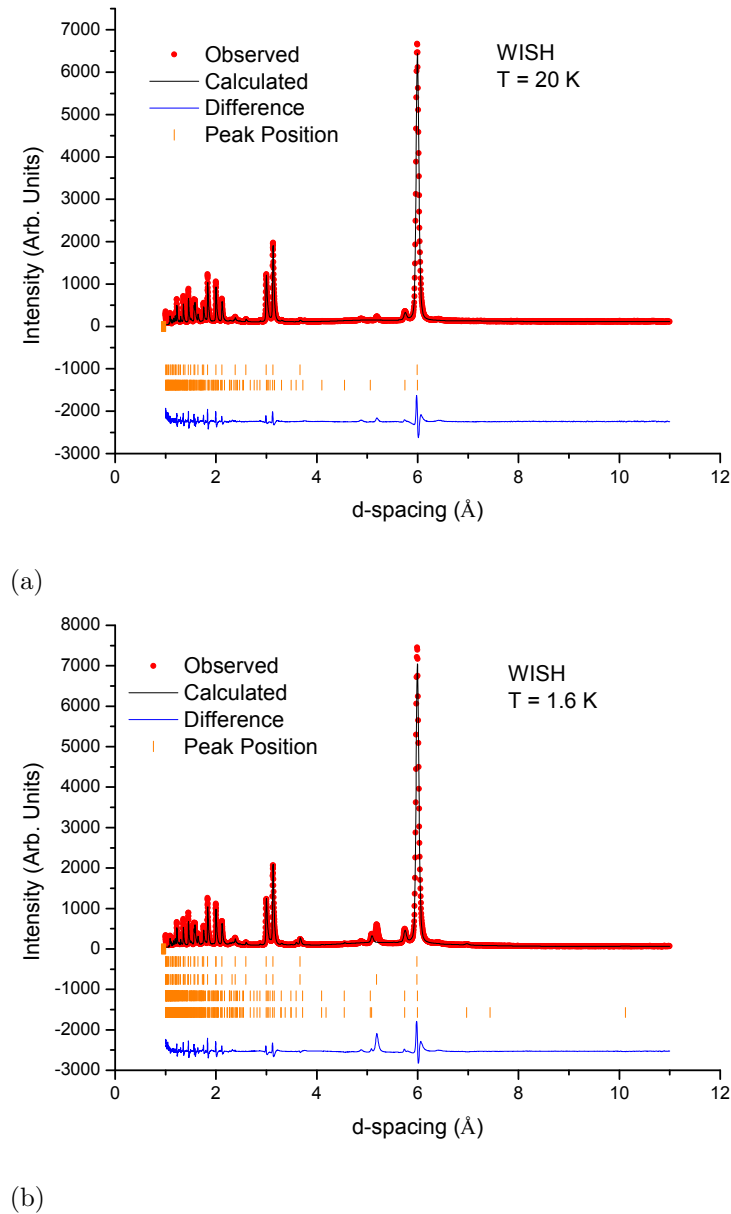


FIGURE 3.41: Fitted diffraction profile for Sample 2 using powder neutron diffraction collected on the WISH diffractometer at (a) 20 K and (b) 1.6 K. Data points and calculated fit are displayed in the upper curve and the difference between the observed and calculated pattern is displayed in the lower curve. Sets of vertical tick marks (from top to bottom) represent the expected positions of nuclear reflections for Sample 2_{cub}, the expected magnetic reflections for Sample 2_{cub}, the expected position of nuclear reflections for Sample 2_{orth} and the magnetic reflections for Sample 2_{orth} respectively. Where there is only one set of vertical tick marks, this represents the nuclear diffraction pattern without magnetic contribution.

however, refinement of the Fe moment did not improve the fit and ultimately was set to zero as a near zero value was unstable in the FullProf Software. A comparison of diffraction patterns collected at a range of temperatures can be seen in Figure 3.42. The

peaks at approximately $50\,000\ \mu\text{s}$ which increase as a function of temperature are those from the suspected oxide and Fe_3O_4 impurities.

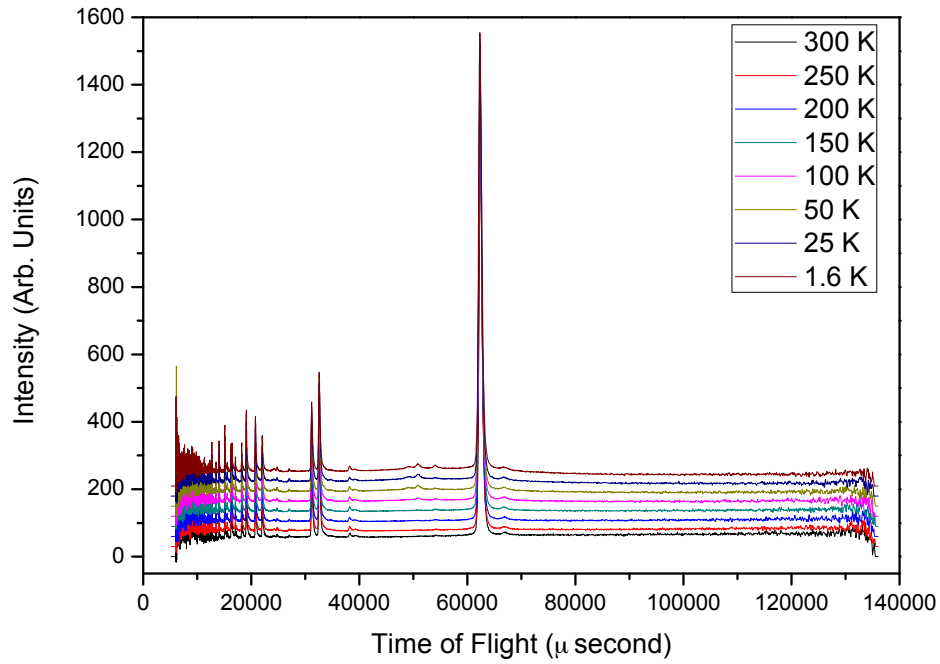


FIGURE 3.42: A comparison of diffraction patterns collected at a range of temperatures of Sample $3b_{\text{cub}}$ with no magnetic ordering.

3.3.7 Sample 4

With a lower Rb occupancy, Sample 4_{cub} is expected to have all Fe nominally 3+, hence the return of long range magnetic ordering. Figure 3.43 shows the refined magnetic moment of the cubic phase as a function of overall Rb occupancy, for Samples 1 - 4 including pyr-FeF₃. It is suggested that as deintercalation and oxidation occur the system becomes more disordered as there is a random arrangement of Fe⁺² and Fe⁺³ on the 16c site. The overall system may be better described as Rb_xFe₄F₁₂ and as the reaction progresses, Rb_xFe⁺²Fe₃⁺³F₆. This would account for the decrease in magnetic moment as a function of Rb occupancy, and why no moment is observed in Sample 3b_{cub}. A spin glass like magnetic transition is suspected, where the disordered arrangement of the Fe oxidation states prevent any periodic ordering. Furthering the reaction, order is restored, hence the return of a net magnetic moment. The orthorhombic phase exhibits similar disorder with a reduction of magnetic moment on both Fe ions, shown in Figure 3.44. Table 3.9 displays the effective magnetic moments of each phase for each Sample analysed including pyr-FeF₃ and RbFe₂F₆ for clarity.

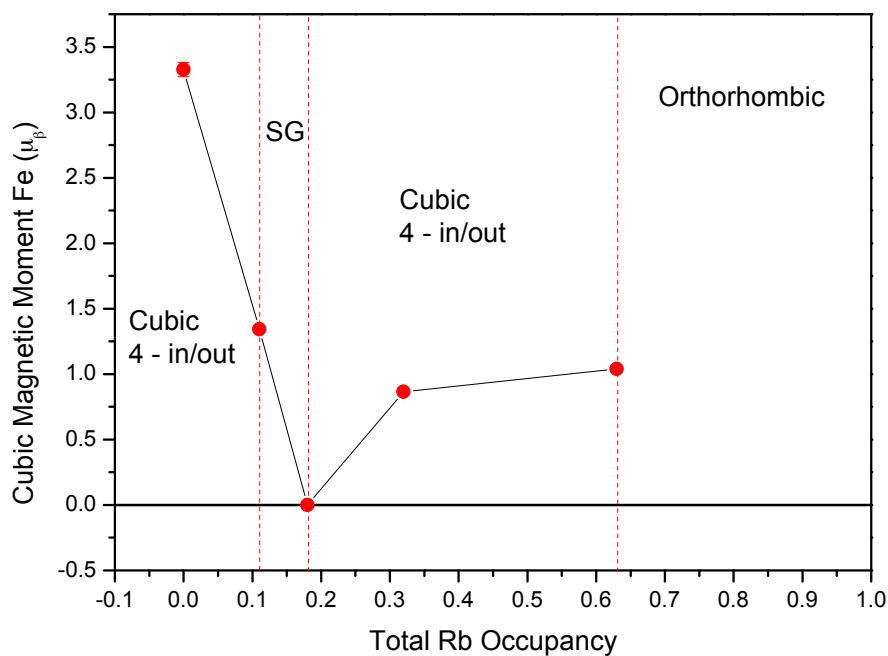


FIGURE 3.43: The refined magnetic moments of the cubic phase as a function of overall Rb occupancy, for Samples 1 - 4 including pyr-FeF₃.

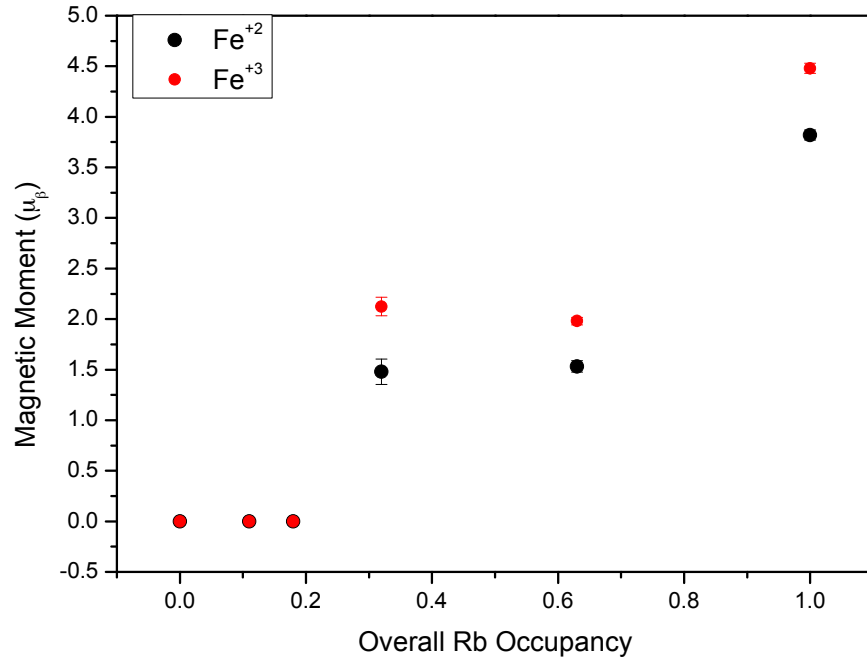


FIGURE 3.44: The refined magnetic moments of the orthorhombic RbFe_2F_6 phase as a function of Rb occupancy, exhibiting similar disorder to that of the cubic phase with a reduction of magnetic moment on both Fe ions.

Sample	Cubic $\text{Fe}^{+3}\mu_\beta$	Orthorhombic $\text{Fe}^{+2}\mu_\beta$	Orthorhombic $\text{Fe}^{+3}\mu_\beta$
RbFe_2F_6	-	3.82	4.48
Sample 1	1.04051	1.53181	1.98058
Sample 2	0.86501	1.4052	2.12413
Sample 3	-	-	-
Sample 4	1.34368	-	-
FeF_3	3.32768	-	-

TABLE 3.9: The effective magnetic moments of each phase for each Sample analysed including pyr- FeF_3 and RbFe_2F_6 .

3.4 Applications

3.4.1 Battery Cycling

In recent years the demand from rechargeable lithium ion batteries has increased due to their wide application to power storage for electrical vehicles and electronic consumable devices.^{112,113} Fluorides have attracted attention due to the conversion reaction with lithium ions. This reaction occurs when the transition metal M, in MX materials (where X = H, N, O, F, P or S), is reduced by lithium to form LiX and the pure metal.¹¹⁴ Transition metal oxides are the materials which have been studied the most with regards to conversion reactions, however, transition metal fluorides are considered to be a special group that react with lithium through conversion reaction.¹¹⁴ The very strong ionic bonding that occurs between the M and X ions result in reduction potentials to LiF and pure metal which can be around 2 V. This is in massive contrast to the potentials below 1.5 V for oxides. This characteristic turns fluorides into alternatives for the positive electrode with noticeably higher specific capacity than intercalation-based candidates, such as LiCoO₂ (280 mAh g⁻¹, theoretical; 140 mAh g⁻¹, practical) or LiFePO₄ (170 mAh g⁻¹, theoretical).¹¹⁴ FeF₃, which crystallises in the ReO₃ structure is the most commonly studied iron fluoride phase. An earlier study reports the reversible intercalation of 0.5 mole Li at 3.4 V. This corresponds to capacities of 140 mAh g⁻¹ that are only partially reversible.¹¹⁵ In comparison to polyanions, (e.g. (PO₄)⁻³), fluorides are more prone to exhibit higher theoretical capacities due to the weight of the fluorine. The theoretical capacity for FeF₃ is 237 mAh g⁻¹ with 1 e⁻ transfer. Once a conversion reaction has occurred, larger capacities are achievable, e.g. 700 mAh g⁻¹ with 3 e⁻ transfer.¹¹⁶

FeF₃ is found with many structure types, including cubic pyrochlore, tetragonal, orthorhombic, rhombohedral and hexagonal tungsten bronze. The crystal structure plays a large role in the electrochemical performance of the material, with pyr-FeF₃ having the advantage of the largest unit cell volume with large open channels, beneficial for the insertion of Li ions. Previous studies have discussed pyr-FeF₃ as a promising cathode material having a large theoretical capacity of 237 mAh g⁻¹. This value is higher than that of LiFePO₄ mentioned above with an operating voltage of ≈3 V.^{117,118} Pyr-FeF₃·0.5H₂O has been reported as a novel cathode material demonstrating a reversible capacity of 135 mAh g⁻¹ at 0.1 C over several hundred cycles indicating a Li insertion of 0.63. The capacity fell to 114 mAh g⁻¹ with Li insertion of 0.5 after 300 cycles. When increasing the rate to 1 C a capacity of 80 mAh g⁻¹ was maintained and could be recovered to 140 mAh g⁻¹ at 0.1 C after cycling at 10 C. When examining Na insertion, the reversible

capacity was extremely high at 250 mAh g^{-1} at 0.1 C over a voltage range of $0.8\text{-}4.0 \text{ V}$, 2.5 times higher than R-FeF_3 .¹⁰⁸

The large open framework structure of pyr-FeF_3 with large unit cell is ideal for Li ion insertion within the 3D inter connected channels. Pyr-FeF_3 was synthesised using methods outlined earlier in this chapter and the electrodes were prepared by mixing pyr-FeF_3 , carbon black, to improve conductivity, and polyvinylidene difluoride (PVdF), as a binder, at a ratio of 8:1:1, which was then placed onto aluminium foil through thin film coating. This was left to dry in a vacuum for approximately 12 h. The electrolyte involved 1 M LiPF_6 in a non-aqueous mixture of ethylene carbonate (EC) and dimethyl carbonate (DMC) with a volume ratio of 1:1. Lithium foil was used as the counter electrode. The cell was assembled in an Ar-filled glovebox. Charge-discharge measurements were performed at ambient temperature with a rate of $C/200$ in a voltage range of $1.25\text{ - }4.5\text{ volt}$. Figure 3.45 shows the capacity as a function of voltage and Figure 3.46 shows the charge and discharge at each cycle. The first discharge curve exhibits a large capacity of 500 mAh g^{-1} with a sloping potential profile. The initial discharge capacity is higher than that of the theoretical value. The initial charge capacity is 380 mAh g^{-1} indicating that not all Li^+ have been removed. This pattern continues throughout 6 discharge/charge cycles. Table 3.10 shows the actual values for all 6 cycles.

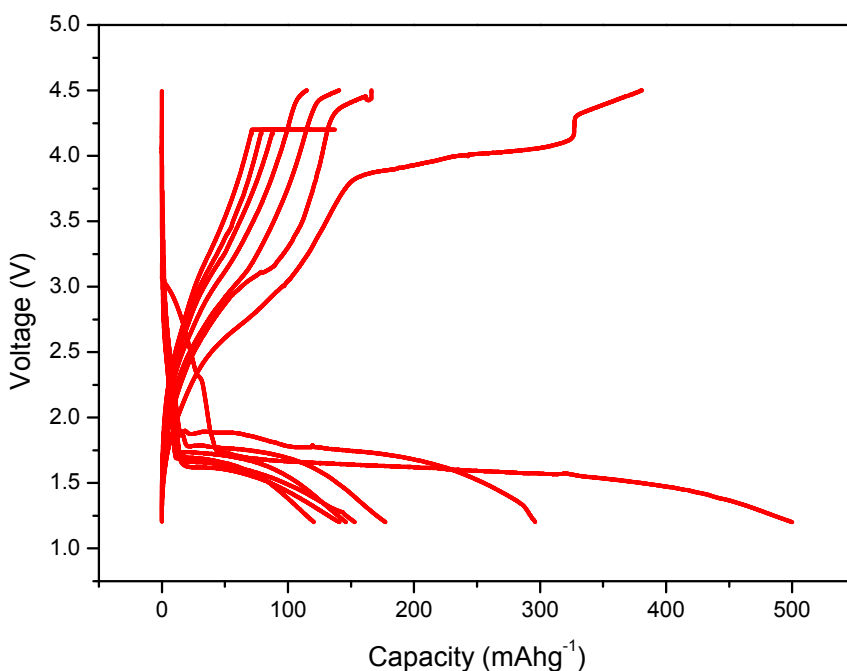
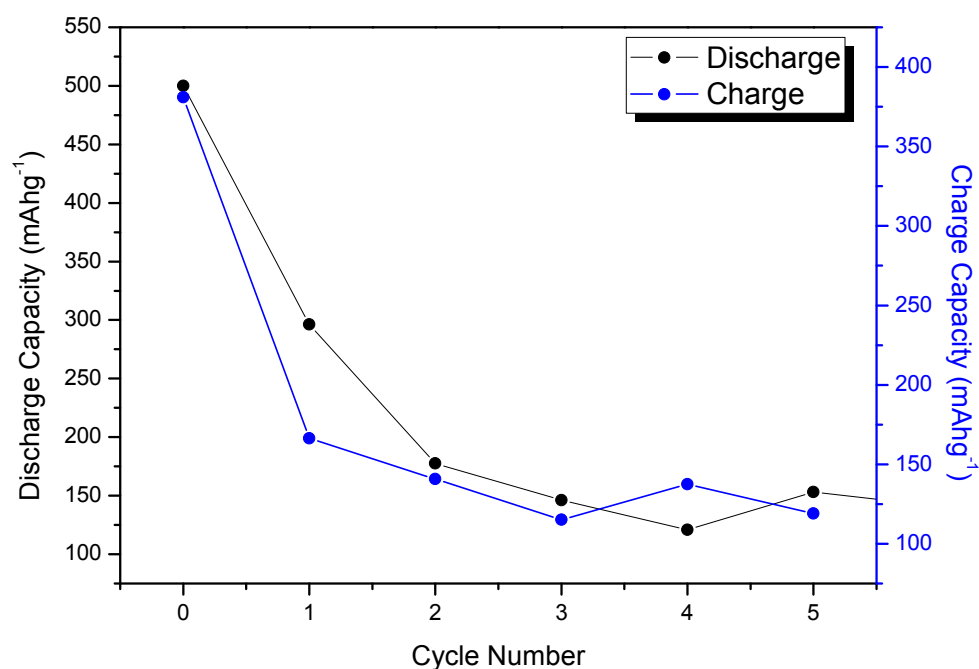


FIGURE 3.45: Charge capacity, in milliamperere per hour per gram, of pyr-FeF_3 as a function of voltage.

Cycle	Discharge (mAh g ⁻¹)	Charge (mAh g ⁻¹)
1	500.07(5)	380.91(3)
2	296.31(8)	166.29(9)
3	177.42(2)	140.83(1)
4	120.75(1)	137.51(5)
5	153.12(5)	119.05(6)
6	140.97(8)	

TABLE 3.10: The Li⁺ discharge/charge values in mAh g⁻¹ for pyr-FeF₃.FIGURE 3.46: The charge and discharge of pyr-FeF₃ for each cycle.

There are four possible reasons for capacity loss throughout cycling, formation of solid-electrolyte interphase (SEI), Li ion trapping within the material, formation of other FeF₃ structures and swelling of pyr-FeF₃ during lithium insertion. Normally, the formation of SEI results from the irreversible electrochemical decomposition of the electrolyte, which compete with the desirable Faradaic half-cell reduction at the electrode surface. SEI would form at the negative electrode because typical electrolytes are not stable at the operating potential of the electrode during charging. The product of this decomposition will form a solid layer on the surface of FeF₃ (the active material). A variety of compounds have observed this layer.^{119,120} Prior to the conversion reaction:



other FeF₃ structures may form, reducing the Li⁺ capacity. When extracting Li from the 3/1 mixture of LiF and Fe, a rutile FeF₂ like structure can form even when the Fe should be oxidised to Fe³⁺ by extraction of three Li⁺ per Fe.¹²¹ Pyr-FeF₃ may also be prone to swelling during discharge, and then when charged attempts to regain its original shape materials are often not flexible enough for this and crack, therefore losing its structure leading to some capacity loss due to the material not being in electronic contact with the conductor coil.

3.5 Conclusion

We have synthesised pure, monophasic pyr-FeF₃. Using a newly designed modified topotactic deintercalation method, Rb can be removed from the defect pyrochlore type RbFe₂F₆ resulting in a new form of microporous materials. The sample crystallises in spinel cubic space group, $Fd-3m$, without impurities, resulting in a structure which can be described as consisting of three-dimensional tunnels produced by corner sharing octahedra. Previous reports of pyr-FeF₃ contain (NH₃)_x or H₂O within the tunnels on the A cation site. Additionally, impurities of HTB-FeF₃ and FeF₂ are observed during Mössbauer spectroscopy where magnetic splitting occurs at a temperature range of 130 K to 77 K.¹¹⁰ This splitting is not observed in the Mössbauer spectroscopy displayed in this work supporting true porosity. The magnetic and crystal structure has been investigated using the BT-1 powder diffractometer and refined in Fullprof using a representational analysis approach with propagation vector $\mathbf{k} = (0,0,0)$ and one irreducible representation Γ_3 , which is consistent with that reported earlier.¹²² The results of the co-refinement of scans collected is presented proving good quality of fit and sample. The magnetism in pyr-FeF₃ can be described as two inter-penetrating networks of tetrahedra with four iron spins aligned towards the center of the tetrahedron in all-in or all-out configurations. The magnetic moment on the iron site was refined using the Fe³⁺ form factor and gave a magnetic moment of 3.57(3) μ_B , which is larger than the value reported earlier but still lower than expected for the single ion. Landau's theory allows a second order phase transition that can be described by just one representation. Therefore, we performed a series of temperature scans up to the point where no long range ordered state is observed to obtain the order parameter. These patterns were analysed using the same model and the refined value of the Fe was presented. Unfortunately, no good power law fit could be obtained for the data, mostly due to non-typical behaviour close to the transition, where the curve deviates. Additionally, we observed an increased diffuse structure forming in the background of the scans, which is larger at temperatures above the transition indicating the presence of short range correlations. The earlier Mössbauer reports,¹¹⁰ indicated a higher ordering temperature (21 K) obtained from the behaviour of the hyperfine field but showed no broadening of absorption line above it suggesting absence of critical fluctuations and indicating that the diffuse component has static rather than dynamic character. This could be an explanation for the non-power law behaviour close to the transition temperature due to internally hindered fluctuations as in spin glass or spin-ice states, which may be present in the paramagnetic state.

Gas absorption measurements were performed to investigate the porosity of pyr-FeF₃, since producing A cation site deficient material has proven difficult with earlier synthetic techniques. Neutron diffraction results gave a formula of pyr-FeF₃-0.05(4) D₂,

significantly lower than gas absorption results, indicating that absorption rate is slow given the time pyr-FeF₃ was held in atmosphere for each instrument. The ability to absorb H₂ and D₂ supports true porosity and the potential for a new family of materials for hydrogen storage/separation.

Preliminary experiments were carried out on pyr-FeF₃ for the potential of battery cycling with Li. Theoretically pyr-FeF₃ has a large capacity, however, this was not demonstrated in this work. It would be advantageous to explore this further to fully understand the capacity limits of this family of fluoride materials to act as a cathode material.

Chapter 4

Synthesis, Structure and Characterisation of CsFe_2F_6

4.1 Introduction

Mixed metal fluorides have become of recent interest due to their variety of functional properties.^{14,123,124} The $\text{AM}^{2+}\text{M}^{3+}\text{F}_6$ family of materials exhibit charge order for a variety of compounds including RbFe_2F_6 and CsFe_2F_6 . CsFe_2F_6 was reported as the first $\text{AM}^{2+}\text{M}^{3+}\text{F}_6$ material with the defect pyrochlore structure to undergo a structural phase transition with temperature.¹⁴ The room temperature structure of RbFe_2F_6 ¹³ was reported in the $Pnma$ space group, as solved with single crystal X-ray diffraction. For CsFe_2F_6 , a sequence of structural transitions were observed between a narrow temperature range of 500 K to 560 K as follows: $Pnma(Z = 4) \rightarrow Imma(Z = 4) \rightarrow I4_1/amd(Z = 4) \rightarrow Fd-3m(Z = 8)$. It is the rotation of the MF_6 octahedra and slight displacement of the Fe atoms that are primarily responsible for the difference between these structures.⁵⁸ The study of CsFe_2F_6 with Mössbauer and Raman spectroscopy confirmed the ordered arrangement of Fe^{3+} and Fe^{2+} ions within the material facilitating the orthorhombic $Pnma$ structure down to a temperature of at least 7 K. SQUID magnetometry measurements indicate strong antiferromagnetic ordering, due to a Weiss temperature of -260 K and Neel temperature of 13.7 K with significant frustration, indicated by a frustration index of 19.¹²⁵ An investigation of the magnetic properties of CsFe_2F_6 using GGA + U methods within the density-functional framework, found the magnetic ground state to be antiferromagnetic. The magnetic interactions are described as being antiferromagnetically ordered between Fe^{3+} - Fe^{3+} and Fe^{2+} - Fe^{2+} along the b-axis and c-axis respectively whereas Fe^{3+} and Fe^{2+} form a kagome plane.¹²⁶

In this thesis, CsFe₂F₆ has been synthesised using a previously described low temperature hydrothermal method.¹³ Neutron diffraction shows a defect pyrochlore structure with antiferromagnetic ordering below 22 K and no structural phase transitions below room temperature. The high frustration index of 18.9(8) along with the calculated effective magnetic moment from SQUID and neutron diffraction data respectively indicate that not all Fe moments are ordered within the system, which is also supported by the observation of diffuse scattering observed at 50 K. Mössbauer Spectroscopy measurements have also been performed to determine the ratio of Fe²⁺ to Fe³⁺, indicating that there is a slightly larger amount of Fe³⁺ present in the material. This could be explained by the presence of a small impurity which may not be detected from neutron diffraction data due to the poor crystallinity or slight disorder of the metal ions over both sites.

4.2 Experimental

4.2.1 Reagents

The reagents used were CsF (Alfa Aesar, 99%), FeF₃ anhydrous (Alfa Aesar, 97% min), FeF₂ anhydrous (Alfa Aesar, 99%) and CF₃COOH (Alfa Aesar, 99%) without any further modification of purification.

4.2.2 Synthesis

The hydrothermal synthesis of CsFe₂F₆ defect pyrochlore was performed using Parr Instrument Company general purpose acid digestion vessels with an internal volume of 45 ml. 0.3463 g (2.28×10^{-3} mol) of CsF, 0.2141 g (2.28×10^{-3} mol) of FeF₂ and 0.2573 g (2.28×10^{-3} mol) of FeF₃ were added to 3 ml (3.90×10^{-2} mol) of CF₃COOH, and 5 ml of H₂O in an autoclave. The autoclave was sealed and gradually heated to 230 °C, held for 24 h before being cooled to room temperature at a rate of 0.1 °C/min. The mother liquid was decanted and the remaining solid washed with H₂O using gravity filtration. The sample was then dried for \approx 12 h at 70 °C before further analysis.

4.3 Results and discussion

4.3.1 Synthesis

AM²⁺M³⁺F₆ materials have typically been synthesised using binary metal fluorides with alkali metal fluorides or NH₄F solutions in platinum tubes which are sealed before being

placed into an autoclave. The autoclave is then heated to temperatures above 350 °C which creates pressures over 2000 bar. Examples of $AM^{2+}M^{3+}F_6$ materials synthesised in this way are $NH_4Fe_2F_6$, NH_4MnFeF_6 , NH_4MnCrF_6 and Rb_4MnFeF_6 .^{127,128} Recently, $RbFe_2F_6$ was synthesised using a low temperature hydrothermal method in which binary metal fluorides were mixed with RbF and a dilute CF_3COOH aqueous solution.¹³ This method has not only been used to synthesis polycrystalline $RbFe_2F_6$, but also for $BaMF_4$, where $M = Mg, Mn, Co, Ni$ and Zn .¹⁹ Figure 4.1 shows the experimental and calculated X-ray diffraction patterns for $CsFe_2F_6$, the experimental diffraction pattern shows a broadening of reflections compared to a standard, indicating that the sample has disorder or poor crystallinity. This method of low temperature hydrothermal synthesis does produce single phase $CsFe_2F_6$, however, solid state synthesis may produce more crystalline samples compared to hydrothermal synthesis. Broadening of the diffraction peaks could relate to the crystal size being within the nano scale.

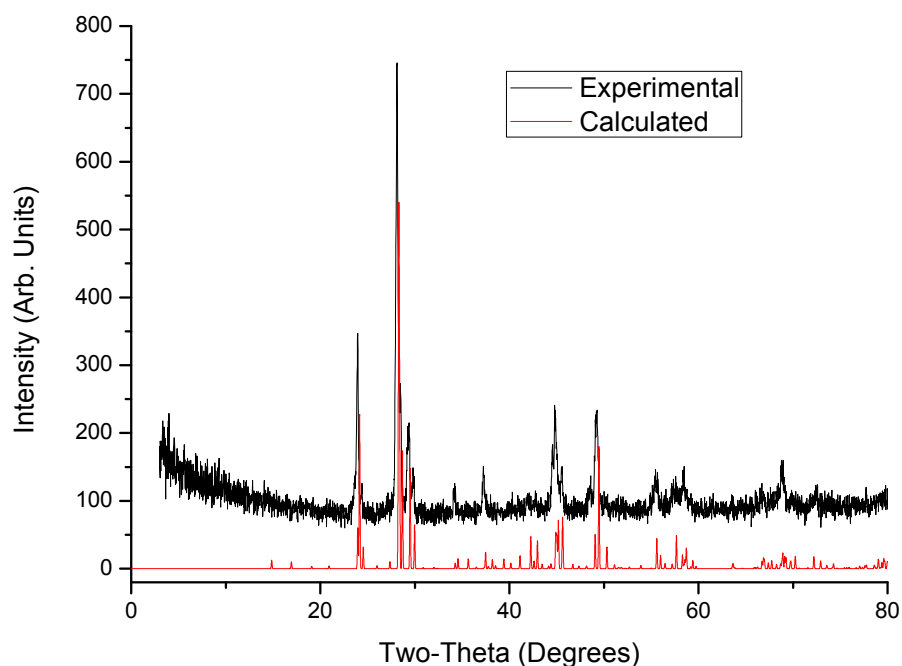


FIGURE 4.1: Comparison of experimental and calculated powder X-ray diffraction patterns for $CsFe_2F_6$.

4.3.2 Structural Properties

$CsFe_2F_6$ was characterised using the Panalytical Empyrean X-ray diffractometer and confirmed to be single phase. An example data set of $CsFe_2F_6$ including the fit from the Rietveld refinement model and the difference plot is shown in Figure 4.2. Refined

values of CsFe₂F₆ gives lattice parameters $a = 7.246(8) \text{ \AA}$, $b = 7.415(9) \text{ \AA}$ and $c = 10.45(1) \text{ \AA}$ with $\alpha = \beta = \gamma = 90^\circ$. These results are close to the published structure, $a = 7.2443(1) \text{ \AA}$, $b = 7.48230(9) \text{ \AA}$ and $c = 10.4238(1) \text{ \AA}$ with $\alpha = \beta = \gamma = 90^\circ$, representing a reduced orthorhombic cell of β -pyrochlore lattice with a $Pnma$ symmetry.⁵⁸

The final refinement of CsFe₂F₆ confirmed a single phase sample and free from any parent ingredients within the experimental limit. The fit parameters are $\chi^2 = 1.10$, $R_p = 8.29\%$ and $R_{wp} = 10.6\%$. Table 4.1 displays the crystallographic data associated with the X-ray refinement of CsFe₂F₆ and Table 4.2 displays the atomic positions.

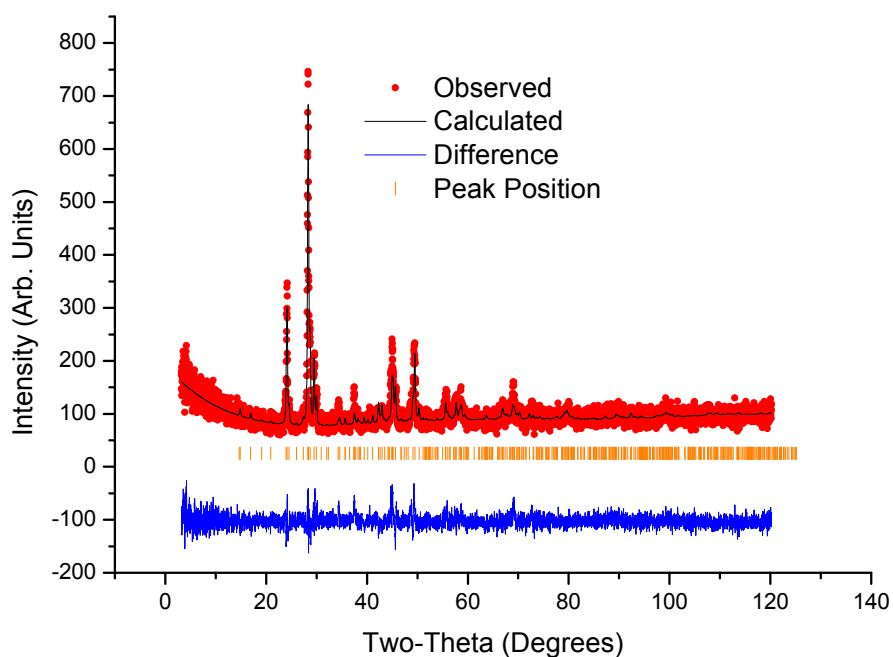


FIGURE 4.2: X-ray diffraction data collected at 300 K (red), calculated profile (black) and the difference (blue) plot for powder sample of CsFe₂F₆. The data were collected using the methods described in Section 2.3.2. The fit parameters are $\chi^2 = 1.10$, $R_p = 8.29\%$ and $R_{wp} = 10.6\%$.

CsFe₂F₆ is a three-dimensional crystal structure with the space group $Pnma$ consisting of corner sharing FeF₆ octahedra, which are separated by Cs⁺ cations, Figure 4.3. The formula of CsFe₂F₆ is better written as CsFe²⁺Fe³⁺F₆ since both the Fe²⁺ and Fe³⁺ are charge ordered within the structure. The overall structure can be described as being built up from two corner sharing FeF₆ octahedra sub-lattices. The Fe³⁺F₆ octahedra share corners along the b-axis and are connected through Fe²⁺F₆ along the c-axis, Figure 4.3b displays the bc-plane where this can be seen. Similarly, the Fe²⁺F₆ octahedra share corners along the a-axis being connected along the c-axis by Fe³⁺F₆, this can be seen along the ac-plane in Figure 4.3a. This ordering results in a Kagome-type network in both

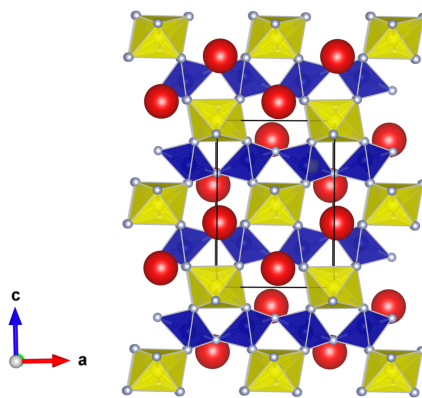
Parameter	CsFe ₂ F ₆
Formula Weight, fw	358.59 g mol ⁻¹
Temperature (K)	298
λ (Å)	1.54056
Crystal Structure	Orthorhombic
Space Group	<i>Pnma</i> (No.62)
a (Å)	7.2443(1)
b (Å)	7.415(9)
c (Å)	10.4238(1)
V (Å ³)	561.901 (0.123)
Z	4
ρ_{calc} (g/cm ³)	4.239
2θ max.	120.00
GOF	1

TABLE 4.1: Crystallographic data for CsFe₂F₆ obtained through rietveld refinement of powder X-ray diffraction.

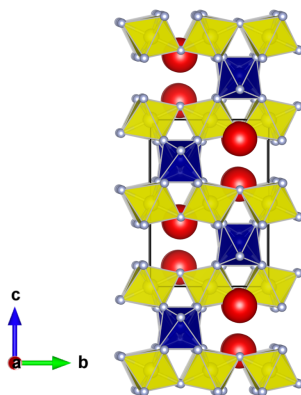
Atom	x	y	z
Cs(1)	0.97(1)	0.25	0.37(1)
Fe(1)	0.77(1)	0.25	0.74(1)
Fe(2)	0.5	0	0.5
F(1)	0.70(2)	0.06(1)	0.61(1)
F(2)	0.36(1)	0.02(1)	0.64(1)
F(3)	0.43(3)	0.25	0.43(2)
F(4)	0.55(2)	0.25	0.81(2)

TABLE 4.2: The refined positions from rietveld refinement of powder X-ray diffraction data of CsFe₂F₆ at 300 K, with lattice parameters $a = 7.2443(1)$ Å, $b = 7.415(9)$ Å and $c = 10.4238(1)$ Å with $\alpha = \beta = \gamma = 90^\circ$.

the ac- and the bc-planes. The Fe²⁺ - F bond distances are in the range of 1.843(19) Å - 2.055(16) Å and the Fe³⁺ - F bond distances range between 1.935(14) Å - 2.010(9) Å, both in a 6-fold coordination environment. The Cs cation is in a 10-fold coordination environment with Cs - F bond distances ranging from 3.09(6) Å - 3.36(3) Å. Table 4.3 shows the values of each bond distance and Figure 4.4 shows the bonding coordination of both Fe and Cs.



(a)



(b)

FIGURE 4.3: CsFe₂F₆ structure, with Fe⁺² shown in blue, Fe⁺³ shown in yellow and Cs in red along the, 4.3a, ac-plane displaying the Fe⁺² ions connected along the c-axis and, 4.3b, Fe⁺³ ions connected along the b-axis with a Cs cation within the pores of the structure.

Bond	Distance Å	Bond	Distance Å
Cs - F(1)	3.10(2) × 2	Fe(1) - F(1)	2.007(16) × 2
Cs - F(1)	3.32(4) × 2	Fe(1) - F(2)	2.055(16) × 2
Cs - F(2)	3.36(3) × 2	Fe(1) - F(4)	1.843(19)
Cs - F(2)	3.55(4) × 2	Fe(1) - F(4)	2.069(19)
Cs - F(3)	3.19(5)	Fe(2) - F(1)	1.935(14) × 2
Cs - F(4)	3.09(6)	Fe(2) - F(2)	1.808(15) × 2
		Fe(2) - F(3)	2.010(9) × 2
		Fe(1) - Fe(2)	3.767(13) × 2
		Fe(1) - Fe(2)	3.612(15) × 2
		Fe(1) - Fe(1)	3.688(3) × 2
		Fe(2) - Fe(2)	3.6991(5) × 2

TABLE 4.3: Bond distances of CsFe₂F₆.

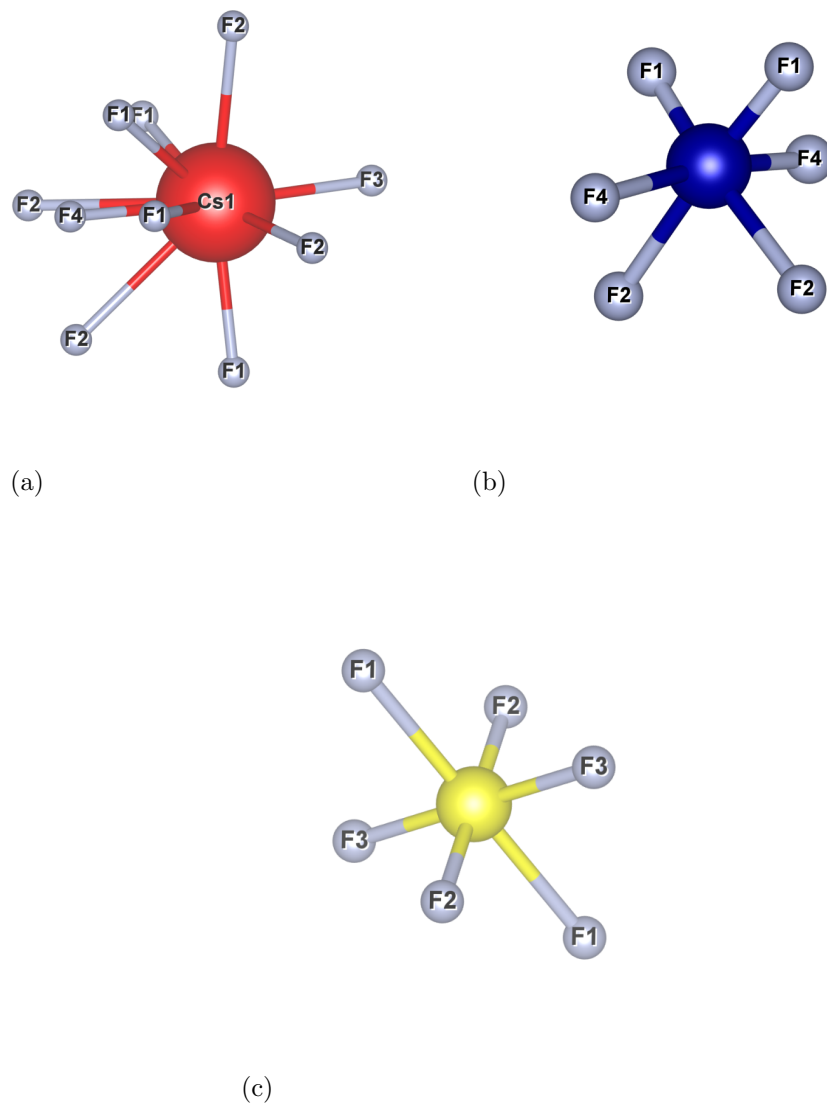


FIGURE 4.4: The 10-fold coordination environment of Cs (4.4a) and the 6-fold coordination environment of Fe^{2+} (4.4b), shown in blue, and Fe^{3+} (4.4c), shown in yellow.

4.3.3 Neutron Diffraction Data

The BT1 instrument, described in Section 2.4.1, was used to collect neutron diffraction data from a powdered sample of CsFe₂F₆ over the temperature range from 300 K to 5 K. Approximately 3 g of CsFe₂F₆ was loaded into a vanadium can and mounted into a CCR, closed cycle refrigerator. A Cu(311) monochromator with a 90° take-off-angle, $\lambda = 1.540 \text{ \AA}$, and an in-pile collimation of 60 minute of arc was used. Figure 4.5 shows a typical fit of experimental data and calculated model, where the fit parameters are $\chi^2 = 2.25$, $R_p = 9.36\%$ and $R_{wp} = 11.36\%$. β -pyrochlores tend to have disorder amongst the two metal cations and have exhibited partial occupancy on the A anion site; the occupancy of Cs was refined, however, there was little change, 0.99(1) to full occupancy, which did not improve the goodness of fit. The occupancy of Cs was then set to 1 for all refinements thereafter.

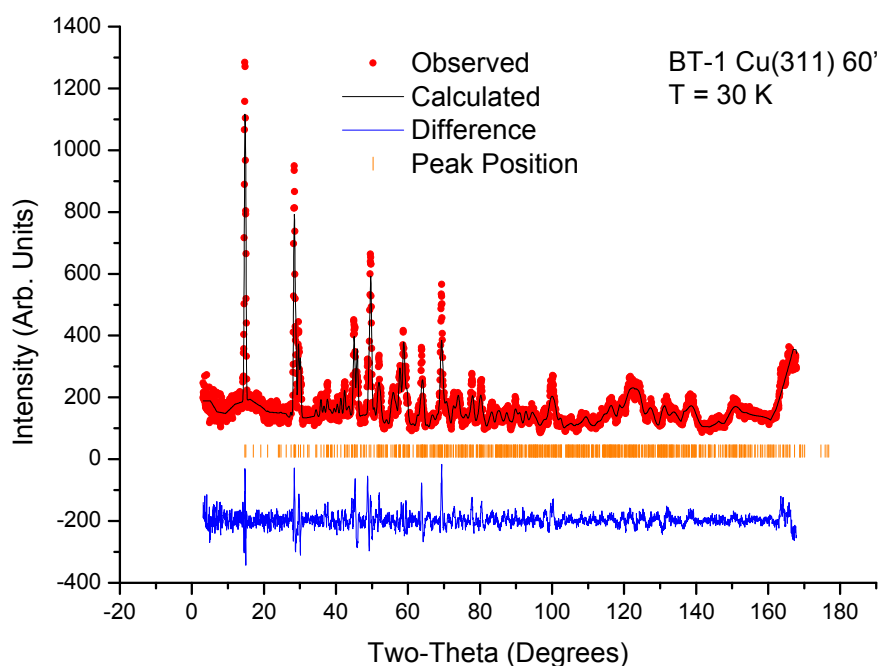


FIGURE 4.5: Refined model of CsFe₂F₆ using powder neutron diffraction collected on the BT1 diffractometer at 30 K. Data points (red) and calculated fit (black) are displayed in the upper curve and the difference (blue) between the observed and calculated pattern is displayed in the lower curve. Sets of vertical tick marks (orange) represent the expected positions of nuclear reflections for CsFe₂F₆. The fit parameters are $\chi^2 = 2.25$, $R_p = 9.36\%$ and $R_{wp} = 11.36\%$.

Figure 4.6 shows the a, b, and c lattice parameter along with the volume of CsFe₂F₆ as a function of temperature obtained from Rietveld refinement of BT1 neutron diffraction. The fitted powder neutron diffraction patterns can be found in Appendix A, as well as

refinement tables, for each temperature used. All lattice parameters show a contraction up to approximately 50 K where there is then a negative thermal expansion which is more pronounced along the b axis. This is supported by the increase in volume, shown in Figure 4.6d. On cooling no structural phase transition is observed and the material remains in a *Pnma* space group throughout, within the resolution of the experiment. The negative thermal expansion could be attributed to short range magnetic interactions that would also explain the diffuse scattering shown in Figure 4.7. The quality of data above this temperature is insufficient to determine at which point this diffuse scattering is no longer observed due to poor signal to noise ratio. It is expected from the variation in the lattice parameters and volume that diffuse scattering is observed at temperatures below 50 K. During refinements the isotropic thermal parameters were refined for all atoms, however, non-physical negative values were obtained over all temperatures. Fluctuations in thermal parameters prevented the refinement from converging and the values were set to zero to allow for a full structural and magnetic refinement. This may be attributed to a combination of the possible disorder on the Fe sites and the data quality. CsFe₂F₆ can be closely compared to RbFe₂F₆ in all respects including isotropic thermal parameters. The Cs cation is disproportional in size to the available space. This rattling effect of the A cation in β -pyrochlores is well researched and can be attributed to the difference in ionic radii (2.72 Å for Cs) and available pore space (≈ 5 Å in CsFe₂F₆), potentially causing thermal oscillation.

The magnetic structure of CsFe₂F₆ was determined from 5 K neutron diffraction data collected on the BT1 instrument. To begin the magnetic refinement, the propagation vector and the symmetry of the magnetic cell must be known. For CsFe₂F₆, all the magnetic reflections, which appear below T_N , can be indexed with the propagation vector of $\mathbf{k} = (0,0,0)$, and representational analysis was used to find the symmetry of the magnetic cell using the software BasIreps in the FULLPROF software suite. BasIreps works by inputting specific parameters or constraints to calculate the basis functions of irreducible representations of the propagation vector group for the magnetic unit cell identifying the allowed magnetic moment on each individual crystallographic site for each irreducible representation. Before the final refinement of the magnetic unit cell, all possible combinations of symmetry operators suggested by BasIreps were trialed, however, only one gave a sensible result fitting the experimental data well. The final atomic position at 5 K are given in Table 4.4 and the Rietveld fit, including observed, calculated and difference profiles as well as the magnetic phase, is shown in Figure 4.8. The magnetic structure is shown in Figure 4.9 with an overall effective magnetic moment of $4.11(6)\mu_B$, lower than the calculated theoretical spin-only value of $7.68(4)\mu_B$. The first Fe site, (0.76(2), 0.25, 0.74(1)) has a magnetic moment of $1.57(2)\mu_B$ confined along the b-axis and can be described as forming antiferromagnetic chains along the a-axis. These

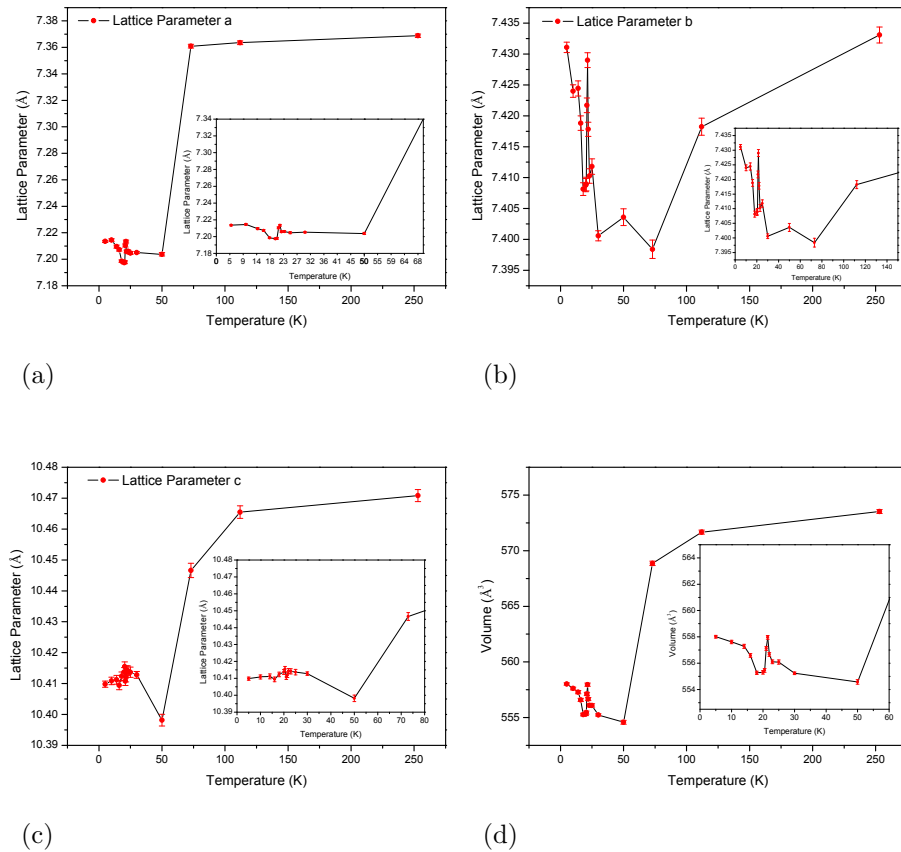


FIGURE 4.6: Lattice parameters, a (4.6a), b (4.6b), c (4.6c) and volume (4.6d) of CsFe₂F₆ as a function of temperature (K) obtained from Rietveld refinement of powder neutron diffraction data from the BT1 diffractometer. There is a consistent decrease in lattice parameter in each lattice as well as the volume of the unit cell, however, a negative thermal expansion is observed after approximately 50 K, more considerably with the b lattice. Error bars present are smaller than point size.

antiferromagnetic chains are perpendicular to the moments of the second Fe at (0.5, 0.5, 0.5). The second Fe has a magnetic moment of $3.76(2)\mu_B$ sitting along the a-axis forming antiferromagnetic chains parallel to the b-axis. The magnetic moment of the second iron suggests that, even though its' magnetic moment is lower than the theoretical spin only moment of high spin Fe³⁺ ($5.92\mu_B$), that it is in a high-spin coordination. The overall magnetic moment of CsFe₂F₆ being lower than expected can be explained by the diffuse scattering observed at low temperature in the neutron diffraction pattern, suggesting that not all moments are in fact ordered due to magnetic frustration. The diffuse scattering is highlighted in Figure 4.7.

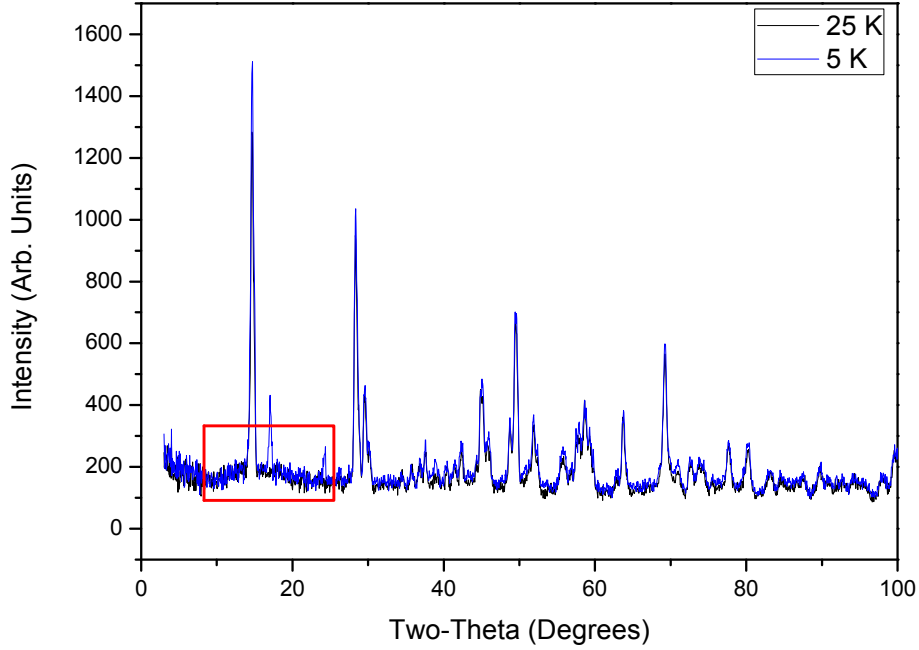


FIGURE 4.7: BT1 neutron diffraction data collected at 5 K and 25 K both displaying diffuse scattering (highlighted by a red box) around the (111) peak. Data collected above 25 K is of insufficient quality to determine the temperature at which this diffuse scattering is no longer present.

Atom	x	y	z	Magnetic Moment (μ_B)
Cs(1)	0.98(2)	0.25	0.36(1)	-
Fe(1)	0.76(1)	0.25	0.74(1)	1.57(2)
Fe(2)	0.5	0	0.5	3.76(2)
F(1)	0.70(1)	0.06(1)	0.61(1)	-
F(2)	0.36(1)	0.02(1)	0.63(1)	-
F(3)	0.44(2)	0.25	0.43(2)	-
F(4)	0.55(2)	0.25	0.82(1)	-

TABLE 4.4: The refined positions from Rietveld refinement of powder neutron diffraction data collected on the BT1 diffractometer of CsFe₂F₆ at 5 K, with lattice parameters $a = 7.211(8)$ Å, $b = 7.425(8)$ Å and $c = 10.41(1)$ Å with $\alpha = \beta = \gamma = 90^\circ$.

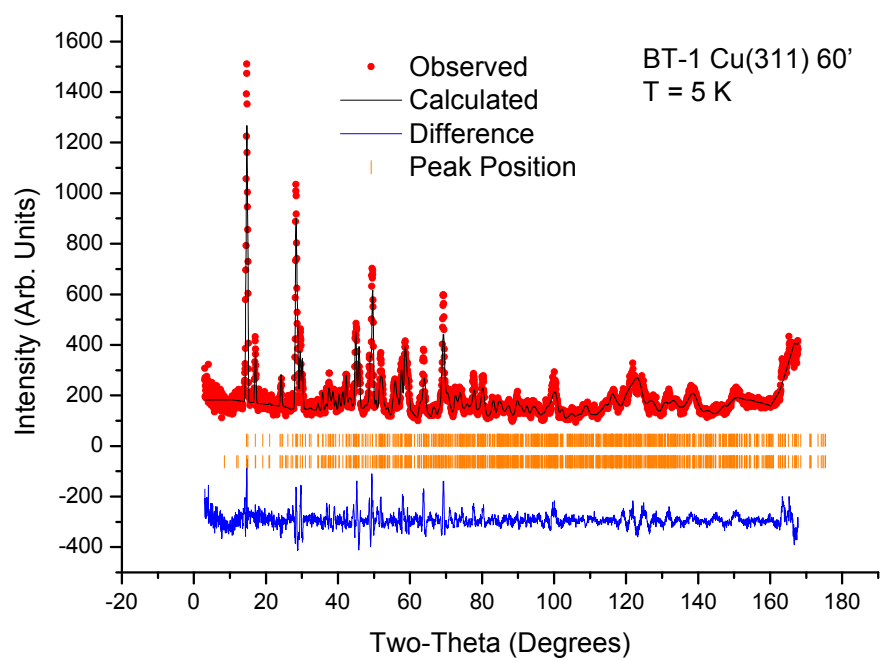


FIGURE 4.8: Fitted powder neutron diffraction data for CsFe₂F₆ using powder neutron diffraction collected on the BT1 diffractometer at 5 K. Data (red) points and calculated fit (black) are displayed in the upper curve and the difference (blue) between the observed and calculated pattern is displayed in the lower curve. Sets of vertical tick marks (orange), from top to bottom, represent the expected positions of nuclear reflections for CsFe₂F₆ and the expected magnetic reflections for CsFe₂F₆ respectively.

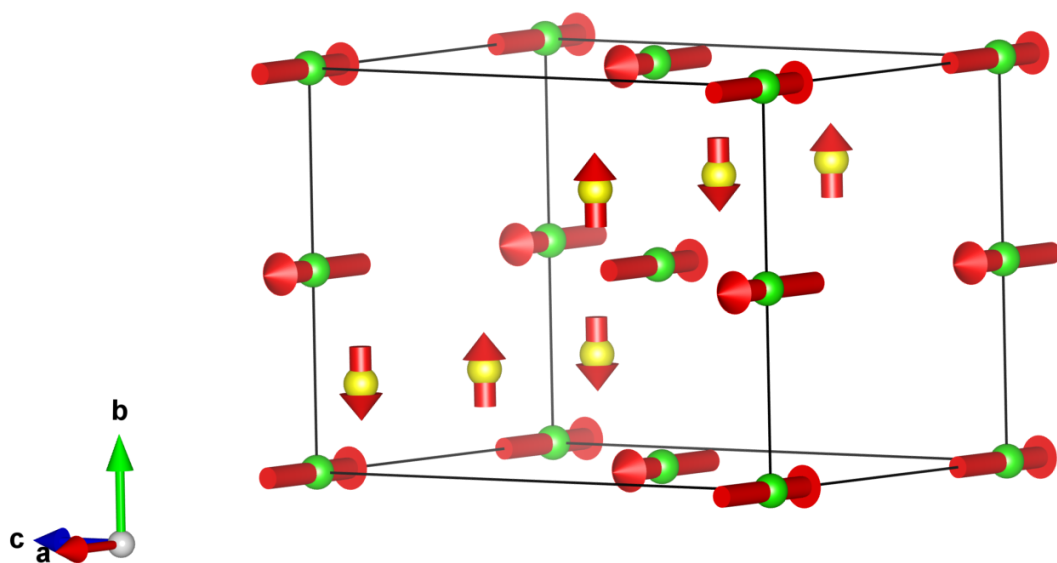


FIGURE 4.9: The magnetic structure of CsFe₂F₆ with an overall effective magnetic moment of $4.11(6)\mu_B$. The first Fe site, $(0.76, 0.25, 0.74)$, in yellow, has a magnetic moment of $1.57(2)\mu_B$ confined along the b-axis and can be described as forming antiferromagnetic chains along the a-axis. These antiferromagnetic chains are perpendicular to the moments of the second Fe at $(0.5, 0.5, 0.5)$, in green. The second Fe has a magnetic moment of $3.76(2)\mu_B$ sitting along the a-axis forming antiferromagnetic chains parallel to the b-axis. This magnetic structure is in good agreement with the magnetic structure of RbFe₂F₆ discussed in the previous Chapter.

4.3.4 Mössbauer Spectroscopy

Mössbauer Spectroscopy was used to determine the oxidation state of Fe to clarify the distribution of charge over the two separate crystallographic sites. The fitted Mössbauer absorption spectrum is shown in Figure 4.10 at 80 K, displaying the individual Fe fits and the sum of quadrupole doublets with different intensity and splitting. The fit to Fe³⁺ gives an isomer shift of $\delta = 0.538(5)$ mm/s and a quadrupole splitting of $\Delta E_Q = 0.716(9)$ mm/s and Fe²⁺ gives an isomer shift of $\delta = 1.439(6)$ mm/s and a quadrupole splitting of $\Delta E_Q = 2.835(11)$ mm/s, both with no magnetic splitting displaying the octahedral coordination of Fe³⁺ and Fe²⁺. With reference to the peak area, the ratio between Fe²⁺ and Fe³⁺ sites are similar being within 3 standard deviations, however, it is suggested that Fe³⁺ is more dominant within the system. This may be due to a small impurity that is not detectable due to poor crystallinity, or slight disorder between the Fe sites. The non-equivalence of the values for Fe³⁺ and Fe²⁺ is consistent with the structure Cs_{0.82}Fe_{0.82}²⁺Fe_{1.18}³⁺F₆. However, taking into account uncertainty, it is viable to say that we are dealing with a structure close to that of the theoretical pyrochlore.¹²⁵ CsFe₂F₆ displays similar Mössbauer parameters to other iron fluoride materials and is consistent with those already reported for CsFe₂F₆,¹²⁹ as shown in Table 4.5.

Material	Fe ²⁺	Fe ²⁺	Fe ³⁺	Fe ³⁺	Temp. (K)	Ref
	I.S(mm/s)	Q.S(mm/s)	I.S(mm/s)	Q.S(mm/s)		
Fe ₂ F ₅ .2H ₂ O	1.60	2.44	0.70	0.65	295	130
Fe ₂ F ₅ .2H ₂ O	1.71	3.28	0.81	0.58	55	130
Fe ₂ F ₅ .7H ₂ O	1.15	3.31	0.7	0.59	300	131
NH ₄ Fe ₂ F ₆	1.36	2.61	0.42	0.72	300	132
RbFe ₂ F ₆	1.315	2.664	0.474	0.720	300	13
CsFe ₂ F ₆	1.27	2.55	0.32	0.73	300	129
CsFe ₂ F ₆	1.358	2.54	0.429	0.82	300	125
CsFe ₂ F ₆	1.439(6)	2.835(11)	0.538(5)	0.716(9)	80	This Work

TABLE 4.5: Mössbauer parameters for iron fluoride materials similar to that of CsFe₂F₆ reported in this work.

4.3.5 Magnetic Properties

The magnetic susceptibility of a powder sample of CsFe₂F₆ was measured from 300 K down to 2 K. Both zero field cooled and field cooled magnetic susceptibility were measured at 100 Oe for 7.56 mg of powdered CsFe₂F₆ using a SQUID magnetometer. The data for the inverse magnetic susceptibility are shown in Figure 4.11. A clear divergence from the paramagnetic trend is seen at 22 K indicating a magnetic ordering at this temperature.

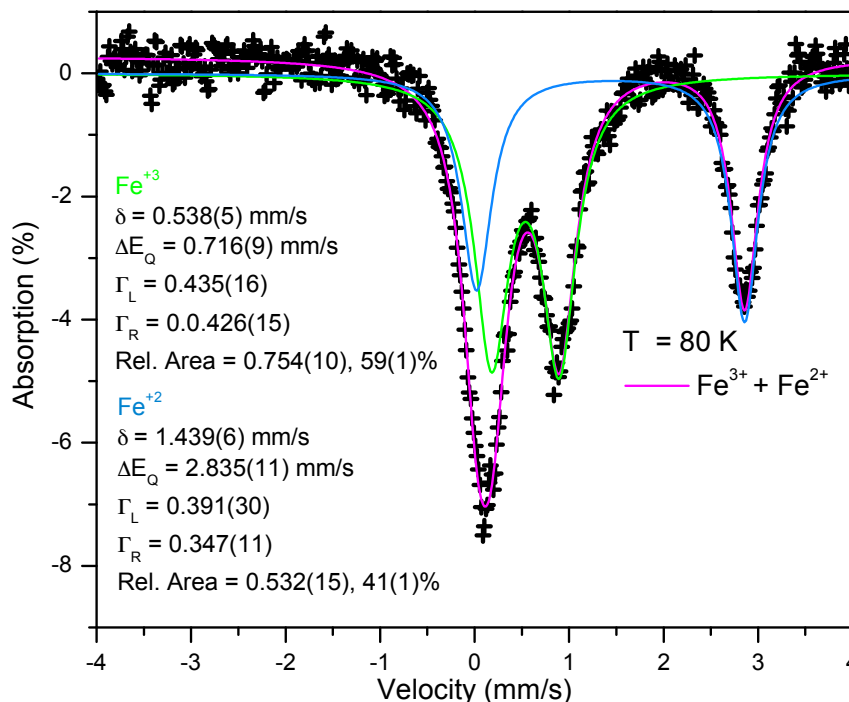


FIGURE 4.10: Mössbauer absorption spectra of CsFe₂F₆ displaying the individual Fe fits and the sum of quadrupole doublets with different intensity and splitting. The fit to Fe³⁺ gives an isomer shift of $\delta = 0.538(5)$ mm/s and a quadrupole splitting of $\Delta E_Q = 0.716(9)$ mm/s and Fe²⁺ gives an isomer shift of $\delta = 1.439(6)$ mm/s and a quadrupole splitting of $\Delta E_Q = 2.835(11)$ mm/s, both with no magnetic splitting displaying the octahedral coordination of Fe³⁺ and Fe²⁺. With reference to the peak area, the ratio between Fe²⁺ and Fe³⁺ sites are similar being within 3 standard deviations, however, it is suggested that Fe³⁺ is more dominant within the system.

The paramagnetic behaviour between 300 K to 200 K, used to calculate the effective magnetic moment and the Weiss temperature, is displayed in Figure 4.12, where the data are fitted with least-squares regression line and the inset shows the linear magnetization vs. field behaviour. The Curie-Weiss temperature has been calculated as $\theta_{CW} = -304(2)$ K indicating a strong antiferromagnetic interaction between the Fe moments consistent with low temperature neutron diffraction analysis. The calculated effective magnetic moment calculated is $8.71\mu_B$ which is in good agreement with the theoretical spin only value of $7.7\mu_B$ (Fe³⁺ = $5.9\mu_B$, Fe²⁺ = $4.9\mu_B$). The frustration index of CsFe₂F₆ is calculated to be 18.9(8), suggesting a largely frustrated material especially when compared to the ordering temperature of 22 K.

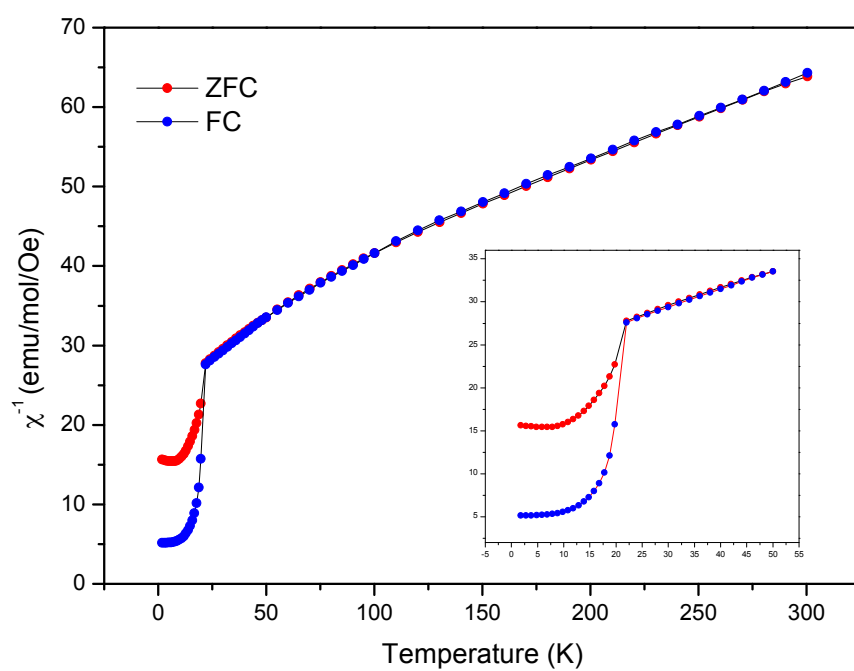


FIGURE 4.11: Temperature dependence of the inverse magnetic susceptibility with the inset showing a close up of the low temperature region where a phase transition takes place at 22 K.

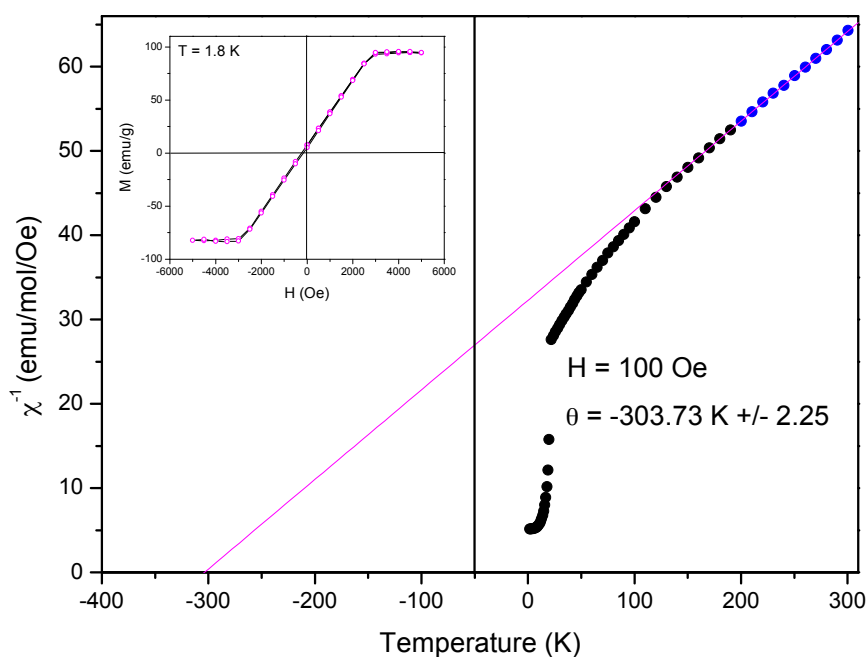


FIGURE 4.12: The magnetic susceptibility for a powder sample of CsFe₂F₆. The inverse suitability as a function of temperature is displayed throughout the paramagnetic region and the fit of this region between 300 K and 200 K is shown. From the fit the effective magnetic moment is calculated as $\mu_{eff} = 8.71 \mu_B$, and the Curie-Weiss constant is $\theta_{CW} = -304(2)$ K. The inset shows the linear magnetisation vs. field at 1.8 K.

4.4 Conclusion

We have synthesised CsFe₂F₆ using a new low temperature hydrothermal method. The first powder neutron diffraction analysis has been carried out exhibiting a pyrochlore-like structure. Antiferromagnetic ordering is observed below 22 K in both SQUID and neutron data, with no obvious structural phase transitions occurring below 300 K. Abnormalities are seen in the negative thermal expansion of lattice parameters and unit cell volume below 50 K suggesting short range correlations before ordering at 22 K. The divergence in the ZFC/FC magnetometry data implies disorder and high levels of magnetic frustration. This is supported by the calculated effective magnetic moment from neutron diffraction data being significantly lower than the theoretical magnetic moment. SQUID data exhibits an effective moment more related to that of the theoretical value. It is possible that there is a disorder in Fe sites throughout the system. This could be inferred from the significantly lower magnetic moment obtained from powder neutron diffraction data, the difference in peak area of both Fe ions from Mössbauer spectroscopy and the larger effective magnetic moment from SQUID magnetometry measurements. This would partially explain the high levels of magnetic frustration.

Chapter 5

Mixed Transition Metal Pyrochlore Fluorides

5.1 Introduction

Typically, materials with the general formula $AM^{2+}M^{3+}F_6$ crystallise in an orthorhombic $Pnma$ space group or cubic $Fd-3m$ space group. Those that crystallise in a $Pnma$ space group include $KCuAlF_6$, $RbAgFeF_6$ and $CsAgAlF_6$.¹³³⁻¹³⁵ There are over one-hundred materials that crystallise in an $Fd-3m$ space group with a structure-type of $RbNiCrF_6$, these include $ACoCrF_6$, $AMgCrF_6$, $ANiCrF_6$ ($A = Rb, Cs$)¹³⁶. Ordering between the M^{2+} and M^{3+} metals is only observed in the $Pnma$ space group and these materials tend to exhibit long range antiferromagnetic ordering at low temperatures whereas materials that crystallise in the $Fd-3m$ space group typically display spin-glass type behaviour. In both cases networks/chains of corner sharing octahedra leave interconnected tunnels in which the A metal cation resides. Generally, when the A cation is monovalent, the divalent and trivalent transition metals are disordered. Charge order has been observed for $RbFe_2F_6$,¹³ $CsFe_2F_6$ ⁵⁸ and $NH_4Fe_2F_6$,¹²⁷ and Jahn-Teller effect which compresses the MF_6 octahedra for M^{2+} cations in $CsCuAlF_6$ ¹³⁵ or $CsAgAlF_6$,¹³⁵ lead to cation order.¹³⁷

$RbFeCrF_6$ has previously been prepared by heating stoichiometric amounts of RbF , FeF_2 and CrF_3 in a sealed platinum tube under dry argon. The platinum tube was heated overnight at 500 °C and the sample ground under dry argon before being heated again for three days at 800 °C. $RbFeCrF_6$ is reported to crystallise in the $Fd-3m$ space group displaying a modified pyrochlore structure with lattice parameter $a = 10.274 \text{ \AA}$ and a density of 3.763 g/cm^3 . The Fe^{2+} and Cr^{3+} are disordered over the 16c site¹³⁸ and although a report has been made of the structure. The same study reports the

room temperature Mössbauer spectroscopy data and the magnetic susceptibility data, where by isomer shifts are consistent with Fe^{2+} and a suggested antiferromagnetic ordering occurs below 5 K, consistent with the appearance of a broad magnetic hyperfine pattern.¹³⁸ Figure 5.1 displays the previously reported cubic $Fd-3m$ space group structure. This Chapter discusses a newly synthesised, charge ordered, spin-glass $RbFeCrF_6$ exhibiting the orthorhombic pyrochlore $Pnma$ space group.

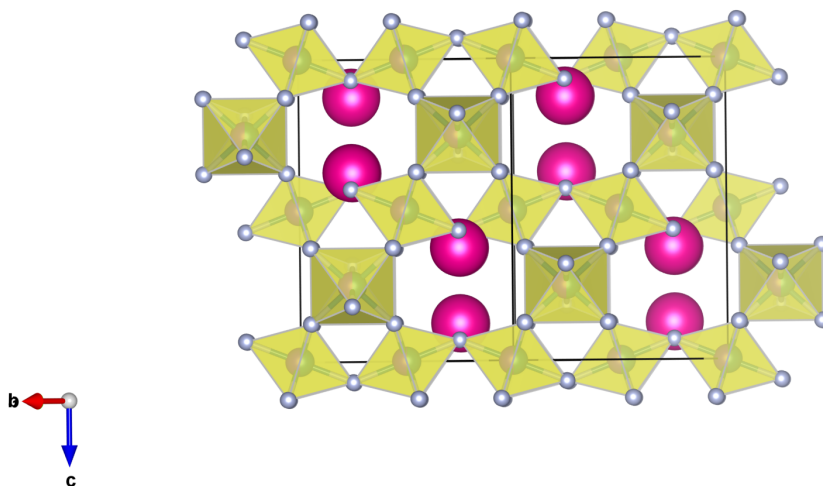


FIGURE 5.1: Previously reported structure of $RbFeCrF_6$, where Rb = pink and the disordered Fe/Cr octahedra are in yellow, crystallising in the $Fd-3m$ space group with lattice parameter $a = 10.274 \text{ \AA}$.¹³⁸

5.2 Experimental

5.2.1 Reagents

The reagents used were CsF (Alfa Aesar, 99%), RbF (Alfa Aesar, 99%), CoF_3 (Alfa Aesar, 99%), NiF_2 (Alfa Aesar, 97%), CrF_3 (Alfa Aesar, 99.98%) FeF_3 anhydrous (Alfa Aesar, 97% min), FeF_2 anhydrous (Alfa Aesar, 99%) and CF_3COOH (Alfa Aesar, 99%) without any further modification of purification.

5.2.2 Synthesis

The hydrothermal synthesis of $ACoCrF_6$, $ANiCrF_6$ and $RbFeCrF_6$ (where A = Cr, Rb) was performed using Parr Instrument Company general purpose acid digestion vessels with an internal volume of 45 ml. 2.28×10^{-3} mol of AF, $M^{2+}F_2$ and $M^{3+}F_3$ were added

to 3 ml (3.90×10^{-2} mol) of CF_3COOH , and 5 ml of H_2O in an autoclave. The autoclave was sealed and gradually heated to $230^\circ C$, held for 24 h before being cooled to room temperature at a rate of $0.1^\circ C/min$. The mother liquid was decanted and the remaining solid washed with H_2O using gravity filtration. The sample was then dried for ≈ 12 h at $70^\circ C$ before analysis.

5.3 Results and Discussion

5.3.1 $RbFeCrF_6$

Crystallographic Structure

Hydrothermal synthesis of $RbFeCrF_6$ produced single crystals which were analysed using a Rigaku Single Crystal SuperNova Diffractometer at 150 K using a molybdenum X-ray source (0.71073 \AA). The resulting data are then analysed using the SHELXL software in collaboration with Jake Minns, University of Kent. Table 5.1 shows the refined crystallographic parameters. The structure was refined in the $Pnma$ space group, with lattice parameters $a = 7.0517(9) \text{ \AA}$, $b = 7.3201(7) \text{ \AA}$ and $c = 10.1210(11) \text{ \AA}$, the structure exhibits a 3D structure comprising of Rb^+ cations located between corner-sharing FeF_6 and CrF_6 octahedra, similar to that of $RbFe_2F_6$ and $CsFe_2F_6$.^{13,58} The $Cr^{3+}F_6$ chains are connected through $Fe^{2+}F_6$ octahedra along the c-axis where the $Fe^{2+}F_6$ octahedra share corners along the b-axis. The $Fe^{2+}F_6$ octahedra share corners along the a-axis connected through $Cr^{3+}F_6$ octahedra along the c-axis. The structure of $RbFeCrF_6$ is shown in Figure 5.2 displaying the FeF_6 and CrF_6 sub-lattices and the Kagome plane which result from the octahedral connectivity in both planes. Relevant atomic coordinates and bond distances are shown in Table 5.2 and Table 5.3 respectively. Unlike typical defect pyrochlores and similar to $RbFe_2F_6$ and $CsFe_2F_6$,^{13,58} $RbFeCrF_6$ does not show any signs of site disorder or partial occupancy, however, through single crystal diffraction alone it can not be confirmed. During the refinement Rb occupancy was initially refined but then set to full occupancy (1) because of the close to 1 value. In comparison to the bond distances of $RbFe_2F_6$ and $CsFe_2F_6$, the Fe-F distances in $RbFeCrF_6$ are more comparable to those of $Fe^{3+}-F$, with three distances, ranging from $1.901(4) \text{ \AA}$ - $1.9255(17) \text{ \AA}$. The bond distances of Cr-F range between $2.085(4) \text{ \AA}$ - $1.963(3) \text{ \AA}$ comparable to those of $Fe^{2+}-F$. The atomic coordinates are comparable to those of $RbFe_2F_6$ ¹³ and $CsFe_2F_6$ with a goodness of fit value of 0.939 indicating that the overall structural characterisation is correct. The checkcif file associated with this refinement is attached in Appendix C.

Parameter	RbFeCrF ₆
Formula Weight, fw	307.30 g mol ⁻¹
Temperature (K)	150
λ (Å)	0.71073
Crystal Structure	Orthorhombic
Space Group	<i>Pnma</i> (No.62)
a (Å)	7.0517(9)
b (Å)	7.3201(7)
c (Å)	10.1210(11)
V (Å ³)	522.43(10)
Z	4
ρ_{calc} (g/cm ³)	5.399
2θ max.	28.6840
GOF	0.939

TABLE 5.1: Crystallographic data for RbFeCrF₆ obtained through rietveld refinement of single crystal X-ray diffraction.

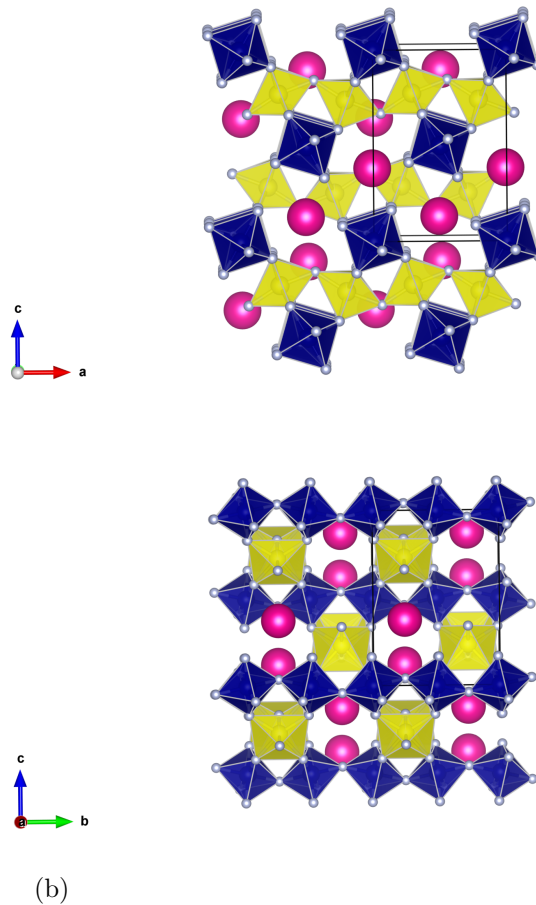


FIGURE 5.2: RbFeCrF₆ three-dimensional crystal structure obtained from single crystal diffraction where pink, dark blue and yellow represent Rb, Cr³⁺F₆ polyhedra and Fe²⁺F₆ polyhedra respectively. Kagome planes are the result of the octahedral connectivity in both planes.

Atom	x	y	z
Rb	0.99081	0.25000	0.37611
Cr	0.79161	0.25000	0.73268
Fe	0.50000	0.00000	0.50000
F3	0.73450	0.06300	0.58490
F2	0.43920	0.25000	0.45900
F1	0.55820	0.25000	0.83850
F4	0.36890	0.01540	0.66370

TABLE 5.2: Atomic coordinates for RbFeCrF₆

Bond	Distance Å	Bond	Distance Å
Rb - F(1)	2.928(5)	Cr(1) - F(1)	1.963(5)
Rb - F(2)	3.270(6)	Cr(1) - F(1)	2.0125(5)
Rb - F(3)	3.026(4) × 2	Cr(1) - F(3)	2.068(4) × 2
Rb - F(3)	3.099(4) × 2	Cr(1) - F(4)	2.085(4) × 2
Rb - F(4)	3.062(4) × 2	Fe(1) - F(2)	1.9255(17) × 2
Rb - F(4)	3.220(4) × 2	Fe(1) - F(3)	1.919(4) × 2
		Fe(1) - F(4)	1.901(4) × 2
		Cr(1) - Fe(1)	3.6226(9) × 2
		Cr(1) - Fe(1)	3.5820(9) × 2
		Fe(1) - Fe(1)	3.6615(4) × 2
		Cr(1) - Cr(1)	3.5412(4) × 2

TABLE 5.3: Relevant bond distances of RbFeCrF₆.

Mössbauer Spectroscopy

Mössbauer spectroscopy was used to determine the oxidation state of Fe and give an indication of the ordering over the two crystallographic sites. The Mössbauer absorption spectrum at 80 K and fit of Fe^{3+} and Fe^{2+} is shown in Figure 5.3. The fit to Fe^{3+} gives an isomer shift of $\delta = 0.365(8)$ mm/s and a quadrupole splitting of $\Delta E_Q = 1.002(30)$ mm/s and Fe^{2+} gives an isomer shift of $\delta = 1.453(2)$ mm/s and a quadrupole splitting of $\Delta E_Q = 2.846(3)$ mm/s, with no magnetic splitting. With reference to the peak area, the ratio between Fe^{2+} and Fe^{3+} sites is 0.920(12) to 0.104, respectively indicating that there is a small amount of Fe^{3+} present. Even though suspected charge ordering is exhibited between Fe^{2+} and Cr^{3+} , from these measurements it suggests that there may be a small amount of Cr^{2+} on the 4a Fe^{2+} position and Fe^{3+} on the 4c Cr^{3+} position. Alternatively, there may be disorder over both sites with Fe^{3+} positioned on the Fe^{2+} site and Cr^{2+} positioned on the Cr^{3+} site. From Mössbauer Spectroscopy only a small amount of Fe^{3+} is present which, if charge disorder occurs, may not be enough for the structure to crystallise in the $Fd-3m$ space group, unlike other charge disordered mixed metal fluorides.

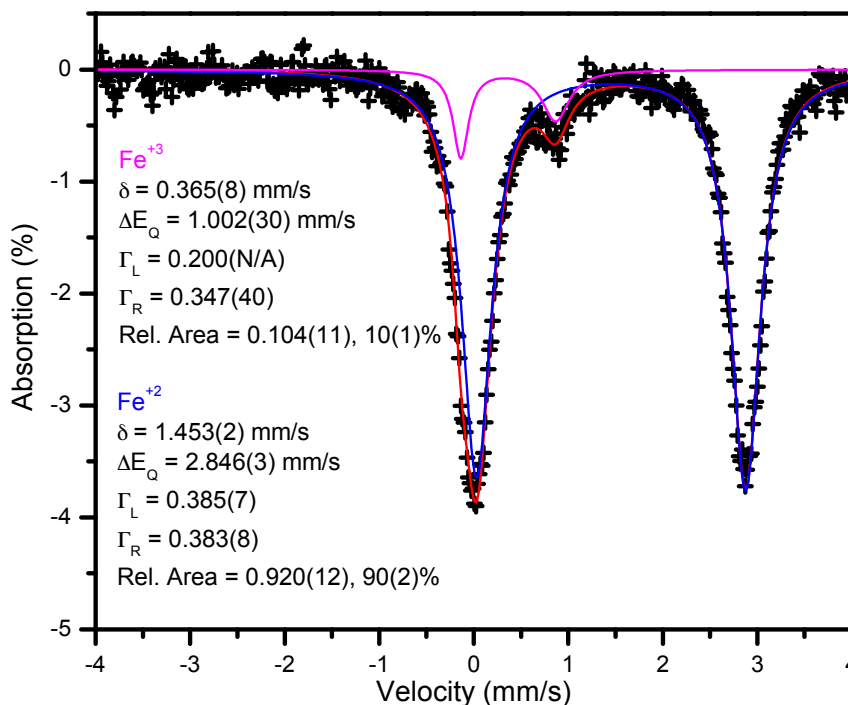


FIGURE 5.3: Mössbauer absorption spectra of $RbFeCrF_6$ at 80 K displaying the individual Fe fits. The values for the isomer shift and quadrupole splitting of each Fe present is given in the Figure. The ratio between Fe^{2+} and Fe^{3+} is 9:1 respectively. No magnetic splitting is observed.

Magnetic Properties

The magnetic properties of polycrystalline $RbFeCrF_6$ have been analysed using dc-susceptibility down to 1.8 K using both field-cooled (FC) and zero-field-cooled (ZFC) data. Figure 5.4 and 5.5 displays temperature variation of the dc magnetic susceptibility and inverse susceptibility in a temperature range 1.8 K - 300 K with an applied external field of 1 kOe representatively. The inset in Figure 5.4 shows an expanded region at low temperature where there is a clear bifurcation between FC and ZFC curves possibly indicating spin glass properties and collective spin freezing with the absence of long range magnetic ordering. It is important to compare with many materials that report spin glassiness, displaying a sharp maximum in ZFC susceptibility, a divergence between ZFC and FC curves below $T_{(f)}$, where $T_{(f)}$ is the temperature at which spin freezing occurs, and also lack long-range magnetic ordering.^{139,140} Neutron scattering along with ac susceptibility is the only definitive way of demonstrating spin glass properties over other possible magnetic states.

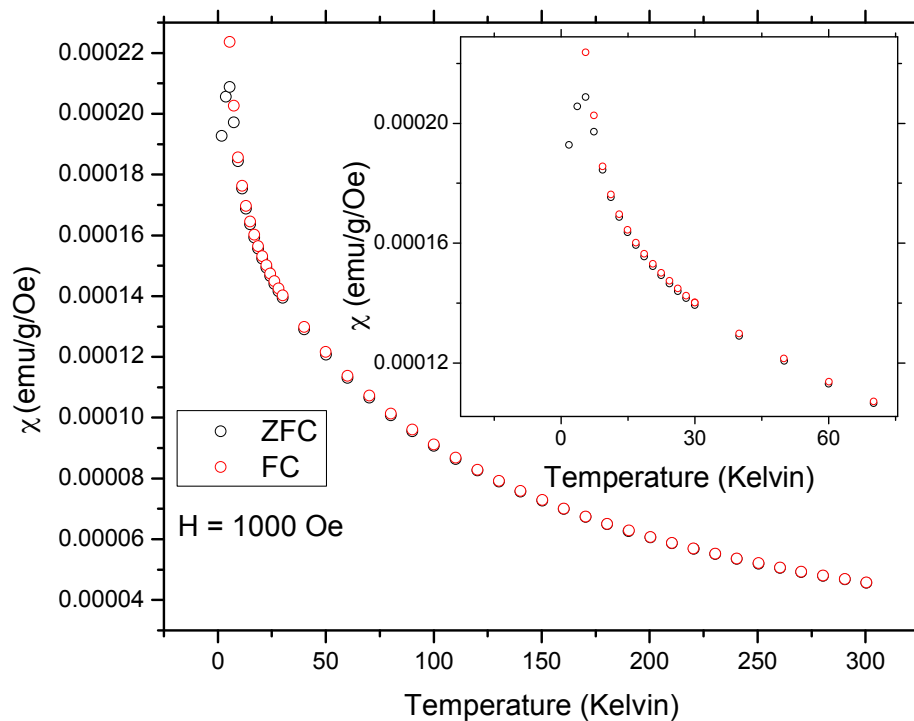


FIGURE 5.4: Temperature variation of ZFC and FC dc magnetic susceptibility in a temperature range 1.8 K - 300 K with an applied external field of 1 kOe. Inset shows the clear bifurcation between ZFC and FC curves typical of spin glass character.

The extrapolation of the paramagnetic region of the inverse susceptibility of $RbFeCrF_6$ in accordance with the Curie-Weiss law is shown in Figure 5.5. The inset shows a close

up of the low temperature region which deviates from typical paramagnetic behaviour. The calculated magnetic moment of the paramagnetic regions is calculated as $0.018\mu_B$ which is in poor agreement with the theoretical spin only value of $6.2\mu_B$ ($Cr^{3+} = 3.87\mu_B$, $Fe^{2+} = 4.9\mu_B$) indicating that Fe^{2+} is potentially in a low-spin state. The extrapolated region gives a calculated Weiss temperature of $\theta_{CW} = -100$ K being exceptionally large compared to the spin freezing temperature, giving a frustration index of $f = 18$, with the frustration index (f) being defined by $f = -\theta/T^*$, where θ is the Weiss temperature and T^* is the magnetic ordering transition. Normally a frustration index of larger than 10 it is considered as a highly frustrated magnet.

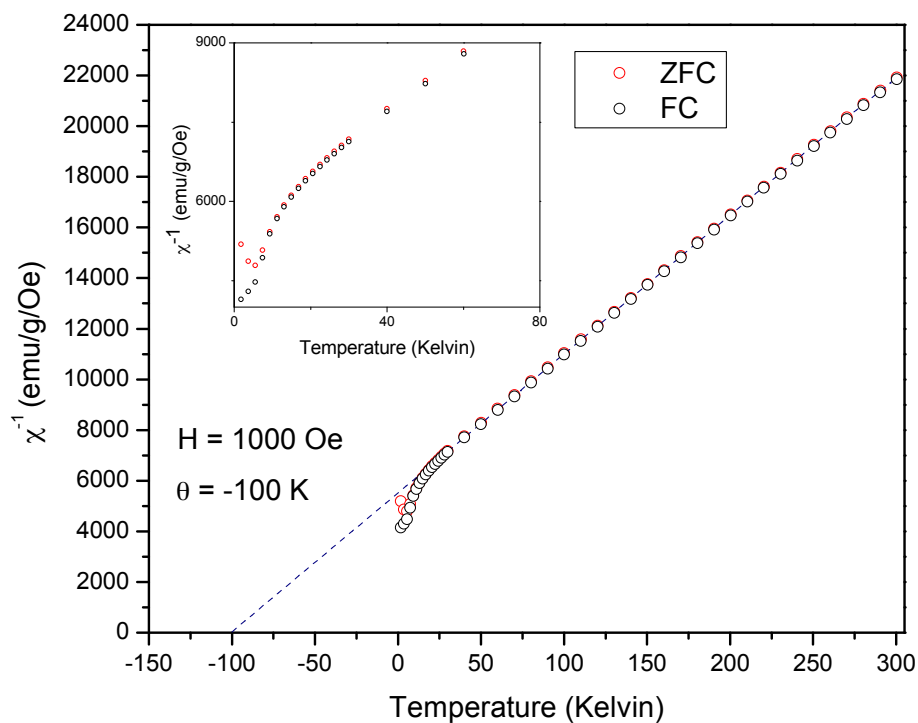


FIGURE 5.5: Inverse susceptibility versus temperature of $RbFeCrF_6$ in a temperature range of 1.8 K - 300 K and an applied magnetic field of 1 kOe. The Curie-Weiss fit (line) with the Curie-Weiss temperature $\theta_{CW} = -100$ K and an effective moment of $0.018\mu_B$. The inset shows a close up of the low temperature deviation from paramagnetic behaviour.

In Figure 5.6, magnetization (M) vs. applied field (H) at 2 K, 20 K and 200 K is shown for $RbFeCrF_6$, in the range of -20 kOe to 20 kOe. At 2 K the MH loops show a small S-like shape which is a typical feature of spin glass materials. Increasing the temperature transforms the S-like shape into a linear paramagnetic shape and at 20 K and 200 K the MH loop is entirely straight indicative of a paramagnetic state. The inset to Figure 5.6

examines the MH loop at 2 K, below $T_{(f)}$, at low applied fields which suggests a coercive field $H_c \approx 250$ Oe.

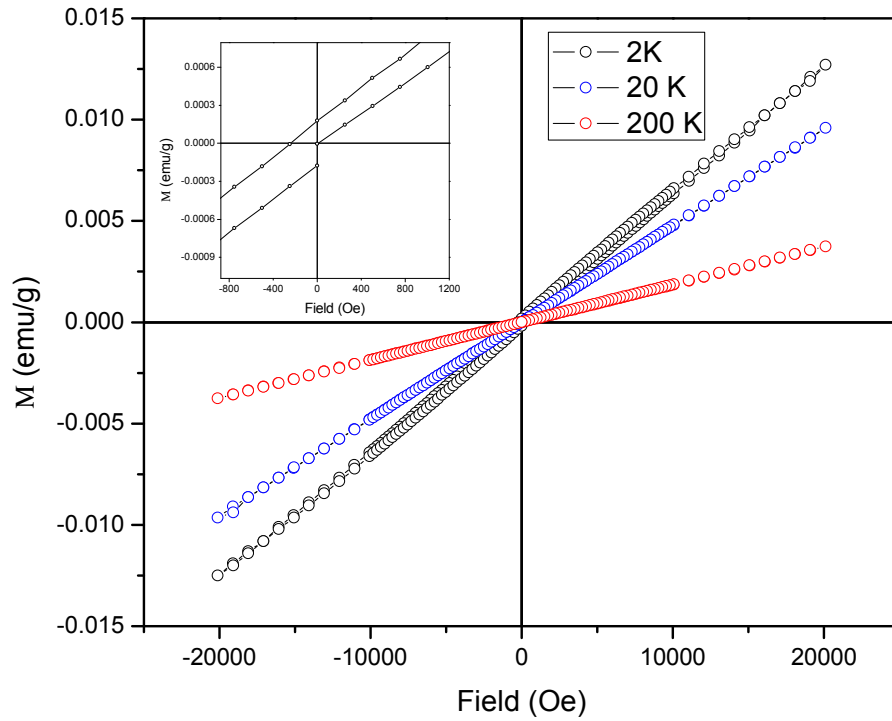


FIGURE 5.6: The hysteresis, magnetization (M) vs. applied field (H), loop at 2 K, 20 K and 200 K for RbFeCrF_6 . The inset shows the low field measurements for 2 K suggesting a coercive field $H_c \approx 250$ Oe.

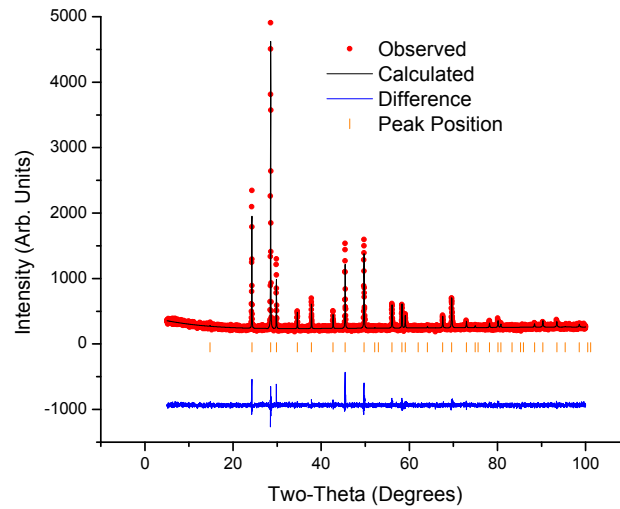
5.3.2 Cubic Mixed Metal Fluorides

The results from this study suggest that RbFeCrF₆ has spin glass magnetic behaviour and does not undergo long range magnetic ordering at low temperatures unlike similar materials, CsFe₂F₆ and RbFe₂F₆. However, similar to CsFe₂F₆ and RbFe₂F₆, RbFeCrF₆ potentially displays crystallographic charge ordering between the two transition metals. A series of other mixed metal fluorides have been synthesised and are heavily reported in the literature with the general formula AM²⁺M³⁺F₆ for comparative purposes. Hydrothermal synthesis, described earlier, produced powder samples of ACoCrF₆ and ANiCrF₆ (where A = Cs, Rb) which were all analysed using in-house powder X-ray diffraction for structure determination. Due to low yield, zero background loading was chosen using a Cu monochromator with a wavelength of 1.5418 Å. Each structure was then refined using the Rietveld method using the FullProf software. An example set of CsCoCrF₆ and RbCoCrF₆ is shown in Figure 5.7, CsNiCrF₆ and RbNiCrF₆ is shown in Figure 5.8. Tables 5.4 and 5.5 display the refined crystallographic parameters respectively. All materials crystallise in the cubic *Fd-3m* space group with a defect pyrochlore structure, exhibiting crystallographic disorder of the M²⁺ and M³⁺ transition metal ions. Comparing the lattice parameters of CsMCrF₆ to RbMCrF₆ shows a consistent increase due to the larger A-site cation, an increase in volume is also observed as expected. Corner sharing MF₆ octahedra leaves interconnecting tunnels in which the A cation resides for all materials. An example of the typical cubic *Fd-3m* space group crystal structure that each material adopts is displayed in Figure 5.9.

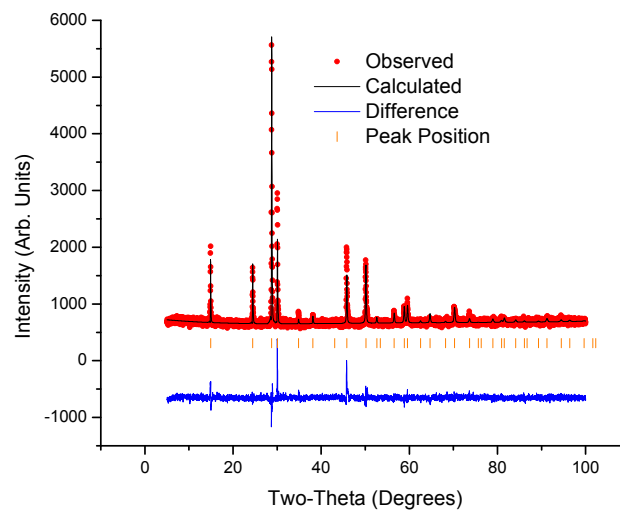
Parameter	CsCoCrF ₆	RbCoCrF ₆
Formula Weight, g mol ⁻¹	357.83	310.39
Temperature (K)	296	296
λ (Å)	1.54059	1.54059
Crystal Structure	Cubic	Cubic
Space Group	<i>Fd-3m</i> (No.227)	<i>Fd-3m</i> (No.227)
a(Å)	10.364(4)	10.2813(3)
b(Å)	10.364(4)	10.2813(3)
c(Å)	10.364(4)	10.2813(3)
V (Å ³)	1113.32(8)	1086.78(5)
Z	8	8
ρ _{calc} (g/cm ³)	4.270	3.795
2θ max.	99.990082	99.990082
GOF	1.5	1.6

TABLE 5.4: Crystallographic data for CsCoCrF₆ and RbCoCrF₆ obtained through rietveld refinement of Powder X-ray diffraction.

Samples synthesised with Ni or Co in replacement of Fe refined in the *Fd-3m* space group with lattice parameters ranging from 10.364(4) Å - 10.223(2) Å. ACoCrF₆ and ANiCrF₆

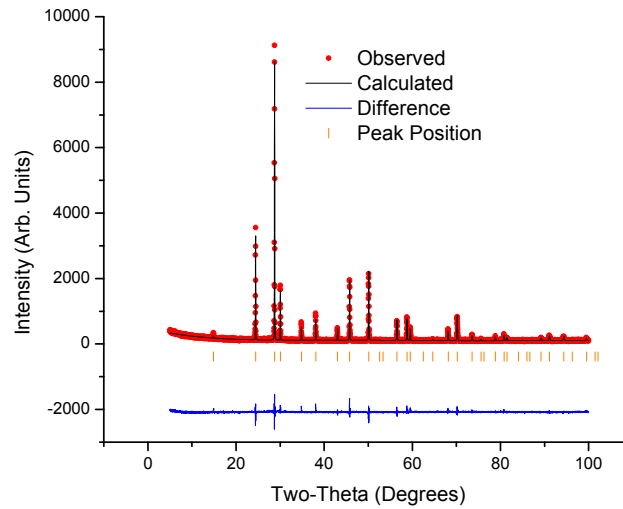


(a)

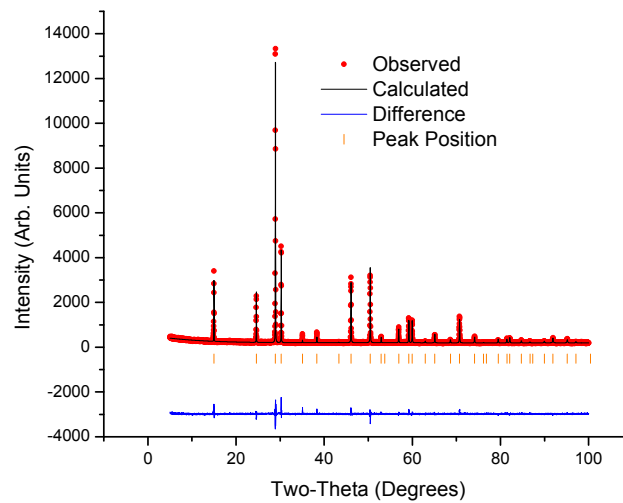


(b)

FIGURE 5.7: Fitted diffraction profiles for (a) $CsCoCrF_6$ and (b) $RbCoCrF_6$ using powder X-ray diffraction collected at 296 K. Data points and calculated fit are displayed in the upper curve and the difference between the observed and calculated pattern is displayed in the lower curve. Sets of vertical tick marks represent the expected positions of nuclear reflections for each material. The fit parameters are $\chi^2 = 2.23$, $R_p = 6.55\%$ and $R_{wp} = 8.67\%$ and $\chi^2 = 2.47$, $R_p = 4.11\%$ and $R_{wp} = 5.89\%$ for $CsCoCrF_6$ and $RbCoCrF_6$ respectively.



(a)



(b)

FIGURE 5.8: Fitted diffraction profiles for (a) $CsNiCrF_6$ and (b) $RbNiCrF_6$ using powder X-ray diffraction collected at 296 K. Data points and calculated fit are displayed in the upper curve and the difference between the observed and calculated pattern is displayed in the lower curve. Sets of vertical tick marks represent the expected positions of nuclear reflections for each material. The fit parameters are $\chi^2 = 2.42$, $R_p = 9.43\%$ and $R_{wp} = 12.3\%$ and $\chi^2 = 2.73$, $R_p = 7.38\%$ and $R_{wp} = 9.71\%$ for $CsNiCrF_6$ and $RbNiCrF_6$ respectively.

Parameter	CsNiCrF ₆	RbNiCrF ₆
Formula Weight, g mol ⁻¹	357.59	310.15
Temperature (K)	296	296
λ (Å)	1.54059	1.54059
Crystal Structure	Cubic	Cubic
Space Group	$Fd-3m$ (No.227)	$Fd-3m$ (No.227)
a (Å)	10.289(2)	10.223(2)
b (Å)	10.289(2)	10.223(2)
c (Å)	10.289(2)	10.223(2)
V (Å ³)	1089.48(4)	1068.58(3)
Z	8	8
ρ_{calc} (g/cm ³)	4.411	4.073
2θ max.	99.990082	99.990082
GOF	1.6	1.6

TABLE 5.5: Crystallographic data for CsNiCrF₆ and RbNiCrF₆ obtained through rietveld refinement of Powder X-ray diffraction.

materials have been heavily documented in the literature and exhibit consistent spin glass behaviour similar to RbFeCrF₆.^{141,142} Dc-susceptibility measurements have been carried out on CsCoCrF₆ and Figure 5.10 displays the field-cooled (FC) and zero-field-cooled (ZFC) inverse susceptibility data between 1.8 K - 300 K. There is a clear deviation

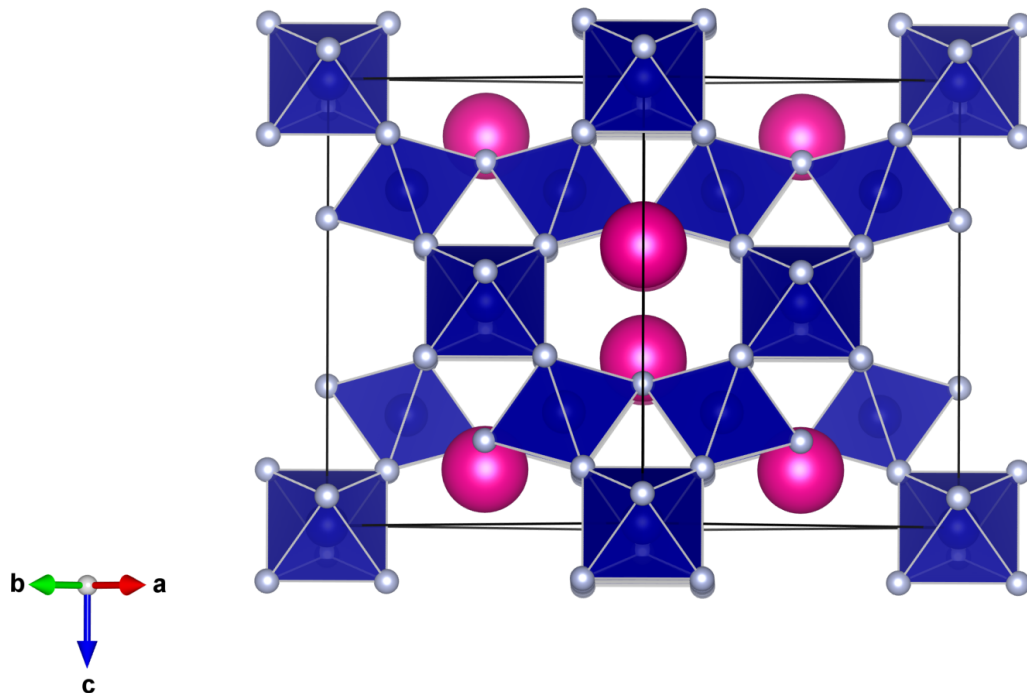


FIGURE 5.9: An example of the typical cubic $Fd-3m$ space group crystal structure that ACoCrF₆ and ANiCrF₆ (where A = Cs, Rb) adopt. The corner sharing MF₆ octahedra are shown in blue and the A cation in pink.

between FC and ZFC data at approximately 3 K typical of the spin-glass transition and similar to that of $RbFeCrF_6$, discussed above. Studying the magnetisation at higher temperatures and extrapolation of the paramagnetic region gives a $\theta_{CW} = -62$ K. This indicated that the magnetic interactions are antiferromagnetic and relatively strong, this is consistent with previous studies.¹⁴³ An investigation into the magnetization of $CsNiCrF_6$ was conducted using the same instrumental parameters as $CsCoCrF_6$. Figure 5.11 displays the (FC) and (ZFC) inverse susceptibility data between 1.8 K - 300 K, however, no deviation is observed between FC and ZFC data. Extrapolation of the paramagnetic region gives $\theta_{CW} = -41$ K, indicating relatively weak antiferromagnetic interactions.

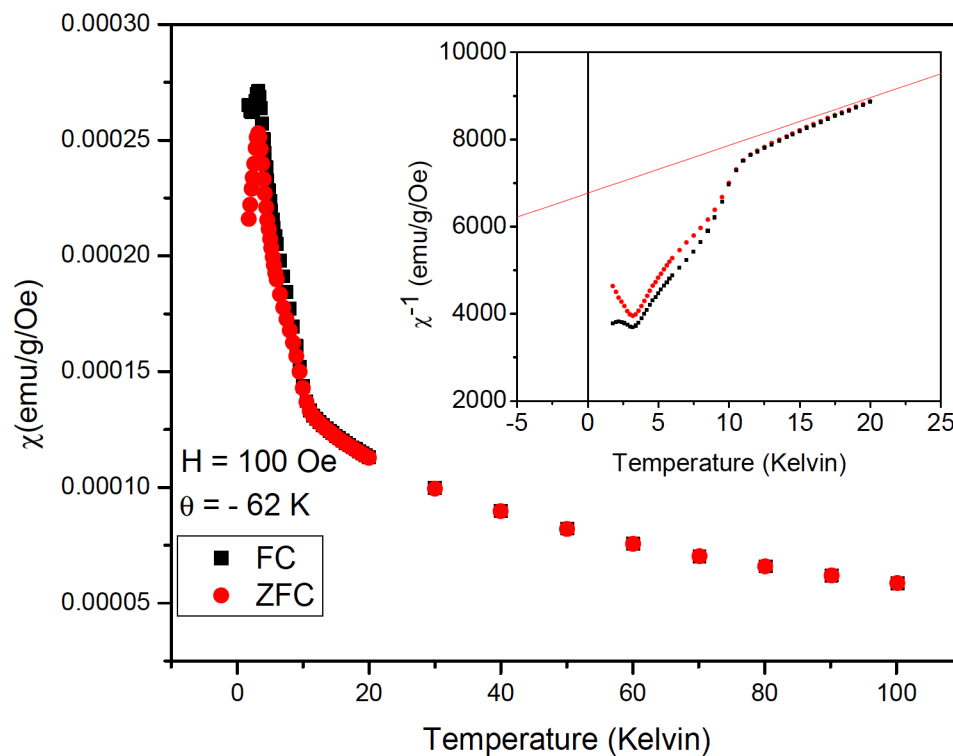


FIGURE 5.10: Temperature variation of ZFC and FC dc magnetic susceptibility of $CsCoCrF_6$ in a temperature range 1.8 K - 300 K with an applied external field of 100 Oe. The inset shows the inverse susceptibility versus temperature in a range of 1.8 K - 20 K. The Curie-Weiss fit (line) has been extrapolated from a higher temperature region (200 K - 300 K) not shown, with the Curie-Weiss temperature $\theta_{CW} = -62$ K.

The BT1 instrument was used to collect neutron diffraction data from a powdered sample of $CsNiCrF_6$ at 5 K to investigate any long range magnetic ordering. Approximately 4 g of $CsNiCrF_6$ was loaded into a vanadium can and mounted into a CCR, closed cycle refrigerator. A Cu(311) monochromator with a 90° take-off-angle, $\lambda = 1.540 \text{ \AA}$, and an in-pile collimation of 60 minute of arc was used. Figure 5.12 shows the fit of experimental

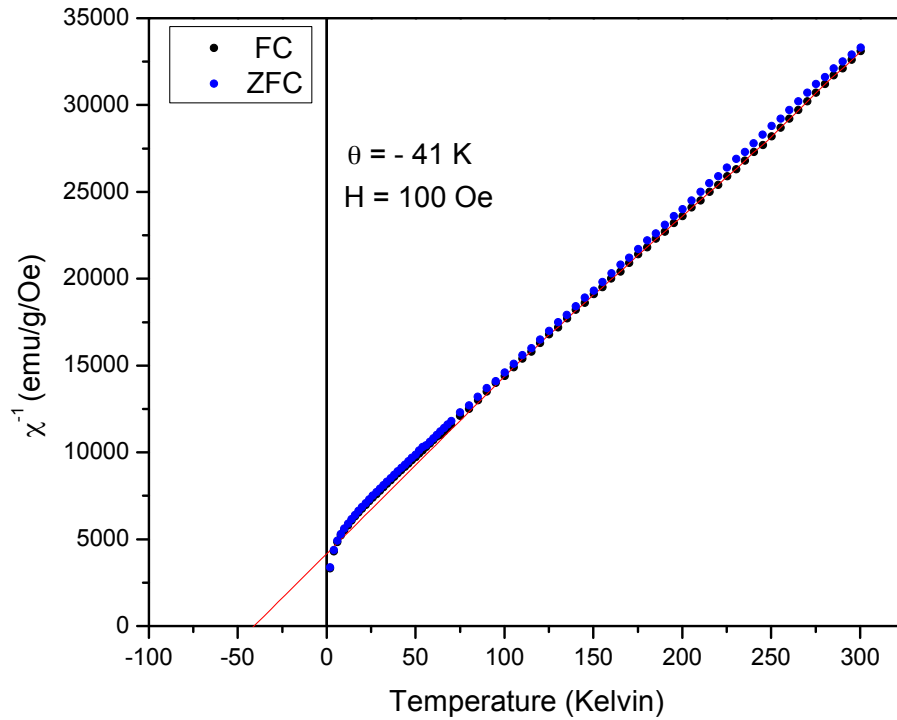


FIGURE 5.11: Inverse susceptibility versus temperature of $CsNiCrF_6$ in a temperature range of 1.8 K - 300 K and an applied magnetic field of 100 Oe. The Curie-Weiss fit (line) with the Curie-Weiss temperature $\theta_{CW} = -41$ K.

data and calculated model, where the fit parameters are $\chi^2 = 3.19$, $R_p = 4.15\%$ and $R_{wp} = 5.39\%$. No long range magnetic ordering was observed at 5 K as expected from the dc-susceptibility data, however, short range diffuse scattering is observed at low angles, indicating the presents of short-range antiferromagnetic ordering. This is in agreement with previous reports of $CsNiCrF_6$ ^{144,145}

It is suggested that $RbFeCrF_6$ magnetically behaves similarly to $CsCoCrF_6$ forming clusters of antiferromagnetically coupled spins with a weak magnetic moment ordering at low temperatures. The spin glass behaviour prevents conventional long range order. It is suggested that although potential charge ordering occurs, possibly driven by the Jahn-Teller distortion of the Fe^{2+} if in high-spin state, there may be a small amount of Fe^{3+} present on the 4c Cr^{3+} position or alternatively on the Fe^{2+} position. This would account for the spin glass type behaviour of $RbFeCrF_6$.

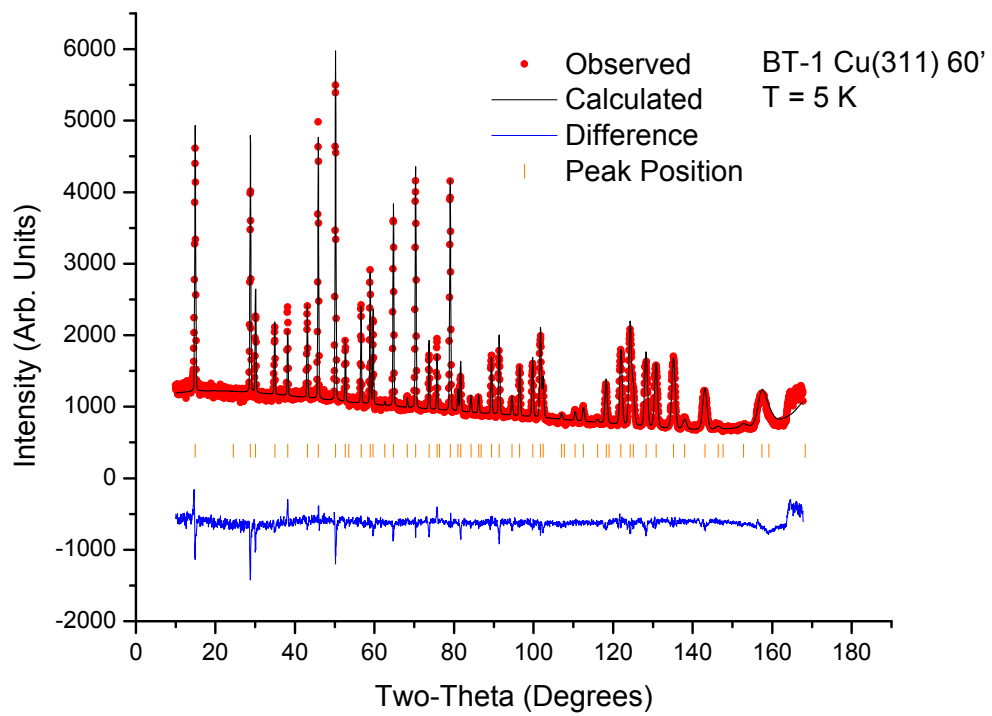


FIGURE 5.12: Fitted diffraction profile for $CsNiCrF_6$ using powder neutron diffraction collected on the BT1 diffractometer at 5 K. Data points (red) and calculated fit (black) are displayed in the upper curve and the difference (blue) between the observed and calculated pattern is displayed in the lower curve. Sets of vertical tick marks (orange) represent the expected positions of nuclear reflections for $CsNiCrF_6$. The fit parameters are $\chi^2 = 3.19$, $R_p = 4.15\%$ and $R_{wp} = 5.39\%$.

5.4 Conclusion

A new pyrochlore-type charge-ordered highly frustrated spin glass material, RbFeCrF₆, has been reported. Similar to CsFe₂F₆ and RbFe₂F₆, RbFeCrF₆ crystallises in the *Pnma* space group, with lattice parameters $a = 7.0517(9) \text{ \AA}$, $b = 7.3201(7) \text{ \AA}$ and $c = 10.1210(11) \text{ \AA}$ exhibiting a 3D structure comprising of Rb cations located between corner-sharing FeF₆ and CrF₆ octahedra. Mössbauer Spectroscopy suggests that a small amount of Fe³⁺ is present, most likely located on the 4c position causing the observed spin-glass like behaviour. The reason for crystallographic ordering between the transition metals is potentially due to Jahn-Teller distortion of the Fe²⁺ ion if in the high-spin state.

Low-temperature hydrothermal synthesis is a useful tool in synthesising the fluoride family with a general formula AM²⁺M³⁺F₆, both those that crystallise in the *Pnma* space group and the *Fd-3m* space group. The ability to synthesis these materials at low temperatures is beneficial in the developing our understating of this family. ACoCrF₆ and ANiCrF₆ (where A = Cs, Rb) materials were synthesised using this method and x-ray diffraction were used to structurally characterise each material. Comparing the A site cation, an increase in lattice parameter and volume is seen when A = Cs, as would be expected for the larger A cation. SQUID magnetometry measurements were performed on CsCoCrF₆ and CsNiCrF₆, both exhibiting spin glass behaviour with antiferromagnetic interactions, CsCoCrF₆ much stronger than CsNiCrF₆. Powder neutron diffraction experiments were performed on CsNiCrF₆ and as expected no long range magnetic ordering was observed, however, diffuse scattering is visible at low angles consistent with weak antiferromagnetic interactions. Neutron diffraction is the only way to fully understand RbFeCrF₆ which can not be fully characterised, structurally or magnetically, with in house techniques alone.

Chapter 6

Conclusions

A series of geometrically frustrated magnetic fluoride materials with a pyrochlore structure have been investigated during this study. Typically hydrothermal synthesis was used to produce fluoride materials with the general formula AM_2F_6 for characterisation or as a starting material for further manipulation. The work contained in this thesis clearly demonstrates a novel synthesis method for a new type of pyrochlore fluoride family, with the general formula, MF_3 . A major accomplishment of this work was the design and characterisation of truly porous pyrochlore FeF_3 , which had formerly only been produced with A site impurities. This novel synthesis route uses a new soft chemistry technique, whereby, a defect pyrochlore, $RbFe_2F_6$, was subjected to a Br_2 solution, resulting in a topotactic deintercalation of the A site Rb cation leading to simultaneous oxidation of the Fe^{2+} ion so that all Fe are nominally Fe^{3+} . The ability to produce pyrochlore FeF_3 , free from molecule or ion impurity with high crystallinity, makes significant advancements in the the field of pyrochlores, opening avenues to explore this new family of material, MF_3 , with particularly interesting physics, especially geometric magnetic frustration such as that exhibited in pyr- FeF_3 with an all-in-all-out ordering. During characterisation of $RbFe_2F_6$, a small feature at 3 K is present during SQUID magnetometry which has not yet been reported. This could potentially be caused by a magnetic transition at low temperatures due to strong distortion of the $Fe^{+2}F_6$ octahedra from a Jahn-Teller effect, whist the $Fe^{+3}F_6$ octahedra remain only slightly distorted.

A new hydrothermal synthesis method was used to produce the defect pyrochlore-like $CsFe_2F_6$ which is analogous to $RbFe_2F_6$ (reported in this work) and $NH_4Fe_2F_6$,¹²⁷ crystallising with an orthorhombic symmetry and an ordered arrangement of Fe^{+2} and Fe^{+3} . The magnetic ordering of $CsFe_2F_6$ is in perfect agreement with that of $RbFe_2F_6$, previous speculation¹²⁵ and computational calculations,¹²⁶ where homogeneous Fe ions are antiferromagnetic, while those between the heterogeneous Fe ions are frustrated. This

work has, for the first time experimentally, explored the magnetic frustration exhibited in CsFe_2F_6 and demonstrated that hydrothermal synthesis is a method of reliably producing frustrated pyrochlores with the general formula AM_2F_6 .

A small portion of this work is centred on using pyr- FeF_3 as a cathode material in lithium batteries due to the large three-dimensional cavities and hence explore the electrochemical intercalation/deintercalation of lithium. Whilst lithium intercalation/deintercalation was achieved, a loss in capacity is noted throughout cycling. Whilst a number of plausible explanations are discussed, data collection did not allow for a full investigation into pyr- FeF_3 acting as a cathode material.

Contrary to reports in the literature,¹³⁸ RbFeCrF_6 appears to crystallise in an orthorhombic $Pnma$ structure rather than the typically seen cubic $Fd-3m$ structure. However, unlike typical orthorhombic $Pnma$ structures, such as CsFe_2F_6 and RbFe_2F_6 , disorder between the Fe and Cr cations, from single crystal x-ray diffraction, is seen. The orthorhombic structure could be reasoned by the presence of Fe^{+3} on the Cr^{+3} position and ordering between Fe^{+2} and Fe^{+3} impurity, as suggested from Mössbauer spectroscopy. In comparison to other mixed transition metal pyrochlore fluorides discussed in this work, such as ACoCrF_6 and ANiCrF_6 (where $A = \text{Cs, Rb}$), it is the only material which crystallises in an orthorhombic structure; both ACoCrF_6 and ANiCrF_6 materials crystallise in the more typical cubic structure, exhibiting behaviour consistent with spin glasses, indicating antiferromagnetic interactions at low temperature. Whilst this is discussed, the quality of data collected did not allow for a full structure solution of RbFeCrF_6 .

This work has greatly added to the field of geometrically frustrated fluorides, designing a new synthesis route to explore a novel family of materials, giving insight into their magnetic and structural properties, as well as their use in gas storage and as a cathode material.

Appendix A

Supplementary Information

All refinements were performed using the Fullprof suite of programs. Refinements were typically conducted for 34-15 background coefficients, fitted using a linear interpolation function. The peak shape was fitted using a Thompson-Cox-Hastings pseudo-Voigt function (Thompson, P.; Cox, D.E.; Hastings, J. M. J. Appl. Crystallogr. 1987, 20, 79). The TCH function can be described through a combination of Lorentzian and Gaussian components. The refined powder neutron diffraction patterns for CsFe₂F₆ taken on the BT-1 Diffractometer using the Ge311 monochromator with 60 min in-pile collimation at various temperatures. Data points (red) and calculated fit (black) are displayed in the upper curve and the difference (blue) between the observed and calculated pattern is displayed in the lower curve. Sets of vertical tick marks (orange) represent the expected positions of nuclear reflections (upper) and magnetic reflections (lower). For where there is only one set a tick marks, no magnetic reflections are observed.

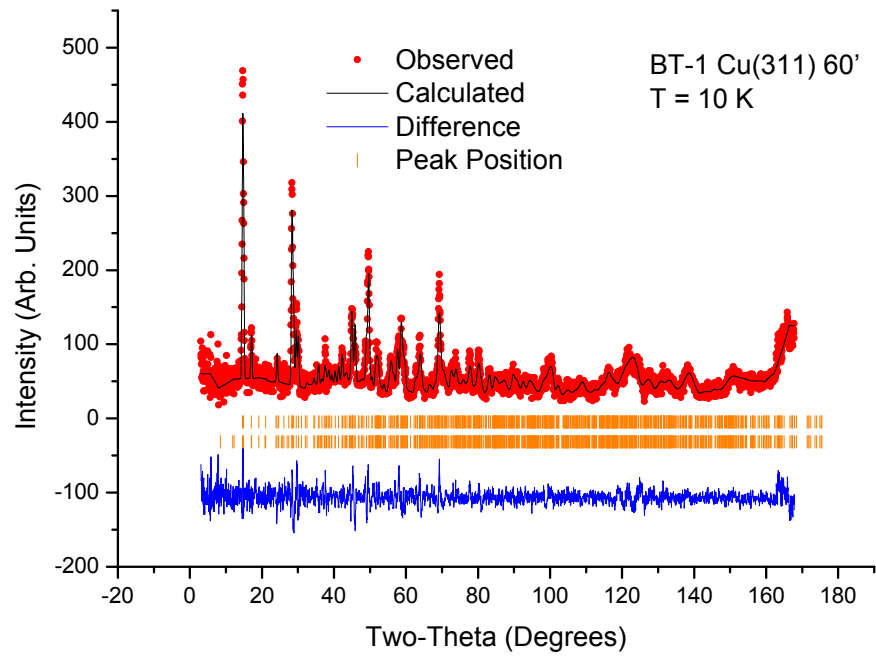


FIGURE A.1: Refined model of CsFe_2F_6 using powder neutron diffraction collected on the BT1 diffractometer at 10 K.

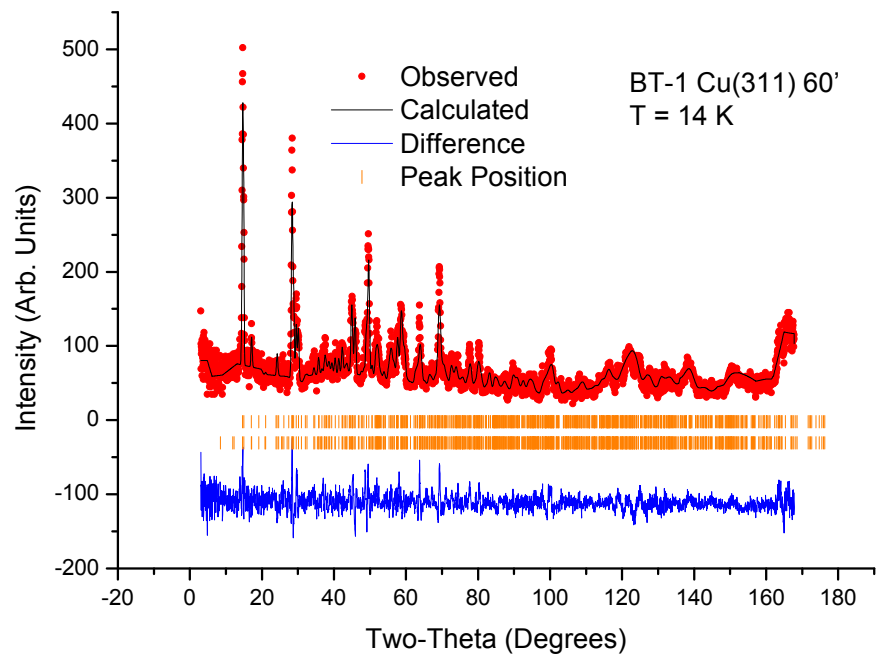


FIGURE A.2: Refined model of CsFe_2F_6 using powder neutron diffraction collected on the BT1 diffractometer at 14 K.

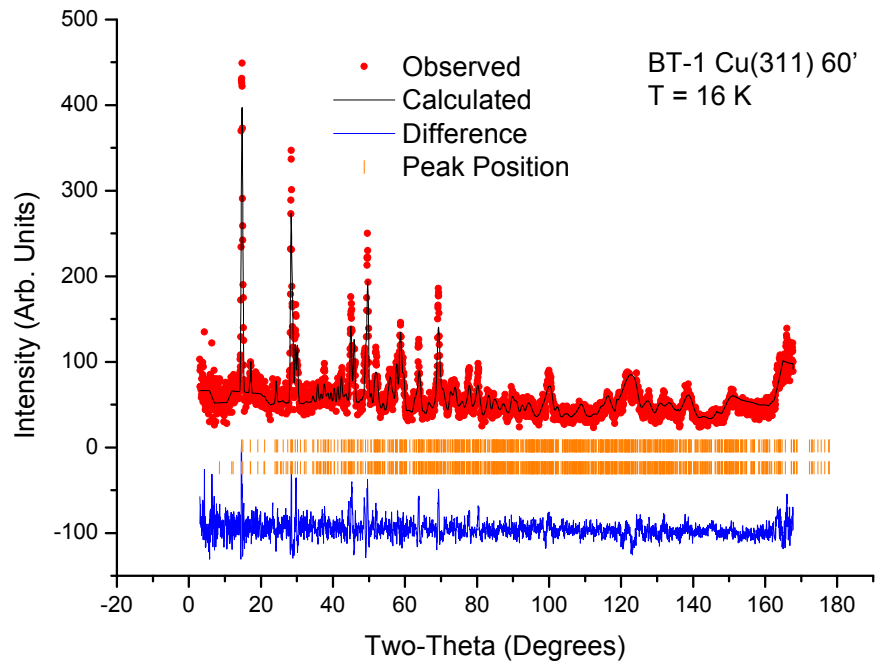


FIGURE A.3: Refined model of CsFe_2F_6 using powder neutron diffraction collected on the BT1 diffractometer at 16 K.

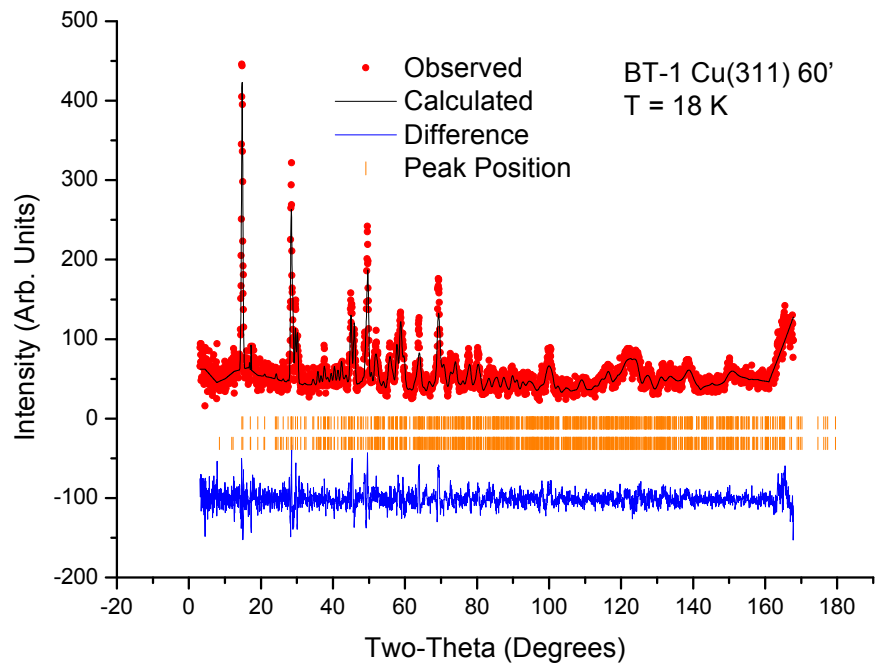


FIGURE A.4: Refined model of CsFe_2F_6 using powder neutron diffraction collected on the BT1 diffractometer at 18 K.

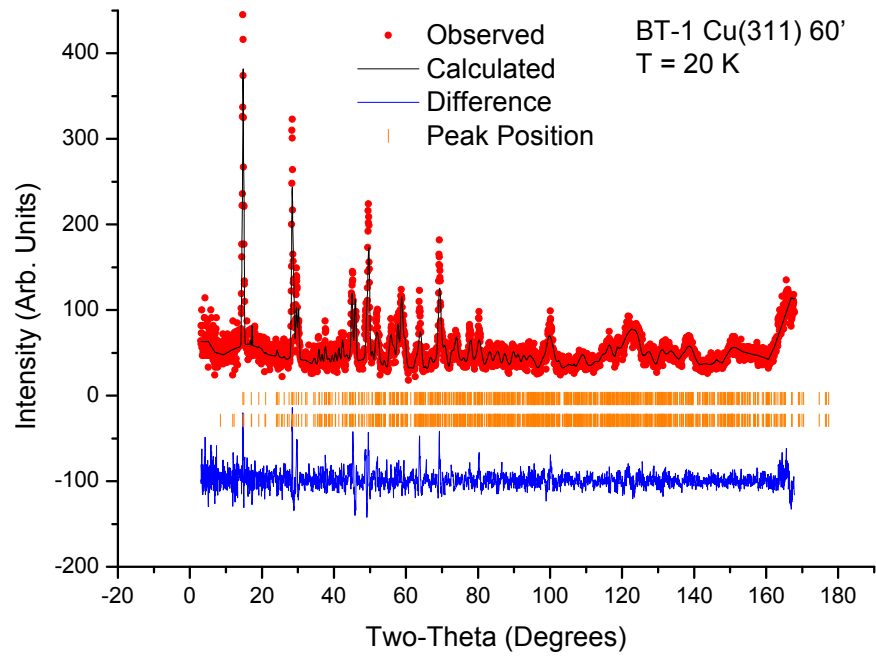


FIGURE A.5: Refined model of CsFe_2F_6 using powder neutron diffraction collected on the BT1 diffractometer at 20 K.

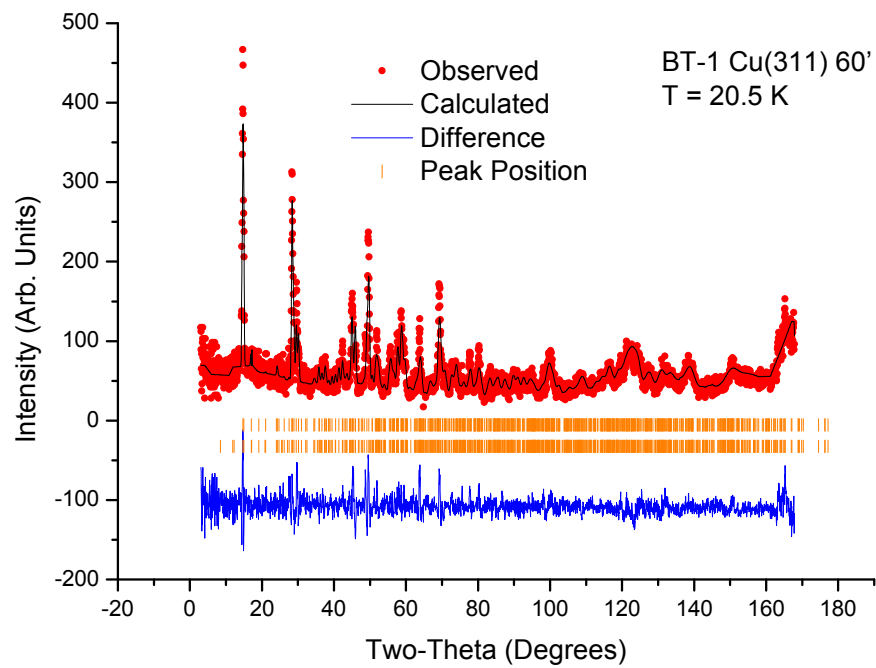


FIGURE A.6: Refined model of CsFe_2F_6 using powder neutron diffraction collected on the BT1 diffractometer at 20.5 K.

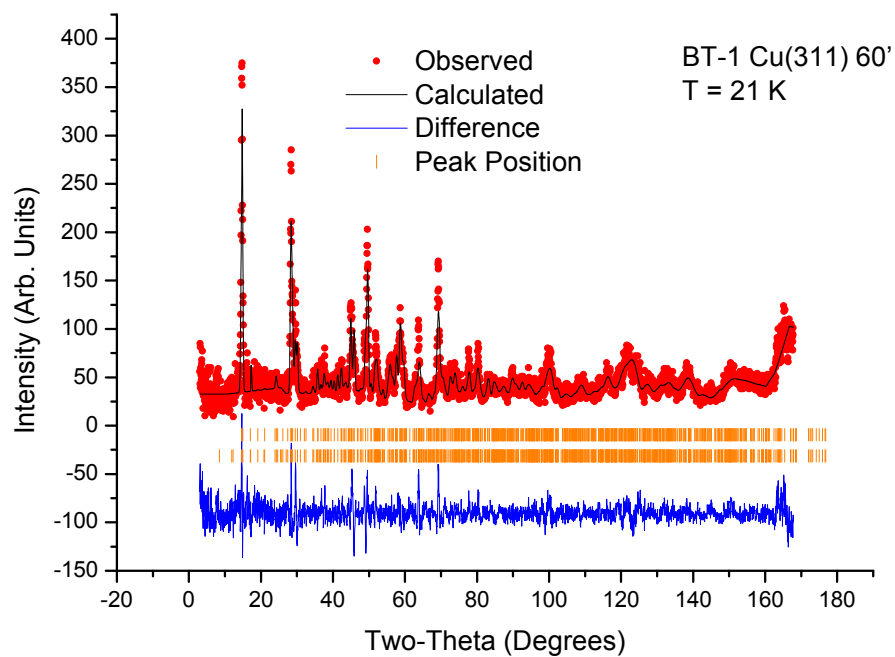


FIGURE A.7: Refined model of CsFe_2F_6 using powder neutron diffraction collected on the BT1 diffractometer at 21 K.

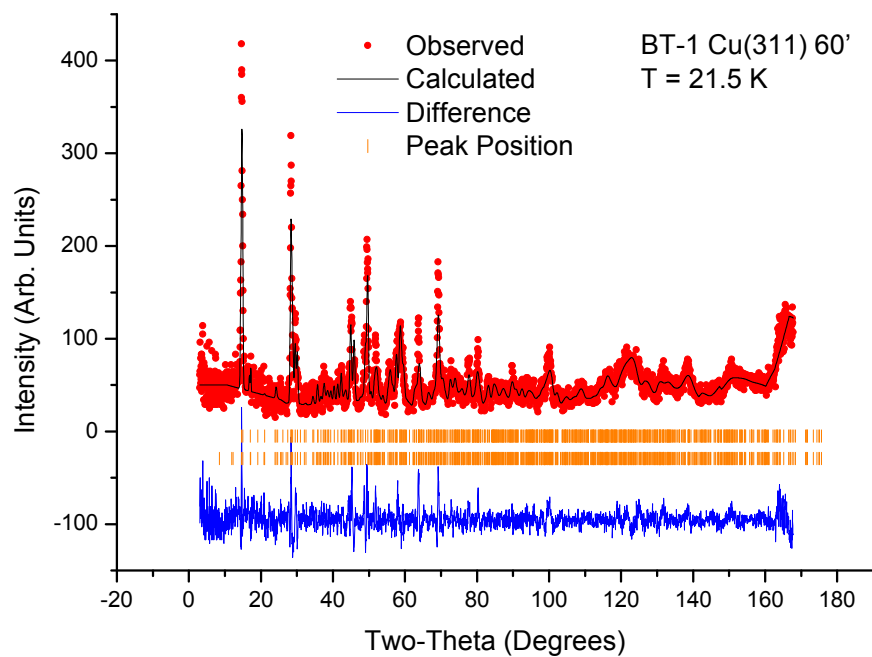


FIGURE A.8: Refined model of CsFe_2F_6 using powder neutron diffraction collected on the BT1 diffractometer at 21.5 K.

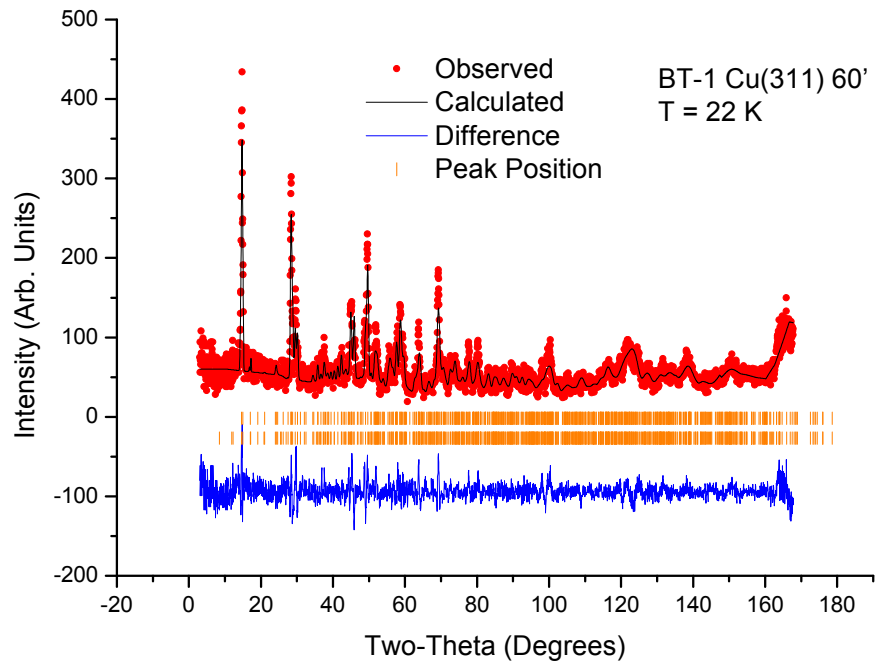


FIGURE A.9: Refined model of CsFe_2F_6 using powder neutron diffraction collected on the BT1 diffractometer at 22 K.

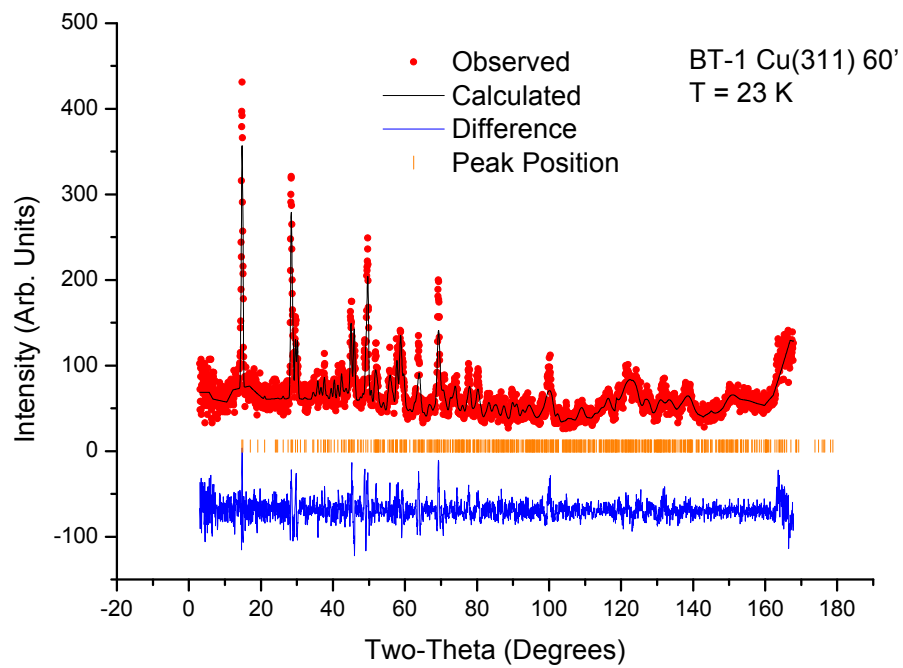


FIGURE A.10: Refined model of CsFe_2F_6 using powder neutron diffraction collected on the BT1 diffractometer at 23 K.

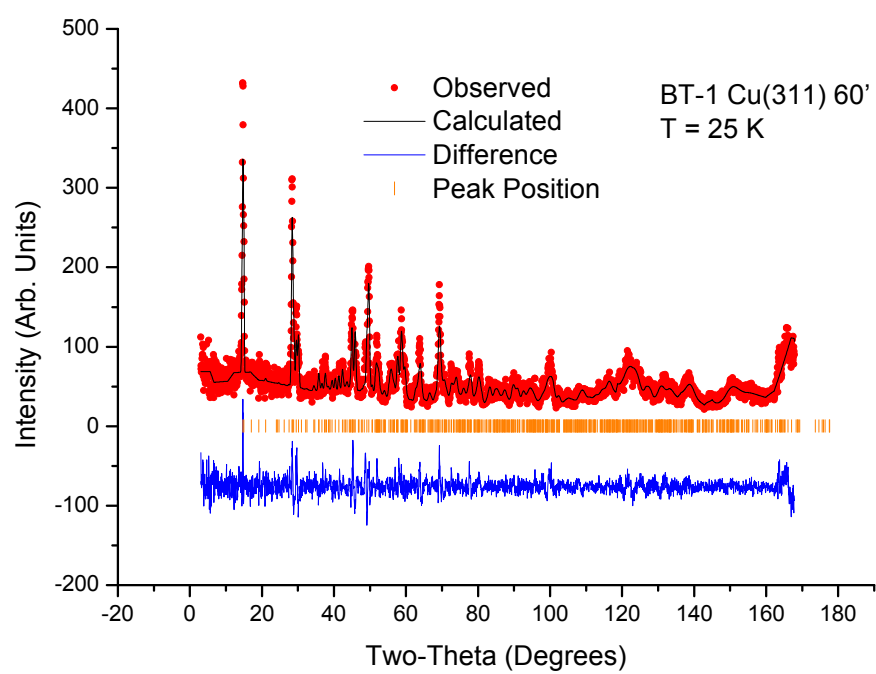


FIGURE A.11: Refined model of CsFe₂F₆ using powder neutron diffraction collected on the BT1 diffractometer at 25 K.

Appendix B

Supplementary Information

The refined powder neutron diffraction patterns for pyr-FeF₃ taken on the BT-1 Diffractometer using the Ge311 monochromator with 60 min in-pile collimation at various temperatures. Data points (red) and calculated fit (black) are displayed in the upper curve and the difference (blue) between the observed and calculated pattern is displayed in the lower curve. Sets of vertical tick marks (orange) represent the expected positions of nuclear reflections (upper) and magnetic reflections (lower). For where there is only one set a tick marks, no magnetic reflections are observed.

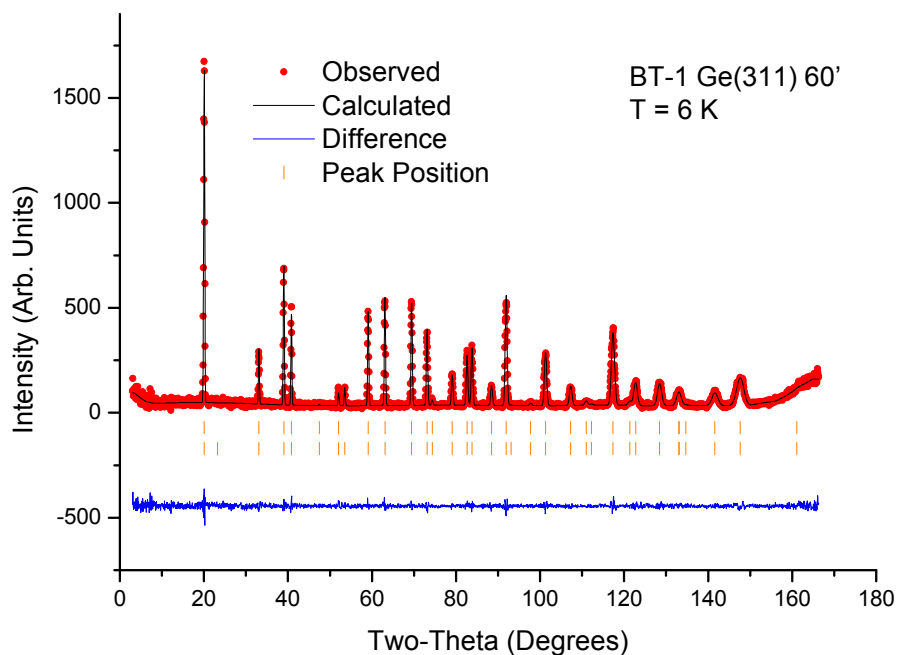


FIGURE B.1: Refined model of pyr-FeF₃ using powder neutron diffraction collected on the BT1 diffractometer at 6 K.

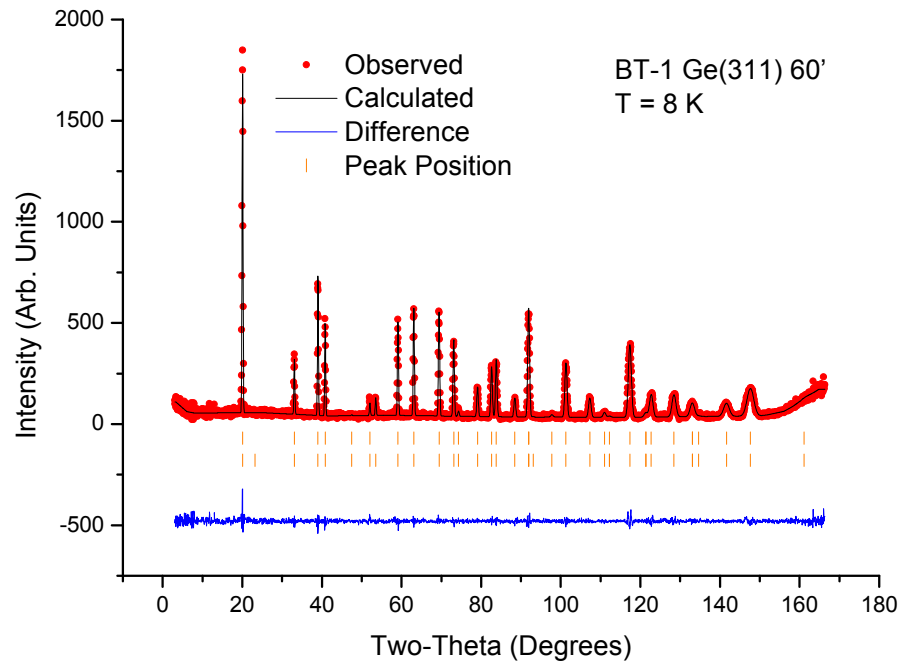


FIGURE B.2: Refined model of pyr-FeF₃ using powder neutron diffraction collected on the BT1 diffractometer at 8 K.

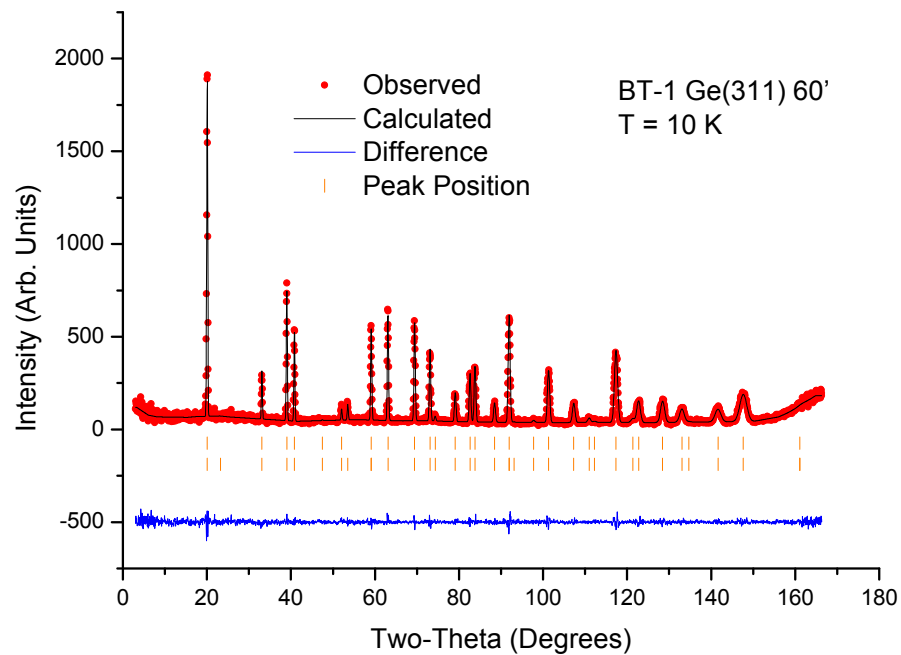


FIGURE B.3: Refined model of pyr-FeF₃ using powder neutron diffraction collected on the BT1 diffractometer at 10 K.

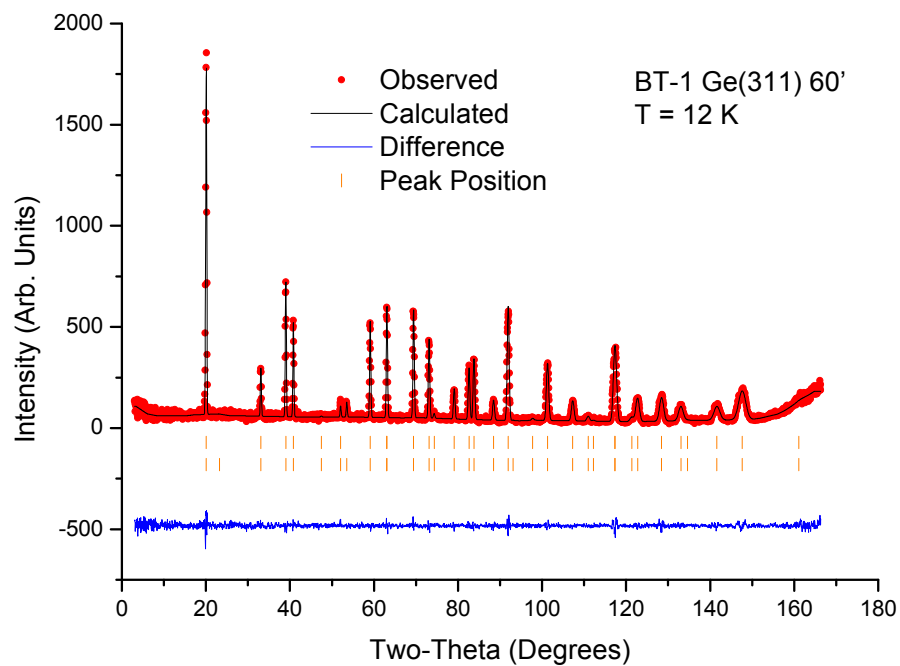


FIGURE B.4: Refined model of pyr-FeF₃ using powder neutron diffraction collected on the BT1 diffractometer at 12 K.

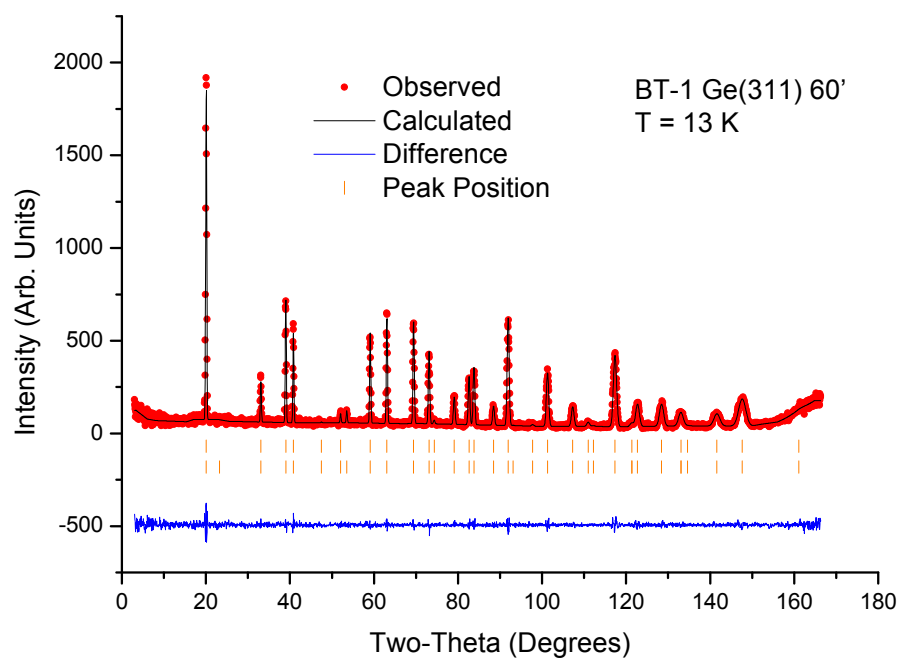


FIGURE B.5: Refined model of pyr-FeF₃ using powder neutron diffraction collected on the BT1 diffractometer at 13 K.

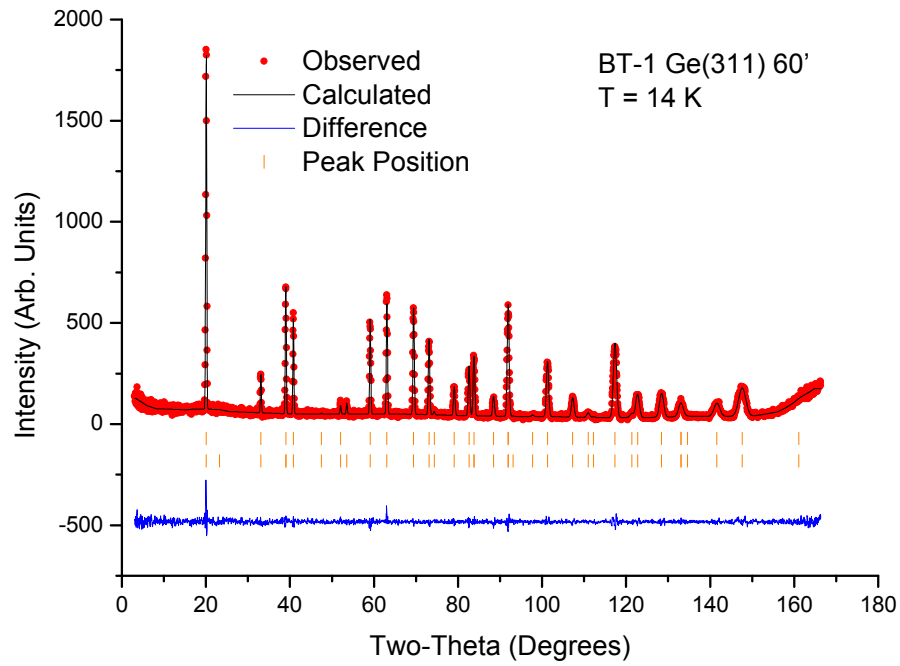


FIGURE B.6: Refined model of pyr-FeF₃ using powder neutron diffraction collected on the BT1 diffractometer at 14 K.

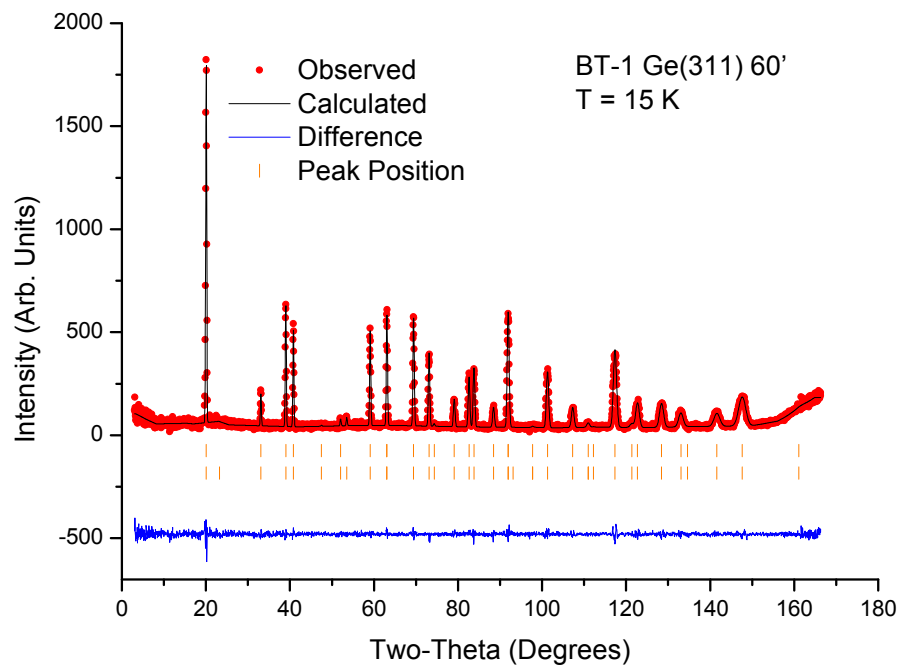


FIGURE B.7: Refined model of pyr-FeF₃ using powder neutron diffraction collected on the BT1 diffractometer at 15 K.

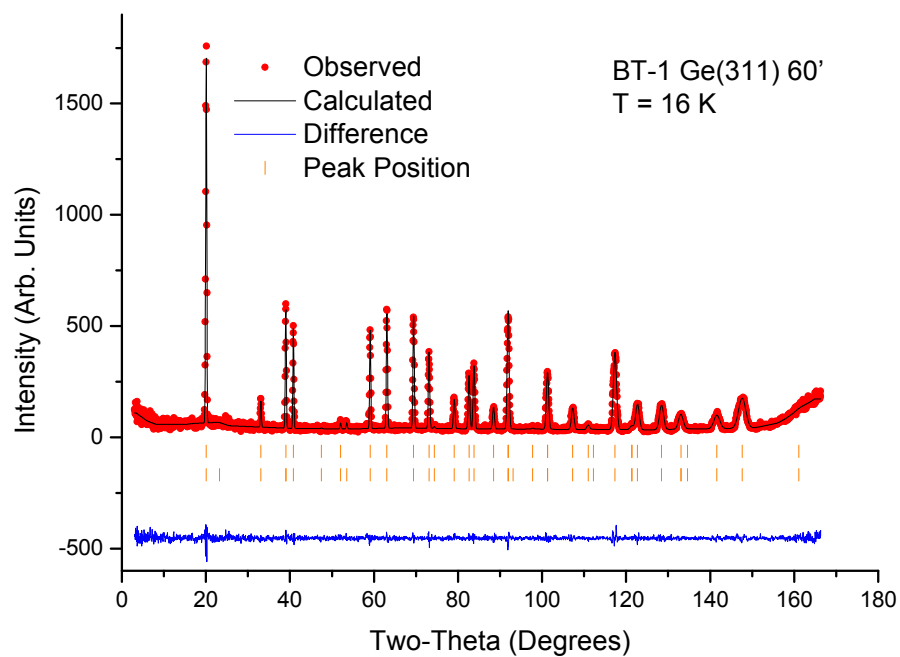


FIGURE B.8: Refined model of pyr-FeF₃ using powder neutron diffraction collected on the BT1 diffractometer at 16 K.

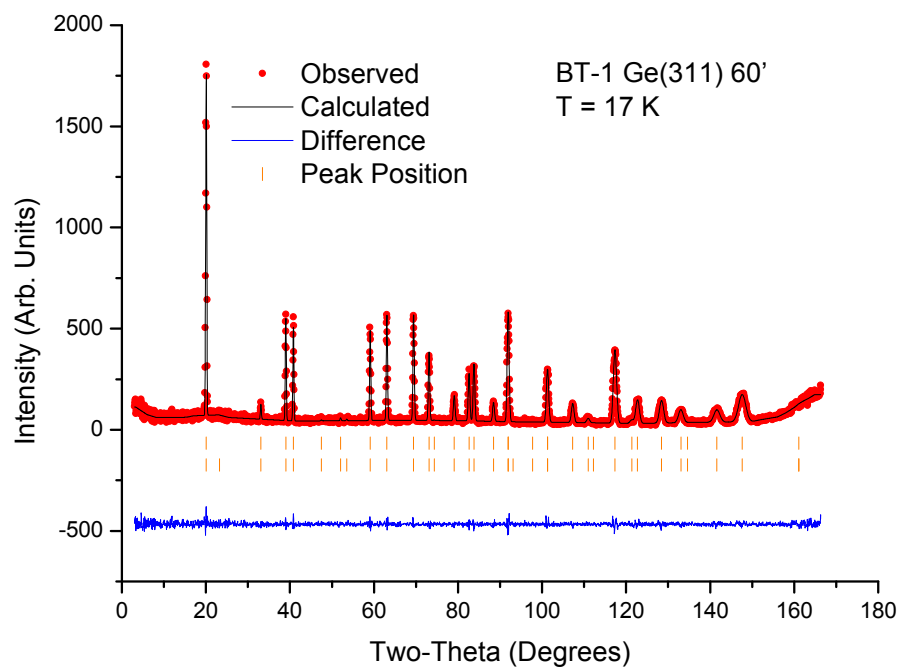


FIGURE B.9: Refined model of pyr-FeF₃ using powder neutron diffraction collected on the BT1 diffractometer at 17 K.

The refined powder neutron diffraction patterns for pyr-FeF₃ taken on the BT-1 Diffractometer using the Ge733 monochromator with 60 min in-pile collimation at various temperatures.

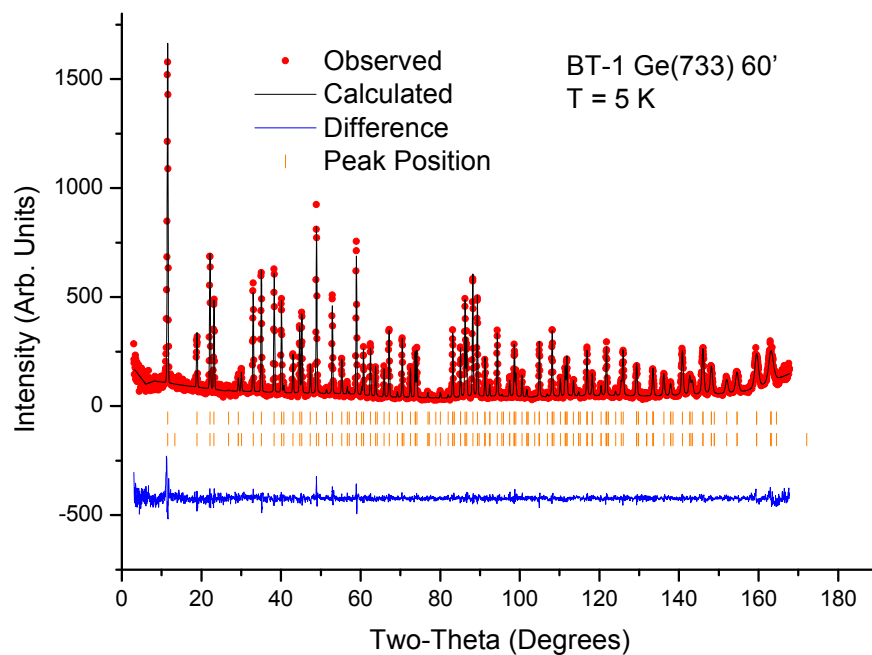


FIGURE B.10: Refined model of pyr-FeF₃ using powder neutron diffraction collected on the BT1 diffractometer at 5 K.

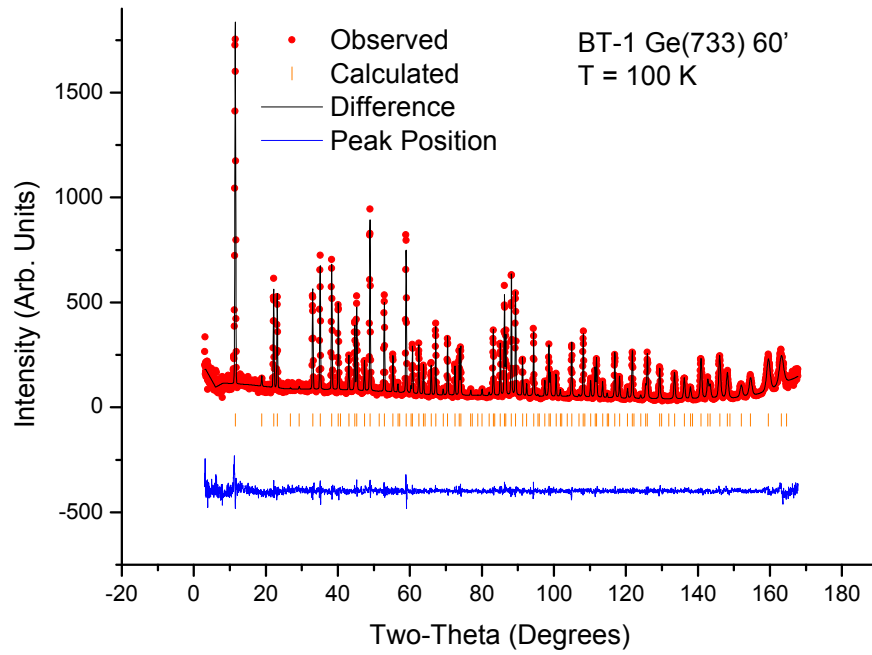


FIGURE B.11: Refined model of pyr-FeF₃ using powder neutron diffraction collected on the BT1 diffractometer at 100 K.

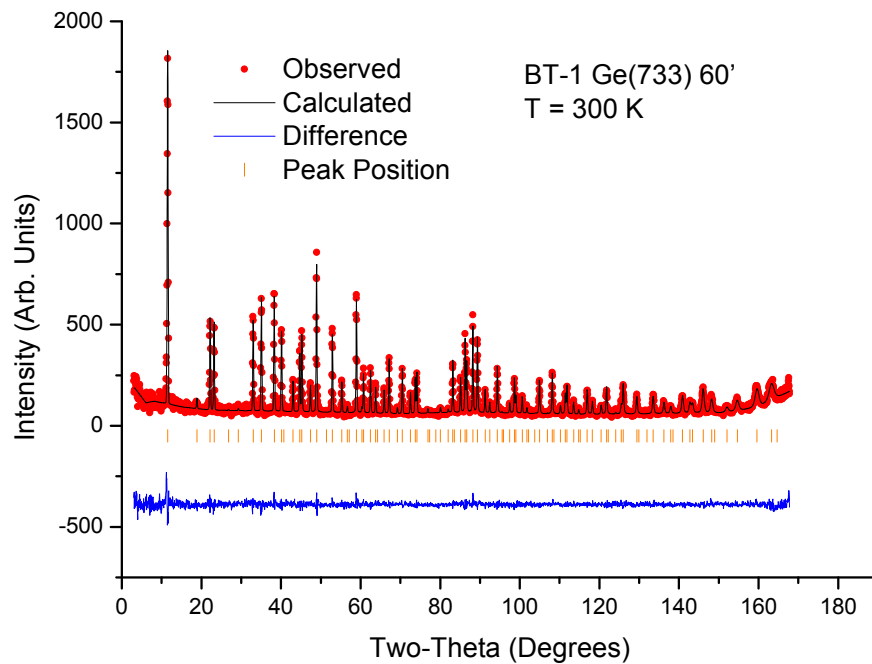


FIGURE B.12: Refined model of pyr-FeF₃ using powder neutron diffraction collected on the BT1 diffractometer at 300 K.


```

Alert level A
EXPT005_ALERT_1_A _exptl_crystal_description is missing
  Crystal habit description.
  The following tests will not be performed.
  CRYSR_01
DIFF003_ALERT_1_A _diffrn_measurement_device_type is missing
  Diffractometer make and type. Replaces _diffrn_measurement_type.
PLAT043_ALERT_1_A Calculated and Reported Mol. Weight Differ by .. 469.45 Check
PLAT051_ALERT_1_A Mu(calc) and Mu(CIF) Ratio Differs from 1.0 by . 49.32 %
PLAT075_ALERT_1_A Occupancy 1.011 Greater Than 1.0 for ..... CR
PLAT183_ALERT_1_A Missing _cell_measurement_reflns_used Value .... Please Do !
PLAT184_ALERT_1_A Missing _cell_measurement_theta_min Value ..... Please Do !
PLAT185_ALERT_1_A Missing _cell_measurement_theta_max Value ..... Please Do !

Alert level C
PLAT041_ALERT_1_C Calc. and Reported SumFormula Strings Differ Please Check
PLAT052_ALERT_1_C Info on Absorption Correction Method Not Given Please Do !
PLAT053_ALERT_1_C Minimum Crystal Dimension Missing (or Error) ... Please Check
PLAT054_ALERT_1_C Medium Crystal Dimension Missing (or Error) ... Please Check
PLAT055_ALERT_1_C Maximum Crystal Dimension Missing (or Error) ... Please Check
PLAT068_ALERT_1_C Reported F000 Differs from Calcd (or Missing)... Please Check
PLAT077_ALERT_4_C Unitcell Contains Non-integer Number of Atoms .. Please Check
PLAT213_ALERT_2_C Atom Cr has ADP max/min Ratio ..... 3.3 prolat
PLAT906_ALERT_3_C Large K Value in the Analysis of Variance ..... 2.677 Check

Alert level G
FORMU01_ALERT_2_G There is a discrepancy between the atom counts in the
  _chemical_formula_sum and the formula from the _atom_site* data.
  Atom count from _chemical_formula_sum:Cr1 F1 Fe1 Rb1
  Atom count from the _atom_site data: Cr0.5055 F3 Fe0.4945 Rb0.5
CELLZ01_ALERT_1_G Difference between formula and atom_site contents detected.
CELLZ01_ALERT_1_G ALERT: Large difference may be due to a
  symmetry error - see SYMMG tests
  From the CIF: _cell_formula_units_Z 8
  From the CIF: _chemical_formula_sum Cr F Fe Rb
  TEST: Compare cell contents of formula and atom_site data

  atom Z*formula cif sites diff
  Cr 8.00 4.04 3.96
  F 8.00 24.00 -16.00
  Fe 8.00 3.96 4.04
  Rb 8.00 4.00 4.00
PLAT004_ALERT_5_G Polymeric Structure Found with Maximum Dimension 2 Info
PLAT045_ALERT_1_G Calculated and Reported Z Differ by a Factor ... 0.13 Check
PLAT199_ALERT_1_G Reported _cell_measurement_temperature ..... (K) 293 Check
PLAT200_ALERT_1_G Reported _diffrn_ambient_temperature ..... (K) 293 Check
PLAT301_ALERT_3_G Main Residue Disorder .....(Resd 1 ) 19# Note
PLAT912_ALERT_4_G Missing # of PCP Reflections Above STh/L= 0.600 105 Note

8 ALERT level A = Most likely a serious problem - resolve or explain
0 ALERT level B = A potentially serious problem, consider carefully
9 ALERT level C = Check. Ensure it is not caused by an omission or oversight
9 ALERT level G = General information/check it is not something unexpected

19 ALERT type 1 CIF construction/syntax error, inconsistent or missing data

```

FIGURE C.2: Page 2 of checkcif.file for single crystal refinement of RbFeCrF₆.

```
2 ALERT type 2 Indicator that the structure model may be wrong or deficient
2 ALERT type 3 Indicator that the structure quality may be low
2 ALERT type 4 Improvement, methodology, query or suggestion
1 ALERT type 5 Informative message, check
```

It is advisable to attempt to resolve as many as possible of the alerts in all categories. Often the minor alerts point to easily fixed oversights, errors and omissions in your CIF or refinement strategy, so attention to these fine details can be worthwhile. In order to resolve some of the more serious problems it may be necessary to carry out additional measurements or structure refinements. However, the purpose of your study may justify the reported deviations and the more serious of these should normally be commented upon in the discussion or experimental section of a paper or in the "special_details" fields of the CIF. checkCIF was carefully designed to identify outliers and unusual parameters, but every test has its limitations and alerts that are not important in a particular case may appear. Conversely, the absence of alerts does not guarantee there are no aspects of the results needing attention. It is up to the individual to critically assess their own results and, if necessary, seek expert advice.

Publication of your CIF in IUCr journals

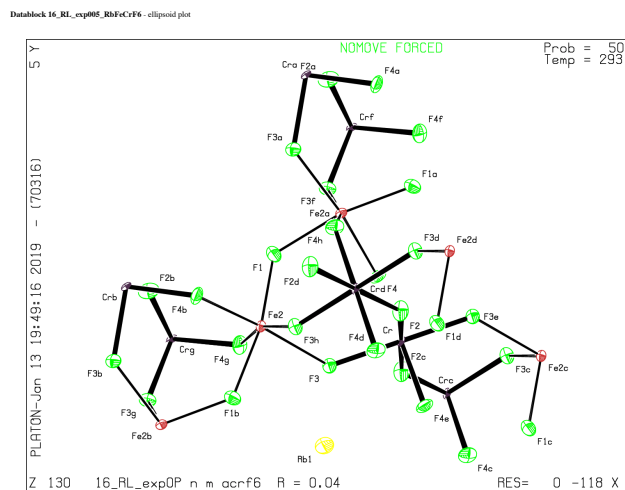
A basic structural check has been run on your CIF. These basic checks will be run on all CIFs submitted for publication in IUCr journals (*Acta Crystallographica*, *Journal of Applied Crystallography*, *Journal of Synchrotron Radiation*); however, if you intend to submit to *Acta Crystallographica Section C* or *E* or *IUCrData*, you should make sure that full publication checks are run on the final version of your CIF prior to submission.

Publication of your CIF in other journals

Please refer to the *Notes for Authors* of the relevant journal for any special instructions relating to CIF submission.

PLATON version of 06/01/2019; check.def file version of 19/12/2018

FIGURE C.3: Page 3 of checkcif.file for single crystal refinement of RbFeCrF₆.

FIGURE C.4: Page 4 of checkcif.file for single crystal refinement of RbFeCrF_6 .

Bibliography

- [1] A. Grzechnik, W. Morgenroth and K. Friese, *Journal of Solid State Chemistry*, 2009, **182**, 1792 – 1797.
- [2] I. Flerov, M. Gorev, K. Aleksandrov, A. Tressaud, J. Grannec and M. Couzi, *Materials Science and Engineering: R: Reports*, 1998, **24**, 81 – 151.
- [3] S. W. Kim, R. Zhang, P. S. Halasyamani and M. A. Hayward, *Inorganic Chemistry*, 2015, **54**, 6647–6652.
- [4] S. Margadonna and G. Karotsis, *Journal of the American Chemical Society*, 2006, **128**, 16436–16437.
- [5] G. Giovannetti, S. Margadonna and J. van den Brink, *Phys. Rev. B*, 2008, **77**, 075113.
- [6] Y. Xu, X. Hao, M. Lv, Z. Wu, D. Zhou and J. Meng, *The Journal of Chemical Physics*, 2008, **128**, 164721.
- [7] S. E. McLain, M. R. Dolgos, D. A. Tennant, J. F. C. Turner, T. Barnes, T. Proffen, B. C. Sales and R. I. Bewley, *Nat Mater*, 2006, **5**, 561–565.
- [8] S. Margadonna and G. Karotsis, *J. Mater. Chem.*, 2007, **17**, 2013–2020.
- [9] G. Wang, Z. Li, L. Zheng and Z. Yang, *Phys. Rev. B*, 2011, **84**, 045111.
- [10] E.-J. Kan, L.-F. Yuan, J. Yang and J. G. Hou, *Phys. Rev. B*, 2007, **76**, 024417.
- [11] D. Kasinathan, K. Koepernik, U. Nitzsche and H. Rosner, *Phys. Rev. Lett.*, 2007, **99**, 247210.
- [12] X. Hao, Y. Xu, Z. Wu, D. Zhou, X. Liu and J. Meng, *Phys. Rev. B*, 2007, **76**, 054426.
- [13] S. Kim, S. Kim, P. Halasyamani, M. Green, K. Bhatti, C. Leighton, H. Das and C. Fennie, *Accomplishments and Opportunities*, 2012, 30.
- [14] P. Hagemuller, *Inorganic Solid Fluorides 1st Edition*, Academic Press, 1985.

- [15] R. Verstraete, H. F. Sijbom, K. Korthout, D. Poelman, C. Detavernier and P. F. Smet, *Journal of Materials Chemistry C*, 2017, **5**, 10761–10769.
- [16] A. Tressaud, *Functionalized inorganic fluorides: synthesis, characterization and properties of nanostructured solids*, John Wiley & Sons, 2010.
- [17] M. D. Donakowski, R. Gautier, H. Lu, T. T. Tran, J. R. Cantwell, P. S. Halasyamani and K. R. Poeppelmeier, *Inorganic chemistry*, 2014, **54**, 765–772.
- [18] A. Tressaud, *Functionalized inorganic fluorides: synthesis, characterization and properties of nanostructured solids*, John Wiley & Sons, 2010.
- [19] S. W. Kim, H. Y. Chang and P. S. Halasyamani, *Journal of the American Chemical Society*, 2010, **132**, 17684–17685.
- [20] W. Massa and D. Babel, *Chemical Reviews*, 1988, **88**, 275–296.
- [21] P. Edwards, *Adv. Inorg. Chem. Radiochem.*, 1982, **25**, 135.
- [22] M. Hidaka and M. Ono, *Journal of the Physical Society of Japan*, 1977, **43**, 258–263.
- [23] A.-M. Hardy, A. Hardy and G. Ferey, *Acta Crystallographica Section B*, 1973, **29**, 1654–1658.
- [24] O. Yakubovich, V. Urusov, W. Massa, G. Frenzen and D. Babel, *Zeitschrift für anorganische und allgemeine Chemie*, 1993, **619**, 1909–1919.
- [25] M. Leblanc, G. Ferey, R. De Pape and J. Teillet, *Acta Crystallographica Section C: Crystal Structure Communications*, 1985, **41**, 657–660.
- [26] P. Ganguly and C. Rao, *Journal of Solid State Chemistry*, 1984, **53**, 193–216.
- [27] C. Brosset, *Zeitschrift für anorganische und allgemeine Chemie*, 1938, **238**, 201–208.
- [28] E. Herdtweck and D. Babel, *Zeitschrift für Kristallographie-Crystalline Materials*, 1980, **153**, 189–200.
- [29] G. Courbion, R. De Pape, G. Knoke and D. Babel, *Journal of Solid State Chemistry*, 1983, **49**, 353–361.
- [30] P. Bukovec and R. Hoppe, *Zeitschrift für anorganische und allgemeine Chemie*, 1984, **509**, 138–144.
- [31] W. Massa and V. Burk, *Zeitschrift für anorganische und allgemeine Chemie*, 1984, **516**, 119–126.

- [32] D. Babel and G. Knoke, *Zeitschrift fuer Anorganische und Allgemeine Chemie (1950)*, 1978, **442**,.
- [33] G. Ferey, M. Leblanc, A. De Kozak, M. t. Samouël and J. Pannetier, *Journal of Solid State Chemistry*, 1985, **56**, 288–297.
- [34] M. E. Lines and A. M. Glass, *Principles and applications of ferroelectrics and related materials*, Clarendon Press Oxford [Eng.], 1977.
- [35] J. Ravez, *Journal de Physique III*, 1997, **7**, 1129–1144.
- [36] J. Ravez, A. Simon, J. R. Au, S. Abrahams, Y. Calage and R. Pape, *Journal of Fluorine Chemistry*, 1989, **45**, 193.
- [37] R. Blinc, P. Cevc, G. Tavčar, B. Žemva, V. Laguta, Z. Trontelj, M. Jagodič, D. Pajić, A. Balčytis and J. F. Scott, *Physical Review B*, 2012, **85**, 054419.
- [38] J. Scott and R. Blinc, *Journal of Physics: Condensed Matter*, 2011, **23**, 113202.
- [39] A. L. Bail, C. Jacoboni and R. D. Pape, *Journal of Non-Crystalline Solids*, 1985, **74**, 205 – 212.
- [40] W. Kurtz, R. Geller, H. Dachs and P. Convert, *Solid State Communications*, 1976, **18**, 1479–1483.
- [41] H. Von Gaertner, *Min. Geol. Palaeontol*, 1930, **1**,.
- [42] C. Wan, Z. Qu, A. Du and W. Pan, *Acta Materialia*, 2009, **57**, 4782–4789.
- [43] C. R. Stanek and R. W. Grimes, *Journal of the American Ceramic Society*, 2002, **85**, 2139–2141.
- [44] M. Pirzada, R. W. Grimes and J. F. Maguire, *Solid State Ionics*, 2003, **161**, 81–91.
- [45] K. Matsuhira, M. Wakeshima, R. Nakanishi, T. Yamada, A. Nakamura, W. Kawano, S. Takagi and Y. Hinatsu, *Journal of the Physical Society of Japan*, 2007, **76**, 043706.
- [46] J. E. Greedan, J. N. Reimers, C. V. Stager and S. L. Penny, *Phys. Rev. B*, 1991, **43**, 5682–5691.
- [47] M. Subramanian, B. Toby, A. Ramirez, W. Marshall *et al.*, *Science*, 1996, **273**, 81.
- [48] J.-I. Yamaura, S. Yonezawa, Y. Muraoka and Z. Hiroi, *Journal of Solid State Chemistry*, 2006, **179**, 336 – 340.

- [49] N. Kolpakova, I. Sinij, M. Polomska and R. Margraf, *Fizika Tverdogo*, 1982, **24**, 1729.
- [50] H. L. Tuller and P. K. Moon, *Materials Science and Engineering: B*, 1988, **1**, 171 – 191.
- [51] T. Mallat, and A. Baiker, *Chemical Reviews*, 2004, **104**, 3037–3058.
- [52] H. Nyman, S. Andersson, B. Hyde and M. O’Keeffe, *Journal of Solid State Chemistry*, 1978, **26**, 123 – 131.
- [53] V. Isupov, *Kristallografiya*, 1958, **3**, 99.
- [54] E. V. Stroganov, *Vestn. Leningr. Univ., Ser. 4: Fiz., Khim.*, 1979, **4**, 46.
- [55] A. Cheetham, B. Fender and M. Cooper, *Journal of Physics C: Solid State Physics*, 1971, **4**, 3107.
- [56] M. Subramanian, G. Aravamudan and G. S. Rao, *Progress in Solid State Chemistry*, 1983, **15**, 55–143.
- [57] I. Morgenst and M. Michel, *Annales de Chime France*, 1971, p. 109.
- [58] M. Molokeev, E. Bogdanov, S. Misyul, A. Tressaud and I. Flerov, *Journal of Solid State Chemistry*, 2013, **200**, 157–164.
- [59] R. R. Jitta, R. Gundeboina, N. K. Veldurthi, R. Guje and V. Muga, *Journal of Chemical Technology & Biotechnology*, 2015, **90**, 1937–1948.
- [60] A. Schafhäütl, *Gelehrte Anzeigen München*, 1845, **20**, 577.
- [61] G. W. Morey and P. Niggli, *Journal of the American Chemical Society*, 1913, **35**, 1086–1130.
- [62] K. Byrappa and M. Yoshimura, *Handbook of Hydrothermal Technology*, William Andrew Publishing, Norwich, NY, 2001.
- [63] A. Rabenau, *Angewandte Chemie International Edition in English*, 1985, **24**, 1026–1040.
- [64] R. E. Riman, W. L. Suchanek and M. M. Lencka, *Annales de Chimie Science des Matériaux*, 2002, **27**, 15 – 36.
- [65] S. Sōmiya and R. Roy, *Bulletin of Materials Science*, 2000, **23**, 453–460.
- [66] D. R. Modeshia and R. I. Walton, *Chem. Soc. Rev.*, 2010, **39**, 4303–4325.

- [67] T. Adschiri, Y.-W. Lee, M. Goto and S. Takami, *Green Chem.*, 2011, **13**, 1380–1390.
- [68] E. Lester, P. Blood, J. Denyer, D. Giddings, B. Azzopardi and M. Poliakoff, *The Journal of Supercritical Fluids*, 2006, **37**, 209 – 214.
- [69] I. U. C. Report of the Executive Committee for 1991, *Acta Crystallographica Section A*, 1992, **48**, 922–946.
- [70] M. Eckert, *Annalen der Physik*, 2012, **524**, A83–A85.
- [71] M. Etter and R. E. Dinnebier, *Zeitschrift für anorganische und allgemeine Chemie*, 2014, **640**, 3015–3028.
- [72] W. L. Bragg, Proceedings of the Royal Society of London A: Mathematical, Physical and Engineering Sciences, 1913, pp. 248–277.
- [73] B. D. Cullity and S. R. Stock, *Elements of X-ray Diffraction*, Pearson Education, 2014.
- [74] H. Rietveld, *Journal of applied Crystallography*, 1969, **2**, 65–71.
- [75] J. Rodriguez-Carvajal, satellite meeting on powder diffraction of the XV congress of the IUCr, 1990.
- [76] J. Chadwick, *Proceedings of the Royal Society of London A: Mathematical, Physical and Engineering Sciences*, 1932, **136**, 692–708.
- [77] D. P. Mitchell and P. N. Powers, *Phys. Rev.*, 1936, **50**, 486–487.
- [78] P. Preiswerk and H. von Halban, *CR Acad. Sci. Paris*, 1936, **203**, 73–75.
- [79] E. O. Wollan and C. G. Shull, *Phys. Rev.*, 1948, **73**, 830–841.
- [80] T. Brückel, 43rd IFF Spring School: "Scattering Methods for Condensed Matter Research: Towards Novel Applications at Future Sources" / M. Angst, Th. Brückel, D. Richter, R. Zorn (Eds.) ; Schriften des Forschungszentrums Jülich / Reihe Schlüsseltechnologien / Key Technologies, Vol. 33, Forschungszentrum Jülich GmbH, JCNS, PGI, ICS, IAS; 2012; 978-3-89336-759-7, Jülich, 2012, pp. A1.1 – A1.41.
- [81] G. L. Squires, *Introduction to the theory of thermal neutron scattering*, Cambridge university press, 2012.
- [82] D. S. Sivia, *Elementary scattering theory: for X-ray and neutron users*, Oxford University Press, 2011.

- [83] *High Resolution Powder Diffractometer - BT1*, <https://www.ncnr.nist.gov/instruments/bt1/>, Accessed: 2018-05-03.
- [84] L. C. Chapon, P. Manuel, P. G. Radaelli, C. Benson, L. Perrott, S. Ansell, N. J. Rhodes, D. Raspino, D. Duxbury, E. Spill and J. Norris, 2011, **22**, 22–25.
- [85] A. R. West, *Solid state chemistry and its applications*, John Wiley & Son, Ltd, 2014.
- [86] S. Power and M. Ferreira, *Crystals*, 2013, **3**, 49–78.
- [87] C. Zener, *Physical Review*, 1951, **82**, 403.
- [88] J. S. Gardner, *Journal of Physics: Condensed Matter*, 2011, **23**, 160301.
- [89] L. Balents, *Nature*, 2010, 199–208.
- [90] A. P. Ramirez, *Material Science*, 1994, **24**, 453–480.
- [91] J. B. Goodenough, *Magnetism And The Chemical Bond*, Interscience Publishers, 1963.
- [92] P. Coppens and J. Penner-Hahn, *Introduction: X-rays in Chemistry*, 2001.
- [93] M. Harris, S. Bramwell, D. McMorrow, T. Zeiske and K. Godfrey, *Physical Review Letters*, 1997, **79**, 2554.
- [94] E. Shoko, G. J. Kearley, V. K. Peterson, H. Mutka, M. M. Koza, J.-i. Yamaura, Z. Hiroi and G. J. Thorogood, *Journal of Physics: Condensed Matter*, 2014, **26**, 305401.
- [95] E. Shoko, Y. Okamoto, G. J. Kearley, V. K. Peterson and G. J. Thorogood, *Journal of Applied Physics*, 2014, **115**, 033703.
- [96] Z. Hiroi, J. ichi Yamaura and K. Hattori, *Journal of the Physical Society of Japan*, 2012, **81**, 011012.
- [97] Y. Nagao, J. ichi Yamaura, H. Ogusu, Y. Okamoto and Z. Hiroi, *Journal of the Physical Society of Japan*, 2009, **78**, 064702.
- [98] Z. Hiroi, S. Yonezawa, Y. Nagao and J. Yamaura, *Phys. Rev. B*, 2007, **76**, 014523.
- [99] Z. Hiroi, J.-I. Yamaura, S. Yonezawa and H. Harima, *Physica C: Superconductivity and its Applications*, 2007, **460-462**, 20 – 27.
- [100] N. Louvain, A. Fakhry, P. Bonnet, M. El-Ghozzi, K. Guerin, M.-T. Sougrati, J.-C. Jumas and P. Willmann, *CrystEngComm*, 2013, **15**, 3664–3671.

- [101] P. Schenk and G. Brauer, in *Handbook of Preparative Inorganic Chemistry (Second Edition)*, ed. G. Brauer, Academic Press, Second Edition edn., 1963, pp. 3 – 107.
- [102] J. Greneche, F. Varret, M. Leblanc and G. Ferey, *Solid state communications*, 1987, **61**, 813–816.
- [103] M. Leblanc, G. Ferey, P. Chevallier, Y. Calage and R. De Pape, *Journal of Solid State Chemistry*, 1983, **47**, 53–58.
- [104] G. Ferey, M. Leblanc, R. De Pape, M. Passaret and M. Bothorel-Razazi, *Journal of Crystal Growth*, 1975, **29**, 209–211.
- [105] C. Li, L. Gu, J. Tong, S. Tsukimoto and J. Maier, *Advanced Functional Materials*, 2011, **21**, 1391–1397.
- [106] R. D. Pape and G. Ferey, *Materials Research Bulletin*, 1986, **21**, 971 – 978.
- [107] C. Li, L. Gu, S. Tsukimoto, P. A. van Aken and J. Maier, *Advanced materials*, 2010, **22**, 3650–3654.
- [108] C. Li, C. Yin, L. Gu, R. E. Dinnebier, X. Mu, P. A. van Aken and J. Maier, *Journal of the American chemical Society*, 2013, **135**, 11425–11428.
- [109] Y. Calage, M. Zemirli, J. Greneche, F. Varret, R. D. Pape and G. Ferey, *Journal of Solid State Chemistry*, 1987, **69**, 197 – 201.
- [110] Y. Calage, M. Leblanc, G. Ferey and F. Varret, *Journal of Magnetism and Magnetic Materials*, 1984, **43**, 195 – 203.
- [111] C. Lacroix, P. Mendels and F. Mila, *Introduction to Frustrated Magnetism: Materials, Experiments, Theory*, Springer, 2013.
- [112] A. Kitajou, H. Komatsu, K. Chihara, I. D. Gocheva, S. Okada and J.-i. Yamaki, *Journal of Power Sources*, 2012, **198**, 389–392.
- [113] Y. Yamada, T. Doi, I. Tanaka, S. Okada and J. ichi Yamaki, *Journal of Power Sources*, 2011, **196**, 4837 – 4841.
- [114] J. Cabana, L. Monconduit, D. Larcher and M. R. Palacín, *Advanced Materials*, 2010, **22**, E170–E192.
- [115] H. Arai, S. Okada, Y. Sakurai and J. ichi Yamaki, *Journal of Power Sources*, 1997, **68**, 716 – 719.
- [116] N. Yabuuchi, M. Sugano, Y. Yamakawa, I. Nakai, K. Sakamoto, H. Muramatsu and S. Komaba, *J. Mater. Chem.*, 2011, **21**, 10035–10041.

- [117] L. Chilin, M. Xiaoke, van Aken Peter A. and M. Joachim, *Advanced Energy Materials*, 2012, **3**, 113–119.
- [118] K. Y. C. Ghulam Alia, Gul Rahmanb, *Electrochimica Acta*, 2017, **238**, 49 – 55.
- [119] P. Verma, P. Maire and P. Novák, *Electrochimica Acta*, 2010, **55**, 6332 – 6341.
- [120] Y.-K. Sun, C. S. Yoon, S.-T. Myung, I. Belharouak and K. Amine, *Journal of The Electrochemical Society*, 2009, **156**, A1005–A1010.
- [121] P. Liu, J. J. Vajo, J. S. Wang, W. Li and J. Liu, *The Journal of Physical Chemistry C*, 2012, **116**, 6467–6473.
- [122] G. Ferey, R. De Pape, M. Leblanc and J. Pannetier, *Rev. Chim. Min.*, 1987, **23**, 474–484.
- [123] M. Songvilay, E. Rodriguez, R. Lindsay, M. Green, H. Walker, J. Rodriguez-Rivera and C. Stock, *Physical review letters*, 2018, **121**, 087201.
- [124] T. Fennell, M. Harris, S. Calder, M. Ruminy, M. Boehm, P. Steffens, M.-H. Lemée-Cailleau, O. Zaharko, A. Cervellino and S. Bramwell, *Nature Physics*, 2018, 1.
- [125] M. V. Gorev, I. N. Flerov, A. Tressaud, E. V. Bogdanov, A. V. Kartashev, O. A. Bayukov, E. V. Eremin and A. S. Krylov, *Journal of Solid State Chemistry*, 2016, **237**, 330–335.
- [126] S. Liu, Y. Xu, Y. Cui, J. Wang, K. Sun, S. Yu and X. Hao, *Journal of Physics: Condensed Matter*, 2017, **29**, 315501.
- [127] G. Ferey, M. LeBlanc and R. de Pape, *Journal of Solid State Chemistry*, 1981, **40**, 1 – 7.
- [128] M. Leblanc, G. Ferey, Y. Calage and R. D. Pape, *Journal of Solid State Chemistry*, 1983, **47**, 24 – 29.
- [129] A. P. Ramirez, *Comments. Cond. Mat. Phys.*, 1996, **18**, 21.
- [130] E. G. Walton, D. B. Brown, H. Wong and W. M. Reiff, *Inorganic Chemistry*, 1977, **16**, 2425–2431.
- [131] E. G. Walton, P. J. Corvan, D. B. Brown and P. Day, *Inorganic Chemistry*, 1976, **15**, 1737–1739.
- [132] N. Greenwood, F. Menil and A. Tressaud, *Journal of Solid State Chemistry*, 1972, **5**, 402 – 409.
- [133] R. Hoppe, *Journal of Fluorine Chemistry*, 1983, **23**, 458.

- [134] B. G. Müller, *Journal of Fluorine chemistry*, 1981, **17**, 317–329.
- [135] Z. Mazej, I. Arčon, P. Benkič, A. Kodre and A. Tressaud, *Chemistry-A European Journal*, 2004, **10**, 5052–5058.
- [136] B. M. Wanklyn, F. R. Wondre, B. J. Garrard, J. Cermak and W. Davison, *Journal of Materials Science*, 1981, **16**, 2303–2309.
- [137] M. Leblanc, V. Maisonneuve and A. Tressaud, *Chemical reviews*, 2014, **115**, 1191–1254.
- [138] E. Banks, J. Deluca and O. Berkooz, *Journal of Solid State Chemistry*, 1973, **6**, 569–573.
- [139] E. Vincent and V. Dupuis, *arXiv preprint arXiv:1709.10293*, 2017.
- [140] I. Bakaimi, R. Brescia, C. M. Brown, A. A. Tsirlin, M. A. Green and A. Lappas, *Physical Review B*, 2016, **93**, 184422.
- [141] M. Harris and M. Zinkin, *Modern Physics Letters B*, 1996, **10**, 417–438.
- [142] M. Alba, J. Hammann, C. Jacoboni and C. Pappa, *Physics Letters A*, 1982, **89**, 423 – 426.
- [143] D. Enkler, A. Roters and M. Steiner, *Solid State Communications*, 1994, **92**, 481 – 484.
- [144] M. P. Zinkin, M. J. Harris and T. Zeiske, *Phys. Rev. B*, 1997, **56**, 11786–11790.
- [145] T. Zeiske, M. Harris and M. Zinkin, *Physica B: Condensed Matter*, 1997, **234**, 766–767.